First Search for the Standard Model Higgs Boson Using the Semileptonic Decay Channel: $H \rightarrow WW \rightarrow \mu\bar{\nu}jj$

Shannon Maura Zelitch
Elkins Park, PA

B.A., New College of Florida, 2000

A Dissertation presented to the Graduate Faculty
of the University of Virginia in Candidacy for the Degree of
Doctor of Philosophy

Department of Physics

University of Virginia
September, 2010

Abstract

This dissertation presents the first search for the standard model Higgs boson (H) in decay topologies containing a muon, an imbalance in transverse momentum ($\not{E}_{\mathrm{T}}$) and jets, using $p\bar{p}$ collisions at $\sqrt{s} = 1.96$ TeV with an integrated luminosity of 4.3 fb^{-1} recorded with the DØ detector at the Fermilab Tevatron Collider. This analysis is sensitive primary to contributions from Higgs bosons produced through gluon fusion, with subsequent decay $H \rightarrow WW \rightarrow \mu\nu jj$ where W represents a real or virtual W boson. In the absence of signal, limits are set at 95% confidence on the production and decay of the standard model Higgs boson for M_H in the range of $115 - 200$ GeV. For $M_H = 165$ GeV, the observed and expected limits are factors of 11.2 larger than the standard model value. Combining this channel with $e\nu jj$ final states and including earlier data to increase the integrated luminosity to 5.4 fb^{-1} produces observed(expected) limits of 5.5(3.8) times the standard model value.

Contents

1 Introduction 1

2 The Standard Model and the Role of the Higgs Boson 5
- 2.1 The Weak and Electromagnetic Forces: $SU(2)_{\mathrm{L}} \times U(1)_{\mathrm{Y}}$ . . . 7
- 2.2 The Strong Force : $SU(3)_{\mathrm{C}}$ . . . 8
- 2.3 The Mass-Free SM Lagrangian . . . 9
- 2.4 Broken Symmetry and the Higgs Mechanism . . . 11
  - 2.4.1 Discrete Symmetry Breaking . . . 11
  - 2.4.2 Continuous Symmetry Breaking and the Generation of a Massless spin 0 Goldstone Boson . . . 13
  - 2.4.3 Continuous Symmetry Breaking and the Creation of a Gauge Field and Massive Spin 0 Higgs Boson . . . 15
- 2.5 The Generation of Mass via the Higgs Mechanism . . . 18
- 2.6 Constraints on the Standard Model Higgs Boson . . . 25
  - 2.6.1 Constraints from Theory . . . 26
  - 2.6.2 Indirect Constraints from Electroweak Measurements . . . 28
  - 2.6.3 Constraints from Previous Direct Searches in Experiment . . . 30
- 2.7 The $H \to WW \to \mu\nu jj$ Channel . . . 33

3 The DZero Experiment 37
- 3.1 Detector Coordinate System . . . 39
- 3.2 Tracking . . . 41
- 3.3 Calorimeter . . . 44
- 3.4 Muon System . . . 49
- 3.5 Luminosity System . . . 52
- 3.6 Trigger and Data Acquisition System . . . 54
  - 3.6.1 Single Muon Triggers . . . 58
  - 3.6.2 Data Acquisition System . . . 60

4 Higgs Candidate Event Selection 61
- 4.1 Tracking . . . 62
- 4.2 Vertex Selection . . . 63
- 4.3 Jet Reconstruction . . . 65
  - 4.3.1 Jet Energy Scale . . . 68
  - 4.3.2 Jet Resolution . . . 72
- 4.4 Muon Reconstruction . . . 74
- 4.5 Electron Reconstruction . . . 77
- 4.6 Missing Transverse Energy ($\not\!\!E_{\mathrm{T}}$) Reconstruction . . . 79
- 4.7 Higgs Boson Reconstruction . . . 80
- 4.8 Event Selection Summary . . . 81
- 4.9 Event Counts after Selection . . . 82

5 Datasets and Simulated Samples 87
5.1 Recorded DØ Physics Data 87
5.2 Simulated Samples 87
5.2.1 Simulated Higgs Signal 90
5.2.2 Simulated Standard Model Background Processes 93

6 Simulated Sample Corrections and Normalization 96
6.1 Reconstruction Efficiency Corrections 96
6.2 Trigger Corrections 97
6.3 Luminosity and Beam-V_z Weighting 98
6.4 ALPGEN MLM matching Corrections 100
6.5 Jet-η Corrections 101
6.6 P_T^Z, P_T^W, and $\Delta R(j1, j2)$ Corrections 103
6.6.1 Various Distributions Before and After Application of Jet and P_T^W Weightings 107
6.6.2 Estimation of Systematic Uncertainties Corresponding to η^{jet}, p_T^W, and $\Delta R(j1, j2)$ Corrections 108
6.7 Monte Carlo Normalization 110
6.7.1 Normalization to Data 111

7 Combined SM Background Processes 113
7.1 Estimating the Multijet Background and V+Jets Contribution 113
7.2 Agreement between Data and Background 116

8 Multivariate Classification of Higgs Signal and SM Backgrounds 119
8.1 Decision Trees 120
8.2 Random Forest 121
8.2.1 Input Distributions 121
8.2.2 Training the Random Forest Classifier 124
8.2.3 Random Forest Output 125

9 Systematic Uncertainties 127
9.1 Flat Systematics 130
9.2 Shape Systematics 131

10 Upper Limits on SM Higgs Boson Production for the $H \to WW$ Semileptonic Decay Channel 140
10.1 CL_S Method of Limit-Setting 140
10.1.1 The Poisson Log-Likelihood Ratio 143
10.1.2 Constraints on Models of Systematics 146
10.1.3 The Profile Log-Likelihood Ratio 149
10.2 Limits for the $H \to WW \to \mu\nu jj$ Channel 150

10.3 Combined Limits for the Muon and Electron Semileptonic Decay Channels 156

11 Current Status and Future Outlook for SM Higgs Boson Searches at the Tevatron 162

12 Conclusions 168

A Random Forest Input Distributions 171

B RF Output Distributions 177

C Vector Boson Fusion in Comparison to Gluon-Fusion Signal 184

D Signal Sources in Addition to Gluon-Fusion $H \to WW \to \mu\nu jj$ 203

1 Introduction

In a universe without mass all particles travel at the speed of light, no atoms form, no planets develop and no life evolves. How do particles obtain their mass? Why are some particles more massive, and some less massive? What is the nature of mass?

The answers to these basic questions may arise from the solution to a problem in the standard model (SM) of particle physics - the mathematical model that describes the fundamental particles and the forces that act between them. In its most basic form, the standard model requires all force carriers to be massless, including the photon that moderates electromagnetic interactions - the attractive or repulsive force between ends of magnets, and the W, which mediates the weak force - the interaction of the neutron decaying to a proton plus lighter particles and hydrogen fusion in the sun. The weak force and the electromagnetic force are different manifestations of the electroweak force, however the photon is massless, but the W is observed in experiment to be one of the most massive elementary particles, indicating a central deficiency in the electroweak component of the standard model.

In 1967, the particle physicist Steven Weinberg proposed applying the relatively new Higgs mechanism (developed by Brout, Englert, Guralnik, Hagan, Higgs and Kibble in 1964) to the standard model expressions for the electroweak force carriers to explain this discrepancy [1] [2] [3] [4]. Beginning with a theory containing massless fields and an associated expression for their kinetic energy minus their potential energy (the Lagrangian), the Higgs mechanism is a series of algebraic manipulations of the Lagrangian to enforce that it is invariant under gauge transformations to all points in space-time (local gauge invariance). In requiring the local gauge invariance of the Lagrangian, additional terms arise giving mass to the W and Z electroweak force mediators, while the photon remains massless. The Lagrangian transformation also

creates an additional massive scalar field with interaction terms that couple it to each massive force carrier. Interpreting these additional terms in the Lagrangian: mass should no longer be thought of as an intrinsic property of a particle but as the result of an interaction between a particle and an invisible uniform field that saturates all space. Using the Higgs mechanism to express the Lagrangian, the manifestation of this field, a spin 0 particle known as the Higgs boson, interacts with massive particles, with the strength of the interaction scaling with the particle mass.

The Higgs boson is now the de facto component of the standard model for describing electroweak symmetry breaking but has yet to be verified by experiment. Particle physicists working at the Fermi National Accelerator Laboratory (Fermilab) in the U.S. and the European Organization for Nuclear Research (CERN) are in a heated race to find the Higgs boson, or prove that some other mechanism must be responsible for the generation of the masses of the bosons, and perhaps all massive elementary particles.

The precise mass of the Higgs boson is not predicted in the standard model, however its modes of decay to different sets of particles (decay channels) are calculable for a given M_H. Upper and lower bounds on its mass have been set by theory and experiment. A very low mass standard model Higgs boson ($M_H < 115$ GeV)[1] has been excluded at the 95% confidence level by the LEP [5] electron/positron collider experiments at CERN. Current theoretical predictions set an upper limit on the mass of the Higgs boson of 800 GeV, accessible only at CERN's Large Hadron Collider (LHC) but give preference (based on a variety of measurements) to a lighter Higgs ($M_H < 200$ GeV) that can also be produced at the Fermilab Tevatron.

The discovery of a standard model Higgs boson at any experiment would be con-

[1]It is common to refer to particle's mass in terms of its energy, from $E = mc^2$ setting the speed of light $c = 1$ by convention.

sidered a triumph for the standard model and will enable physicists to begin probing the origins of mass. Equally interesting is the possibility of no experiment finding a standard model Higgs boson. The standard model defines the properties of the Higgs boson and relates its mass to the masses of other particles measured in experiment, such as the top quark. If the properties or the mass of the particle observed is inconsistent with the constraints from the properties of other particles, that will definitively indicate some new type of physics beyond the standard model. With the possibility of new physics, the exclusion of a standard model Higgs boson becomes a goal as important as discovery.

The proton-antiproton ($p\bar{p}$) high energy[2] collisions at the Fermilab Tevatron influence which Higgs boson production mechanisms and decay channels can be most effectively utilized in searches by the DØ [6] and CDF [7] experiments, the two large detector collaborations at the Tevatron. Each experiment develops optimized analyses over probable decay channels, and results from the analyses are combined to set stringent limits on the production of a standard model Higgs boson. Given standard model expectations for Higgs boson production, the first hints of this elusive particle could appear at the Tevatron with fewer than 10 fb^{-1} of integrated luminosity[3].

This dissertation documents a search for the standard model Higgs boson using 4.3 fb^{-1} of data from the DØ detector experiment in a previously unutilized channel that contributes to the region of maximum sensitivity at the Tevatron, $H \rightarrow WW$ with final state: two jets[4], one muon and missing transverse energy. The results of combining this channel with one including an electron instead of a muon and adding earlier data are also shown. The $H \rightarrow WW \rightarrow \mu\nu jj$ final state[5] was included for the first

[2]The two beams collide with a center-of-mass energy of about 2 TeV, or 2×10^{12} electron-volts.

[3]A fb^{-1}of integrated luminosity translates to roughly 1.8 billion recorded $p\bar{p}$ collisions at DØ.

[4]One of the W bosons decays to a quark antiquark pair which create collated streams (jets) of particles as they begin to move apart.

[5]In our notation $\mu\nu$ may represent either the decay of $W^+(\bar{\mu}\nu)$ or $W^-(\mu\bar{\nu})$.

time in the July 2010 Tevatron combined limit on production of a standard model Higgs [8], excluding M_H in the mass range $158 - 175$ GeV at 95% confidence level. The inclusion of the semileptonic final states added an additional 6% to the combined Tevatron sensitivity at $M_H = 165$ GeV.

Chapter 2 introduces the standard model, followed by a description of the Higgs mechanism of electroweak symmetry breaking, current constraints on the standard model Higgs boson from theory and experiment, and an overview of the $H \rightarrow WW \rightarrow \mu\nu jj$ channel. A description of the DØ detector used to collect the data is presented in Chapter 3. The reconstruction of physics objects from the $p\bar{p}$ collision events and the physics object attributes required for an event to be selected for inclusion in this analysis are described in Chapter 4. Chapter 5 discusses the recorded data and simulated samples analyzed in this dissertation. The modeling of background processes that also leave a final state of $\mu\nu jj$ in the detector is discussed in Chapters 6−7. The random forest multivariate technique used to discriminate between Higgs-like events and background-like events is described in Chapter 8. Upper limits on the production of a standard model Higgs boson from the $H \rightarrow WW \rightarrow \mu\nu jj$ channel, the limit setting process, and the treatment of systematic uncertainties in this analysis are presented in Chapters 9−10. Finally, concluding sections discuss the current status and the future outlook for direct Higgs boson searches at the Tevatron.

2 The Standard Model and the Role of the Higgs Boson

The standard model (SM) is a gauge theory[6] of the twelve spin 1/2 fermions that make up the matter of the universe and the 12 spin 1 bosons that govern the fermion interactions.

The fermions are found in three generations of matter with increasing mass. Each generation includes an associated charged and neutral lepton, and two quarks. The properties of the standard model fermions are summarized in Table 1 [9].

Fermion Type	Generation			q(e)	J
Leptons	ν_e	ν_μ	ν_τ	0	1/2
	e	μ	τ	-1	1/2
Quarks	u	c	t	2/3	1/2
	d	s	b	-1/3	1/2

Table 1: Standard model fermions, q(e) is electric charge in units of proton charge, J is spin.

In particle physics the language of group theory is used to describe the properties of symmetries of the standard model sectors. Groups are described in terms of the number of $N \times N$ unitary matrices that form the group ($U(N)$). If the $U(N)$ matrices also have determinants equal to ± 1 the group is denoted $SU(N)$. The generators of a group allow for a complete representation of a group. Each generator is the sum or product of other group generators, with the number of generators of the group $SU(N)$ equal to $N^2 - 1$. The number of generators of a group that can be simultaneously diagonalized is said to be the *rank* of a group given by $N-1$. The three types of groups used to describe the standard model symmetries are $U(1), SU(2)$ and $SU(3)$ [10]. The group $U(1)$ has a single parameter θ and can be written $U = e^{-i\theta}$,

[6] In a gauge theory the Lagrangian is invariant under local gauge transformations to any space-time point: $\psi \rightarrow e^{i\theta(x)}\psi$.

the unit circle. An element of $SU(2)$ is described by two parameters, a Pauli matrix (σ_j) and a number (α_j) and can be written $U = e^{-i\sigma_j\alpha_j/2}$. The generators of the group $SU(2) = 2^2 - 1$ are the three Pauli spin matrices times 1/2, ($\frac{\sigma_j}{2}$) :

$$\sigma_1 = \begin{pmatrix} 0 & 1 \\ 1 & 0 \end{pmatrix} \quad \sigma_2 = \begin{pmatrix} 0 & -i \\ -i & 0 \end{pmatrix} \quad \sigma_3 = \begin{pmatrix} 1 & 0 \\ 0 & -1 \end{pmatrix} \tag{2.1}$$

$$\det = -1 \qquad \det = 1 \qquad \det = -1$$

where σ_3 is the $2 - 1 = rank1$ diagonal generator. The eight generators of $SU(3) = 3^2 - 1$ are the Gell-Mann matrices:

$$\lambda_1 = \begin{pmatrix} 0 & 1 & 0 \\ 1 & 0 & 0 \\ 0 & 0 & 0 \end{pmatrix} \qquad \lambda_2 = \begin{pmatrix} 0 & -i & 0 \\ -i & 0 & 0 \\ 0 & 0 & 0 \end{pmatrix} \tag{2.2}$$

$$\lambda_3 = \begin{pmatrix} 1 & 0 & 0 \\ 0 & -1 & 0 \\ 0 & 0 & 0 \end{pmatrix} \qquad \lambda_4 = \begin{pmatrix} 0 & 0 & 1 \\ 0 & 0 & 0 \\ 1 & 0 & 0 \end{pmatrix}$$

$$\lambda_5 = \begin{pmatrix} 0 & 0 & -i \\ 0 & 0 & 0 \\ i & 0 & 0 \end{pmatrix} \qquad \lambda_6 = \begin{pmatrix} 0 & 0 & 0 \\ 0 & 0 & 1 \\ 0 & 1 & 0 \end{pmatrix}$$

$$\lambda_7 = \begin{pmatrix} 0 & 0 & 0 \\ 0 & 0 & -i \\ 0 & i & 0 \end{pmatrix} \qquad \lambda_8 = \frac{1}{\sqrt{3}} \times \begin{pmatrix} 1 & 0 & 0 \\ 0 & 1 & 0 \\ 0 & 0 & -2 \end{pmatrix}$$

where λ_3 and λ_8 are the $3 - 1 = rank2$ diagonal generators.

The standard model has a gauge symmetry described by:

$SU(3)_{\mathrm{C}} \times SU(2)_{\mathrm{L}} \times U(1)_{\mathrm{Y}}$, where $SU(3)_{\mathrm{C}}$ is the symmetry group of the strong force,

$SU(2)_{\mathrm{L}}$ is the symmetry group of the weak force, and $U(1)_{\mathrm{Y}}$ is the symmetry group of the weak hypercharge, related to the symmetry of the electromagnetic force. The forces a fermion experiences and the interactions in which it participates depend upon the types of charge it carries. Quarks experience the strong force (via gluons), weak force (via $W^{\pm}$ and Z bosons), and electromagnetic forces (via photons). Leptons experience weak and electromagnetic forces.

Gauge Boson	q(e)	J	Symmetry Group	Interactions	Interacts With
γ	0	1	$U(1)_{\mathrm{Y}}$	Electromagnetic	charged particles
$W^{\pm}, Z$	$\pm 1, 0$	1	$SU(2)_{\mathrm{L}}$	Weak	quarks, leptons
gluons	0	1	$SU(3)_{\mathrm{C}}$	Strong	quarks

Table 2: Standard model gauge bosons listed with their associated electric charge: q(e), spin (J), symmetry group, the force they mediate and the particles with which they interact. Gluons, because they carry color charge, are self-interacting.

2.1 The Weak and Electromagnetic Forces: $SU(2)_{\mathrm{L}} \times U(1)_{\mathrm{Y}}$

There are three types of charge associated with the electromagnetic and weak force: electric charge (q), weak isospin (I) and weak hypercharge (Y). These charges are related via the Gell-Mann-Nishijima formula: $q = I_3 + Y/2$ where $I_3 = \pm\frac{1}{2}$ are the eigenvalues of the weak isospin $|\overrightarrow{I}|$.

The three gauge fields associated with the three $\sigma_j/2$ generators of the $SU(2)_{\mathrm{L}}$ symmetry group: $W^1_\mu, W^2_\mu, W^3_\mu$, with the field strength tensor: $W^i_{\mu\nu} = \partial_\mu W^i_\nu - \partial_\nu W^i_\mu + g\epsilon^{ijk} W^j_\mu W^k_\nu$. Here g is the $SU(2)_{\mathrm{L}}$ coupling strength, and ϵ^{ijk} (i,j,k = 1,2,3) is the antisymmetric tensor.[7]

The $U(1)_{\mathrm{Y}}$ group has one generator and one associated field: B_μ. Its field strength tensor has the more simple form: $B_{\mu\nu} = \partial_\mu B_\nu - \partial_\nu B_\mu$. The component of the standard

[7] ϵ^{ijk} will flip sign if any two indices are interchanged. This dissertation will also use the convention of Einstein notation in which repeated indices indicate summation.

model Lagrangian density from the electromagnetic and weak sector is:

$$\begin{aligned} L_{SU(2)_{\mathrm{L}}\times U(1)_{\mathrm{Y}}} = & -\frac{1}{4}W^{i}_{\mu\nu}W^{i\mu\nu} - \frac{1}{4}B_{\mu\nu}B^{\mu\nu} \qquad \text{(gauge interactions)} \\ & + \bar{L}_i i D^{\mathrm{EW}}_{\mu}\gamma^{\mu}L_i + \bar{e}_{Ri} i D^{\mathrm{EW}}_{\mu}\gamma^{\mu}e_{Ri} \qquad \text{(gauge} - \text{lepton int.)} \\ & + \bar{Q}_i i D^{\mathrm{EW}}_{\mu}\gamma^{\mu}Q_i \qquad \text{(gauge} - \text{quark int.)} \\ & + \bar{u}_{Ri} i D^{\mathrm{EW}}_{\mu}\gamma^{\mu}u_{Ri} + \bar{d}_{Ri} i D^{\mathrm{EW}}_{\mu}\gamma^{\mu}d_{Ri} \qquad \text{(gauge} - \text{quark int.)} \end{aligned} \tag{2.3}$$

where L_i is a left-handed lepton doublet, e_{Ri} a right handed lepton singlet, Q_i is a left-handed quark doublet and u_{Ri} and d_{Ri} are right handed quark singlets, γ^{μ} is the Dirac matrix[8] and D^{EM}_{μ} is the covariant derivative[9] [11] [12] [13].

2.2 The Strong Force : $SU(3)_{\mathrm{C}}$

The strong force governs the interactions of particles that carry color charge, gluons and quarks. The generators of the $SU(3)_{\mathrm{C}}$ symmetry group described above correspond to the eight color-carrying gluon fields $G^{1,2,\ldots,8}_{\mu}$. The field strength tensor of the strong force is: $G^{a}_{\mu\nu} = \partial_{\mu}G^{a}_{\nu} - \partial_{\nu}G^{a}_{\mu} + g_s f^{abc}G^{b}_{\mu}G^{c}_{\nu}$ where g_s is the coupling strength and f^{abc} are the structure constants defined in terms of the Gell-Mann matrices: $[\lambda_a, \lambda_b] = 2if^{abc}\lambda_c$ with $(a, b, c = 1, 2, ...8)$.

The component of the standard model Lagrangian density coming from $SU(3)_{\mathrm{C}}$ is

[8] The Dirac matricies are defined to be:

$$\gamma^0 = \begin{pmatrix} 0 & 1 \\ 1 & 0 \end{pmatrix} \qquad \gamma^i = \begin{pmatrix} 0 & \sigma_i \\ -\sigma_i & 0 \end{pmatrix}$$

[9] $D^{\mathrm{EM}}_{\mu} = \partial_{\mu} + ig\frac{\sigma^i}{2}W^i_{\mu} + \frac{ig'}{2}B_{\mu}$ where σ^i are the Pauli spin matrices and g' is the weak hypercharge coupling.

given by:

$$
\begin{aligned}
L_{SU(3)_{\mathrm{C}}} &= -\frac{1}{4}G^a_{\mu\nu}G^{a\mu\nu} && (\text{gluon} - \text{gluon interactions}) \\
&+ \bar{Q}_i i D^{\text{quark}}_\mu \gamma^\mu Q_i && (\text{quark} - \text{gluon interactions}) \\
&+ \bar{u}_{Ri} i D^{\text{quark}}_\mu \gamma^\mu u_{Ri} + \bar{d}_{Ri} i D^{\text{quark}}_\mu \gamma^\mu d_{Ri} && (\text{quark} - \text{gluon interactions})
\end{aligned} \tag{2.4}
$$

where Q_i is a left-handed quark doublet and u_{Ri} and d_{Ri} are right handed quark singlets, and D^{quark}_μ is the covariant derivative[10] [11] [12] [13].

2.3 The Mass-Free SM Lagrangian

Combining components of the standard model Lagrangian from the electromagnetic and weak sector (2.3) and the strong sector (2.4) yields:

$$
\begin{aligned}
L_{SM} = L_{SU(3)_{\mathrm{C}}} + L_{SU(2)_{\mathrm{L}}\times U(1)_{\mathrm{Y}}} &= -\frac{1}{4}G^a_{\mu\nu}G^{a\mu\nu} - \frac{1}{4}W^i_{\mu\nu}W^{i\mu\nu} - \frac{1}{4}B_{\mu\nu}B^{\mu\nu} \\
&+ \bar{L}_i i D^{\text{lepton}}_\mu \gamma^\mu L_i + \bar{e}_{Ri} i D^{\text{lepton}}_\mu \gamma^\mu e_{Ri} \\
&+ \bar{Q}_i i D^{\text{EW}}_\mu \gamma^\mu Q_i \\
&+ \bar{u}_{Ri} i D^{\text{EW}}_\mu \gamma^\mu u_{Ri} + \bar{d}_{Ri} i D^{\text{EW}}_\mu \gamma^\mu d_{Ri} \\
&+ \bar{Q}_i i D^{\text{quark}}_\mu \gamma^\mu Q_i \\
&+ \bar{u}_{Ri} i D^{\text{quark}}_\mu \gamma^\mu u_{Ri} + \bar{d}_{Ri} i D^{\text{quark}}_\mu \gamma^\mu d_{Ri}
\end{aligned} \tag{2.5}
$$

The resultant Lagrangian is invariant under $SU(3)_{\mathrm{C}}$ and $SU(2)_{\mathrm{L}} \times U(1)_{\mathrm{Y}}$ gauge transformations, however the fields are massless.

[10] $D^{\text{quark}}_\mu = \partial_\mu - ig_s \frac{\sigma^i}{2} G^a_\mu - ig \frac{\sigma^a}{2} W^a_\mu - ig' \frac{Y_{\text{quark}}}{2} B_\mu$

An attempt to add a fermion field mass term to the Lagrangian by hand gives [14]:

$$L_{\text{mass}} = -m\bar{\psi}\psi \tag{2.6}$$
$$= -m(\bar{\psi}_L\psi_R + \bar{\psi}_R\psi_L)$$

Here the fermion field ψ represents any standard model fermion. Table 3 shows how the left and right handed fermion fields from (2.6) transform, Table 4 shows the associated electroweak charges. L_i and Q_i transform as doublets under $SU(2)_{\text{L}}$ while e_{Ri}, u_{Ri} and d_{Ri} transform as singlets. Because of this transformation mis-match, our L_{SM} (2.5) is no longer gauge invariant under $SU(2)_{\text{L}} \times U(1)_{\text{Y}}$. The L_{SM} is still gauge invariant for $SU(3)_{\text{C}}$ because Q_i, u_{Ri} and d_{Ri} all transform as color triplets.

				$SU(3)_{\text{C}}$	$SU(2)_{\text{L}}$
L_i	$\begin{pmatrix} \nu_e \\ e \end{pmatrix}_L$	$\begin{pmatrix} \nu_\mu \\ \mu \end{pmatrix}_L$	$\begin{pmatrix} \nu_\tau \\ \tau \end{pmatrix}_L$	singlet	doublet
e_{Ri}	e_R	μ_R	τ_R	singlet	singlet
Q_i	$\begin{pmatrix} u \\ d \end{pmatrix}_L$	$\begin{pmatrix} c \\ s \end{pmatrix}_L$	$\begin{pmatrix} t \\ b \end{pmatrix}_L$	triplet	doublet
u_{Ri}	u_R	c_R	t_R	triplet	singlet
d_{Ri}	d_R	s_R	b_R	triplet	singlet

Table 3: Transformations under $SU(3)_{\text{C}}$ and $SU(2)_{\text{L}}$ for fermion left-handed doublets, lepton: (L_i), quark (Q_i) and fermion right-handed singlets, lepton: (e_{Ri}), quark: (u_{Ri},d_{Ri}).

Difficulties also arise when trying to add mass terms for the gauge fields [11]. Taking the gauge field transformation: $W^{i\mu}(x) \to W^{i\mu}(x) + \partial_\mu\alpha^i(x) + gf^{ijk}\alpha^j W^{k\mu}$ and adding a mass term of the form $L_{mass} = \frac{1}{2}M_W^2 W^i_\mu W^{i\mu}$:

$$\frac{1}{2}M_W^2 W^i_\mu W^{i\mu} \to \frac{1}{2}M_W^2(W^{i\mu} + \partial_\mu\alpha^i + gf^{ijk}\alpha^j W^{k\mu})(W^i_\mu + \partial^\mu\alpha_i + gf_{ijk}\alpha_j W_{k\mu})$$
$$= \frac{1}{2}M_W^2 W^i_\mu W^{i\mu} + \text{non} - \text{zero terms} \neq \frac{1}{2}M_W^2 W^i_\mu W^{i\mu}$$

Particles	q(e)	I_3	Y
$(\nu_e, \nu_\mu, \nu_\tau)$	0	1/2	-1
(e_L, μ_L, τ_L)	-1	-1/2	-1
(e_R, μ_R, τ_R)	-1	0	-2
(u_R, c_R, t_R)	2/3	0	4/3
(d_R, s_R, b_R)	-1/3	0	-2/3

Table 4: Fermion charges, electric: q(e), weak isospin: I_3, hypercharge: Y

The gauge field mass terms also violate $SU(2)_{\mathrm{L}} \times U(1)_{\mathrm{Y}}$ gauge invariance.

Fermion and gauge boson masses have been measured to be non-zero in experiment, so there are indeed mass terms in the Lagrangian, but these mass terms must break the $SU(2)_{\mathrm{L}} \times U(1)_{\mathrm{Y}}$ invariance. The Higgs mechanism for breaking the $SU(2)_{\mathrm{L}} \times U(1)_{\mathrm{Y}}$ gauge symmetry and adding mass terms to the L_{SM} is described in the next section.

2.4 Broken Symmetry and the Higgs Mechanism

To introduce the Higgs mechanism, we will first look at a simple example of symmetry breaking (Sec. 2.4.1), we will then expand upon the example and see how a broken continuous symmetry manifests as a massless spin 0 field (Sec. 2.4.2). Finally we will see how imposing a local gauge invariance under broken symmetry generates a massive spin 0 field (Sec. 2.4.3) [10] [11] [12] [13] [14].

2.4.1 Discrete Symmetry Breaking

Consider the Lagrangian:

$$L = \frac{1}{2}(\partial_\mu \phi)^2 - (\frac{1}{2}m^2\phi^2 + \frac{1}{4}\lambda\phi^4) \tag{2.7}$$

where ϕ is a real scalar field. The Lagrangian is symmetric under the transformation $\phi \to -\phi$. We find the minimum potential energy by setting $\partial V/\partial\phi = \phi(m^2+\lambda\phi^2) = 0$ and solving for ϕ. The two solutions are $\phi = 0$, and $\phi = \pm\sqrt{\frac{-m^2}{\lambda}}$. A choice of the second solution for the minimum potential will spontaneously break the $\phi \to -\phi$ symmetry intact in the Lagrangian. The choice of ϕ at minimum potential is known as the vacuum expectation value (v): $\pm\sqrt{\frac{-m^2}{\lambda}} = v$.

The Lagrangian can be re-written assuming that ϕ will have small fluctuations about v by using a field with a vacuum expectation value of 0: $\phi \to \chi(x) + v$, where $\chi = \phi - v$:

$$L_{\phi\to\chi+v} = \frac{1}{2}(\partial_\mu(\chi+v))^2 - \frac{1}{2}m^2(\chi+v)^2 - \frac{1}{4}\lambda(\chi+v)^2 \tag{2.8}$$

writing the mass in terms of the v: $m^2 = -\lambda v^2$ and treating v as a constant, the terms reduce to:

$$\begin{aligned}
&\frac{1}{2}(\partial_\mu(\chi+v))^2 \to \frac{1}{2}(\partial_\mu\chi)^2 \\
&\frac{1}{2}m^2(\chi+v)^2 \to \frac{1}{2}(-v^2\lambda)^2(\chi+v)^2 \to -\frac{\lambda v^2\chi^2}{2} - \lambda v^3\chi - \frac{\lambda v^4}{2} \\
&\frac{1}{4}\lambda(\chi+v)^2 \to \frac{\lambda\chi^4}{4} + \frac{3\lambda v^2\chi^2}{2} + \frac{\lambda v^4}{4} + \lambda v^3\chi + \lambda v\chi^3
\end{aligned}$$

The Lagrangian is now (ignoring constant terms):

$$L_{\phi\to+\chi+v} = \frac{1}{2}(\partial_\chi\phi)^2 - \frac{1}{2}(2\lambda v^2)\chi^2 \tag{2.9}$$

plus additional self-interaction terms of $\mathcal{O}^{3+}$. The form of the term $\frac{1}{2}(2\lambda v^2)\chi^2$ gives the mass of the χ field as $v\sqrt{2\lambda}$.

2.4.2 Continuous Symmetry Breaking and the Generation of a Massless spin 0 Goldstone Boson

The Goldstone theorem states whenever a transformation under a continuous symmetry group leaves the Lagrangian invariant but creates a non-zero vacuum expectation value, the theory will contain a spin zero massless particle [15]. The symmetry broken in Sec. 2.4.1 was discrete, not continuous. Expanding upon the above example, we can see the creation of a particle through symmetry breaking.

We define a complex field ϕ in terms of two real fields: $\phi = \frac{1}{\sqrt{2}}(\phi_1 + i\phi_2)$ and a Lagrangian of the form:

$$L = \partial_\mu \phi^\dagger \partial^\mu \phi - \left(m^2 \phi^\dagger \phi - \lambda(\phi^\dagger \phi)^2\right) \tag{2.10}$$

We minimize the potential with respect to $\phi^\dagger\phi$ and find $\phi^\dagger\phi = m^2/\lambda$. Substituting:

$$\partial_\mu \phi^\dagger \partial^\mu \phi = \frac{1}{2}(\partial_\mu \phi_1)^2 + \frac{1}{2}(\partial_\mu \phi_2)^2 \qquad \phi^\dagger \phi = \frac{1}{2}(\phi_1^2 + \phi_2^2) \tag{2.11}$$

we can write (2.10) as:

$$\frac{1}{2}(\partial_\mu \phi_1)^2 + \frac{1}{2}(\partial_\mu \phi_2)^2 - \frac{1}{2}m^2(\phi_1^2 + \phi_2^2) + \frac{1}{4}\lambda(\phi_1^4 + \phi_2^4) + \frac{1}{2}\lambda\phi_1^2\phi_2^2 \tag{2.12}$$

with potential:

$$V = \frac{1}{2}m^2(\phi_1^2 + \phi_2^2) - \frac{1}{4}\lambda(\phi_1^4 + \phi_2^4) - \frac{1}{2}\lambda\phi_1^2\phi_2^2 \tag{2.13}$$

The full Lagrangian is symmetric under the rotation $\phi_1 \leftrightarrow \phi_2$ which is a U(1) continuous symmetry. From the form of the minimum potential: $\partial_\mu \phi^\dagger \partial^\mu \phi = (\phi_1^2 + \phi_2^2) = m^2/\lambda$ a choice of a minimum of ϕ_1 or ϕ_2 will break this symmetry. If we choose $\phi_2 = 0$,

$\phi_1^2 = m^2/\lambda$ the vacuum expectation value is: $v = |m|/\sqrt{\lambda}$, $(v_1 = |m|/\sqrt{\lambda}, v_2 = 0)$.

Again we will write the Lagrangian assuming ϕ will have small fluctuations about v. Unlike the single scalar field in the first example, our ϕ is made up of two fields ϕ_1 and ϕ_2, thus we will write these fluctuations with respect to two fields, χ and ψ:

$$\phi = \frac{1}{\sqrt{2}}(\phi_1 + i\phi_2) \qquad\qquad \phi \to \frac{|m|}{\sqrt{\lambda}} + \frac{1}{\sqrt{2}}(\chi + i\psi) \tag{2.14}$$

Like the above example where $\phi \to v + \chi$, fields χ and ψ should be written so they each have a v of zero: $\chi = \phi_1 - v_1 = \phi_1 - |m|/\sqrt{\lambda} = \phi_1 - v$, $\chi = \phi_1 - v_2 = \phi_1 - 0$. Taking the original Lagrangian (2.12) and making the substitutions $\phi_1 \to \chi + |m|/\sqrt{\lambda}$, $\phi_2 \to \psi$:

$$\begin{aligned}
\frac{1}{2}(\partial_\mu\phi_1)^2 + \frac{1}{2}(\partial_\mu\phi_2)^2 &\to \frac{1}{2}(\partial_\mu\chi)^2 + \frac{1}{2}(\partial_\mu\psi)^2 \\
-\frac{1}{2}|m|^2(\phi_1^2 + \phi_2^2) &\to -\frac{1}{2}|m|^2(\chi^2 + \frac{2|m|\chi}{\sqrt{\lambda}} + \frac{|m|^2}{\lambda} + \psi^2) \\
\frac{1}{4}\lambda(\phi_1^4 + \phi_2^4) &\to \frac{1}{4}\lambda(\chi^4 + \frac{4|m|^2\chi^2}{\lambda} + \frac{|m|^4}{\lambda^2} + \frac{4|m|\chi^3}{\sqrt{\lambda}} + \frac{2|m|^2\chi^2}{\lambda} + \frac{4|m|^3\chi}{\lambda^{2/3}} + \psi^4) \\
\frac{1}{2}\lambda\phi_1^2\phi_2^2 &\to \frac{1}{2}\lambda(\psi^2\chi^2 + \psi^2\frac{2|m|\chi}{\sqrt{\lambda}} + \psi^2\frac{|m|^2}{\lambda})
\end{aligned}$$

We are interested in the masses of these fields, so we inspect those terms that are quadratic in ϕ_1 and ϕ_2, and ignore the interaction terms of $\mathcal{O}^3$ and higher:

$$\begin{aligned}
\frac{1}{2}(\partial_\mu\phi_1)^2 + \frac{1}{2}(\partial_\mu\phi_2)^2 &\to \frac{1}{2}(\partial_\mu\chi)^2 + \frac{1}{2}(\partial_\mu\psi)^2 \\
-\frac{1}{2}m^2(\phi_1^2 + \phi_2^2) &\to -\frac{1}{2}|m|^2\left(\chi^2 + \psi^2\right) \\
\frac{1}{4}\lambda(\phi_1^4 + \phi_2^4) &\to \frac{3}{2}|m|^2\chi^2 \\
\frac{1}{2}\lambda\phi_1^2\phi_2^2 &\to \frac{1}{2}|m|^2\psi^2
\end{aligned}$$

The Lagrangian is now:

$$L = \frac{1}{2}(\partial_\mu \chi)^2 + \frac{1}{2}(\partial_\mu \psi)^2 + \frac{1}{2}(2|m|^2)\chi^2 + \mathcal{O}^{3+} \tag{2.15}$$

The broken U(1) symmetry has left the Lagrangian with one massive scalar field, χ with mass $\sqrt{2}|m|$, and one massless scalar field (no quartic term in the Lagrangian), ψ, the spin 0 Goldstone Boson.

2.4.3 Continuous Symmetry Breaking and the Creation of a Gauge Field and Massive Spin 0 Higgs Boson

The Lagrangian (2.10) in Sec. 2.4.2 had a global U(1) symmetry and thus was invariant under the transformation: $\phi \rightarrow e^{-i\theta}\phi$. If we require that a Lagrangian : $L = \frac{1}{2}(\partial_\mu \phi)^2 - V(\phi)$ is invariant under the local gauge transformation: $\phi \rightarrow e^{-iq\theta(x)}\phi$, the field and its derivative no longer transform in the same way: $\partial_\mu(e^{-iq\theta(x)}\phi) = -iq\partial_\mu\theta(x)(e^{-iq\theta(x)}\phi) + e^{-iq\theta(x)}\partial_\mu\phi$. The Lagrangian will need additional terms in order to absorb the $-iq\partial_\mu\theta(x)(e^{-iq\theta(x)}\phi)$ resulting from this gauge transformation. To illustrate how these additional terms may be generated we will look at the Lagrangian of a charged particle in an electromagnetic field.

Electric and magnetic fields can be expressed in terms of a four-vector potential field A_μ [16]. The field strength tensor for A_μ is $F_{\mu\nu} = \partial_\mu A_\nu - \partial_\nu A_\mu$ and the Lagrangian for this gauge field is: $L = -\frac{1}{4}F_{\mu\nu}F^{\mu\nu}$. To include the interaction of A_μ with a particle ζ of charge q, the Lagrangian would have the additional Dirac kinetic energy and mass

terms for ζ, and an interaction term:

$$
\begin{aligned}
L &= L_{field} + L_{Dirac} + L_{interaction} \\
L_{field} &= -\frac{1}{4}F_{\mu\nu}F^{\mu\nu} \\
L_{Dirac} &= i\bar{\zeta}\gamma^{\mu}\partial_{\mu}\zeta - m\bar{\zeta}\zeta \\
L_{interaction} &= -q\bar{\zeta}\gamma^{\mu}\zeta A_{\mu}
\end{aligned}
\tag{2.16}
$$

Using the transformations: $\zeta \to e^{i\theta(x)}\zeta$ and $A_{\mu} \to A_{\mu}{}' = A_{\mu} - \frac{1}{q}\partial_{\mu}\theta(x)$:

$$
\begin{aligned}
L_{field} &\to -\frac{1}{4}[\partial_{\mu}(A_{\nu} - \frac{1}{q}\partial_{\nu}\theta) - \partial_{\nu}(A_{\mu} - \frac{1}{q}\partial_{\mu}\theta)][F^{\mu\nu'}] \\
&= -\frac{1}{4}[\partial_{\mu}A_{\nu} - \frac{1}{q}\partial_{\mu}\partial_{\nu}\theta - \partial_{\nu}A_{\mu} + \frac{1}{q}\partial_{\nu}\partial_{\mu}\theta][...] \\
&= -\frac{1}{4}[\partial_{\mu}A_{\nu} - \partial_{\nu}A_{\mu}][...]
\end{aligned}
\tag{2.17}
$$

$$
\begin{aligned}
L_{Dirac} &\to ie^{-i\theta}\bar{\zeta}\gamma^{\mu}\partial_{\mu}(e^{i\theta}\zeta) - me^{-i\theta}\bar{\zeta}e^{i\theta}\zeta \\
&= ie^{-i\theta}\bar{\zeta}\gamma^{\mu}[i\partial_{\mu}\theta e^{i\theta}\zeta + e^{i\theta}\partial_{\mu}\zeta] - m\bar{\zeta}\zeta \\
&= -\bar{\zeta}\gamma^{\mu}\zeta\partial_{\mu}\theta + i\bar{\zeta}\gamma^{\mu}\partial_{\mu}\zeta - m\bar{\zeta}\zeta
\end{aligned}
\tag{2.18}
$$

$$
\begin{aligned}
L_{interaction} &\to -qe^{-i\theta}\bar{\zeta}\gamma^{\mu}e^{i\theta}\zeta(A_{\mu} - \frac{1}{q}\partial_{\mu}\theta) \\
&= -q\bar{\zeta}\gamma^{\mu}\zeta A_{\mu} + \bar{\zeta}\gamma^{\mu}\zeta\partial_{\mu}\theta
\end{aligned}
\tag{2.19}
$$

Under this transformation, the extra terms from L_{Dirac} (2.18) and $L_{interaction}$ (2.19) cancel, leaving us with the original Lagrangian (2.16). Using the covariant derivative $D_{\mu}\zeta = \partial\mu + iqA_{\mu}$ we can now write a general Lagrangian for a complex scalar field ζ

and massless gauge field A_μ as:

$$L = -\frac{1}{4}F_{\mu\nu}F^{\mu\nu} + D_\mu\zeta^\dagger D^\mu\zeta - V(\zeta) \tag{2.20}$$

As in the example in Sec. 2.4.2, ζ can be written in terms of two real fields ϕ_1 and ϕ_2, thus we will write these fluctuations with respect to two fields, χ and ψ:

$$\zeta = \frac{1}{\sqrt{2}}(\phi_1 + i\phi_2) \qquad\qquad \zeta \to v + \frac{1}{\sqrt{2}}(\chi + i\psi) \tag{2.21}$$

where the form of v is dependent upon the minimum potential.

Expanding the $D_\mu\zeta^\dagger D^\mu\zeta$ term in the Lagrangian using $D_\mu\zeta = \partial\mu + iqA_\mu$ yeilds:

$$D_\mu\zeta^\dagger = [\partial_\mu + iqA_\mu][v + \frac{1}{\sqrt{2}}(\chi - i\psi)] = \partial_\mu v + \frac{\partial_\mu\chi}{\sqrt{2}} - \frac{i\partial_\mu\phi}{\sqrt{2}} + iqvA_\mu + \frac{iqA_\mu\chi}{\sqrt{2}} + \frac{qA_\mu\chi}{\sqrt{2}} \tag{2.22}$$

$$D^\mu\zeta = [\partial^\mu - iqA^\mu][v + \frac{1}{\sqrt{2}}(\chi + i\psi)] = \partial^\mu v + \frac{\partial^\mu\chi}{\sqrt{2}} + \frac{i\partial^\mu\phi}{\sqrt{2}} - iqvA^\mu - \frac{iqA^\mu\chi}{\sqrt{2}} + \frac{qA^\mu\chi}{\sqrt{2}}$$

Ignoring constant terms which have no impact on the Lagrangian and interaction terms of $\mathcal{O}^{3+}$ this reduces to:

$$D_\mu\zeta^\dagger D^\mu\zeta = \frac{1}{2}(\partial_\mu\chi)^2 + \frac{1}{2}(\partial_\mu\psi)^2 - \sqrt{2}qvA_\mu\partial^\mu\psi + q^2v^2A_\mu A^\mu \tag{2.23}$$

Inspecting the Lagrangian we now have five degrees of freedom, the two for χ and ψ that correspond to the original complex field ζ, and three for A_μ which now has additional degree of freedom beyond the two it had as a massless field. Because we must maintain the same total degrees of freedom, one of the degrees of freedom must not be real. We can make a gauge transformation to give the final Lagrangian a cleaner form. Using the fact that v is just a number, we define $v \to \frac{v'}{\sqrt{2}}$ and make the

gauge transformation:

$$A_\mu \to A_\mu - \frac{\partial_\mu \psi}{qv'}$$
$$-\sqrt{2}qvA_\mu \partial^\mu \psi \to qv' A_\mu \partial_m u\psi - (\partial_\mu \psi)^2$$
$$q^2 v^2 A_\mu A^\mu \to \frac{q^2 v'^2}{2} A_\mu A^\mu - qv' A_\mu \partial_\mu \psi - \frac{(\partial_\mu \psi)^2}{2}$$

This transformation, known as the unitary gauge, gives a final Lagrangian independent of ψ:

$$L = -\frac{1}{4}F_{\mu\nu}F^{\mu\nu} + \frac{1}{2}(\partial_\mu \chi)^2 + \frac{q^2 v'^2}{2} A_\mu A^\mu - V + \text{interaction terms} \tag{2.24}$$

Using the potential (2.13) from Sec. 2.4.2 this Lagrangian becomes:

$$L = -\frac{1}{4}F_{\mu\nu}F^{\mu\nu} + \frac{1}{2}(\partial_\mu \chi)^2 + \frac{q^2 v'^2}{2} A_\mu A^\mu + \frac{1}{2}(2m^2)\chi^2 + \text{interaction terms} \tag{2.25}$$

The massless Goldstone boson has disappeared: $\zeta \to \frac{v'}{\sqrt{2}} + \frac{\chi}{\sqrt{2}}$, leaving a massive scalar field χ ($m_\chi = \sqrt{2}m$) and a massive vector field A_μ ($m_A = qv$). The Goldstone theorem states whenever a transformation under a continuous symmetry group leaves the Lagrangian invariant but creates a non-zero vacuum expectation value, the theory will contain a spin 0 massless particle. Through the Higgs mechanism the massless scalar field resulting from spontaneous symmetry breaking of a local gauge can donate its degree of freedom to generate mass for a gauge field. [14]

2.5 The Generation of Mass via the Higgs Mechanism

If we look at the gauge bosons of the electromagenetic and weak sector of the standard model, we have three massive bosons: $W^\pm, Z$ and one massless boson, the photon.

We will need at least three donated degrees of freedom to make the $W^{\pm}, Z$ bosons massive, thus a doublet of complex fields with four associated scalar fields is used:

$$\Phi = \begin{pmatrix} \phi^{+} \\ \phi^{0} \end{pmatrix} \tag{2.26}$$

Starting with the electromagnetic and weak Lagrangian (2.3) from Sec. 2.1 we add the additional invariant terms:

$$D_{\mu}^{\mathrm{EM}}\Phi^{\dagger}D_{\mathrm{EM}}^{\mu}\Phi - m^{2}\Phi^{\dagger}\Phi - \lambda(\Phi^{\dagger}\Phi)^{2} \tag{2.27}$$

Following the prescription of the above sections, we choose a non-zero vacuum expectation value for ϕ^0 after minimizing the potential. As in the previous section we move to the unitary gauge and Φ is re-written:

$$\phi^{0} \rightarrow \frac{v'}{\sqrt{2}} + \frac{H(x)}{\sqrt{2}} \qquad\qquad \Phi \rightarrow \begin{pmatrix} 0 \\ \frac{v'}{\sqrt{2}} + \frac{H(x)}{\sqrt{2}} \end{pmatrix} \tag{2.28}$$

The real scalar field, $H(x)$, written in terms of small fluctuations of Φ about the vacuum expectation value is the Higgs boson. Properties of the Higgs field are summarized in Table 5. Using the methods of the previous section we will inspect the additional invariant terms added to $\mathrm{L}_{\mathrm{SU(2)_L \times U(1)_Y}}$ and see that the addition of the Φ terms leads to the masses of the $W^{\pm}, Z$ bosons and the mass of the Higgs boson itself.

Field	$SU(3)_{\mathrm{C}}$	$SU(2)_{\mathrm{L}}$
$\Phi = \begin{pmatrix} \phi^+ \\ \phi^0 \end{pmatrix}$	singlet	doublet
Field	q(e)	I_3
ϕ^+ ϕ^0	1 0	1/2 -1/2

Table 5: Properties of the spin zero standard model Higgs complex doublet, with charges, electric: q(e), weak isospin: I_3. The hypercharge of Φ is non-zero but does not have a predicted value.

Expanding Eqn. (2.27):

$$D_\mu^{\mathrm{EM}}\Phi^\dagger D_{\mathrm{EM}}^\mu\Phi = |D_\mu\Phi|^2 = \left|(\partial_\mu + ig\frac{\sigma_i}{2}W_\mu^i + \frac{ig'}{2}B_\mu)\begin{pmatrix} 0 \\ \frac{v'}{\sqrt{2}} + \frac{H(x)}{\sqrt{2}} \end{pmatrix}\right|^2$$

$$\partial_\mu\begin{pmatrix} 0 \\ \frac{v'}{\sqrt{2}} + \frac{H(x)}{\sqrt{2}} \end{pmatrix} = \begin{pmatrix} 0 \\ \frac{\partial_\mu v'}{\sqrt{2}} + \frac{\partial_\mu H}{\sqrt{2}} \end{pmatrix} \tag{2.29}$$

$$\begin{aligned} \frac{ig\sigma_i}{2}W_\mu^i\begin{pmatrix} 0 \\ \frac{v'}{\sqrt{2}} + \frac{H(x)}{\sqrt{2}} \end{pmatrix} &= \frac{ig}{2}\left(\sigma_1 W_\mu^1 + \sigma_2 W_\mu^2 + \sigma_3 W_\mu^3\right)\begin{pmatrix} 0 \\ \frac{v'}{\sqrt{2}} + \frac{H(x)}{\sqrt{2}} \end{pmatrix} \\ &= \frac{ig}{2}\begin{pmatrix} (W_\mu^1 - iW_\mu^2)(\frac{v'}{\sqrt{2}} + \frac{H(x)}{\sqrt{2}}) \\ -W_\mu^3(\frac{v'}{\sqrt{2}} + \frac{H(x)}{\sqrt{2}}) \end{pmatrix} \end{aligned} \tag{2.30}$$

$$\frac{ig'B_\mu}{2}\begin{pmatrix} 0 \\ \frac{v'}{\sqrt{2}} + \frac{H(x)}{\sqrt{2}} \end{pmatrix} = \begin{pmatrix} 0 \\ \frac{ig'B_\mu}{2}\left(\frac{v'}{\sqrt{2}} + \frac{H(x)}{\sqrt{2}}\right) \end{pmatrix} \tag{2.31}$$

Recall from Sec. 2.1 that W_μ^i are the fields associated with $SU(2)_{\mathrm{L}}$, B_μ is the field associated with $U(1)_{\mathrm{Y}}$, g is the $SU(2)_{\mathrm{L}}$ coupling strength and g' is the weak hypercharge

coupling. Putting the (2.29), (2.30), (2.31) components together:

$$|D_\mu\Phi|^2 = \left| \begin{array}{c} \frac{ig}{2}(W^1_\mu - iW^2_\mu)\left(\frac{v'}{\sqrt{2}} + \frac{H(x)}{\sqrt{2}}\right) \\ \frac{\partial_\mu v'}{\sqrt{2}} + \frac{\partial_\mu H}{\sqrt{2}} - \frac{ig}{2}W^3_\mu(\frac{v'}{\sqrt{2}} + \frac{H(x)}{\sqrt{2}}) + \frac{ig'B_\mu}{2}\left(\frac{v'}{\sqrt{2}} + \frac{H(x)}{\sqrt{2}}\right) \end{array} \right|^2 \tag{2.32}$$

$$|D_\mu\Phi|^2 = \frac{g^2}{8}(W^1_\mu - iW^2_\mu)^2(v'+H)^2 + \frac{(\partial_\mu H)^2}{2} + \frac{1}{8}(g'B_\mu - gW^3_\mu)^2(v'+H)^2 \tag{2.33}$$

dropping the constant term $\frac{(\partial_\mu v')^2}{2}$ which will not contribute to the Lagrangian. We define the $W^\pm_\mu$ (W boson), Z_μ (Z boson) and A_μ (photon) fields in terms of the $(v'+H)^2$ coefficients:

$$W^\pm_\mu = \frac{(W^1_\mu \mp iW^2_\mu)}{\sqrt{2}} \qquad Z_\mu = -\frac{(g'B_\mu - gW^3_\mu)}{\sqrt{g'^2+g^2}} \qquad A_\mu = \frac{(g'B_\mu + gW^3_\mu)}{\sqrt{g'^2+g^2}} \tag{2.34}$$

Inspecting (2.33) there are terms proportional to $(W_\mu)^2$ and $(\mathrm{Z}_\mu)^2$, but no term proportional to $(A_\mu)^2$:

$$\frac{g^2}{8}(W^1_\mu - iW^2_\mu)^2(v'+H)^2 = \frac{1}{2}\frac{v'^2g^2}{4}W^+_\mu W^{-\mu}(1+\frac{H}{v'})^2 \tag{2.35}$$

$$\frac{1}{8}(g'B_\mu - gW^3_\mu)^2(v'+H)^2 = \frac{1}{2}\frac{v'^2(g'^2+g^2)}{4}Z_\mu Z^\mu(1+\frac{H}{v'})^2 \tag{2.36}$$

From the terms quadratic in $W^\pm_\mu$ and Z_μ we see the W and Z bosons are massive, while the photon is massless:

$$M_W = \frac{v'g}{2} \qquad M_Z = \frac{v'\sqrt{g'^2+g^2}}{2} \qquad M_A = 0 \tag{2.37}$$

Expanding the term from (2.35):

$$\begin{aligned}\frac{1}{2}\frac{v'^2 g^2}{4}W_\mu^+ W^{-\mu}(1+\frac{H}{v'})^2 &= \frac{1}{2}(M_W)^2(1+\frac{H}{v'})^2 \\ &= \frac{1}{2}(M_W)^2(1+\frac{2H}{v'}+\frac{H^2}{v'^2})W_\mu^+ W^{-\mu} \\ &= \frac{1}{2}(M_W)^2 W_\mu^+ W^{-\mu} + \frac{(M_W)^2}{v'}HW_\mu^+ W^{-\mu} + \frac{(M_W)^2}{v'^2}H^2 W_\mu^+ W^{-\mu}\end{aligned}$$

one can also see that the couplings of form HVV are proportional to $\frac{M_V^2}{v'}$ and HHVV are proportional to $\frac{M_V^2}{v'^2}$ (where $V = Z$ or W).

The contribution to the Lagrangian from the potential (2.27) is:

$$V(\Phi) = m^2\Phi^\dagger\Phi + \lambda(\Phi^\dagger\Phi)^2 \tag{2.38}$$

$$m^2\Phi^\dagger\Phi \rightarrow \frac{1}{2}(m^2)(v'+H)^2 \tag{2.39}$$

$$\lambda(\Phi^\dagger\Phi)^2 \rightarrow \frac{\lambda}{4}(v'+H)^4 \tag{2.40}$$

The vacuum expectation value from minimizing the potential is $v'^2 = \frac{-m^2}{\lambda}$ where $m^2 < 0$, and we can re-write the potential with:

$$\begin{aligned}\frac{1}{2}(m^2)(v'+H)^2 &= \frac{-\lambda v'^4}{2} - \lambda v'^3 H - \frac{\lambda v'^2 H^2}{2} \\ \frac{\lambda}{4}(v'+H)^4 &= \frac{\lambda v'^4}{4} + \lambda v'^3 H + \frac{3\lambda v'^2 H^2}{2} + \lambda v' H^3 + \frac{\lambda H^4}{4}\end{aligned}$$

Ignoring the constant terms, this reduces to:

$$V = \lambda v'^2 H^2 + \lambda v' H^3 + \frac{\lambda H^4}{4} \tag{2.41}$$

Putting this together with the $\frac{(\partial_\mu H)^2}{2}$ term from (2.33), the mass of the Higgs boson,

kinetic and self-interaction terms of the Lagrangian are:

$$L_H = \frac{(\partial_\mu H)^2}{2} + \frac{1}{2}(-2m^2)H^2 - \lambda v' H^3 - \frac{\lambda H^4}{4} \tag{2.42}$$

Choosing the non-zero vacuum expectation value in the neutral ϕ^0 rather than the charged ϕ^+, we have an associated electromagenitc charge $q = 0$ for Φ, leaving the symmetry of $U(1)_{EM}$ unbroken.

$$SU(2)_{\mathrm{L}} \times U(1)_{\mathrm{Y}} \rightarrow U(1)_{\mathrm{EM}}$$

We now have three massive gauge bosons corresponding to the broken symmetry of $SU(2)_{\mathrm{L}}$ (3 generators), and one massless boson for the $U(1)_{\mathrm{EM}}$ (one generator) symmetry which is still conserved. Mass terms for the fermions can also be generated through a similar procedure using the same complex Higgs doublet.

The mass of the Higgs boson can be written in terms of the vacuum expectation value: $\sqrt{-2m^2} = \sqrt{2\lambda v'^2}$. The vacuum expectation value has been measured in experiment[11] to be $v' = 246$ GeV, while λ is yet unknown. As shown above, the strength of the Higgs-gauge boson coupling is proportional to M_V^2. Similarly, the strength of Higgs-fermion coupling is proportional to M_f (Fig. 1).

We have outlined the Higgs mechanism for generating masses through electroweak (EW) symmetry breaking for the standard model fermions and W and Z bosons while leaving the photon massless. While the fermion and boson masses predicted by the EW symmetry breaking are in agreement with current standard model observations,

[11] v' is related to the Fermi coupling G_μ measured in muon decay [17]:

$$\frac{G_\mu}{\sqrt{2}} = \frac{1}{2v'^2}$$

where $G_\mu = 1.16637 \times 10^5$ GeV^2 and $v' = 246$ GeV

a consequence of the EW symmetry breaking is the addition of new massive neutral scalar, the Higgs boson, which has not yet been observed in experiment. The current theoretical and experimental constraints on the standard model Higgs boson are discussed in the next section.

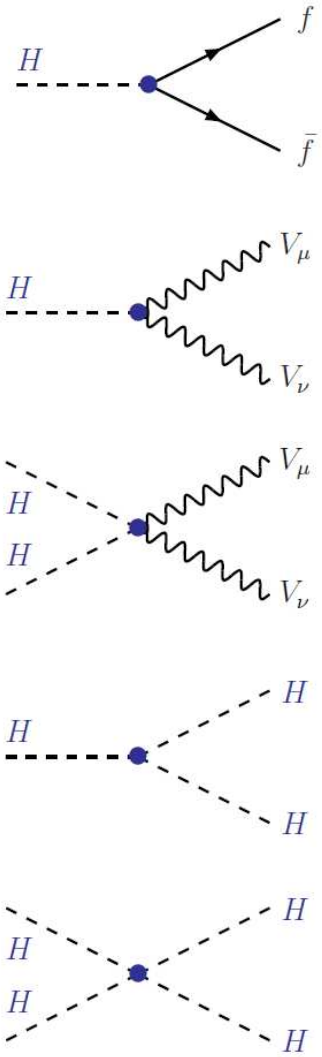

$$g_{Hff} = m_f/v = (\sqrt{2}G_\mu)^{1/2}\, m_f \qquad \times (i)$$

$$g_{HVV} = 2M_V^2/v = 2(\sqrt{2}G_\mu)^{1/2}\, M_V^2 \qquad \times (-ig_{\mu\nu})$$

$$g_{HHVV} = 2M_V^2/v^2 = 2\sqrt{2}G_\mu\, M_V^2 \qquad \times (-ig_{\mu\nu})$$

$$g_{HHH} = 3M_H^2/v = 3(\sqrt{2}G_\mu)^{1/2}\, M_H^2 \qquad \times (i)$$

$$g_{HHHH} = 3M_H^2/v^2 = 3\sqrt{2}G_\mu\, M_H^2 \qquad \times (i)$$

Figure 1: Coupling of the Higgs boson to standard model bosons and fermions with associated coupling strengths [11]. The couplings are given in terms of the vacuum expectation value, v, as well as the Fermi coupling constant, G_μ. The term $g_{\mu\nu}$ is the Minkowski metric. The branching ratio of ZZ is an order of magnitude smaller than WW over the entire range of the SM Higgs boson mass due to the reduced neutral current coupling size in comparison to charged current couplings [18]. Production cross sections for WW versus ZZ at the Fermilab Tevatron also reflect this factor of ten difference [19].

2.6 Constraints on the Standard Model Higgs Boson

The standard model does not predict a specific mass for the Higgs boson (M_H), but does predict the mechanisms for a standard model Higgs boson to be produced and to

decay in terms of M_H. From the interaction terms of L_{SM} the couplings of the Higgs boson to other standard model particles can be determined and production and decay mechanisms of the Higgs boson defined in terms of the particle masses. Constraints on M_H from theory and from direct and indirect observation by experiment will be discussed in this section[12].

2.6.1 Constraints from Theory

Although the standard model does not predict a precise mass for the Higgs boson, examination of the form of the Higgs potential leads to upper and lower bounds on M_H [14]. The scalar Higgs component of the SM Lagrangian in the previous section was:

$$L_H = \frac{(\partial_\mu H)^2}{2} + \frac{1}{2}(-2m^2)H^2 - \lambda v' H^3 - \frac{\lambda H^4}{4} \tag{2.43}$$

The self-interaction terms of $\mathcal{O}^{3+}$ are proportional to λ and the strength of the fourth order λ coupling will change as a function of an effective energy scale Q like[13]:

$$\frac{d\lambda}{dt} = \frac{3\lambda}{4\pi^2} \quad t \equiv log\left(\frac{Q^2}{Q_0^2}\right) \qquad \text{with the solution} \qquad \frac{1}{\lambda(Q)} = \frac{1}{\lambda(Q_0)} - \frac{3}{4\pi^2}\, log\left(\frac{Q^2}{Q_0^2}\right)$$

[12]This dissertation uses the convention of natural units. Setting $c = 1$, units of energy (eV) will be used for:

$$\text{Mass}: \frac{E}{c^2} \to E$$
$$\text{Momentum}: \frac{E}{c} \to E$$

[13]This comes from the simplification of the one-loop beta function for the top quark and gauge bosons, β_λ :

$$16\pi^2\beta_\lambda = 12\left(\lambda^2 - \left(\frac{M_t}{v'}\right)^4 + \lambda\left(\frac{M_t}{v'}\right)^2\right) - (3g'^2 + 9g^2)\lambda + \frac{9}{4}\left[\frac{g'^4}{3} + \frac{2g'^2g^2}{3} + g^4\right]$$

which reduces to $\beta_\lambda = (12\lambda^2)/(16\pi^2)$ when all non-Higgs couplings are ignored. Please see Ref. [20].

where Q_0 is some reference scale. The $\lambda(Q)$ must be positive for the Higgs potential to be bounded and finite for M_H to be bounded. Because $\lambda(Q)$ must be positive, we can re-write the expression using $Q_0 = v'$ to be:

$$\lambda(v') \leq \frac{4\pi^2}{3\ log\left(\frac{Q^2}{v'^2}\right)} \tag{2.44}$$

As $Q \to \infty, \lambda(v') \to 0$ and the potential no longer has interaction terms. From the mass term, λ can be written in terms of the M_H and v: $\lambda = M_H^2/(2v'^2)$.

$$M_H^2 \leq \frac{8\pi^2 v'^2}{3\ log\left(\frac{Q^2}{v'^2}\right)} \tag{2.45}$$

This states a Higgs boson of mass M_H is allowed by the standard model through an energy scale Q. This is sometimes referred to as the *triviality* of the Higgs potential.

Including the top quark and gauge bosons in the theory, one can put a more stringent upper bound on M_H. Taking M_H to be heavy such that $\lambda = \frac{M_H^2}{2v'^2} > M_t, g', g$ the expression for $\frac{d\lambda}{dt}$ becomes:

$$\frac{d\lambda}{dt} = \frac{12\lambda}{16\pi^2}\left(\lambda + \left(\frac{M_t}{v'}\right)^2 - \frac{1}{4}(g'^2 + 3g^2)\right) \tag{2.46}$$

From the form of $\frac{d\lambda}{dt}$ one can see that the expression will become negative if:

$$\frac{M_H^2}{2v'^2} = \lambda > \frac{1}{4}(g'^2 + 3g^2) - \left(\frac{M_t}{v'}\right)^2$$

at which point the potential is no longer bounded by the mass of the top quark and can continue to grow.

A lower bound on M_H can be found from exploiting the fact that λ must be positive

for all energy scales for the potential to be minimized and a vacuum expectation value found. Including the top quark and gauge bosons in the theory and inspecting $\frac{d\lambda}{dt}$ as $\lambda \to 0$ the expression becomes:

$$\frac{d\lambda}{dt} = \frac{3}{4\pi^2}\left(\frac{M_t}{v'}\right)^4 + \frac{9}{64\pi^2}\left[\frac{g'^4}{3} + \frac{2g'^2g^2}{3} + g^4\right] \quad \text{with the solution}$$
$$\lambda(Q) = \lambda(v') + \left[\frac{3}{4\pi^2}\left(\frac{M_t}{v'}\right)^4 + \frac{9}{64\pi^2}\left[\frac{g'^4}{3} + \frac{2g'^2g^2}{3} + g^4\right]\right] \; log\left(\frac{Q^2}{v'^2}\right)$$

Requiring that $\lambda(Q)$ must be positive, this can be re-written in terms of M_H:

$$M_H^2 > 2v'^2\left[\frac{3}{4\pi^2}\left(\frac{M_t}{v'}\right)^4 + \frac{9}{64\pi^2}\left[\frac{g'^4}{3} + \frac{2g'^2g^2}{3} + g^4\right]\right] \; log\left(\frac{Q^2}{v'^2}\right) \tag{2.47}$$

We now have an upper and lower bound on M_H dependent upon some energy scale Q. The standard model with the Higgs boson as described is only valid up to a cutoff energy Λ dependent upon M_H. Beyond Λ, perturbation theory can not be used to calculate production cross sections and decay widths for the Higgs boson [21]. If we take Q to be the energy scale (Λ) at which the standard model is no longer valid and new physics occurs, we can plot the range of M_H allowed as a function of Λ (Fig. 2).

2.6.2 Indirect Constraints from Electroweak Measurements

The masses of the W and Z bosons are sensitive to loop corrections from the top quark and the Higgs boson (Fig. 3). These corrections can be written in terms of the masses as [14]:

$$\left(\frac{M_W^2}{M_Z^2}\right) = 1 - \frac{\pi\alpha(M_Z)}{\sqrt{G_F}M_W^2(1 - function[M_t^2, \log(\mathrm{M_H})])} \tag{2.48}$$

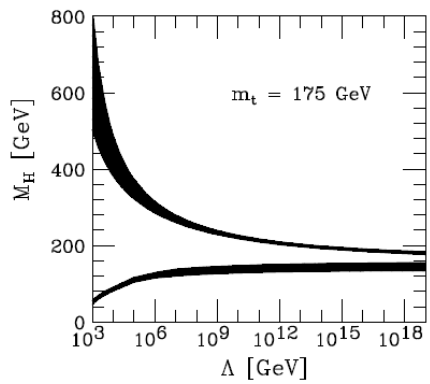

Figure 2: M_H vs. Λ for $M_t = 175$ GeV. The region above the upper band is derived from restriction $\lambda \neq \infty$, the region below is forbidden by the restriction $\lambda > 0$ [21] [14] [22].

Because the mass of the Z boson is already known within ± 21 MeV [9] the range of M_H allowed by the standard model can be constrained by precision measurements of the top quark and W boson masses. Figs. 4 and 5 show the constraints on M_H from combined measurements of M_t, M_W, and other electroweak observables at Fermilab, CERN and SLAC. A fit of electroweak precision data within the framework of the standard model yields:

$$M_H = 89^{+35}_{-26} \text{ GeV, or}$$

$$M_H < 158 \text{ GeV at the 95\% confidence level (C.L.)}$$

when including uncertainties from theory. [23]

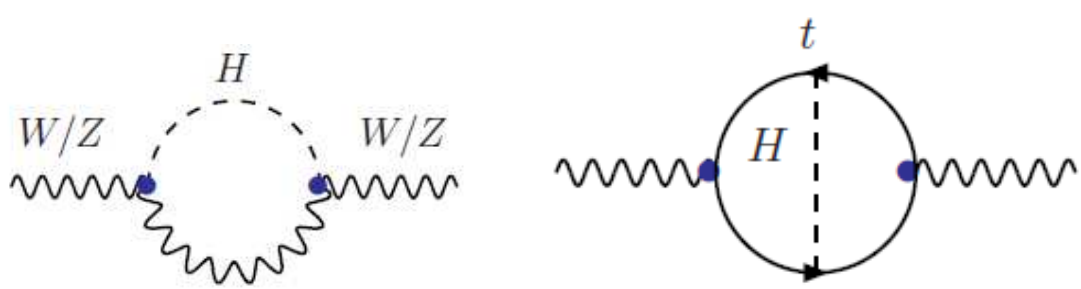

Figure 3: Loop corrections to W/Z from Higgs boson (H) and top quark (t). [11]

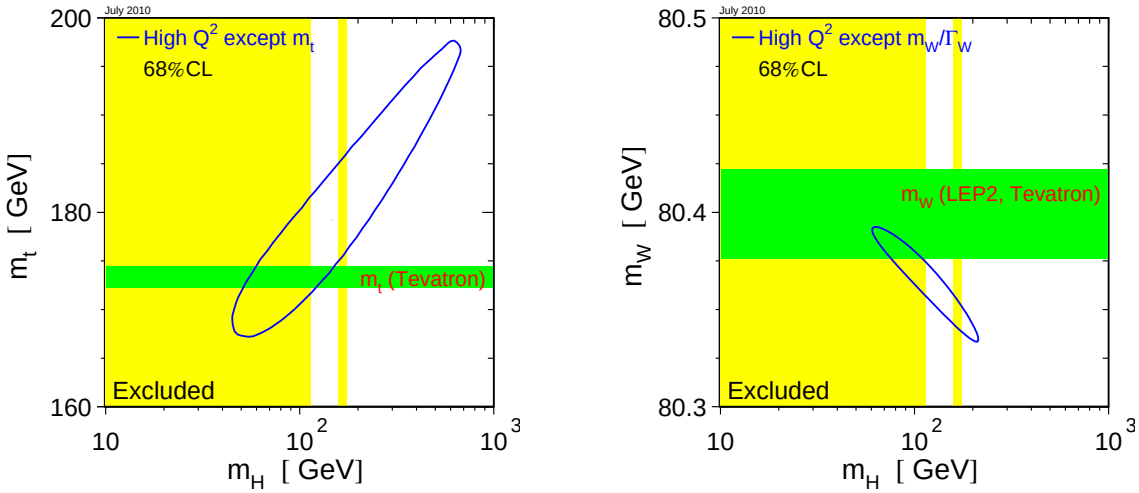

Figure 4: Left: M_t vs. M_H, the ellipse is the 68% confidence band on the allowed standard model M_H in terms of M_t based on electroweak observables (other than M_t) from LEP, SLAC and the Tevatron. The green band is the measured value of $M_t \pm 1\sigma$, the yellow bands are those M_H excluded by direct Higgs searches (see Sec. 2.6.3). Right plot: M_W vs. M_H.

2.6.3 Constraints from Previous Direct Searches in Experiment

Constraints on M_H exist from collider experiments at both CERN and Fermilab. The environment of a collider experiment strongly influences which production mechanisms and decay channels can be utilized to effectively search for the Higgs boson. Both the center-of-mass energy ($\sqrt{s}$), and the leptonic or hadronic composition of the colliding beams play a part in devising the most effective search strategies.

In 2003 experiments at the Large Electron Positron collider (LEP) at CERN reported a lower bound on the mass of the Higgs boson: $M_H > 114.4$ GeV at 95% C.L. using 2.46 fb^{-1} of data collected at $\sqrt{s}$= $189 - 209$ GeV [5]. Expectations based on the Higgsstrahlung process $e^+e^- \to HZ$, shown in Fig. 6, were used to set this limit.

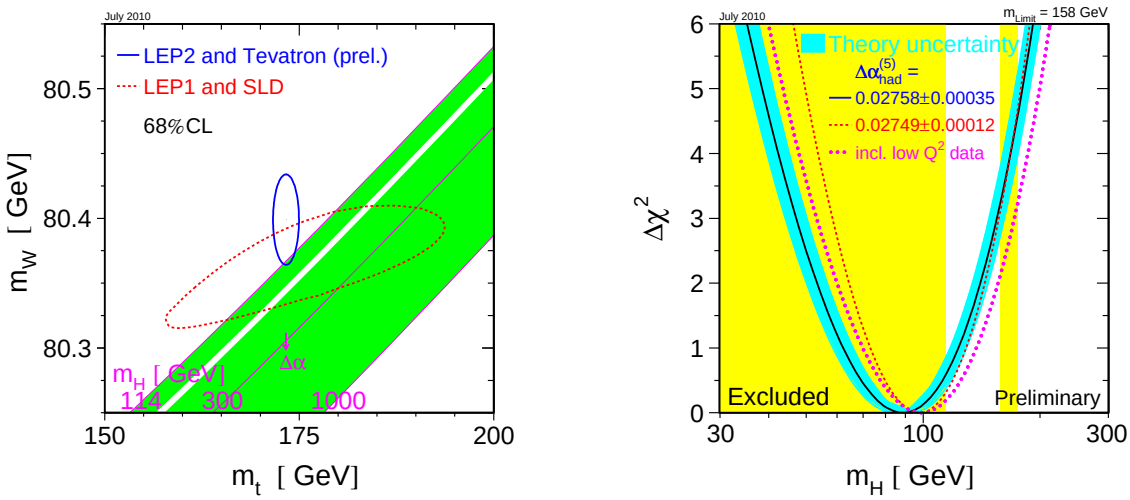

Figure 5: Left: 68% C.L. for the allowed SM region of M_W vs. M_t from direct measurements (solid ellipse) and indirect measurements (dashed ellipse). The band is the SM Higgs mass for each M_t, M_W point for $M_H < 1000$ GeV. The overlap of the ellipses and band is the expected M_H. The arrow represents the $\pm 1\sigma$ $\alpha(M_Z)$ uncertainty on M_H. Right: Minimized χ^2 fit to the EW data for M_H in black with a theory uncertainty band in turquoise. The lightly shaded bands are M_H regions excluded by direct search. [24]

Figure 7b shows branching ratios (BR) for decays of the standard model Higgs boson in terms of M_H. At the energies accessible to LEP, the dominant decay is $H \to \bar{b}b$ with a smaller contribution from $H \to \tau^+\tau^-$. The lower bound on the mass of the Higgs boson utilized multiple decay channels, with the largest contribution coming from the four-jet final state:$(H \to b\bar{b})(Z \to q\bar{q})$.

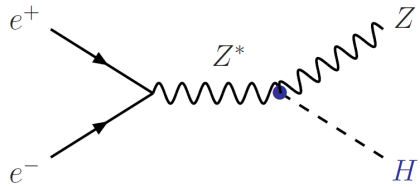

Figure 6: Standard model Higgs boson production process used in the LEP searches [11].

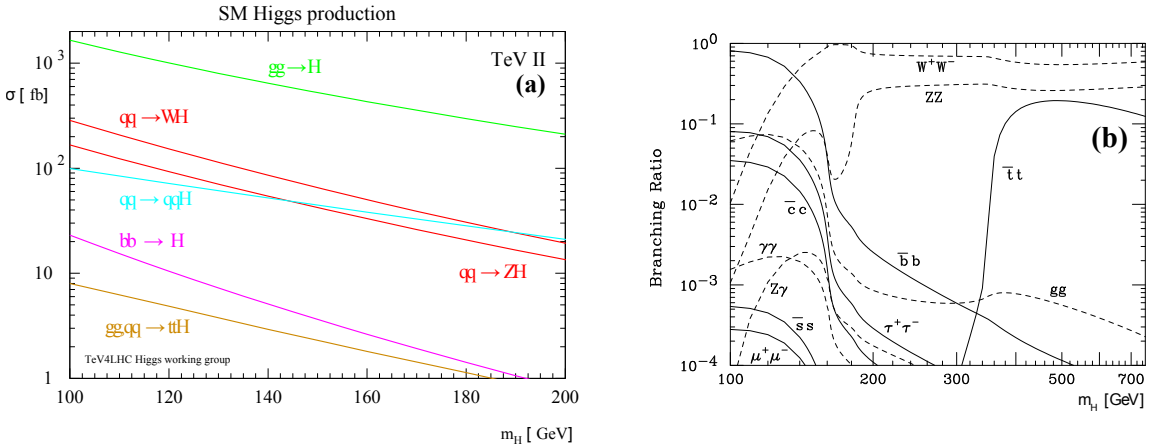

Figure 7: (a) Standard model Higgs boson production rates for the Tevatron ($\sqrt{s}$= 1.96 TeV) [25] and (b) branching ratios [26] as functions of M_H.

The maximum value of M_H accessible at LEP was bounded by the threshold: $M_{Hmax} < (\sqrt{s} - M_Z)$ with maximum $\sqrt{s} = 209$ GeV. The Fermilab Tevatron with $p\bar{p}$ collisions at $\sqrt{s} = 1.96$ TeV has expand the search, with masses up to $M_H \simeq 200$ GeV.

The three dominant production mechanisms used for direct searches at the Tevatron are gluon-gluon fusion, $gg \to H$, the associated production channels, $q\bar{q} \to VH$ where $VH = WH, ZH$, and vector boson fusion (VBF) $q\bar{q} \to q\bar{q}H$. Production cross sections for the Tevatron are shown in Fig. 7a. Feynman diagrams for the above processes are shown in Fig. 8.

Searches at the Tevatron utilize the decay modes: $H \to b\bar{b}$, $H \to \tau^+\tau^-$, $H \to \gamma\gamma$ and $H \to W^+W^-$ [27]. Branching ratios for $M_H < 140$ GeV are dominated by $H \to b\bar{b}$, for larger M_H the subsequent decay is mainly to pairs of vector bosons (Fig. 7b).

In fall of 2009 the CDF and DØ collaborations combined results from 90 separate Higgs searches using $2.01 - 5.4$ fb^{-1} of data and provided the first exclusions on the

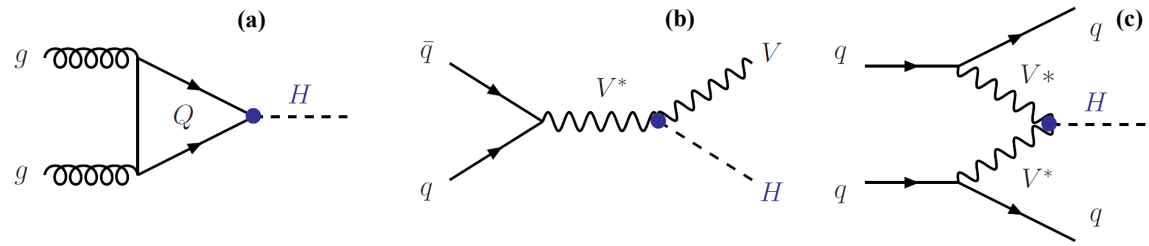

Figure 8: The three main Higgs production mechanisms used in direct searches at the Tevatron: (a) gluon-gluon fusion, (b) associated production and (c) vector boson fusion. In the diagrams q is a quark, Q is a heavy quark, and V represents a W or Z boson [11].

production of a standard model Higgs boson since LEP [27]:

$$163 < M_H < 166 \text{ GeV at } 95\% \text{ C.L.}$$

In July of 2010 the CDF and DØ collaborations combined results from 129 separate direct Higgs searches using 6.7 fb^{-1} of data and expanded the exclusion range to [8]:

$$158 < M_H < 175 \text{ GeV at } 95\% \text{ C.L.}$$

2.7 The $H \to WW \to \mu\nu jj$ Channel

The fall 2009 combined exclusion from CDF and DØ only utilized decays of $H \to WW$ with fully leptonic final states: $H \to WW \to \bar{\ell}\nu\ \ell'\bar{\nu}'$, where $\ell^{(\prime)} = e$ or μ. This dissertation presents the first search in the *semileptonic* decay channel: $H \to WW \to \mu\nu jj$. This channel was included in the July 2010 update of the combined limits from the Tevatron.

In the semileptonic decay of $H \to WW$ shown in Fig. 9, one W boson decays to a lepton and an associated neutrino, the other decays to a quark-antiquark pair that hadronizes into two jets of particles (Fig. 10). For $M_H < 2 \times M_W$ at least one W boson

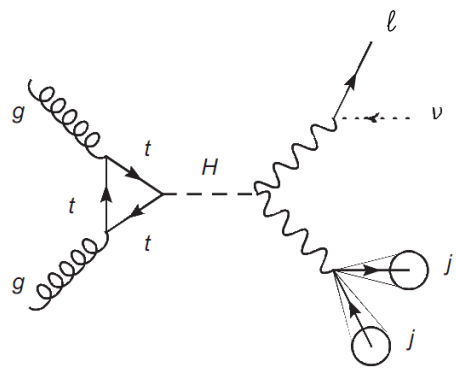

Figure 9: The semileptonic final state of $H \rightarrow WW$.

must be virtual. When the W boson that decays to leptons is close to on-shell, the p_z component of the neutrino can be calculated, and the $H \rightarrow WW \rightarrow \mu\nu jj$ mode can be fully reconstructed (Sec. 4.7). While the semileptonic channels must contend with increased backgrounds from W+jets final states, this is partially compensated by the increased branching fractions for hadronic decays of the W boson. In our region of maximum sensitivity, $M_H \approx 2 \times M_W$, the probability of a $H \rightarrow WW \rightarrow \ell\nu jj$ final state is a factor of four higher than the sum of the fully leptonic channels (Fig. 11a) [9].

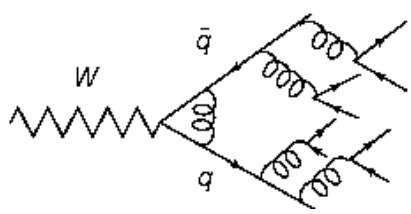

Figure 10: $W \rightarrow q\bar{q}$. The quarks originating from the deacy of the W radiate gluons that can create additional $q\bar{q}$ pairs. The parton showers form two distinct jets of hadrons.

In the W+jets background jets can originate from light quarks (u,d,s), or from heavy quarks (b,c). Figure 11b shows the cross section $\times$ branching ratio for the $H \rightarrow WW \rightarrow \mu\nu jj$ process along with its largest background, W+2 jets. After W+jets events, the second largest background comes from Z+jets events where $Z \rightarrow \mu\mu$ and one of the muons is not reconstructed in the event. Diboson events (WW,

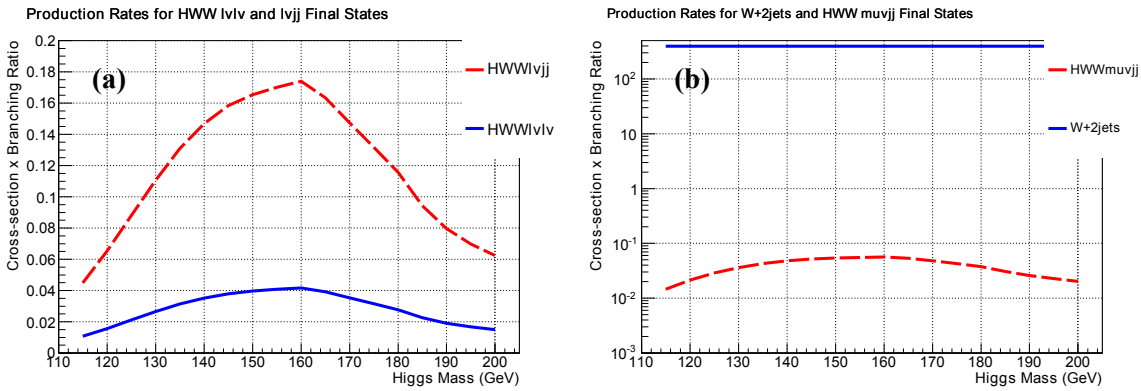

Figure 11: (a) Cross section $\times$ branching ratio for the $H \rightarrow WW \rightarrow \bar{\ell}\nu\ \ell'\bar{\nu}'$ (solid line) and $H \rightarrow WW \rightarrow \ell\nu jj$ (dashed line) decay channels as a function of M_H where $l = e$ or μ. (b) Log plot of cross section $\times$ branching ratio of the $H \rightarrow WW \rightarrow \mu\nu jj$ (dashed line) and W+2 jets (solid line) background process as a function of M_H [25] [26].

WZ, ZZ), top quark events (single top, $t\bar{t}$), and multijet events where one of the jets has a muon component can leave $\mu\nu jj$ signatures in the detector. These processes also have considerably larger production cross sections than $H \rightarrow WW$. The data, signal, and simulated background samples used in the $H \rightarrow WW \rightarrow \mu\nu jj$ analysis are discussed in Chapter 5. Corrections to background models for physics modeling and detector effects are described in Chapter 6. The multijet background is estimated from data, and the technique used to derive this background is discussed in Sec. 7.1.

The kinematics of the decays of Higgs bosons are different from other standard model processes with a $\mu\nu jj$ final state, and a number of physical quantities can be identified to discriminate between signal and background. Because the number of expected events from the decay of Higgs bosons is low in comparison to background standard model processes, this search uses a multivariate technique to enhance separation of signal from background.

Detailed studies of the background in the simulation and data are necessary to ensure that all major backgrounds are identified and well modeled. We choose distri-

butions that are well modeled in background data and sensitive to signal/background differences to train a random forest of decision trees that discriminate between the two types of events. This trained random forest is then tested on statistically independent sets of signal and background events, and on data. We compare the results from data with models based on background-only and signal+background events and set upper limits on the production of a standard model higgs boson. The output of the multivariate analysis from this channel is then combined with other analysis channels to maximize sensitivity to production of the standard model Higgs boson. The use of the random forest discriminant is explained in Chapter 8. Chapter 9 describes the sources of systematic uncertainties effecting this measurement, and Chapter 10 presents the limit setting procedure and results of the measurement.

The DØ detector used to collect the data utilized in the $H \rightarrow WW \rightarrow \mu\nu jj$ search is discussed in the next section.

3 The DZero Experiment

The data analyzed in this dissertation were collected with the DZero (DØ) detector, a multi-purpose particle detector located at the Fermilab Tevatron, the world's highest energy proton-antiproton ($p\bar{p}$) collider. This section contains an overview of the Fermilab accelerator chain that provides the high energy proton and antiproton beams to the Tevatron, followed by a brief description of the design and function of the major subsystems comprising the DØ detector.

An illustration of the Fermilab accelerator chain is shown in Fig. 12. In the first step of proton production, hydrogen gas striking a cesium target produces H^- ions that are collected and accelerated to a 750 keV beam by a Cockcroft-Walton accelerator. The H^- beam is further accelerated to 400 MeV and broken into bunches spaced 5 ns apart in a linear accelerator (Linac). The Linac provides a potential of 1 MV/meter and a pulse length of 20 ms accelerates the protons to 400 MeV.

The next acceleration stage is the Booster a, synchrotron accelerator using magnets to bend and focus the beam as it travels through the ring, and radio frequency (RF) cavities that impart energy to the traveling beam, adjusting frequency to beam velocity until the protons reach 8 GeV. As the H^- bunched beam is fed into the Booster it passes through a carbon foil which strips off the two electrons resulting in a beam of pure protons. Using this charge changing injection, the intensity of the circulating beam can be increased without increasing the phase-space area of the beam [28]. It takes protons 2.2 ms to travel the circumference of the Booster, allowing the protons to circulate thought the Booster multiple times before the next bunch of H^- ions exits the Linac. Following the Booster, the 8 GeV beam of protons then travels to the Main Injector synchrotron for acceleration up to 150 GeV for injection to the Tevatron, or to 120 GeV for antiproton production.

Antiproton production begins by colliding the 120 GeV proton beam with a fixed target made from nickel. Antiprotons are produced at the rate of 1 antiproton for every 5×10^4 incident protons with of a wide range of energies. These are focused by a lithium lens and sent through a RF cavity to produce a beam of more uniform energy. As antiprotons are accumulated, they are sent to the Recycler ring located inside the Main Injector ring for storage. When enough antiprotons have been accumulated, they are sent to the Main Injector which brings both the proton and antiproton beams to energies of 150 GeV before injecting them into the Tevatron [29] [30].

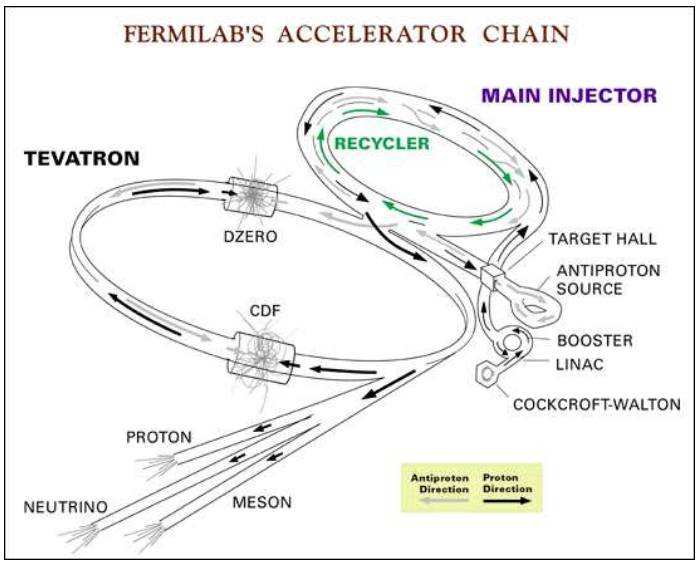

Figure 12: The Fermilab accelerator chain [31]. Proton beams are created from hydrogen gas. Antiprotons are created in collisions of a portion of the proton beam with a fixed nickel target. Protons and antiprotons circulate the Main Injector reaching beam energies of 150 GeV before being injected to the Tevatron. In the Tevatron ring each the beams are accelerated to energies of 980 GeV before colliding at the DZero and CDF detectors [31].

Data are collected in "stores" where 36 bunches of protons and 36 bunches of antiprotons are injected into the Tevatron Main Ring, accelerated to beam energies of 980 GeV, and then circulated for periods of $8-20$ hours. The bunches of protons and antiprotons travel in separate helical orbits in the ring, and are focused by quadrapole

magnets to collide at two interaction regions, one in the center of the DØ detector, and the other in the center of the Collider Detector at Fermilab (CDF), a second multi-purpose detector. The 36 bunches are split into three superbunches of 12, which are spaced 2.6 μs apart. The $p\bar{p}$ collisions have a center of mass energy ($\sqrt{s}$) of 1.96 TeV and occur every 392 ns as a superbunch passes through the interaction region (the DØ detector).

3.1 Detector Coordinate System

Figure 13 shows a side view of the DØ detector. The three major components of the detector are (from the beam line radially outward): a tracking system composed of silicon microstrips and scintillating fibers; a metal absorber/liquid-argon calorimeter system, and a muon system composed of drift tubes and scintillation counters [32]. A detailed description of the DØ detector can be found in Ref. [32].

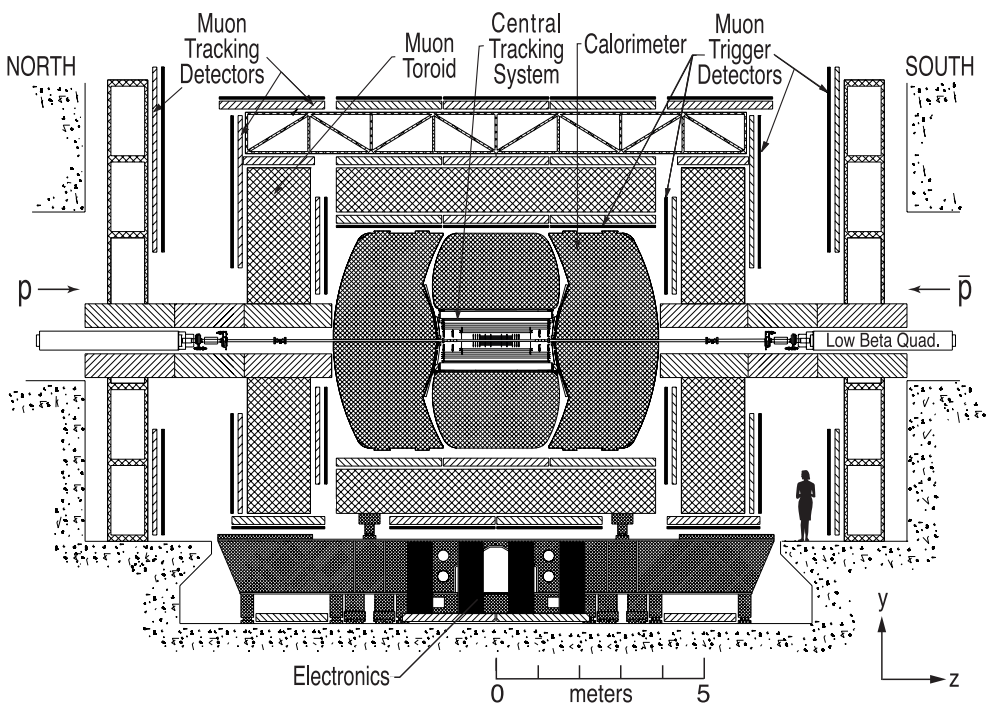

Figure 13: Sideview of the DØ detector with sub-detector systems labled. [32]

The coordinate system used to describe the DØ detector is defined as follows. The x-axis is in the direction away from the center of the Tevatron ring, the y-axis points upwards, and the z-axis points in the direction of the proton beam (Fig. 13). A cylindrical coordinate system (θ, ϕ, z) is typically used to describe locations within the detector. Again, z is in the direction of the proton beam, ϕ is the azimuthal angle about z, where $\phi = 0$ coincides with the $+x$ direction and $\phi = \frac{\pi}{2}$ coincides with the $+y$ direction, and θ is the polar angle from the $+z$-axis. Because the angle θ is not a Lorentz invariant quantity, the *rapidity* of a particle, (y) is used to describe particle trajectories and the distance between physics objects. A particle's rapidity is defined as [33]:

$$y = \frac{1}{2} \ln \left(\frac{E + p_z}{E - p_z} \right) = \frac{1}{2} \ln \left(\frac{1 + \beta \cos\theta}{1 - \beta \cos\theta} \right) \tag{3.1}$$

$$\beta \cos\theta = \tanh y \tag{3.2}$$

in terms of particle energy (E) and the particle's momentum in the direction of the beam line (p_z), or in terms of θ and $\beta = p/E$. In the limit of particle momentum $\gg$ mass, $\beta \to 1$ and (3.2) is rewritten as $\cos\theta = \tanh y$, which is a good approximation of the rapidity. The quantity *pseudorapidity* (η) is defined as the rapidity of a particle with zero mass, and can be written as:

$$\eta = -\ln \left(\tan \left(\frac{\theta}{2} \right) \right) \tag{3.3}$$

$$\beta \cos\theta = \tanh \eta \tag{3.4}$$

Pseudorapidity depends only on θ, the angle between a particle's momentum vector and the beam axis, and is also often used to describe the locations of detected objects and distance between two or more objects. Because proton-antiproton collisions do

not always occur in the center ($z = 0$) of the detector, a distinction is made between *detector eta* (η_{det}) which is calculated with respect to the center of the detector, and *physics eta* (η) which is calculated from the position of the proton-antiproton collision.

3.2 Tracking

The innermost DØ detector subsystems compose the central tracking system. These are arranged in a series of concentric cylinders radiating outward from the beam line. The DØ central tracking system uses information from two detectors, the Silicon Microstrip Tracker (SMT) and the Central Fiber Tracker (CFT). The SMT and CFT are enclosed within a solenoid magnet which curves the paths of charged particles with a momentum component transverse to the beam line, allowing for particle momenta measurement. The central tracking system records charged tracks with $|\eta| < 3$ and determines the location of the proton-antiproton primary interaction vertex with a resolution of 35 micrometers [32]. Precise measurements of kinematic quantities transverse to the beam line, such as transverse momentum: $p_T = \sqrt{p_x^2 + p_y^2} = p \sin\theta$ depend on the primary vertex resolution. Figure 14 shows a side view of the DØ tracking system. The tracking sub-components are described below.

- Silicon Microstrip Tracker (SMT)

  In the SMT, six 12 cm long barrel segments, each with four concentric silicon-based read-out layers, measure the radius (r) and ϕ of points (hits) along the tracks of charged particles. Twelve large diameter disks (F-disks) made of double sided silicon wedge-shaped detectors are interspersed with the barrels, and four larger diameter discs (H-disks) are located far forward in the detector to allow detection of tracks at high η [34] [32]. As charged particles pass through the SMT the absorbed energy ionizes the silicon, creating electron-hole pairs.

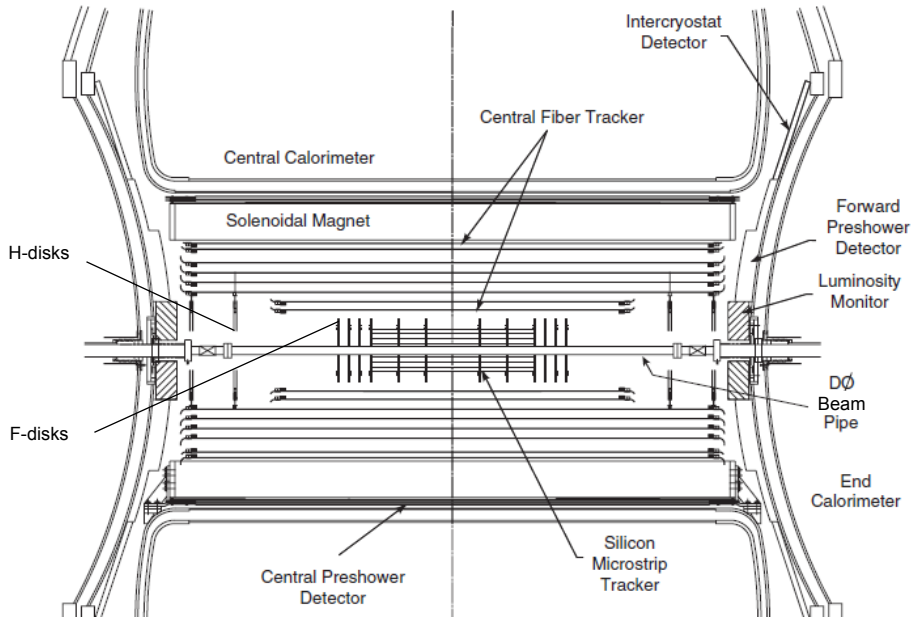

Figure 14: Sideview of the DØ tracking system with sub-detector systems labled. [32]

An electric field from applied voltage pulls these electrons to read-out strips where they are detected as signal current [9]. The locations of these currents in the SMT allow for the reconstruction of charged track position in the detector. The SMT barrel segments cover a radial range of 2.7 to 10.5 cm, the F-disks cover a radial range of 2.6 to 10.0 cm, and the H-disks cover 9.5 to 26.0 cm [32]. Two additional layers of single-sided silicon sensors are centered at radial distances of 16.1 mm and 17.6 mm from the beam line (Layer 0) [35].

· Central Fiber Tracker (CFT)

The CFT is composed of eight concentric cylinders of plastic scintillating fibers spanning the radial range of 20 to 52 cm from the center of the beam line. In each cylinder two layers of fibers run parallel to the beam line, and two layers are positioned at a 3° offset from parallel. This detector resolves tracks with a resolution of 100 μm and is used for fast triggering on track candidates above

a selected p_T threshold. The scintillating fibers are attached to clear fiber waveguides that transmit the light to visible light photon counters (VLPC). The attenuation length (distance over which the signal is attenuated to 1/e of its original value) for the scintillator fibers is 5m, where the fiber lengths are $1.7 - 2.5$m, and the clear fiber attenuation length is 8m with physical lengths of 8-12m [32]. As high energy particles traverse the scintillating fibers they leave a trail of excited polystyrene molecules. These molecules then release a small fraction of their excitation energy as ultraviolet photons. A doping agent in the fiber absorbs these UV photons and releases lower energy blue wavelength photons that are more efficiently transported by the clear fibers to the VLPC's. The VLPC's have an efficiency of $\geq 75\%$ and are can detect a single photon [9].

· Solenoidal Magnet

The solenoid magnet is located between the tracking and calorimetry systems. Two layers of wound superconducting Cu:NbTi strands provide a 1.9 T magnetic field parallel to the beam line. The magnet has a thickness of about one radiation length (discussed in Sec. 3.3) at $\eta = 0$ and is 1.42 m in diameter. Charged particles traveling through the magnetic field curve under the Lorentz force, and the radius of curvature (ρ) of a track is related to the transverse momentum of the track via :

$$p_T = \frac{0.3 \ \times \ B \ \times \ \rho}{\cos\lambda} \tag{3.5}$$

where λ is the angle traversed in one helical revolution with respect to a circular path (the pitch angle of the helical path) and $\cos\lambda \approx 1$ [9].

The relative momentum resolution of the tracking system for 1, 10 and 100 GeV tracks is given as a function of η in Figure 15.

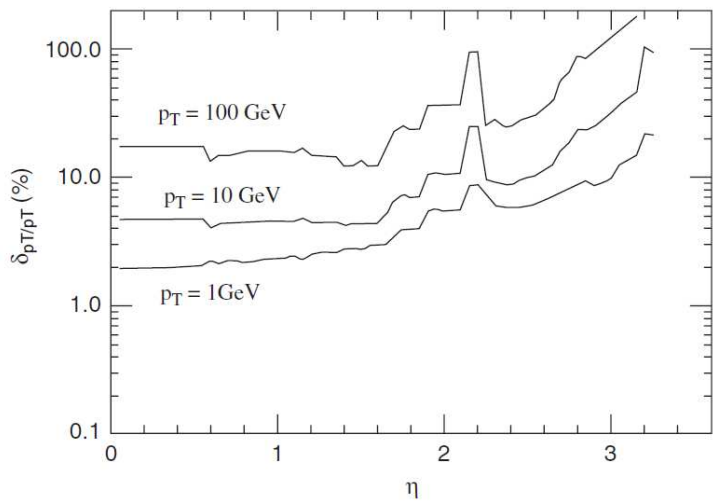

Figure 15: Resolution versus η for p_T = 1, 10, 100 GeV tracks in the DØ central tracking system. [32]

3.3 Calorimeter

DØ uses a sampling calorimeter to measure the energy of electrons, photons and jets, for particle identification and for the measurement of the transverse energy in an event for the identification of neutrinos. The calorimeter is composed of three major sections housed in separate cryostats. Each uses liquid argon as the active medium to sample ionization from electromagnetic and hadronic showers. The central calorimeter (CC) covers the region $|\eta| < 1.1$. The end calorimeters (EC) extend coverage to $|\eta| \approx 4$ for the EM calorimeter, and to $|\eta| \lesssim 5$ in the hadronic calorimeter. The innermost electromagnetic section (EM) uses uranium plates as the absorber material. It is followed by a fine hadronic (FH) section also using uranium plates and an outermost coarse hadronic (CH) section that uses copper and stainless steel absorber plates [36]. The DØ calorimeter shown in Fig. 16 is described in more detail below.

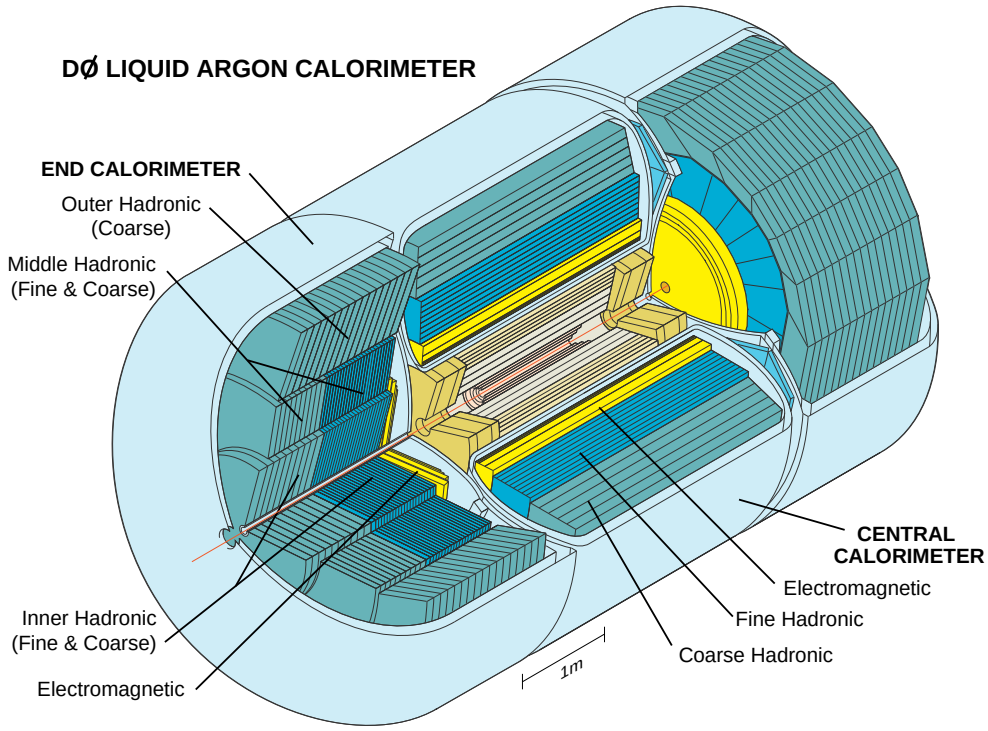

Figure 16: The DØ calorimeter. [32]

· EM Calorimeter

The EM central calorimeter covering $|\eta| < 1.1$ employs liquid argon interspersed with 3 mm depleted uranium plates as the absorber material. The EM end calorimeters extend the coverage to $|\eta| \approx 4$ and use 4 mm depleted uranium absorbers. When a high energy electron enters the uranium it looses its energy primarily through bremsstrahlung. A photon incident on the absorber will lose its energy primarily by e^+e^- pair production. The resulting cascade of lower energy electrons and photons has an approximate length scale determined by the radiation length (X_0) of the absorber material (see Table 6). For a given material, X_0 is defined to be the average distance a high energy electron travels before its remaining energy is reduced by a factor of $1 - e^{-1}$. High energy photons loose energy by pair production with a mean free path of $\frac{9}{7}X_0$ [9].

Showering particles ionize the liquid argon as they enter from the absorber material and the ionization electrons are collected on read-out cells held at positive potential relative to the absorber plates held at ground. The transverse sizes of the read-out cells are comparable to the transverse size of an EM shower given by the Molière radius (R_{M})[14] of the absorber material (see Table 6) and scale with η and the depth in the detector (r) [36]. The read-out cells are segmented in towers of $0.1\eta \times 0.1\phi$ through the calorimeter. The EM calorimeter is split into four layers spanning 20 X_0. The layer spanning $3.4 \rightarrow 10.2$ X_0 in the CC ($4.2 \rightarrow 12.1$ X_0 EC), contains (on average) the maximum energy density of the EM shower and its read-out is segmented twice as finely as the other depths (0.05×0.05 in $\Delta\eta \times \Delta\phi$). A shower in the EM calorimeter without a corresponding track in the SMT/CFT indicates a neutral particle such as a photon.

Material	X_0 (cm)	λ_{I} (cm)	R_{M} (cm)
Uranium	0.3166	11.03	1.009
Copper	1.436	15.32	1.568
Iron (steel)	1.757	16.77	1.719

Table 6: Radiation lengths (X_0), nuclear interaction lengths (λ_{I}), and Molière radii (R_{M}) for absorber materials used in the DØ calorimeter [38].

· Hadronic Calorimeter

The hadronic calorimeter measures energies of hadronic shower components that are not contained by the EM calorimeter (shown in Fig. 17). The fine hadronic section (FH) in the CC and EC uses 6 mm uranium absorber plates. The coarse hadronic (CH) section uses 46.5 mm absorber plates of copper (CC) or stainless steel (EC) [32]. Hadrons interact with the nuclei of the absorber

[14] 90% of the EM shower is longitudinally contained in 1 R_{M}, 99% is contained in 3 R_{M}. [37]

material, losing some of their energy breaking up nuclear bonds and creating secondary shower particles, mostly pions, but also protons, neutrons and other hadrons. The neutral pions decay to photon pairs, which can create high energy EM showers. Charged pions and kaons can decay to muons and neutrinos which interact minimally, or not at all with the calorimeter material [39] [9]. The resulting hadronic shower is both longer and wider than an EM cascade and 20-30% of its energy is undetectable, mainly lost to nuclear binding energies [37]. To accommodate the larger showers, the transverse read-out cell size in the hadronic calorimeter is larger than in the EM calorimeter. As in the EM calorimeter, the transverse cell sizes scale with η and r.

The length scale of hadronic showers are measured in terms of the nuclear interaction length (λ_{I}) which is considerably larger than X_0 for a given material (see Table 6). To accommodate the longer showers, the fine hadronic and coarse hadronic calorimeter sub-detectors are significantly larger than the EM calorimeter [39] [37] [40]. In the central calorimeter, the fine hadronic sub-detector is split into three layers of ($0.1\eta \times 0.1\phi$) segmented cells spanning 3.1 λ_{I}, the coarse hadronic central section has a single layer of 3.2 λ_{I}. In the EC, the inner calorimeter has four fine layers of 1.1 λ_{I}, and one coarse layer of 4.1 λ_{I}. The middle calorimeter has four fine 0.9 λ_{I} layers and one coarse layer of 4.4 λ_{I}. The outer hadronic portion of the EC consists of stainless steel plates inclined 60° with respect to the beam line with a total maximum thickness of 6 λ_{I} [32].

Because of the large and variable fraction of hadronic energy lost to nuclear breakup, the energy resolution of the hadronic calorimeter is worse than the resolution for the EM calorimeter. Comparing the single particle energy reso-

lution (σ_E/E) for an electron or pion in the DØ calorimeter [36] [37]:

$$e : \frac{\sigma_E}{E} = \frac{15\%}{\sqrt{E}} + 0.3\% \qquad \pi : \frac{\sigma_E}{E} = \frac{45\%}{\sqrt{E}} + 4\% \tag{3.6}$$

where the term of form $\frac{a}{\sqrt{E}}$ is the intrinsic resolution of the calorimeter, governed by the configuration and choice of absorber and ionizing material, and the constant term comes from the non-uniformity of the calorimeter response[15].

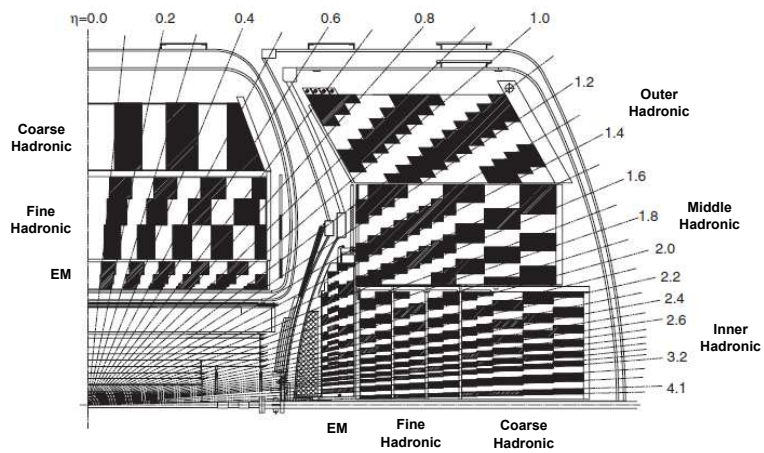

Figure 17: The DØ Calorimeter segmentation and η coverage. The projective $\eta \times \phi$ towers are shown as alternating shaded and white bands [32].

· Inter Cryostat Detector

The energy resolution degrades in the region between the central and forward calorimeters due to detector non-uniformity, and the presence of uninstrumented material due to the cryostat walls. The resolution of this inter-cryostat region is improved by the addition of a layer of 0.5 inch thick plastic scintillators of granularity $0.1\eta \times 0.1\phi$ to the region $1.1 < |\eta| < 1.4$ to sample shower energies between cryostats. The location of the Inter Cryostat Detector with respect to the EC and CC is shown in Figure 18. Energy resolution is further improved by

[15] A small additional term of form $\frac{b}{E}$ scaling with calorimeter noise has been neglected.

the addition of "massless gap" layers that sample ionization produced between the EC cryostat walls and the first layer of the calorimeter [32].

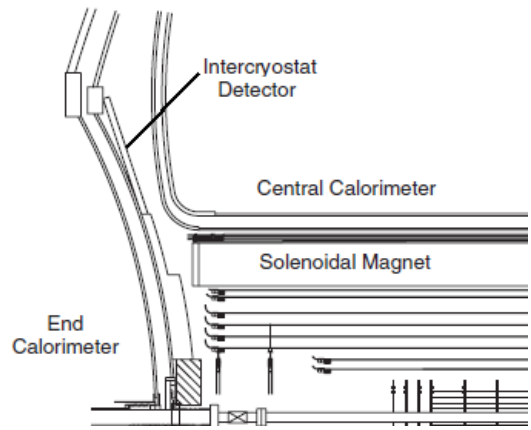

Figure 18: Location of the Inter Cryostat Detector. [32]

· Central and Forward Pre-shower Detectors

Electrons and photons may interact with the material of the solenoid before reaching the calorimeter, creating EM cascades before entering the calorimeter. Pre-shower detectors in this region aid in electron/pion separation and corrections to energy reconstruction in the upstream calorimeter. The central pre-shower detector covers the region $|\eta| < 1.3$ and is located between the solenoid and the central calorimeter. The forward pre-shower detectors cover $2.5 < |\eta| < 1.5$ and are attached to the inner surfaces of the end calorimeter cryostats.

3.4 Muon System

Muons are ≈ 200 times more massive than electrons and travel at lower velocities reducing relativistic effects that cause radiative energy loss. Consequently, the amount of bremsstrahlung radiation from muons is reduced in comparison to electrons, and

muons deposit minimal energy as ionization in the calorimeter [9]. The central and forward muon detectors comprise the outer-most subsystem of the DØ detector (Fig. 19). The central system includes a toroidal magnet, drift chambers and scintillation counters covering $|\eta| < 1$. The forward system provides coverage of $1 < |\eta| < 2$ and is comprised of end toroidal magnets, mini drift tubes (MDT) for track reconstruction, and scintillation counters.

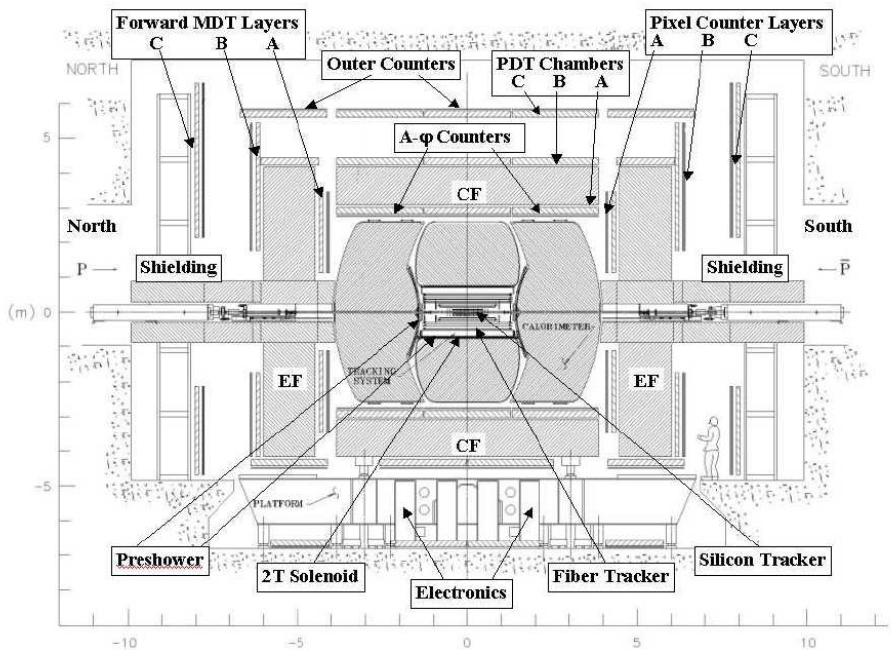

Figure 19: The DØ detector with muon sub-sytems labeled. [41]

· Central Muon System

The central muon system has three layers (A, B, C) of drift chambers composed of proportional drift tubes (PDT). Layer A is located within the toroidal magnet, B and C are outside the magnet. Each PDT is a 10 cm x 5.5 cm rectangular aluminum enclosure filled with a gas mixture of mostly Argon (with methane and CF_4). As a muon passes through a PDT it produces an ionization trail of electron-ion pairs in the gas. An applied electric field draws the freed

electrons towards an anode wire. Copper cathode pads above and below the anode wire collect ions and provide hit position information. As the electrons travel they continue to ionize the gas resulting in a cascade of charge reaching the anode. For each PDT hit the charge deposited on the cathode pads and the drift time between the hit and the anode charge collection (proportional to track - anode distance) is used to determine the path a muon takes in the detector [32] [9]. Scintillation counters (labeled A-ϕ in Fig. 19) cover the top and sides of the layer C drift chambers. These counters provide a timing signal to select muons associated with proton-antiproton collisions coincident with specific bunch-crossing times and "out-of-time" cosmic muons.

The central torriodal magnet (CF) and end torroidal magnets (EF) located between layers A and B (Figure 20) create fields of 1.8 T (CF) and 1.9 T (EF) parallel to the PDT arrays for muon momentum measurement. While the momentum measurement provided by the tracking system is more accurate, having an additional measurement from the muon system allows for more accurate matching of tracks between subsystems [41].

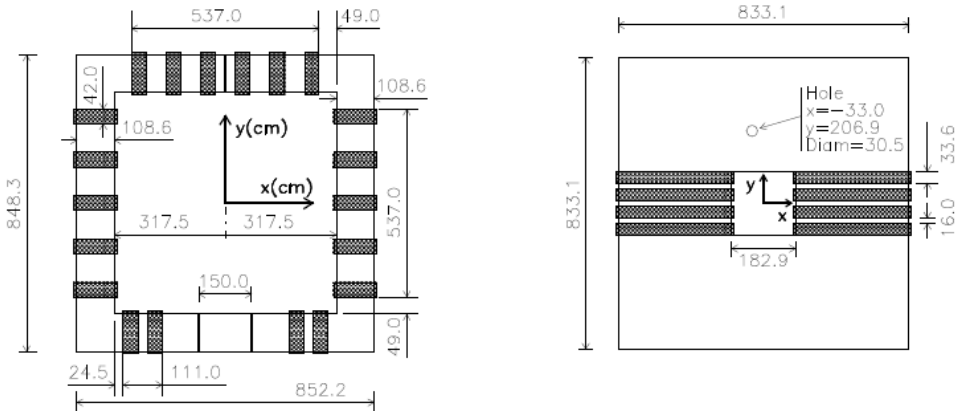

Figure 20: Right: central toroid magnet (CF) with 22 coils. Left: end toroid magnet (EF) with 8 coils. [41]

· Forward Muon System

The forward muon system is used to provide momentum measurements for muons that do not travel through all of the layers of the central tracker ($|\eta_\mu| > 1.6$) and is split into octants in ϕ. The MDT arrays of the forward muon system follow the same A,B,C structure of the central muon system. An MDT is similar to a PDT but is a 0.94 cm x 0.94 cm cross-section enclosure filled with a gas mixture of mostly carbon tetrafluoride, has a 90% shorter drift time and has a track position resolution of < 1 mm [41][32]. The scintillation counters (labeled Pixel Counter Layers A,B,C in Fig. 19) are more finely segmented than the central muon system counters to accommodate the larger backgrounds from beam halo and calorimeter punch through from high energy hadrons in the forward detector regions [41].

3.5 Luminosity System

The luminosity is determined by counting the number of inelastic $p\bar{p}$ collisions using two dedicated Luminosity Monitors (LM) located $\pm$ 140 cm from the center of the detector (see Figure 21). Each LM is a disk comprised of 24 plastic wedge-shaped scintillators covering an $|\eta|$ range of $2.7 - 4.4$ with an array of photo-multiplier tube (PMT) read-outs. An inelastic $p\bar{p}$ collision results in a cascade of particles produced along the beam line from the hard parton collision and the proton and antiproton remnants. The LM measures the position of $p\bar{p}$ collision in the detector ($\mathrm{V_z}$) from the difference in time-of-flight of particles hitting the two scintillator disks:

$$\mathrm{V_z} = \frac{\mathrm{c}}{2}\left(\mathrm{t}_{-140\mathrm{cm}} - \mathrm{t}_{+140\mathrm{cm}}\right) \tag{3.7}$$

Particles coming from a $p\bar{p}$ collision in the detector interaction region will have $V_z \approx 0$. Interactions that result from the beam halo (hadronic and electronic showers generated by beam particles escaping from the stable beam center and interacting with the beam pipe) must be excluded from the luminosity measurement [42]. Halo interactions are distinguished from $p\bar{p}$ interactions by requiring that $|\mathrm{V_z}| < 97$ cm. The LM time-of-flight resolution is ≈ 0.3 ns, with a V_z resolution of 6 cm [43] [32]. Instantaneous luminosity ($\mathcal{L}$) is related to the number of $p\bar{p}$ collisions, N by:

$$\mathcal{L} = \frac{1}{\sigma_{eff}} \frac{dN}{dt} \tag{3.8}$$

where the effective $p\bar{p}$ cross section (σ_{eff}), referred to as the luminosity constant, is related to the inelastic $p\bar{p}$ cross section via:

$$\sigma_{eff} = \sigma_{p\bar{p}} \times \epsilon \times A = 48.3 \pm 1.9 \pm 0.6\mathrm{mb}\ (10^{-27}\mathrm{cm}^2) \tag{3.9}$$

where A is the probability of the collision remnants to be in the η range of the LM (acceptance) and ϵ is the efficiency for the LM to record the event if the collision remnants are in the detector acceptance [43] [44][16]. Because of the difficulty of measuring the number of independent $p\bar{p}$ collisions in a single bunch crossing, the LM instead counts the number of bunch crossings where no collisions occur and determines the average number of crossings from Poission statistics.

Blocks of 60 seconds are used for instantaneous luminosity measurement (dt), with each sequential block of time receiving an incremented luminosity block number (LBN). To calculate the total luminosity accumulated for a period of data-taking, the instantaneous luminosity is integrated over time. The integrated luminosity for

[16]The first error on σ_{eff} is from the inelastic $p\bar{p}$ cross-section, the second is from Luminosity Monitor ϵ, A [44]

a given data set is used to normalize cross sections of physics processes based on the numbers of events observed.

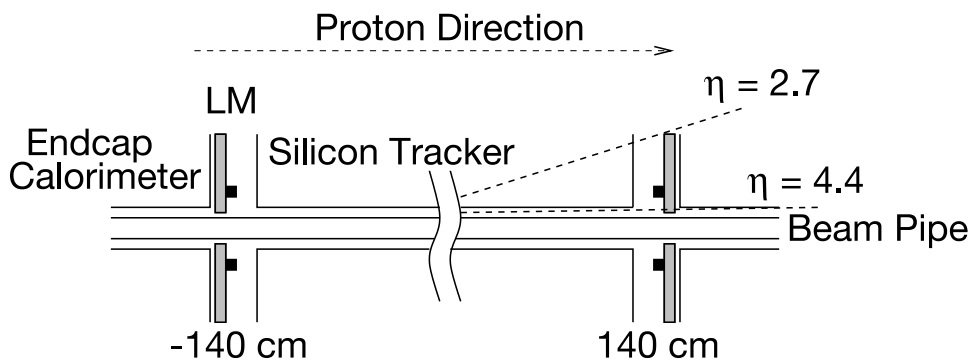

Figure 21: Position of the Luminosity Monitors in the DØ detector. [32]

3.6 Trigger and Data Acquisition System

During operation of the colliding beam there are 1.714×10^6 bunch crossings every second. From Eqn. (3.8), the number $p\bar{p}$ collisions per crossing is:

$$\int \mathcal{L} \times \sigma_{eff} \times dt = \int dN \tag{3.10}$$

For a store with luminosity of $\mathcal{L} = 350 \times 10^{30}$ cm^{-2}s^{-1} :

$$\frac{\langle \text{number of inelastic collisions} \rangle}{\text{bunch crossing}} = \frac{\mathcal{L} \times \sigma_{eff}}{\text{crossing rate}} \tag{3.11}$$

more than nine collisions are possible per crossing. This represents an overwhelming data rate on the order of Terrabytes/s. Given that the majority of these events do not produce data that are useful for further analysis, a three level triggering system is employed to reduce the 1.7 MHz collision rate to 200 events per second (200 Hz) written to tape. The trigger must perform selections in real-time to identify events

of interest while discarding the data from most of the collisions [45] [46]. The three levels of the DØ trigger are described below, and block diagrams of the DØ trigger and data flow are shown in Figs. 22−23.

- Level 1 Trigger (L1)

  L1 is a hardware-based trigger that analyzes read-outs from the sub-detector systems for features such as tracking hits that indicate a charged particle with high p_T, calorimeter transverse energy deposits above certain energy thresholds, and muons above certain p_T thresholds. The L1 system must evaluate data from collisions in real time to prevent loss of efficiency for physics signals of interest. Therefore, L1 algorithms are designed to be fast and inclusive, serving as a first pass in data selection. After L1, the rate of events accepted for further processing is reduced from 1.7 MHz to 1800 Hz.

  The DØ trigger framework (TFW) coordinates 128 programmable trigger terms from the L1 systems and makes the decision to reject the event, or pass the information to the L2 trigger. The TFW is also responsible for applying trigger prescales, which reduce the number of trigger accepts for more common processes to keep the rate passed to L2 ≈1800 Hz.

  The L1 Calorimeter Trigger (L1CAL) uses EM transverse energies in $\eta \times \phi$ regions in the EM calorimeter and total transverse energies from adding corresponding $\eta \times \phi$ regions in the EM and hadronic calorimeters. The L1 central track trigger (L1CTT) reconstructs the paths of charged particles using information from the CFT, and central and forward pre-shower detectors. L1CTT also stores sorted track lists and preshower clusters to be used directly in L2/L3 trigger decisions, or to be used as inputs for other for trigger systems. L1CalTrk matches energy clusters from L1Cal to L1CTT tracks. The L1Muon system

looks for patterns using hits from muon wire chambers matched to muon scintillation counters, and tracks matched from the L1CTT to the muon scintillation counters. Four separate muon p_T thresholds are used, and two sets of matching criteria: matching only in scintillator layer A, or matching in both A and B layers [32].

- Level 2 Trigger (L2)

  The average time available to examine events can be increased to ≈ 1 ms at L2 without introducing dead time in the data processing. The correlations between tracking and the calorimeter and muon objects are refined at L2 beyond the 128 L1 selections passed into the L2 Global (L2Global) processor. Trigger decisions are based on "global" physics objects made from direct inputs from L1, or by creating new objects in dedicated L2 sub-detector preprocessors. The Level 2 trigger contains a combination of dedicated hardware for data processing and embedded Linux-based systems running L2 analysis software. The rate is reduced from 1800 Hz entering L2 to 800 Hz passed to L3.

  The calorimeter preprocessor (L2Cal) identifies jets, EM objects and imbalances of transverse momentum in an event. The L2CTT improves the measurement of charged particle tracks from the CFT at L1 using inputs from the L1CTT and SMT barrels. L2CTT sends two track lists to L2Global, one sorted by p_T, and the other by perpendicular distance to the beam line (impact parameter) used for tagging decays of B-hadrons [32]. Two muon preprocessors use the L1Muon information from the PDT/scintillators of the central muon system (L2MUC) and MDT/scintillators of the forward muon system (L2MUF) to create track segments from small regions of the detector (track stubs) which are sent to L2Global. L2 muon candidates use timing information from the scintillators

relative to the beam crossing and track p_T, η, ϕ [32] [47].

· Level 3 Trigger (L3)

L3 is a software-based trigger running specific algorithms on a Linux-farm of 300 nodes to unpack raw data and reconstruct hits from (x, y, ϕ) positions into tracks to find vertices, and reconstruct EM objects, muons, jets, $\not\!\!E_{\mathrm{T}}$. The algorithms that are run depend on the particular L2 trigger decisions passed for the event and include p_T thresholds, hit requirements, and relationships between reconstructed objects. Algorithms used at L3 are similar to offline reconstruction algorithms described in Chapter 4. Hit positions are clustered, and track candidates are fit (see Sec. 4.1) from the outermost CFT or SMT layer to the innermost layer, requiring a minimum reconstructed track curvature based on the p_T of the reconstructed track (CFT) or minimized χ^2 (SMT). At L3 the primary vertex (V_z) is found with a 0.5 mm accuracy using CFT-tracks. Jets are reconstructed using a simple cone algorithm using calorimeter cell information (Sec. 4.3) and primary vertex position with $\not\!\!E_{\mathrm{T}}$ calculated with respect to the primary vertex position. L3 electrons are selected using clusters of $\eta \times \phi$ towers with minimum E_T requirements necessary to remain within data rates, and require that less than 10% of the energy of the cluster is associated with the hadronic calorimeter (Sec. 4.5). L3 muon track finding algorithms link track segments from wire and scintillator inside and outside the toroidal magnet based on regions defined at L2 to create 3D tracks. The vertex information at L3 improves muon momentum resolution over the $V_z = 0$ assumed at L2 and the improved muon momentum information is used for better cosmic-muon out-of-time hit rejection (Sec. 4.4). Missing E_T is calculated at L3 from sums of E_T of calorimeter cells in rings of constant η around the reconstructed vertex

(Sec. 4.6). At L3, the rate written to permanent storage is reduced to 200 Hz.

3.6.1 Single Muon Triggers

For an event to be written to tape it must satisfy the selection criteria applied at L1, L2 and L3. Events used in the $H \rightarrow WW \rightarrow \mu\nu jj$ analysis have satisfied at least one trigger from a suite triggers based on the requirement of at least one muon (SINGLE MUON triggers). Example L1, L2, L3 requirements from a SINGLE MUON trigger used in this analysis follow [48]:

- L1 Muon [49]:
  - $|\eta| < 1.6$
  - one matched scintillator hit in layers $A - \phi$ and $B - \phi$ (tight scintillator requirements)
  - one hit in drift-chamber layer A, matched to a scintillator hit in $A - \phi$ (loose wire requirements)
  - one matched scintillator hit in layer $A - \phi$ and one hit in drift-chamber layer A matched to a CTT track with $p_T > 13$ GeV.
- L2 Muon [50] [51]:
  - three PDT hits in layer A and three PDT hits in layer B or C (medium quality)
  - hits in the A, B, or C layer scintillator within 10ns of the beam crossing (tight scintillator timing)
  - $p_T > 3$ GeV

- OR -

- 3 PDT hits in layer A and 3 PDT hits in layer B or C (medium quality)
- no scintillator timing cuts
- matched to an STT/CTTtrack with $p_T > 8$ GeV, where $|\text{track}_\phi - \text{muon}_\phi| < \frac{\pi}{20}$.

· L3 Muon [52]:

- one scintillator hit and two wire hits in layer B or C, or a (wire or scintillator) hit in layer A and a (wire or scintillator) hit in layer B or C (loose quality)
- matched to a CFT/SMT track of ten or more hits with $p_T > 10$ GeV
- calorimeter energy in a hollow cone of $0.1 < \Delta R < 0.4$ around the muon matched track is under 2.5 GeV
- sum of p_T of all tracks in a hollow cone of $0.01 < \Delta R < 0.4$ around the muon matched track is under 2 GeV

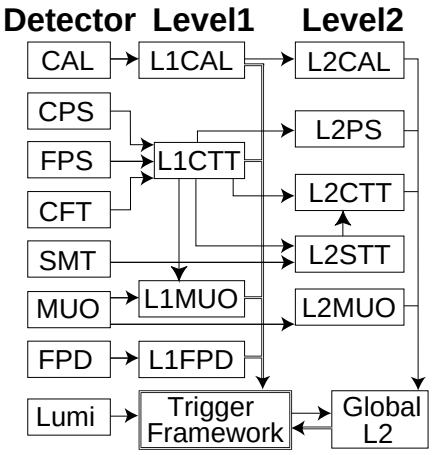

Figure 22: Block diagram of the DØ L1, L2 trigger system. Events passing L2 are sent to the L3 farm [32].

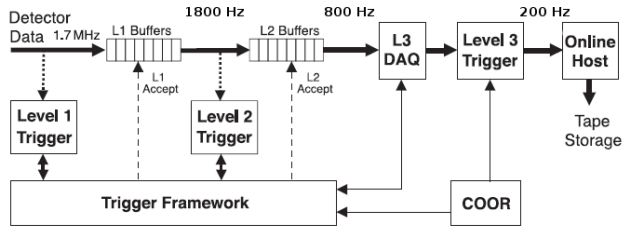

Figure 23: DØ data flow. Rates are reduced from 1.7 MHz to 1800 kHz at L1, from 1800 Hz to 800 Hz at L2, and from 800 Hz to 200 Hz written to tape at L3. L1 is hardware based with simple signatures in each sub-detector, L2 is software and firmware based with the formation of physics objects (e, μ, jets, tracks), L3 is software based with simple versions of the offline reconstruction algorithms [32].

3.6.2 Data Acquisition System

Physics data during colliding beam are recorded in $2-4$ hour periods called runs. Run control and detector configurations are handled by the central coordination program (COOR) of the data acquisition (DAQ) system. At the beginning of a run COOR receives input from users on which list of triggers and prescales to use and sends the necessary configuration commands to the rest of the system to carry out those requests. During a data taking run the online host system receives event data from L3 farm nodes and distributes that data to logging and monitoring programs examined in real time in the DØ detector control room. The DAQ system automatically pauses the current run if there is a problem with a detector subsystem that compromises data quality and sends a corresponding alarm to the monitoring systems. In addition to providing real time monitoring information to the DØ control room, the DAQ system records specific sub-detector monitoring information for post-collection data quality decisions. Event data is recorded to tape and marked with a unique identifier composed of the sequential run number and event number based on the order of events satisfying the trigger criteria, and maintained in a robotic tape system located in the Fermilab Feynman Computing Center [32] [53] where they are accessed for reconstruction and event analysis (Chapter 4).

4 Higgs Candidate Event Selection

After recording the data additional processing is required to fully reconstruct physics objects and to save the information in a format that is readily accessible for data analysis. The DØ Offline Reconstruction Program (DØRECO) [54] takes the trigger and detector signals from collider data or from simulations and creates the reconstructed physics objects that are used for analysis. The DØRECO program access the same information available at the L3 trigger without the processing time constraints, employing more precise reconstruction algorithms to extract the highest quality observables from data.

DØRECO associates sub-detector signals with specific positions in the detector, creating energy clusters in the calorimeter, and tracks in the CFT, SMT and muon system. Tracks are used to calculate the primary $p\bar{p}$ interaction vertex in the event, secondary vertices from overlapping $p\bar{p}$ collisions, and vertices displaced from the beam line resulting from the decay of long lived particles. The offline tracking algorithms used by DØRECO can require orders of magnitude more processing time than is available at the trigger level. Muons, EM objects, jets and $\not\!\!E_{\mathrm{T}}$ are also reconstructed using more sophisticated algorithms.

DØRECO outputs data for each event to a small event thumbnail (TMB) that is converted to the DØ Common Analysis Format (CAFe) [55] and stored for later analysis. These reduced data files contain all of the high quality physics objects and discard most of the original data from the detector facilitating rapid access to the entire DØ data set. CAFe is maintained by the DØ Common Samples Group [56]. Packages of C++ code compatible with the CAFe format are provided for physics object selection and corrections by various DØ working groups.

Object identification algorithms used in DØRECO for the tracks, primary vertices,

charged leptons, jets and $\not\!\!E_{\mathrm{T}}$ are briefly described in the following section, along with the physics object qualities necessary for the event to be selected for analysis.

4.1 Tracking

As charged particles traverse the silicon strips of the SMT and scintillating fibers of the CFT they curve under the influence of the solenoidal magnetic field. Two algorithms are run sequentially to reconstruct helical tracks from clusters of signal hits from the central tracking detectors: the Histogram Track Finder (HTF) (for higher p_T tracks) and the Alternative Algorithm (AA) (for lower p_T tracks). Unique reconstructed tracks are ordered by the number of hits, then by number of misses, then by the χ^2 of the fit hypotheses to the helical path [57] [58].

The HTF begins with a hit in a transverse plane of the detector and translates the (x, y) position into line of trajectories in track parameter space defined in terms of the track's curvature from the magnetic field (ρ, see Eqn. (3.5)) and its azimuthal angle (ϕ) with respect to the impact parameter at the point of closest approach to the axis of the beam. A 2-D histogram of (ϕ, ρ) cells are drawn with one line of cells filled for each hit in the transverse plane. The trajectory of the candidate track is the peak of the 2-D histogram (Fig. 24) [59].

The AA begins with a hit in three consecutive SMT barrel or disk layers beginning with the innermost layer. The first and second hit must have a $\Delta\phi < 0.08$ with respect to the axis of the beam. The helix defined by the third hit is required to have a minimum radius of $r_{min} = 30$ cm and maximum axial impact of $impactMax = 2.5$ cm measured from the position of the proton and antiproton beam overlap (beam spot) (Fig. 24). Additional hits in subsequent SMT layers are sought in an expectation window built from this "track hypothesis", where the fit of the hypothesis must satisfy

a maximum χ^2 requirement. If there is no hit in the expectation window, but there are hits in the detector layer, this is recorded as a "miss". The track hypothesis ends at the outer radius of the detector, or after three misses. Primary interaction vertices of the $p\bar{p}$ collisions (see Sec. 4.2) are found using AA tracks. Track candidates formed in the CFT follow a similar process, but have the additional requirement that the track hypothesis have a small impact parameter with respect to the primary vertex [58].

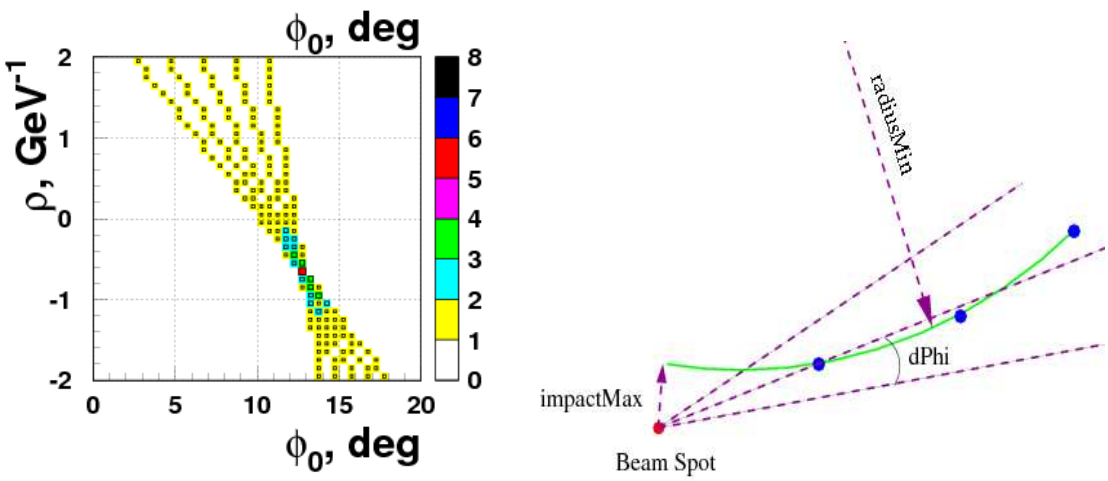

Figure 24: Left: HTF 2-D (ϕ, ρ) histogram of track trajectory projections. The peak of the histogram corresponds to the track candidate [59]. Right: Diagram of track parameters used the AA algorithm [58].

4.2 Vertex Selection

Multiple $p\bar{p}$ collisions are possible in each bunch crossing, and it is necessary to distinguish the location of the hard collision (referred to as the primary vertex, PV) from vertices reconstructed from tracks originating from overlapping soft collisions ("minimum bias" vertices). The PV position (V_z) is used to calculate p_T and $\not{E}_{\mathrm{T}}$ in an event, and jets selected for this analysis must have at least two tracks originating from the PV.

The DØ adaptive vertex fitting algorithm [60] is used to reconstruct primary and

secondary vertices from the reconstructed tracks described in Sec. 4.1. First tracks with $p_T > 0.5$ GeV, at least 2 SMT hits are fit into a common vertex to determine the approximate location and width of the beam. The sub-set of these tracks used for vertex reconstruction are selected using distance of closest approach significance: the distance of closest approach with respect to the beam position divided by the uncertainty on the distance of closest approach. A vertex is found for every cluster of tracks within a $\Delta z < 2$ cm span. For each of these vertices an iterative fit is performed, first a χ^2 is calculated for every track (including those tracks from outside the Δz) and the current vertex fit, and a weight is calculated for that track based on the associated χ^2. The vertex is then re-fit using the new track weights and the process is repeated. Tracks are discarded from the fit as their associated weights diminish, and the vertex fit is considered final when the change in total weights from one iteration to the next falls below a pre-set threshold.

Tracks originating from overlapping minimum bias interactions have a softer p_T spectrum than tracks from the hard collision. To select the PV for the hard collision from the minimum bias soft collision vertices a multiplicative probability based on track p_T is formed. The vertex found to have the lowest probability of being from minimum bias is designated the primary vertex [61].

The adaptive vertex fitting technique used to identify and reconstruct event vertices is nearly 100% efficient in PV selection in both DØ data and Monte Carlo [62].

In this analysis events are selected to have a PV:

- $V_z < 60$ cm. This ensures that the calorimeter towers are approximately projective for the developing jets.
- matched to at least three tracks.

4.3 Jet Reconstruction

In the $H \rightarrow WW \rightarrow \mu\nu jj$ analysis, one of the W bosons decays to a $q\bar{q}$ pair. The quarks each carry a single color charge, and due to color confinement, as the quarks move apart the potential from the color field of the gluon(s) connecting them becomes so great that $q\bar{q}$ pairs are pulled from the vacuum. Resultant quarks join together making a spray of colorless hadrons: mesons ($q\bar{q}$) and baryons (qqq). As discussed in Sec. 3.3, the sprays of hadrons deposit most of their energy in roughly collinear streams in the hadronic calorimeter.

The RunII cone algorithm clusters the energy deposits in towers of $\eta \times \phi$ cells in the hadronic calorimeter to identify the "jets" of particles coming from partons from the hard interaction, and separate them from the soft collisions resulting from beam remnants [63]. Each calorimeter cell is treated as a massless object and has an associated momentum four-vector made from its measured energy in the direction defined by the PV position and the cell center. The momentum four-vectors of all cells in a tower are summed, excluding those cells whose energy is below a signal noise threshold. Towers with more than one contributing cell are considered massive objects. Those towers with $p_T > 0.5$ GeV are used as seeds and clustered together with towers within $\sqrt{(\Delta y)^2 + (\Delta\phi)^2} < 0.3$ to make multi-tower pre-clusters with $p_T > 1$ GeV[17].

Beginning with the highest p_T pre-cluster, the momentum four-vectors of cells in all towers in a $\sqrt{(\Delta y)^2 + (\Delta\phi)^2} < 0.5$ cone are combined. The new p_T weighted cone center is the center of a proto-jet. The midpoints between all pairs of proto-jets are then used to search for additional proto-jets. This reduces the dependence of the algorithm on certain higher order effects [64]. This iterative process continues

[17]Here, y refers to rapidity.

until a list of stable proto-jets with $p_T > 3$ GeV is found. Proto-jets formed can have contributing towers that overlap, and must be split or merged to avoid double counting tower energies. In order of decreasing p_T, if the leading proto-jet overlaps with a trailing proto-jet, and 50% of the trailing proto-jet's p_T is contained within the leading proto-jet, the cells from all towers are summed and a new proto-jet is formed. Otherwise the shared cells are allocated to the proto-jet whose center is closer in $y \times \phi$ space. After this merging and splitting process, all jets with $p_T < 6$ GeV are discarded. Jets are matched with tracks in central tracking via $\Delta R = \sqrt{(\Delta\eta)^2 + (\Delta\phi)^2}$ requirements to either the jet axis, or single towers from the jet [63]. For additional details on the RunII cone algorithm see Ref. [64].

To confirm that reconstructed jets have originated from a hard collision and not from noise in the hadronic calorimeter, three additional jet identification criteria are imposed: at least 5% of the jet's energy must come from the EM calorimeter ($EMfraction > 0.05$), and less than 40% of the jet's energy can come from the coarse hadronic calorimeter ($CHfraction < 0.40$), there is also a requirement that the p_T from the calorimeter at reconstruction corresponds to the p_T at the L1 trigger [65]. Separate read out paths for L1 and the precision calorimeter data can be compared to identify calorimeter noise present at reconstruction.

For the L1 confirmation the $0.1\eta \times 0.1\phi$ towers used in the jet reconstruction are mapped to the more coarsely granulated $0.2\eta \times 0.2\phi$ towers used in L1 trigger decisions. To make the comparison more exact, the four $0.1\eta \times 0.1\phi$ towers included in a trigger tower are included in the comparison. The L1 confirmation requirement is based on the ratio:

$$\mathrm{L1_{ratio}} = \frac{\mathrm{E_T^{L1}}}{\mathrm{E_T^{Reco}}} \tag{4.1}$$

where E_T^{L1} is the scalar sum of p_T in the trigger towers and E_T^{Reco} is the vector sum of p_T from corresponding towers (excluding the coarse hadronic calorimeter cells). The minimal $\mathrm{L1_{ratio}}$ threshold requirement is dependent upon the η of the jet candidate [66]. Events selected for analysis have at least two jets with:

- $p_T > 20$ GeV: Due to inaccuracies in modeling the energy measurements in the inner cryostat region (ICR), events in the simulation (see Chapter 5) include an excess of lower p_T jets measured in the ICR ($0.8 < |\eta_{\mathrm{det}}| < 1.5$). To compensate for this modeling inaccuracy, the jet p_T requirement is raised to $p_T > 23$ GeV if the second leading jet has a detector eta in the ICR. Figures 25−26 show second leading jet physics eta with and without a higher p_T selection applied to jets in the ICR.
- $|\eta_{det}| < 2.5$
- L1 confirmation
- $0.05 < EMfraction < 0.95$
- $CHfraction < 0.40$
- Vertex confirmation: Each jet must be associated with ≥ 2 tracks originating from the PV to avoid jets from overlapping minimum bias collisions. Vertex confirmed MC jets are randomly removed in bins of V_z and η to correct for the differences in efficiency for MC versus data [67]. The tracks have the qualities: $p_T(track) > 0.5$ GeV; $\Delta R(track, jet) < 0.5$; distance of closest approach between track and PV: $Z < 1.0$ cm, $R < 0.5$ cm.

The efficiencies for reconstructed jets to pass the L1 trigger, $EMfraction$, $CHfraction$ and vertex confirmation cuts are different in data and Monte Carlo. Studies using dijet events are performed to parametrize these differences in bins of p_T and η. Monte

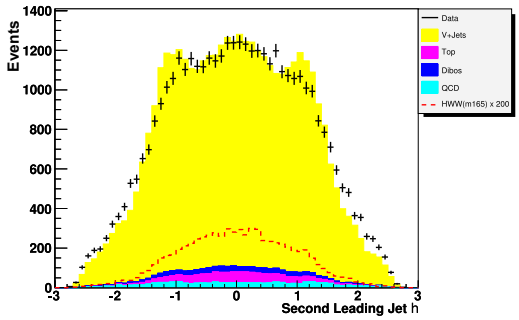

Figure 25: Sub-leading jet η, without a higher p_T cut when jet is in the ICR for data (black) versus combined background (stacked solid colors). Two MC excesses are seen as "horns" in the ICR. The jet η correction described in Sec. 6.5 has not been applied in this distribution.

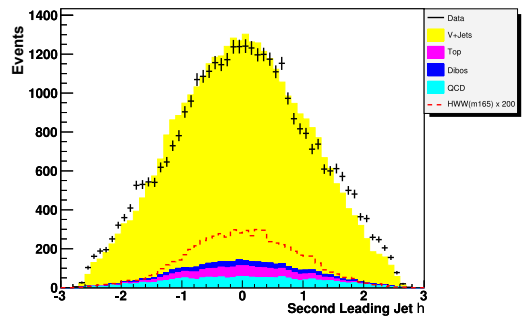

Figure 26: Sub-leading jet η, with $p_T > 23$ GeV when the jet is in the ICR for data (black) vs. combined background (stacked solid colors). The MC excesses in the ICR are significantly reduced. The jet η correction described in Sec. 6.5 has not been applied in this distribution.

Carlo jets are removed on a bin-by-bin basis to bring the efficiencies for simulated events into agreement with data [68] [67].

4.3.1 Jet Energy Scale

The DØ jet energy scale (JES) corrects the measured energies of reconstructed jets back to the energy of the particles resulting from the parton shower and hadronization by accounting for detector and algorithm effects. The components of the JES correction are [69] [70]:

- O (the offset energy correction): for the energy in the event not attributed to the hard $p\bar{p}$ collision such as overlapping minimum bias collisions, and electronic noise.
- F_η (the relative response correction): for variations in the response of the calorimeter in different η regions.

- R_{cc} (the absolute response correction): for losses due to uninstrumented detector regions, and differences in the response of the calorimeter to hadrons versus EM objects.

- S (the showering correction): for energy deposited inside and outside the ΔR jet cone due to showering in the calorimeter and the bending of charged particle paths in the magnetic field.

The JES correction has the form:

$$E_{\text{corrected}} = \frac{E_{\text{uncorrected}} - O}{F_\eta \times R_{cc} \times S} \tag{4.2}$$

The offset correction, O, is derived from data and includes a component for multiple interactions (MI) and a component for noise and event pile-up from previous interactions (NP). The MI correction is derived from the average energy of towers in a fixed radius cone from minimum bias events recorded by the Luminosity Monitor as a function of η, luminosity, and number of reconstructed vertices. The NP correction is derived from the average energy of towers in a fixed radius cone as a function of η and luminosity from zero bias events (events recorded at fixed beam crossing times without an explicit trigger firing) without Luminosity Monitor hits, and without a reconstructed vertex.

The R_{cc} correction is measured using p_T balance in $\gamma + 1$jet events in the central calorimeter. At particle level the p_T of the photon will closely match the p_T of the recoiling hadrons. At the reconstructed level, there will be an imbalance of energies,

measured as the $\not{E}_{\mathrm{T}}$ of the event[18]:

$$p_{T\ \mathrm{jet}}^{\mathrm{meas}} + p_{T\ \gamma}^{\mathrm{meas}} \simeq -\not{E}_{\mathrm{T}} \tag{4.3}$$

where $p_{T\ \mathrm{jet}}^{\mathrm{meas}}$ is the calorimeter response to the jet multiplied by the particle level p_T: $p_{T\ \mathrm{jet}}^{\mathrm{meas}} = R_{cc} \cdot p_{T\ \mathrm{jet}}^{\mathrm{particle}}$ and $p_{T\ \gamma}^{\mathrm{meas}} = R_{\gamma} \cdot p_{T\ \mathrm{jet}}^{\mathrm{particle}}$. The jet response will depend on an accurate measure of the photon response, R_{γ}. R_{γ} is derived from in $Z \to ee$ data using MC comparisons of relative response of the calorimeter for electrons and photons. The jet response is then found using the projection of $\not{E}_{\mathrm{T}}$ in the direction of the photon in the transverse plane:

$$\frac{R_{cc}}{R_{\gamma}} = 1 + \frac{\not{E}_{\mathrm{T}} \cdot \mathbf{p}_{T\ \gamma}^{\mathrm{meas}}}{|\mathbf{p}_{T\ \gamma}^{\mathrm{meas}}|} \tag{4.4}$$

after correcting for the photon response, and setting $R_{\gamma} = 1$. R_{cc} is measured in bins of $\mathrm{E}'(p_{T\ \gamma}^{\mathrm{meas}}, \eta_{jet})$, a quantity that is highly correlated with particle jet energy, but has a finer resolution:

$$\mathrm{E}' = p_{T\ \gamma}^{\mathrm{meas}} \cosh(\eta_{\mathrm{jet}}) \tag{4.5}$$

R_{cc} represents the response to the total hadronic recoil balancing the photon. The quantity E' is nearly independent of the choice of jet algorithm and is later mapped to the measured energies of jets to determine the corrections to be applied to specific jet algorithms.

The response for quark initiated jets is higher than the response for gluon initiated jets in $\gamma + 1$jet events. The gluon jets tend to have higher particle multiplicity and a softer p_T spectrum, with a correspondingly lower single pion response at lower

[18]Because $p_{T\ \mathrm{jet}}^{\mathrm{meas}}$ depends on the chosen algorithm this is only an approximate relationship.

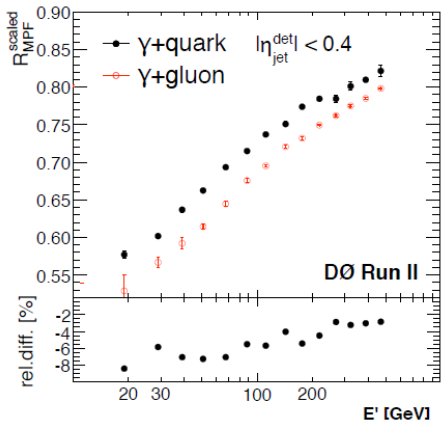

Figure 27: Response to quark and gluon initiated jets in the central calorimeter and their relative differences in $\gamma + 1$jet events as a function of E′ [69].

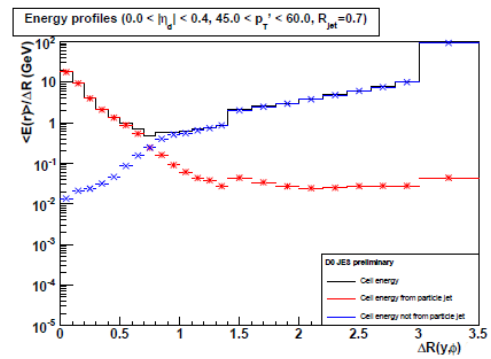

Figure 28: MC template used to correct jets for the amount of particle jet energy inside and outside the ΔR jet cone. Total cell energy is in black, cell energy from the particle jet is in red and cell energy not from the particle-jet is in blue [69]

energies. Figure 27 shows the quark and gluon jet responses and relative differences in percent for central calorimeter jets as a function of E′ [69].

The relative response correction, F_η, calibrates jets at forward η so the response to jets is independent of calorimeter η. F_η is derived in a similar manner to R_{cc} using p_T balance in $\gamma + 1$jet events and also in dijet events to include larger statistics for forward jets at high energies where the photon (or jet) is central and the other jet is at any η. F_η is parametrized in terms of E′ and detector η.

The showering correction is determined in $\gamma + 1$jet events with only one reconstructed vertex, the PV of the hard scatter. Using MC, templates are made from particle level information on the amount of energy contained within a fixed ΔR of the jet axis compared with the total particle level jet energy. Figure 28 shows an example template with total calorimeter cell energy (in black) as a function of ΔR from the jet axis with energy contributions from the particle jet in red, and from non-particle jet sources in blue. These templates are fit to data, and the showering

correction, S, is determined in η, p_T bins as:

$$S = \frac{E_{\text{jet}}^{\text{Rcone}} - E_{\text{non-jet}}^{\text{Rcone}}}{E_{\text{jet}}^{\infty}} \tag{4.6}$$

where $E_{\text{jet}}^{\text{Rcone}}$ is the energy of the particle level jet deposited inside $\Delta R < Rcone$, $E_{\text{non-jet}}^{\text{Rcone}}$ is energy deposited in $\Delta R < Rcone$ from sources other than the particle level jet, and E_{jet}^{∞} is the total energy of the particle level jet.

4.3.2 Jet Resolution

Differences in the simulation of data for response of the calorimeter for single particles can result in biases when modeling jets. The procedure of jet smearing, shifting and removing (JSSR) [71] in Monte Carlo events is applied to improve modeling in the simulation. This correction is derived using the p_T imbalance in back-to-back well isolated $\gamma + 1$jet and $Z + 1$jet ($Z \to ee$) events, where the p_T imbalance (ΔS):

$$\Delta S = \frac{p_T^{jet} - p_T^{Z/\gamma}}{p_T^{Z/\gamma}} \tag{4.7}$$

After η dependent corrections are applied, the ΔS distributions are plotted for various p_T^{γ} bins (Fig. 29). Repeating this analysis in both MC and data gives a measure of the *relative* performance of the calorimeter between the simulation and the data. Any systematic difference in response for data and MC: $\langle \Delta S \rangle_{\text{data}} - \langle \Delta S \rangle_{\text{MC}} \neq 0$, must be corrected in the simulation. In deriving the correction, the ΔS distributions are fit with a function composed of the product of an error function and a Gaussian. A plot of the turn-on curve (error function) versus p_T^{jet} for various detector regions is shown in Fig. 29. The central value of the Gaussian gives information on the jet energy scale, the width of the Gaussian gives information on the jet energy resolution

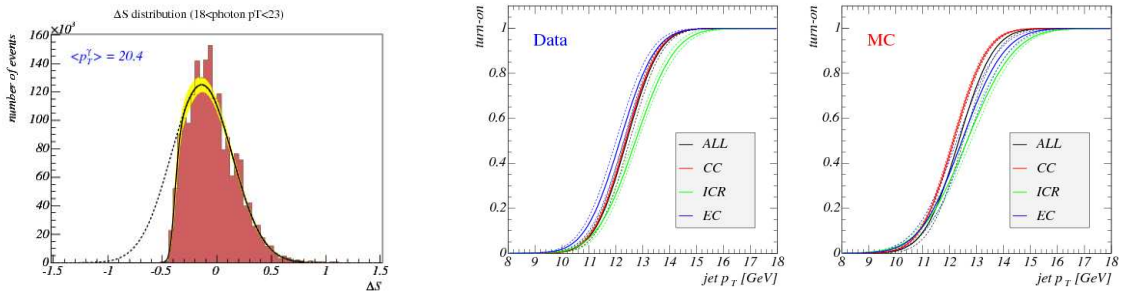

Figure 29: Left: ΔS distribution in the $18-23$ GeV p_T^γ bin. The solid line uses a fit function made from an error function multiplied by a Gaussian. The dashed line is the Gaussian from the fit. Right: Error function turn-on curves for data and MC for various detector regions as a function of p_T [71].

(JER), and the ratio of areas under the error function×Gaussian (solid line) and Gaussian-only (dashed line) curves give information on the jet reconstruction and identification efficiency.

Corrections to the simulated jet p_T from JER (jet *smearing*) are multiplicative factors randomly drawn from a Gaussian with width equal to the quadratic difference in the Gaussian widths of the data and MC fits:

$$\sigma_{\text{JER}} = \sqrt{(\sigma_{\text{Gauss}}^{\text{data}})^2 - (\sigma_{\text{Gauss}}^{\text{MC}})^2} \tag{4.8}$$

Corrections to the simulated jet p_T from the relative JES (jet *shifting*) are taken from a fit of the difference in Gaussian means for the data and MC as a function of jet p_T. Figure 29 shows the turn-on curves for data and MC plateau at ≈ 15 GeV, jets with $p_T < 15$ GeV are randomly removed from MC (jet *removal*) to match the data. Because of differences in data vs. MC turn-on curves in the ICR, an additional 2% of MC jets in the ICR are randomly selected for removal, independent of jet p_T.

In the Sec. 4.3.1 it was noted that the response for gluon jets was lower than the response for quark-jets. The $Z+1$jet events used for the JSSR jet shifting derivation

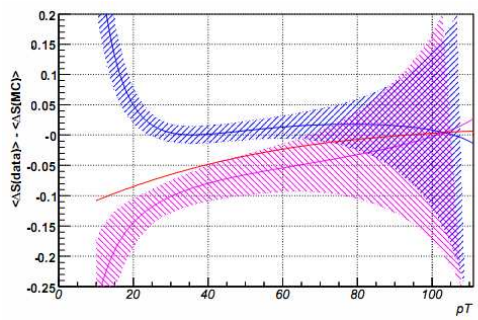

Figure 30: Relative JES data and MC in quark (blue) and gluon (fuchsia) initiated jets in $Z + 1jet$ events. Hashed lines represent statistical errors. The nominal JSSR shifting correction is shown in red [72].

have a high ratio of gluon-jet to quark-jet events. Figure 30 shows the difference in Gaussian means for data and MC fits as a function of jet p_T in $Z + 1$jet events for quark jets (primarily u and d quarks, in blue), and gluon jets (in fuchsia). The nominal JSSR jet shifting represents an ensemble of jets with both quark and gluon components and is shown as a red line. Because events with quark jets have a relative response close to zero, the JSSR shifting correction is not applied to those physics processes with u, d, or c quark dominated final states [72].

4.4 Muon Reconstruction

Information used in reconstruction of muons depends on three sub-detector systems at DØ: separate algorithms form tracks within the muon system [73], match central tracks to muon tracks [74], and extrapolate signatures of minimum ionizing particles in the calorimeter to central tracks [75].

In the muon system, hits in the wire chambers are combined and then fit into straight line segments using a linked list algorithm [73]. Wires in the various muon sub-detectors are located in x-z, y-z and x-y planes. A translation to a common set of coordinates is performed, then segments are formed in individual wire chambers and

scintillator octants. Longer segments are formed by merging segments from separate wire hits. Segments are then matched to scintillator hits by extrapolating the x position and determining if the Δy between the segment and scintillator hit is less than the sum of the errors on segment-y and hit-y. The scintillator hit is used to update MDT hits axial position (along the direction of the wire) in the segment to determine more accurate drift times.

Selections on arrival times of pulses in scintillator pads in the muon spectrometer are applied to reject cosmic rays. As the arrival of cosmics is uncorrelated with $p\bar{p}$ collisions, they typically produce "out of time" hits, while muons from $p\bar{p}$ collisions produce hit-times close to the crossing time expected from $p\bar{p}$ bunches. The distance of closest approach (DCA) of the muon to the PV is also effective for rejecting cosmic-ray events [76].

The TrackHalo and CalorimeterHalo isolation criteria are designed to separate $W \to \mu\bar{\nu}$ signal from heavy flavor background ($B \to \mu + X$). Because muons from heavy flavor decays tend to be embedded inside a jet, these variables are defined in terms of any tracks that accompany the muon track or calorimeter energy deposited along the vector of the muon momentum. TrackHalo is the scalar sum of the p_T of all tracks within $\sqrt{(\Delta\eta)^2 + (\Delta\phi)^2} = \Delta R < 0.5$ of the muon, excluding the track matched to the muon. CalorimeterHalo is the scalar sum of transverse calorimeter energy clusters in hollow cone around the muon with $0.1 < \Delta R < 0.4$ using cells in the EM calorimeter and first layer of the hadronic calorimeter [76].

Each event selected for inclusion in this analysis has exactly one muon satisfying:

- $p_T > 15$ GeV
- $|\eta_{detector}| < 1.6$
- $\Delta z(\text{muon}, \text{Primary Vertex}) < 1$ cm

- ≥ 2 hits in A layer wires
- ≥ 2 hits in BC layer wires
- ≥ 1 hit in A layer scintillator
- ≥ 1 hit in BC layer scintillator for forward muons
- Cosmic Veto: scintillator hit times in layers A/B/C < 10 ns from bunch crossing
- Matched central track with $\chi^2/(\text{degree of freedom}) < 4.0$
- Distance of closest approach (DCA) (x, y) between matched central track and PV < 0.04 cm with a SMT hit, DCA < 0.2 cm without an SMT hit
- Distance to closest jet: $\Delta R(\text{muon}, \text{jet}) > 0.5$
- TrackHalo < 2.5 GeV
- CalorimeterHalo < 2.5 GeV

To reduce background from $Z \to \mu\mu$ and maintain orthogonality in event selection with other Higgs boson searches, events are excluded from analysis if they include a second muon satisfying:

- $p_T > 10$ GeV
- $|\eta_{detector}| < 1.6$
- $\Delta z(\text{muon}, \text{Primary Vertex}) < 1$ cm
- Cosmic Veto: scintillator hit times in layers A/B/C < 10 ns
- DCA (x, y) between matched central track
  and PV < 0.04 cm with a SMT hit,
  DCA < 0.2 cm without an SMT hit
- Distance to closest jet: $\Delta R(\text{muon}, \text{jet}) > 0.5$

As in the jet corrections, the efficiencies for passing muon reconstruction require-

ments are different in data and Monte Carlo events. To derive correction scale factors that are applied to each Monte Carlo event, high p_T muons from $Z \to \mu\mu$ events are used to parametrize individual efficiencies in track and calorimeter isolation, muon hit qualities, and track qualities in terms of instantaneous luminosity, muon η, ϕ and p_T [77]. The p_T of muons in Monte Carlo are smeared on an event by event basis using a correction to track curvature ($charge\ q/p_T$) where the correction is a function of muon q/p_T and η derived by comparing $Z \to \mu\mu$ and $J/\Psi \to \mu\mu$ events in data and Monte Carlo [78].

4.5 Electron Reconstruction

The development of EM showers in the DØ calorimeter was discussed in Sec. 3.3. An electron is defined as a cluster in the EM calorimeter with a central tracking track that extrapolates to the cluster. The electron reconstruction beings with a simple cone algorithm [79] which uses $0.1\eta \times 0.1\phi$ towers of cells with $E_T > 0.5$ GeV as seeds for clustering. Around each seed, a cone of towers $\Delta R < 0.4$ is clustered. The cluster must have $E_T > 1.5$ GeV when summing the EM and hadronic layers, with 90% of the energy of the cluster confined to the EM calorimeter ($EMfraction > 0.9$) to be kept as an electron candidate. Clusters are then checked for isolation in the calorimeter. As discussed in Sec. 3.3, EM showers are shorter and more narrow than hadronic showers, and the *isolation* of the EM cluster is defined as:

$$isolation = \frac{\text{totalE}(\Delta\text{R} < 0.4) - \text{emE}(\Delta\text{R} < 0.2)}{\text{emE}(\Delta\text{R} < 0.2)} \tag{4.9}$$

where totalE($\Delta R < 0.4$) is the total energy in the EM and hadronic towers in a cone of $\Delta R < 0.4$ around the seed, and emE($\Delta R < 0.2$) is the total energy in the EM towers in a cone of towers $\Delta R < 0.2$ around the seed. The *isolation* must be less

than two for the cluster to pass preselection requirements.

Clusters are then matched with tracks with $p_T > 1.5$ GeV within a $\Delta\eta \times \Delta\phi$ window of 0.05×0.05 around the centroid of the EM cluster. The track associated with the EM cluster is the candidate track with the best spacial probability ($\chi^2_{spacial}$) given by:

$$\chi^2_{spacial} = \left(\frac{\delta\eta}{\sigma_\eta}\right)^2 + \left(\frac{\delta\phi}{\sigma_\phi}\right)^2 \tag{4.10}$$

where $\delta\eta$ and $\delta\phi$ are the differences between the cluster and track η and ϕ in the third EM layer (containing the average shower maximum), and σ_η and σ_ϕ are the RMS widths[19] of the $\delta\eta$ and $\delta\phi$ distributions [80] [81].

In addition to the above *isolation* and $EMfraction$ requirements, more demanding multi-variable discriminators are also used. A 7×7 covariance matrix is created from 7 correlated shower shape observables: the $EMfraction$ in layers $1-4$ of the EM calorimeter, the total EM energy, V_z, and the transverse shower width in ϕ. The inverse of this covariance matrix (H_{ij}) is calculated for every tower in η. A χ^2 of this H_{ij} is defined as:

$$\mathrm{HMx7} = \chi^2 = \sum_{\mathrm{ij}} (\mathrm{x_i} - \mathrm{m_i})\mathrm{H_{ij}}(\mathrm{x_j} - \mathrm{m_j}) \tag{4.11}$$

where x_i and x_j are observed values of variables i and j, and m_i and m_j are the mean values of the observables measured in Monte Carlo. Electron showers will have low values of HMx7 [82] [83]. A likelihood is built from probabilities for the cluster to come from a real electron $P_{sig}(x)$ or from background, such as a jet faking an electron

[19] Widths are given by $\sigma = \frac{1}{\sqrt{N}} \sum_{i=1}^{\mathrm{Nbins}} (x_i - \mathrm{mean})^2$ where N is the total number of events, x_i are the number of events in bin i and mean is the mean of the distribution.

$P_{bkg}(x)$. The probability $P(x) = \prod_i P(x_i)$, where individual probabilities are based on the variables: number of tracks in $\Delta R < 0.05$, scalar sum of p_T of tracks in cone with $0.05 < \Delta R < 0.4$ around candidate track, $\chi^2_{spacial}$, EMclusterE_T/trackp_T , DCA to PV, $EMfraction$, $isolation$, and H-matrix χ^2 [84] [83].

To maintain orthogonality in event selection with other direct Higgs searches, events are excluded from this analysis if they include an electron with:

· $isolation < 0.15$

· $EMfraction > 0.90$

· HMx7< 50

· $likelihood > 0.85$

· $p_T \geq 15$ GeV

· $|\eta_{detector}| < 2.5$

4.6 Missing Transverse Energy ($\not\!\!E_{\mathrm{T}}$) Reconstruction

In any $p\bar{p}$ collision the component of the momentum from the hard scatter parallel to the beam line (longitudinal momentum) is randomly drawn from the parton momentum distributions of the colliding proton and antiproton. The momentum of the $p\bar{p}$ system transverse to the beam line is approximately zero at the initial collision and must be conserved in the final state of the hard scatter. From an imbalance in final state transverse momentum ($\not\!\!E_{\mathrm{T}}$) the presence of non-interacting particles such as neutrinos can be inferred. Cells in the EM calorimeter, fine hadronic calorimeter, and ICD, along with the PV position to are used to calculate the direction and the magnitude of $\not\!\!E_{\mathrm{T}}$. For each calorimeter cell, the energy, calorimeter layer, ϕ and η are recorded [85]. The uncorrected $\not\!\!E_{\mathrm{T}}$ is calculated from the sums of cells with E > 0.1

GeV :

$$uncorrected\ \overrightarrow{\not{E}_{\mathrm{T}}} = \sum_{cells}^{i} -\overrightarrow{E_T^i} \tag{4.12}$$

This can be projected onto the x and y axes to determine: $\overrightarrow{\not{E}_{\mathrm{T}x}}$ and $\overrightarrow{\not{E}_{\mathrm{T}y}}$. Any corrections to calorimeter objects including JES corrections, electron and photon energy corrections, muons escaping the calorimeter, and removal of noisy cells must be propagated to the $\not{E}_{\mathrm{T}}$ [86] [87]. Events selected for the $H \rightarrow WW \rightarrow \mu\nu jj$ analysis have $\not{E}_{\mathrm{T}} > 15$ GeV. An unknown fraction of the momentum of the incident proton and antiproton is lost down the beam line, however, in the $H \rightarrow WW \rightarrow \mu\nu jj$ analysis, the missing transverse energy is expected to originate from the neutrino produced in the leptonic W decay and a constraint on M_W is used to estimate the p_z of the neutrino. The mass of the leptonic W boson can be expressed as: $(E^\mu + E^\nu)^2 - (p_x^\mu + p_x^\nu)^2 - (p_y^\mu + p_y^\nu)^2 - (p_z^\mu + p_z^\nu)^2 = M_W^2$. A solution for p_z^ν can be found from the substitution of the individual muon and neutrino $E^2 - \mathbf{p}^2 = m^2$ expressions into the leptonic W boson equality.

4.7 Higgs Boson Reconstruction

Each event passing preselection is considered in the hypothesis that the $\mu\bar{\nu}jj$ in the final state originates from a Higgs boson decaying to a pair of W bosons with subsequent leptonic and hadronic final states. The system of the hadronic W boson is formed from the addition of the momentum four-vectors of the two leading p_T jets passing all jet selection criteria. The system of the leptonic W boson is formed from adding the momentum four-vectors of the single muon passing preselection and the neutrino (from the $\not{E}_{\mathrm{T}}$). The system of the reconstructed H is formed from the momentum four-vectors corresponding to two W bosons.

As mentioned above, the neutrino four-vector is reconstructed using a mass constraint on the leptonic W assuming the W is on-shell. Using this constraint, when $M_H < 160$ GeV and the leptonic W boson may be highly virtual, the invariant mass of the WW system will be improperly reconstructed. Because of this limitation, the invariant mass of the WW system is only used in the analysis when considering values of $M_H \geq 160$ GeV (see Chapter 8).

4.8 Event Selection Summary

A kinematics-based preselection is applied to the data, signal and background events before they are passed to the final multivariate analysis. By studying the properties of the physics objects in the signal events over a wide range of M_H, kinematic requirements can be selected to enrich the amount of signal candidates in the data passing preselection, while suppressing the background. The physics object preselections applied are chosen to be minimally restrictive while still allowing the background to be well modeled. Gains in efficiency through more inclusive preselection must be balanced with any loss in sensitivity due to the additional systematical uncertainties incurred from analysis-specific corrections. Events are required to satisfy the following criteria for inclusion in this analysis:

- At least one trigger fired from the SINGLE MUON trigger suite.
- At least two jets with:
  - $p_T > 20$ GeV (second leading jet $p_T > 23$ if its $\eta_{detector}$ is in the ICR).
  - $|\eta_{detector}| < 2.5$
  - jet vertex confirmation
- Missing E_T ($\not{E}_{\mathrm{T}}$) > 15 GeV.

- One muon with $p_T^\mu > 15$ GeV and $|\eta_\mu| < 1.6$. Events with a second muon or a single electron are vetoed (see Sec. 4.4 and Sec. 4.5) .

- In order to suppress background from multijet events (discussed in Sec. 7.1) we require events to pass an additional *triangle cut* on the transverse mass of the leptonic W (m_T^W):
  $m_T^W > 40 - (0.5)\cdot \not{E}_{\mathrm{T}}$, where:

$$m_T^W = \sqrt{(p_T^\nu + p_T^\mu)^2 - (\mathbf{p}_T^\nu + \mathbf{p}_T^\mu)^2}.$$

The *triangle cut* is illustrated in Fig. 31, showing the relation between the m_T^W and $\not{E}_{\mathrm{T}}$ in the $H \to WW \to \ell\nu jj$ electron channel for data (top left), multijet (top middle), $W + jets$ (top right), and three different signal masses, $M_H = 145$ GeV (bottom left), $M_H = 160$ GeV (bottom middle), and $M_H = 185$ GeV (bottom right). Figures 32 - 35 show normalized distributions after preselection of p_T^μ, $\not{E}_{\mathrm{T}}$, and leading and sub-leading jet p_T distributions for various M_H. Multiple distributions showing data and combined background agreement after preselection are found in Sec. 7.2.

4.9 Event Counts after Selection

Final event counts for data and background events after applying the selection criteria are shown in Table 7. The total number of background events is scaled to agree with the number of data events at this stage by correcting the normalization of the V+jets contribution as described in Sec. 6.7. This rescaling allows for meaningful shape comparisons between data and combined backgrounds. Table 8 shows the event yield for gluon-fusion signal, and efficiency for gluon-fusion signal events to pass selection criteria (assuming SM Higgs boson cross sections and decays from Table 10 and integrated luminosity from Table 13).

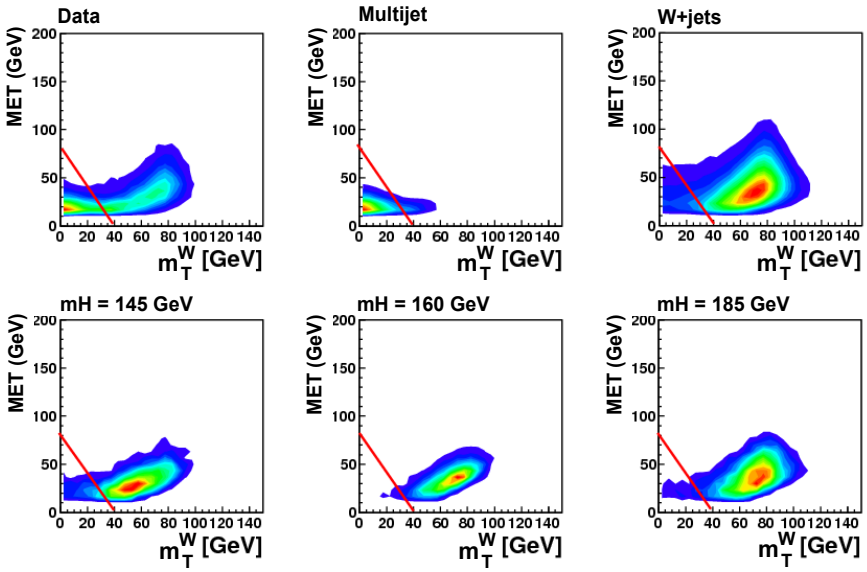

Figure 31: $\not\!\!E_{\rm T}$ vs. m_T^W in the $H \rightarrow WW \rightarrow e\nu jj$ channel for data (top left), multijet (top middle), W+jets (top right), and the signal masses, $M_H = 140$ GeV (bottom left), $M_H = 160$ GeV (bottom middle), and $M_H = 180$ GeV (bottom right). The red line indicates the *triangle cut* selection: $m_T^W > 40 - (0.5) \cdot \not\!\!E_{\rm T}$. Similar results are seen in the muon channel [88].

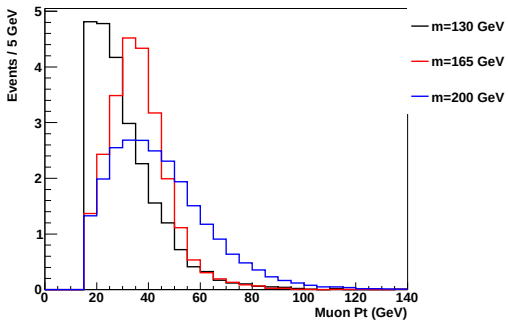

Figure 32: Muon p_T, shown for $M_H = 130$ GeV (in black), $M_H = 165$ GeV (in red) and $M_H = 200$ GeV (in blue). Histograms have been normalized to equal area for shape comparison.

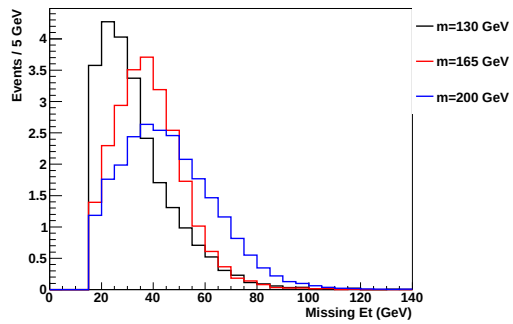

Figure 33: Missing E_T, shown for $M_H = 130$ GeV (in black), $M_H = 165$ GeV (in red) and $M_H = 200$ GeV (in blue). Histograms have been normalized to equal area for shape comparison.

A global event weight is applied to each simulated event including the products of normalization factors for the luminosity and cross section, as well as the various

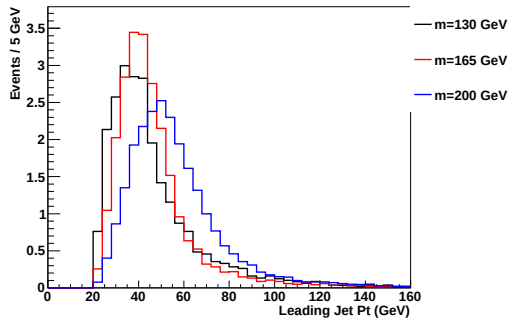

Figure 34: Leading jet p_T, shown for $M_H = 130$ GeV (in black), $M_H = 165$ GeV (in red) and $M_H = 200$ GeV (in blue). Histograms have been normalized to equal area for shape comparison.

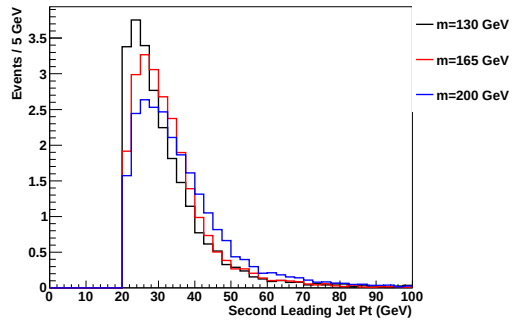

Figure 35: Second leading jet p_T, shown for $M_H = 130$ GeV (in black), $M_H = 165$ GeV (in red) and $M_H = 200$ GeV (in blue). Histograms have been normalized to equal area for shape comparison.

weightings for efficiencies and kinematical corrections discussed in Chapter 6. Table 9 shows the number of events removed following sequential preselection requirements. The top section of Table 9 shows the unweighted number of simulated and data events passing sequential kinematic preselections, the bottom portion shows integrated numbers of background events when including event weights.

Numbers of Events Passing Preselection						
Data	Total Bkd	W+jets	Z+jets	Diboson	Top	Multijet
36234	36234.0	30016.0	2415.9	882.3	1235.9	1683.9

Table 7: Total numbers of events in data and background sources after applying preselections.

Number of Signal Events passing Pre-Selection		Efficiency for Signal Events to pass Pre-Selection Cuts	
mH (GeV)		mH (GeV)	(%)
115	1.21	115	1.93
120	2.41	120	2.64
125	4.07	125	3.31
130	6.35	130	4.11
135	8.81	135	4.82
140	11.78	140	5.74
145	14.98	145	6.77
150	17.78	150	7.69
155	20.3	155	8.54
160	23.85	160	9.81
165	23.82	165	10.43
170	21.53	170	10.46
175	20.32	175	11.04
180	18.23	180	11.29
185	15.28	185	11.59
190	13.18	190	11.85
195	11.79	195	12.09
200	10.78	200	12.36

Table 8: Number of gluon-fusion ($gg \to H$) signal events passing selection criteria and efficiency for events to pass selection criteria (assuming SM Higgs boson cross sections and decays from Table 10 and integrated luminosity from Table 13).

Event counts from cafe framework, event weights = 1.0

cut	Z+Jets	W+Jets	Top	Diboson	mH = 165	DATA
common lnujj skim	4785738	7504048	6107743	150691	93347	126728321
abs(Vz) < 60 cm	4150202	6376621	5144584	141812	87624	35967778
dR(Jet,Mu) > 0.5, Mu Pt > 15 GeV	2372209	5547522	866222	113288	42302	6856926
NPTight Iso, Mu Pt > 15 GeV	2174989	5060537	722847	103499	34651	3688915
MET > 15 GeV	1304272	4680044	580036	84426	32017	2516353

Integrated event weights from outside cafe framework (no V+Jets s_factor applied)

cut	Z+Jets	W+Jets	Top	Diboson	mH = 165	DATA	Mulitjet
>=2 VC Jets, Pt > 15 GeV and SingleMuOR Trigger	5942.86	65837.5	1387.65	1244.76	31.2928	104308	28640.9
Jet0 Pt > 20 GeV	5315.59	58336	1386.71	1231.84	30.7816	91632	26569.1
Jet1 Pt > 20 GeV	2902.83	29099.9	1332.01	949.768	24.4836	46084	13261.3
Wtrmass > 40 - 0.5 x MET	2208.26	27077.9	1235.91	882.297	23.8197	36234	1683.93

Table 9: Number of events passing sequential preselection cuts. Processing occurs in two stages. The first is within the DØ Common Analysis Format (CAFe) framework (event counts shown have event weights = 1). The second processing stage occurs in dedicated analysis code, where the event counts given are the integrated event weights.

5 Datasets and Simulated Samples

5.1 Recorded DØ Physics Data

The data used in this analysis were collected with the DØ detector between June 2006 and June 2009. The integrated luminosity of this data sample is 4.28 fb^{-1}.

Data is collected during $8-20$ hour periods of colliding beam, referred to as stores. Each store is broken down into $2-4$ hour run periods that are further divided into 60 second luminosity blocks (Sec. 3.5). Runs that are recorded as having problems with the calorimeter, CFT, SMT or Muon system, individual luminosity blocks considered bad by the calorimeter, and events flagged with known noise patterns [89] have been excluded from the analysis.

5.2 Simulated Samples

Monte Carlo generators are commonly used in high energy physics to test theoretical predictions, differentiate between physics effects and detector effects in data, and to determine the analysis specific kinematic restrictions to enhance signal and suppress background in data selection.

As discussed in Sec. 2.7 there are many standard model processes originating from a $p\bar{p}$ collision that can leave a $\mu\bar{\nu}jj$ signature in the DØ detector. To differentiate an event coming from an H decay from an event coming from a background process it is essential to understand the differences in the kinematics of the events. Event generators use probability distributions of input variables taken from both theory and experiment to describe initial and final state properties of a collision to create accurate models of specific physics processes.

The two main event generators used in this analysis are PYTHIA [90] and the

matrix-element generator ALPGEN [91], interfaced to PYTHIA for subsequent parton showering and hadronization. Both ALPGEN and PYTHIA use the leading order CTEQ6L1 parton distribution functions [92] to model initial states for partons in the $p\bar{p}$ collisions.

In a PYTHIA-generated event, the incoming p and $\bar{p}$ are characterized in terms of their flavor composition and energy of their constituents by parton distribution functions (PDF). A parton from the p and from the $\bar{p}$ may start showers of initial-state radiation (ISR) using branchings like $q \rightarrow q + g$ that are space-like[20]. The initial hard scatter that follows is made from one parton from each of the ISR showers, producing outgoing partons that can then branch into time-like[21] final state radiation (FSR), or produce short lived particles, such as W or Z bosons, or $H \rightarrow WW$. The beam remnants, partons in the initial shower not involved in the hard scatter, produce additional soft collisions. Outgoing quarks and gluons fragment and shower into color neutral hadrons using a string hadronization model.

In the string hadronization model, the confinement of quarks is modeled using strings with transverse size of 1 fm, with an potential energy of 1 GeV per fm of stretch. As a $q\bar{q}$ pair separates the potential energy increases until it passes a threshold beyond which the string breaks, pulling a $q'\bar{q}'$ pair from the vacuum, creating the color neutral pairs $q\bar{q}'$ and $q'\bar{q}$ that decay further until showering partons have energy < 1 GeV. For three partons, such as $q\bar{q}g$, there are two strings originating from the gluon, one between q, g and one between $g, \bar{q}$. The formation of hadrons from fragmentation products (and their subsequent decays, if the hadron is unstable) are governed by the allowed phase-space. The allowed branching ratios and decay rates for leptons as well as all hadrons made from d,u,s,c and b quarks are reproduced.

[20] In a space-like branching: $a \rightarrow bc$, a and b have $m^2 = E^2 - \overrightarrow{p}^2 < 0$

[21] $m^2 = E^2 - \overrightarrow{p}^2 \geq 0$

The ALPGEN leading order generator is used to create the final state quarks and gluons arising from the hard scatter for events with high jet multiplicities. ALPGEN uses a recursive numerical Legendre transform of the effective action starting from the $SU(3)_{\mathrm{C}} \times SU(2)_{\mathrm{L}} \times U(1)_{\mathrm{Y}}$ Lagrangian to compute the scattering amplitude for any physical initial and final states [93] [91]. To create ALPGEN events the parameters of the hard process type (i.e. W+jets) such as jet multiplicity, jet p_T, jet η, and ΔR between jets are defined. For each event, a sub-process (i.e. $q\bar{q} \rightarrow Wgg$ for jet multiplicity = 2) is randomly chosen along with a point in the accessible sub-process phase-space, and a possible flavor configuration. Spin and color are randomly assigned for each parton, and a matrix element is evaluated. An event weight (differential cross-section) associated with the probability that event will occur is then recorded. To convert the events which are randomly distributed in phase-space to a more meaningful configuration, the events are scanned and selected based on their weights to give final parton states with the frequency predicted by theory.

The quarks and gluons generated with the matrix-element in ALPGEN are passed to PYTHIA for subsequent parton showering and hadronization to produce the final state jets. To ensure that the final jet multiplicity corresponds to the multiplicity requested in exclusive jet bins, the MLM matching algorithm is used [94]. In MLM matching, after the showering in PYTHIA, each post-shower jet is defined by a cone of $\Delta R < 0.7$ with $E_T > 8$ GeV. If each jet is matched to a matrix-element parton within $\Delta R < 0.7$, the event is kept, if there are one or more jets not matched to a parton, the event is discarded [95].

To simulate the effects on the particles as they traverse the detector, generated events are passed through the DØ GEANT Simulation of the Total Apparatus Response (DØgstar) [96] [97]. DØgstar tracks the paths of individual particles as they interact with the regions of the detector under the influence of the magnetic field.

The events are then passed to the program DØSim, which overlays events from data taken without a trigger requirement (zero bias data) to simulate minimum bias pile-up and the effects of additional interactions, and simulates the electronics noise from the calorimeter, SMT and muon sub-detector systems [98]. The output from DØSim is fed into DØRECO for event reconstruction.

5.2.1 Simulated Higgs Signal

Higgs signal samples are produced in the mass range $115 - 200$ GeV in 5 GeV steps with the Monte Carlo event generator PYTHIA. Only the gluon-fusion signal process shown in Fig. 9 is included in this analysis. The signal samples model the process $H \rightarrow WW \rightarrow \mu\nu jj$ produced at leading order in PYTHIA and then normalized to the next-to-next-to-leading order cross section for gluon-fusion production [99]. Production cross sections multiplied by branching ratios for standard model Higgs bosons are listed in Table 10. Production cross sections and branching ratios for various decay channels are listed in Table 11.

This analysis focuses on the gluon-fusion production ($gg \rightarrow H$) signal for limit setting and our preselection has been optimized for sensitivity to $gg \rightarrow H$ events. Decays of the Higgs boson from vector boson fusion (VBF) production ($qq \rightarrow qqH$, Fig. 8) are an additional signal source for this analysis, though VBF cross sections are are an order of magnitude lower than the gluon-fusion production process at $M_H > 125$ (Table 11). An initial study of using VBF signal in the current analysis framework can be found in Appx. C. The addition of VBF to gluon-fusion only signal provides $\sim$15% higher signal yield at the preselection level, however the differences in kinematics cause the VBF samples to be classified as more background-like than signal-like when our multi-variate analysis techniques are applied.

Additional signals will have small contributions to the total signal yield, such as:

MH (GeV)	ggF $HWWllvv$ (fb)	ggF $HWWlvjj$	VBF $HWWlvjj$
100	2.06	8.58	0.46
105	3.92	16.35	0.94
110	6.80	28.38	1.75
115	10.76	44.91	2.86
120	15.65	65.31	4.28
125	21.09	88.02	6.13
130	26.51	110.61	8.06
135	31.36	130.86	9.87
140	35.20	146.87	11.33
145	37.94	158.31	12.74
150	39.64	165.42	13.79
155	40.76	170.09	14.59
160	41.70	174.00	15.30
165	39.17	163.43	15.16
170	35.31	147.36	14.18
175	31.58	131.78	13.06
180	27.70	115.60	11.67
185	22.62	94.39	9.92
190	19.08	79.64	8.58
195	16.73	69.80	7.65
200	14.97	62.46	6.89

Table 10: Cross sections multiplied by branching ratios for standard model Higgs boson production via gluon fusion and VBF. Column 2 gives WW decays to two same-flavor leptons (e,μ), and in columns 3-4 WW decays to one lepton + jets. Uncertainties are $\approx$10% of the listed values.

	SM Higgs Production Cross Sections (fb)				SM Higgs Branching Ratios (%)		
mH	gg to H	VBF	WH	ZH	H to WW	H to ZZ	H to bb
100	1861	99.50	291.9	169.8	1.052	0.107	80.330
105	1618	93.30	248.4	145.9	2.307	0.203	78.570
110	1413	87.10	212.0	125.7	4.585	0.416	75.900
115	1240	79.07	181.9	108.9	8.268	0.830	71.950
120	1093	71.65	156.4	94.4	13.640	1.527	66.490
125	967	67.37	135.1	82.3	20.780	2.549	59.480
130	858	62.50	116.9	71.9	29.430	3.858	51.180
135	764	57.65	101.5	63.0	39.100	5.319	42.150
140	682	52.59	88.3	55.3	49.160	6.715	33.040
145	611	49.15	77.0	48.7	59.150	7.771	24.450
150	548	45.67	67.3	42.9	68.910	8.143	16.710
155	492	42.19	58.9	37.9	78.920	7.297	9.880
160	439	38.59	50.8	33.1	90.480	4.185	3.740
165	389	36.09	44.6	30.0	95.910	2.216	1.290
170	349	33.58	40.2	26.6	96.390	2.351	0.854
175	314	31.11	35.6	23.7	95.810	3.204	0.663
180	283	28.57	31.4	21.1	93.250	5.937	0.535
185	255	26.81	28.2	18.9	84.500	14.860	0.415
190	231	24.88	25.1	17.0	78.700	20.770	0.340
195	210	23.00	22.4	15.3	75.880	23.660	0.292
200	192	21.19	20.0	13.7	74.260	25.330	0.257

Branching Ratios Independent of Higgs mass (%)

VV to evjj	14.53	VV to lvlv	10.50
VV to muvjj	14.29	W to lv	32.40
VV to tauvjj	15.21	VV to llqq	14.12

Table 11: Standard model Higgs boson production cross sections and branching ratios.

gluon-fusion $H \rightarrow WW \rightarrow \tau\nu jj$ (taunujj), gluon-fusion $H \rightarrow ZZ \rightarrow lljj$ (ggHZZ), and associated production $WH \rightarrow \ell\bar{\nu}bb$ (WHlvbb). The WH channel contributes negligibly in the most sensitive region of this analysis, however future work will clearly benefit from repeating this analysis at low mass to better utilize this channel. While the taunujj events passing preselection are kinetically similar to the main $H \rightarrow WW \rightarrow \mu\nu jj$ signal, only a small fraction ($< 2\%$) of events originating pass the preselection ($M_H = 160$ GeV) due to their softer muon p_T spectrum. Appendix D includes a study of incorporating multiple signals in the limit setting process. The main contributions from additional signals come from the WH channel at low masses and VBF in the high mass range.

5.2.2 Simulated Standard Model Background Processes

The W+jets and Z+jets (V+jets) processes constitute the largest background for this analysis and are simulated with ALPGEN+PYTHIA. V+jets final states can contain light partons (i.e., *gluons* or u, d, s, c quarks) (lp) or both light partons and heavy flavor (hf) (b quarks and c quarks). Samples for $V + lp$ and $V + hf + lp$ are produced in bins of exclusive numbers of final state light partons (exclusive). The highest multiplicity bin allows events to include additional jets not matched to matrix-element partons via the MLM method (inclusive) [100]. To avoid double counting of heavy flavors, events with b or c quarks are removed from $V + lp$ samples, and events with c quarks are removed from $V + bb$ samples [101]. The $t\bar{t}$ samples are generated with ALPGEN+PYTHIA and a single-top quark sample was produced using the Monte Carlo generator CompHep [102]. The WW, WZ and ZZ (diboson) background samples are produced with PYTHIA.

Figure 36 shows the Feynman diagrams for the main backgrounds of the $H \rightarrow WW \rightarrow \mu\nu jj$ channel, Table 12 lists the corresponding cross sections for each process.

The cross sections for background processes are calculated at Next-to-Leading Order (diboson), and Next-to-Next-to-Leading Order (V+jets and *top*). The cross sections listed are not modified in the heavy flavor skimming process.

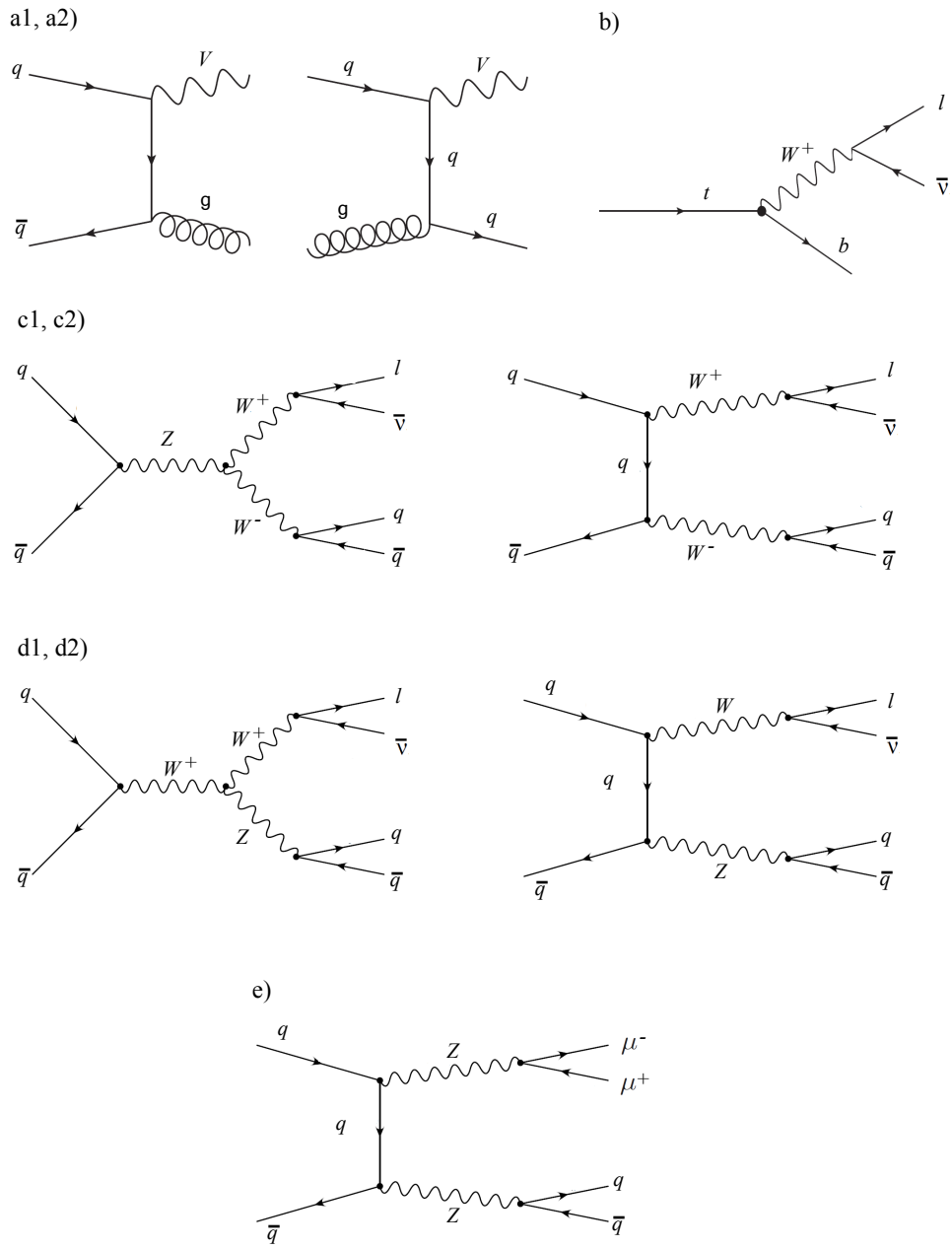

Figure 36: Background processes for the $H \rightarrow WW \rightarrow \mu\nu jj$ analysis: a1, a2) V+jets processes where $V = W, Z$; b) single top quark background (occurring twice for $t\bar{t}$); c1, c2) WW production; d1, d2) WZ production; and e) is ZZ production.

Background	cross-section [pb]	order
$W \to l\nu$+0 lp excl	5863	NNLO
$W \to l\nu$+1 lp excl	166.4	NNLO
$W \to l\nu$+2 lp excl	395.2	NNLO
$W \to l\nu$+3 lp excl	21.84	NNLO
$W \to l\nu$+4 lp excl	16.8	NNLO
$W \to l\nu$+5 lp incl	6.7	NNLO
$W \to l\nu$+2b+[0-3] lp incl	30.58	NNLO
$W \to l\nu$+2c +[0-3] lp incl	87.91	NNLO
$Z/\gamma^*(M_Z = [15, 75]$ GeV$) \to \mu\mu$ + [0-3] lp incl	516.1	NNLO
$Z/\gamma^*(M_Z = [15, 75]$ GeV$) \to \mu\mu$ +2b + [0-2] lp incl	1.55	NNLO
$Z/\gamma^*(M_Z = [15, 75]$ GeV$) \to \mu\mu$ +2c + [0-2] lp incl	11.81	NNLO
$Z/\gamma^*(M_Z = [75, 130]$ GeV$) \to \mu\mu$ + [0-3] lp incl	244.4	NNLO
$Z/\gamma^*(M_Z = [75, 130]$ GeV$) \to \mu\mu$ +2b + [0-2] lp incl	1.42	NNLO
$Z/\gamma^*(M_Z = [75, 130]$ GeV$) \to \mu\mu$ +2c + [0-2] lp incl	3.82	NNLO
$Z/\gamma^*(M_Z = [130, 1960]$ GeV$) \to \mu\mu$ + [0-3] lp incl	1.79	NNLO
$Z/\gamma^*(M_Z = [130, 1960]$ GeV$) \to \mu\mu$ +2b + [0-2] lp incl	0.012	NNLO
$Z/\gamma^*(M_Z = [130, 1960]$ GeV$) \to \mu\mu$ +2c + [0-2] lp incl	0.032	NNLO
$Z/\gamma^*(M_Z = [250, 1960]$ GeV$) \to \mu\mu$ + [0-3] lp incl	0.155	NNLO
$Z/\gamma^*(M_Z = [250, 1960]$ GeV$) \to \mu\mu$ +2b + [0-2] lp incl	0.0012	NNLO
$Z/\gamma^*(M_Z = [250, 1960]$ GeV$) \to \mu\mu$ +2c + [0-2] lp incl	0.0029	NNLO
$t\bar{t} \to$ inclusive	7.04	NNLO
single top $\to$ inclusive	3.28	NNLO
$WW \to$ inclusive	11.66	NLO
$WZ \to$ inclusive	3.45	NLO
$ZZ \to$ inclusive	1.37	NLO

Table 12: Standard Model cross sections for backgrounds. The Z/γ^* samples are produced in four bins of exclusive M_Z.

6 Simulated Sample Corrections and Normalization

Two types of corrections are applied to the Monte Carlo (MC) samples to improve modeling of the data. Physics motivated corrections may include k-factors for normalizations and/or kinematical modifications from higher-order perturbative corrections. Kinematical or shape corrections may also be determined by direct comparison between Monte Carlo samples and data. The second type corrects for inaccuracies in the detector modeling. The global event weight applied to each simulated event includes the products of normalization factors along with the corrections discussed in this section.

6.1 Reconstruction Efficiency Corrections

The efficiency to reconstruct leptons in data is lower that for leptons in simulated events. A correction factor (weight) is applied to the MC events to correct for the difference in these efficiencies. The muon ID, track, ΔR and isolation efficiency corrections corresponding to the selection criteria discussed in Sec. 4.4 were provided by the DØ Muon ID group. The p_T for the muon was also smeared in the simulation to match the resolution in data.

Efficiencies for jet reconstruction (Sec. 4.3) were applied using parametrizations provided by the DØ Jet ID group. The overall JES is corrected and differences in energy scale and resolution between data and MC are improved through the JSSR algorithm [71]. Because the JSSR shifting was derived by correcting final states with a mixture of gluon/light quark jets to be consistent with light quark jet final states (Sec. 4.3.2), JSSR shifting is applied to all Monte Carlo samples except $H \to WW$,

diboson and top, which are dominated by light quark final states and $Z + cc$ and $W + cc$, dominated by c quark jets which are similar to jets from light quarks [72].

6.2 Trigger Corrections

A trigger weight is applied to each event in the MC to simulate the effect of the trigger selection in data. The trigger weight for a given event represents the probability that the same event in the data would have passed the trigger requirements. This probability represents the efficiency for the muon in the simulated event to pass at least one of the available SINGLE MUON triggers[22]. Trigger efficiencies are measured using a tag-and-probe method in $Z \to \mu\mu$ events with two high p_T muons and dimuon invariant mass $\approx M_Z$. A *tag* muon must pass L1, L2, L3 selection requirements for a SINGLE MUON trigger that is not prescaled with luminosity, and is required to be well isolated, pass muon ID selection, and have $p_T > 30$ GeV. The *probe* muon has $p_T > 20$ GeV, and is matched to specific L1, L2, L3 SINGLE MUON trigger term requirements, either passing, or not passing trigger selection. The probe muon provides an unbiased sample for trigger efficiency estimation. The details of the efficiency measurements can be found in Refs [103, 104]. Figure 37 shows an illustration of the tag-and-probe method. The turn-on curves in trigger efficiencies are parametrized as a function of p_T^μ, η^μ for specific muon object identifications (corresponding to the probe muon qualities) as described in Sec. 4.4.

Only a subset of the SINGLE MUON triggers are active for any given trigger configuration and trigger efficiencies are measured separately for each configuration used to select the recorded data. The trigger weight applied to each MC event is the average weight for all configurations, weighted by the amount of integrated luminosity

[22] A future update to this analysis will extend the trigger suite to include the MUON+JET triggers, that were poorly modeled for the data presented here.

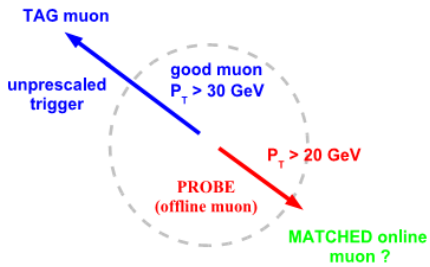

Figure 37: Illustration of the tag-and-probe method. By selecting $Z \to \mu\mu$ events where one high quality *tag* muon has fired a SINGLE MUON trigger, we can use the *probe* muon to extract unbiased efficiency measurements [104].

corresponding to each trigger configuration. SINGLE MUON trigger efficiencies are $\sim$74% in this analysis.

Luminosities collected with different versions of the trigger are listed in Table 13.

Trigger version	Int. Luminosity
15a	534.44
15b	688.02
15c	397.31
16	2661.90
total	4281.67

Table 13: Integrated luminosity (pb^{-1}) collected with different versions of the trigger used in the $H \to WW \to \mu\nu jj$ analysis.

6.3 Luminosity and Beam-V_z Weighting

Each simulated event includes an overlay of zero bias data at the time of generation to model luminosity dependent event properties such as resolution and reconstruction efficiencies. These zero bias data are collected from each run in a data taking period in a separate read out path from the triggered data and are used to model variations on the performance of the detector due to differing beam intensities.

The reconstruction algorithms for tracking and isolation described in Chapter 4 become less efficient at higher luminosities due to increased numbers of hits interfering with pattern recognition and multiple interactions leaving additional energy deposits in the calorimeter which reduce the efficiencies associated with isolation criteria and affect the energy measurements for a calorimeter objects.

Figure 38 shows efficiency versus instantaneous luminosity for muon track reconstruction in data and MC for the data set used in this analysis. The rate at which new high luminosity data is collected and processed through DØRECO is considerably higher than the rate at which complete high statistics MC samples are produced, therefore we weight the instantaneous luminosity profile in MC to match the luminosity profile of the dataset under analysis. Luminosity profiles span 200 bins of $0 - 400 \times 10^{30}$ cm^{-2}s^{-1} with event-by-event weights determined from:

$$weight_i(\mathcal{L}) = \frac{\mathcal{L}_i^{\text{data}}}{\mathcal{L}_i^{\text{MC}}} \tag{6.1}$$

where i is the bin index of the unweighted instantaneous luminosity and $\mathcal{L}_i$ is the corresponding bin content. Luminosity weights have a maximum value of 3.0 to prevent individual outlying events from excessively impacting the overall analysis.

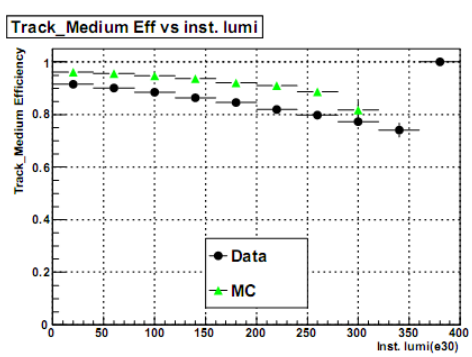

Figure 38: Efficiency for reconstruction of muon tracks in data and MC as a function of instantaneous luminosity. Reconstructed track qualities are described in Sec. 4.4 [77].

The V_z of the primary vertex is used to calculate the $\not{E}_{\mathrm{T}}$ and p_T of the jets and muon in each event. In simulated events, the V_z distribution is a Gaussian of width $\sigma_z^{\mathrm{MC}} = 25$ cm centered at $z = 0$, in data the width of the V_z distribution is a function of the Gaussian intensity profile of the proton and antiproton beams and the β function that determines the amplitude and oscillation of the transverse motion of bunches [105]. Beam V_z weighting is used to weight Monte Carlo events generated with a Gaussian vertex distribution to the actual vertex distribution in the data [106]. The width of the V_z distribution broadens as the beam emittance increases (and luminosity decreases) during a store. V_z distributions are measured in zero bias data in bins of run number range (data epoch) and luminosity. A weight is applied to each simulated event to correct the generic vertex distribution to the distribution measured in data:

$$weight(\mathcal{L}^{\mathrm{MC}}, V_z^{\mathrm{MC}}) \approx \mathcal{L}^{\mathrm{dataset}} \cdot \sum^{\mathrm{Epoch}(\mathcal{L}^{\mathrm{MC}})} \frac{\mathrm{Gaus}^{\mathrm{Epoch}}(\sigma_z, Z_z^0, V_z^{\mathrm{MC}})}{\mathrm{Gaus}^{\mathrm{MC}}(25, 0, V_z^{\mathrm{MC}})} \tag{6.2}$$

where Z_z^0 is the mean of the Gaussian formed by overlapping proton beams, σ_z is the Gaussian width, V_z^{MC} is the z position of the MC event being weighted, and $\mathcal{L}^{\mathrm{MC}}$ is the luminosity of the zero bias overlay from the MC event. Here, $\mathrm{Gaus}(\sigma, \mu, \mathrm{z}) = \frac{1}{\sqrt{2\pi\sigma^2}} e^{\left(\frac{-(z-\mu)^2}{2\sigma^2}\right)}$. The weight has a term for each data epoch considered in the analysis dataset, and the values of Z_z^0 and σ_z are the measurements corresponding to the luminosity bin containing $\mathcal{L}^{\mathrm{MC}}$. The $\mathcal{L}^{\mathrm{dataset}}$ is the total integrated luminosity for the data set being considered, which is the sum of the integrated luminosity of each data epoch.

6.4 ALPGEN MLM matching Corrections

The effect of varying MLM matching parameters in ALPGEN was evaluated for the DØ measurement of diboson production decaying to $\ell\bar{\nu}jj$ final states [107]. A p_T threshold of 9.5 GeV for matching jets to partons from the generator was found to better describe the data than the default value $p_T > 8$ GeV used to generate the Monte Carlo (see Sec. 5.2). A weighting function based on event dijet mass ($m^{(j1,j2)}$) applies this correction to the V+jets background. By examining the degradation of a χ^2 statistic in the data/simulation comparisons, uncertainties due to the tuning of this parameter are propagated through this analysis.

6.5 Jet-η Corrections

The V+jets events generated at leading order in ALPGEN do not accurately model jet η (η^{jet}) distributions observed in the data. In particular the η^{jet} distributions observed in data are more broad than in ALPGEN. Because V+jets events represent the major source of background in this channel, proper modeling of kinematic properties in this sample is an important requirement for modeling of signal sensitivities. To compensate for observed deviations between ALPGEN and data, a weighting factor is applied to each simulated event in both the W+jets and Z+jets samples. Two weightings are applied in succession, one for the eta of the second leading jet followed by another for the leading jet. The weightings are designed to correct for inaccuracies in physics modeling. Effects due to detector asymmetries are not explicitly corrected, but contribute to the derived systematic uncertainties.

The fitting process proceeds as follows. First the background is separated into two components: V+jets events generated in ALPGEN (including heavy flavor samples) and all *other* sources (diboson, top, multijet). These latter samples are subtracted

x	p0	p1	p2	p3	Applied to:
2nd jet eta	0.98192	-0.147617	0.0971125	-0.0103107	V+Jets
Lead jet eta	0.994558	-0.15633	0.110227	-0.013032	V+Jets
W PT	0.199822	9.44458	-0.0677133	0.986106	W+Jets
dR(Jet1,Jet2)	0.920644	-0.0184028	0.0154883	0.00053879	V+Jets

Table 14: ALPGEN reweighting parameters.

from the data, and the V+jets samples are normalized to the background subtracted data. Because this is a correction for ALPGEN modeling, data and MC discrepancies are similar in analyses which use the same background sources and identical kinematic selections for physics objects. Data and background samples are combined for the $H \to WW \to \mu\nu jj$ and $H \to WW \to e\nu jj$ analyses, and corrections are derived on the combined sample to reduce any analysis-specific bias.

Each correction is applied as an event weight derived from equation (6.3):

$$weight(\eta^{\text{jet}}) = p0 + p1 \cdot (\eta^{\text{jet}})^2 + p2 \cdot (\eta^{\text{jet}})^4 + p3 \cdot (\eta^{\text{jet}})^6 \tag{6.3}$$

Table 14 lists the weighting parameters that are applied in both the electron and muon channels.

When fitting for the parameters of the weighting function an additional term is added to the χ^2-function to preserve the normalization of the V+jets sample. This term is of the form:

$$\frac{\left[\sum_{i=1}^{Nbins} w_i^{V+\text{jets}} - w_i^{V+\text{jets}} \cdot weight_i(\eta^{\text{jet}})\right]^2}{\sum_{i=1}^{Nbins} (\sigma_i^{V+\text{jets}})^2} \tag{6.4}$$

where $w_i^{V+\text{jets}}$ is the weighted content of each bin in η, $weight_i(\eta^{\text{jet}})$ is defined in

Eqn. 6.3, and $\sigma_i^{V+\text{jets}}$ is the statistical error on the content of the bin. By imposing this additional constraint, the background incurs negligible changes in normalization after application of the derived weights.

Although the fit function can represent gross features of the distributions, remaining data/Monte Carlo differences in various bins can substantially increase χ^2 values. After the first fit iteration, bin errors are inflated by $\sqrt{\chi^2/d.o.f}$ and the fit is repeated. This conservatively broadens uncertainties in the fit parameters used in estimating uncertainties from the weighting procedure described in Sec. 6.6.2.

Figure 39 shows stages from the weighting procedure. Figure 39a shows the agreement of data and combined backgrounds for the sub-leading η^{jet} before weighting, Fig. 39b shows the agreement of V+jets data and MC before weighting, Fig. 39c shows the fit to the ratio of V+jets data to V+jets MC, and Fig. 39d shows the agreement of data and combined background after weighting. After weighting the data with respect to the η of the sub-leading jet, the process is repeated for the η of the leading jet.

6.6 P_T^Z, P_T^W, and $\Delta R(j1, j2)$ Corrections

The Z and W boson p_T distributions are not accurately modeled by the PYTHIA and ALPGEN Monte Carlo generators for events with boson $p_T \lesssim 100$ GeV. The differential cross section for Z boson production as a function of p_T ($\frac{1}{\sigma} \times \frac{d\sigma}{dp_T}$ GeV^{-1}) has been measured at DØ using $Z \to ee$ data events [108]. Using the cross section for data, the Z+jets Monte Carlo samples are weighted based on p_T^Z using:

$$weight(p_T^Z) = a + b \cdot \left[1 + erf\left(\frac{p_T^Z - c}{\sqrt{2} \cdot d}\right)\right] \tag{6.5}$$

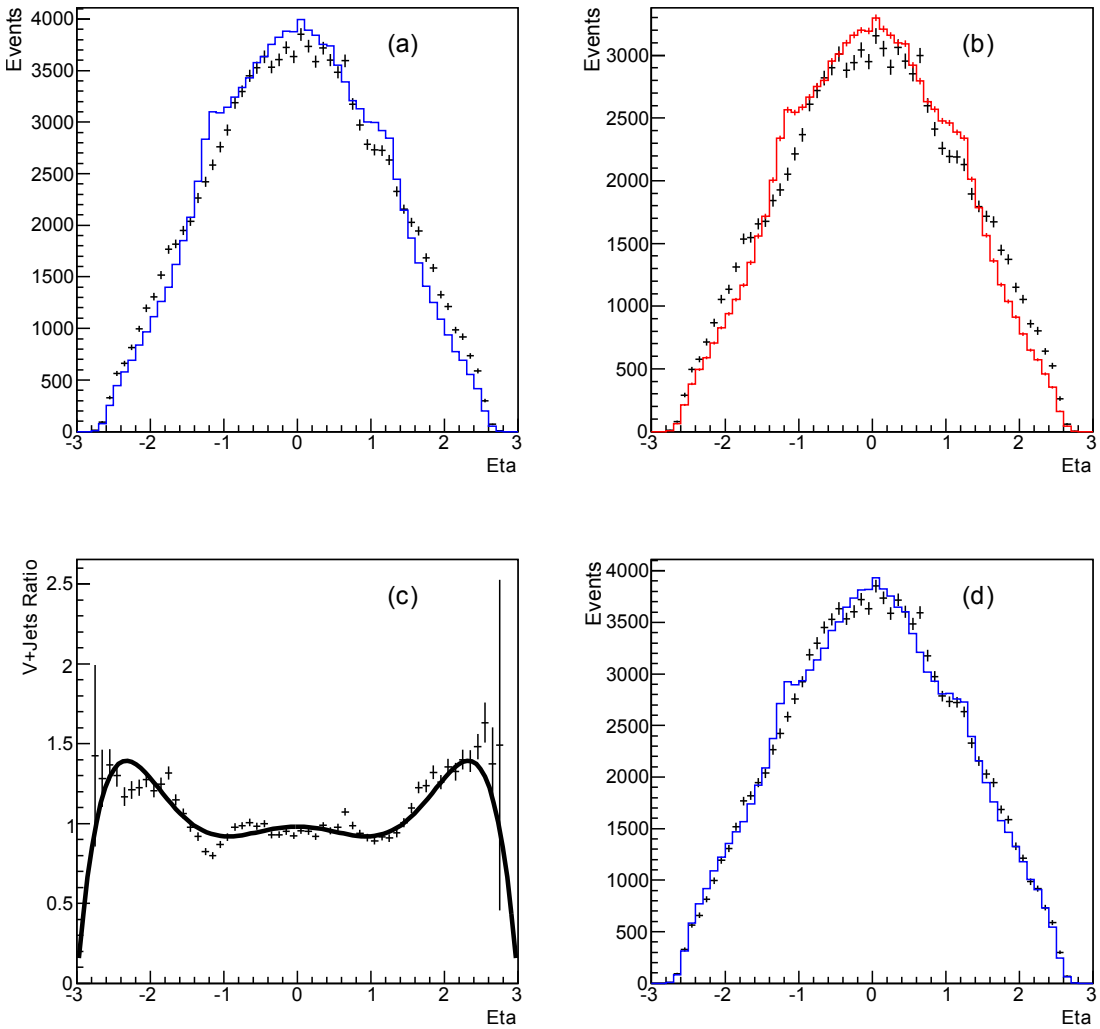

Figure 39: Weighting for sub-leading jet η-distribution. (a) Data (points) and all backgrounds. (b) Background subtracted data and V+jets sample. (c) Fit to ratio data/V+jets. (d) Data and all backgrounds after second jet η weighting for the combined electron and muon channels. Because of the jet $|\eta_{det}| < 2.5$ preselection requirement (Sec. 4.3), there are very low statistics for jets with $|\eta| > 2.5$.

where erf is the error function and the parameters a, b, c, d depend upon the event generator used in simulation and the minimum p_T of the jets in the event [109]. Because there is no such p_T dependent cross section measurement for W bosons from data, the W p_T correction is derived from the Z p_T data distribution. The Z p_T

distribution is multiplied by the p_T dependent NLO cross section ratio of W and Z to get a reference histogram. This reference histogram is then divided by the ALPGEN inclusive W+jets p_T distribution, and the ratio is fit using the function (6.5). The fit results are used to weight ALPGEN W+jets events [110].

To account for residual discrepancies in modeling the p_T^W distribution, we proceed to derive a p_T^W correction based on the specific samples and selection criteria used in this analysis. To account for correlations between p_T^W and the separation of the two jets, $\sqrt{(\eta^{j1} - \eta^{j2})^2 + (\phi^{j1} - \phi^{j2})^2} = \Delta R(j1, j2)$, also showing systematic differences between data and MC, we perform a simultaneous fit in both p_T^W and ΔR. The corrections are determined though a simultaneous fit of the data in the two distributions. The fitting procedure proceeds as in Sec. 6.5. First, we subtract all non-W+jets backgrounds from the data (Fig. 40). We then fit a pair of weighting functions (Eqns. 6.6-6.7) to the ratio of data to MC in the 2D (p_T^W, ΔR) distributions. Again the χ^2-function contains a term to constrain the normalization of the entire sample after both weights are applied. The residuals (data-MC)/σ_{data} in the 2D (p_T^W, ΔR) distribution before and after weighting are shown in Fig. 41. The ΔR and p_T^W distributions before and after weighting are shown in Figs. 42−43. The p_T^W reweighting is applied only to $W + jet$ MC, $\Delta R(j1, j2)$ weighting is applied to all V+jets samples.

$$weight(p_T^W) = p3 + p0 \cdot \left[1 + erf\left(\frac{p_T^W - p1}{100 \cdot \sqrt{2} \cdot p2}\right)\right] \tag{6.6}$$

$$weight(\Delta R) = p0 + p1 \cdot (\Delta R) + p2 \cdot (\Delta R)^2 + p3 \cdot (\Delta R)^3 \tag{6.7}$$

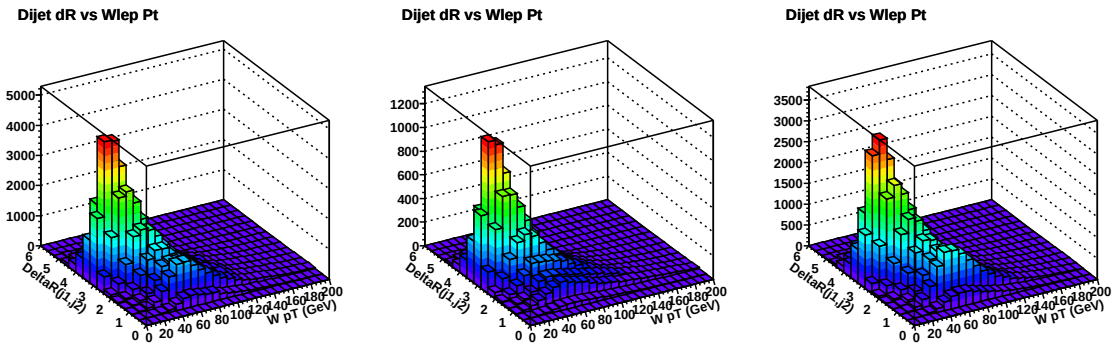

Figure 40: Data distribution in p_T^W and $\Delta R(j1, j2)$ before removal of non-W+jets components (left). The p_T^W and $\Delta R(j1, j2)$ distribution for non-W+jets MC and multijet sources (middle). The W+jets MC p_T^W and $\Delta R(j1, j2)$ for the combined electron and muon channels.

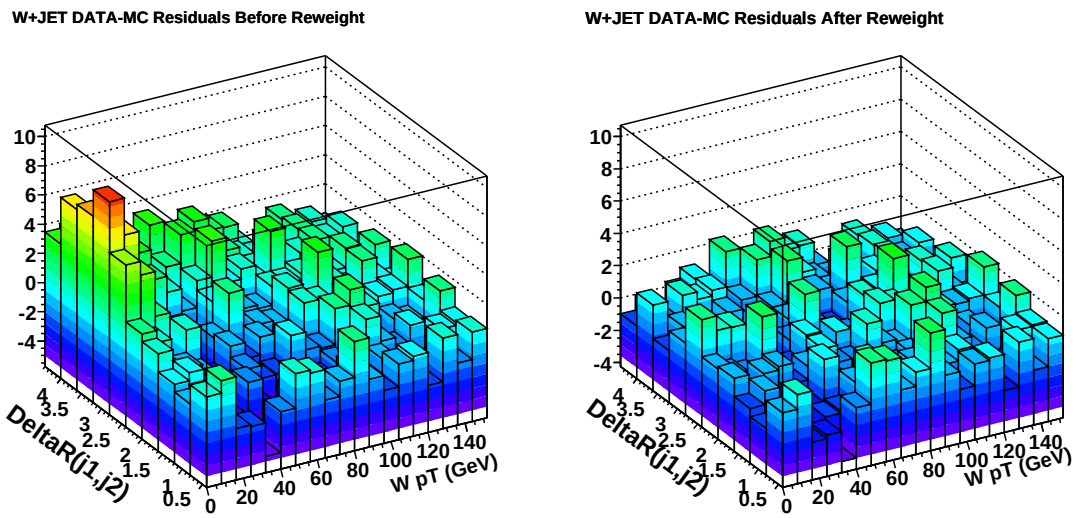

Figure 41: Residuals in W+jets Data-MC for $\Delta R(j1, j2)$ vs. p_T^W before (left) and after (right) weightings are applied to combined electron and muon channels.

6.6.1 Various Distributions Before and After Application of Jet and P_T^W Weightings

Figures 44−45 show the effects of the above weightings on various physics distributions used in this analysis. The χ^2 probability at the top of each plot is the usual p-value obtained by integrating the residual χ^2 distribution above that observed in

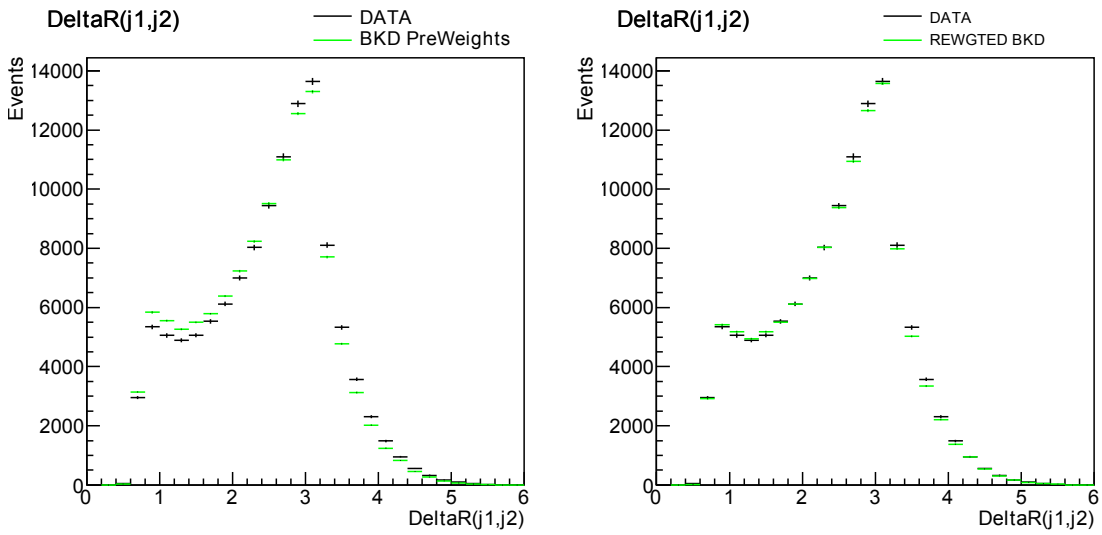

Figure 42: $\Delta R(j1, j2)$ in data (black) and background (green). Before weighting (left) and after weighting (right) for the combined electron and muon samples.

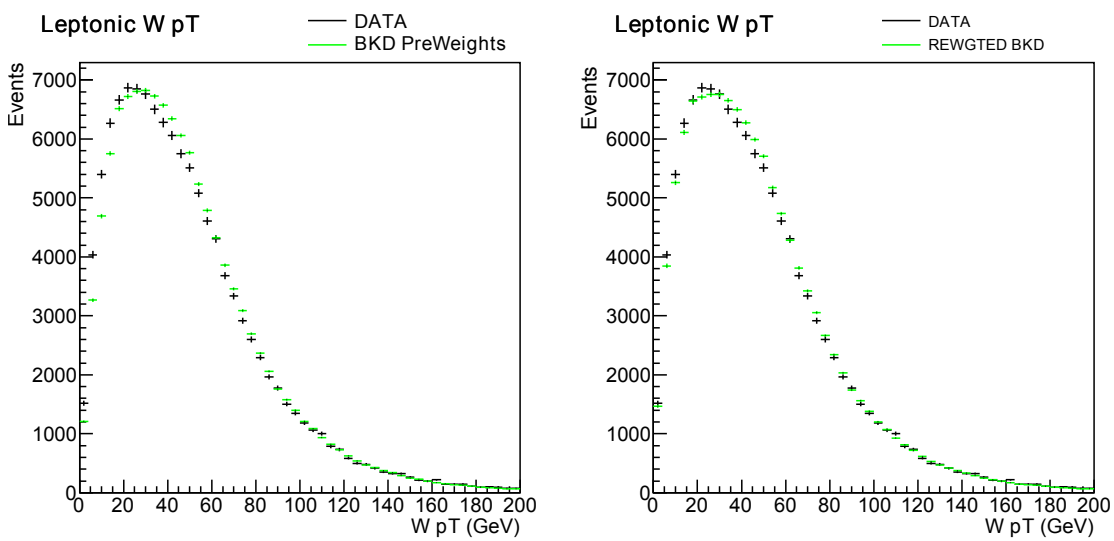

Figure 43: p_T^W in data (black) and background (green). Before weighting (left) and after weighting (right) for the combined electron and muon channels.

the data.

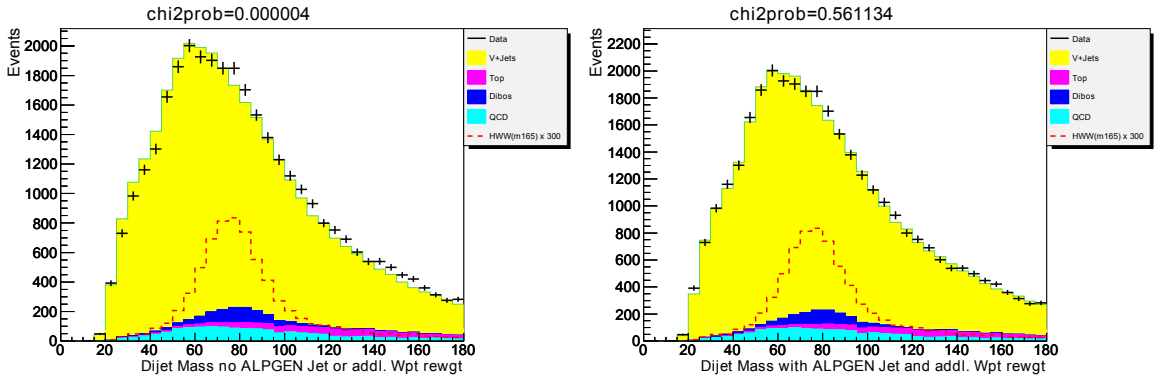

Figure 44: Dijet mass before (left) and after (right) ΔR_{jj} weighting in the muon channel.

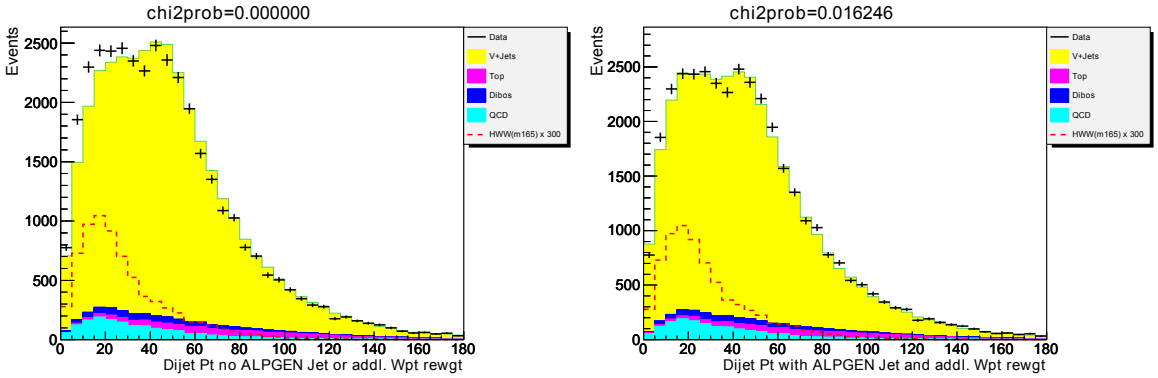

Figure 45: Dijet p_T before (left) and after (right) weighting in the muon channel.

6.6.2 Estimation of Systematic Uncertainties Corresponding to η^{jet}, p_T^W, and $\Delta R(j1, j2)$ Corrections

Uncertainties in shape of the corrected distributions from the weighting paramaterization are determined using the error (covariance) matrix calculated with respect to the minimization of the χ^2 function. The inclusion of the normalization constraint in the χ^2 function used in our fits tends to reduce the size of normalization uncertainties associated with the fit parameters and to enhance shape variations between regions with higher and lower statistics. Error propagation via correlations of fit parameters using the error matrix results in upper and lower bounds at each value of the indepen-

dent variable (eg. $\eta^{\rm jet}$, p_T^W,...). As an approximate procedure to estimate shape-only variations due to the weighting, we calculate upper and lower weight corrections via the error matrix, and then scale the variations so that the normalization of the sample is preserved.

For the weighting of the η of the sub-leading jet, nominal and upper/lower weight functions are shown in Fig. 46 (left). Fractional uncertainties on the weighted distributions are shown in the right panel. Figs. 47 and 48 show the results for the p_T^W and $\Delta R(j1, j2)$ weightings.

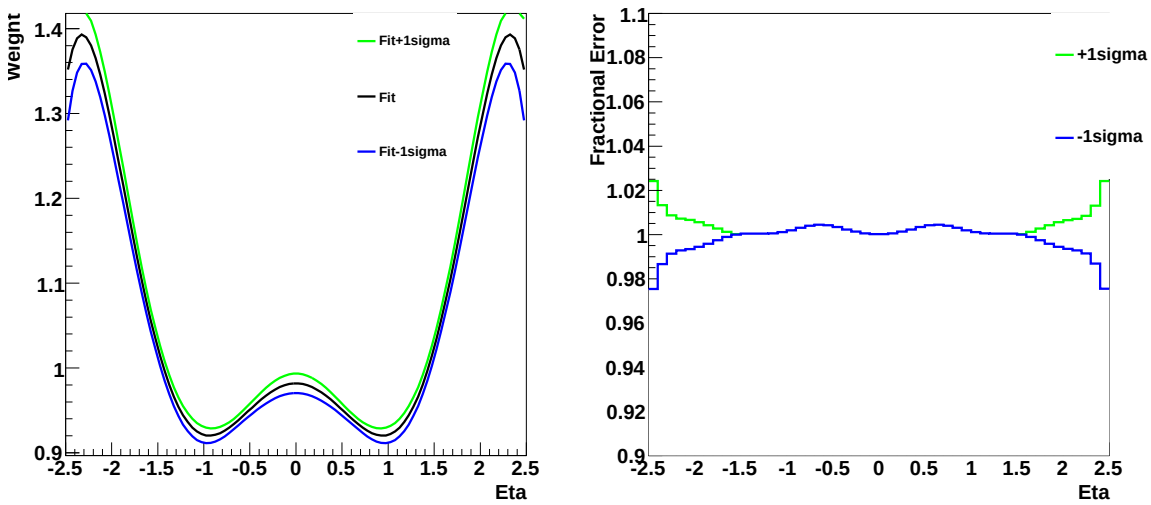

Figure 46: Uncertainties in sub-leading jet η weighting in V+jets sample. Nominal, upper, and lower corrections, based on error matrix (left). Fractional uncertainty after removing normalization changes (right) for the combined electron and muon channels.

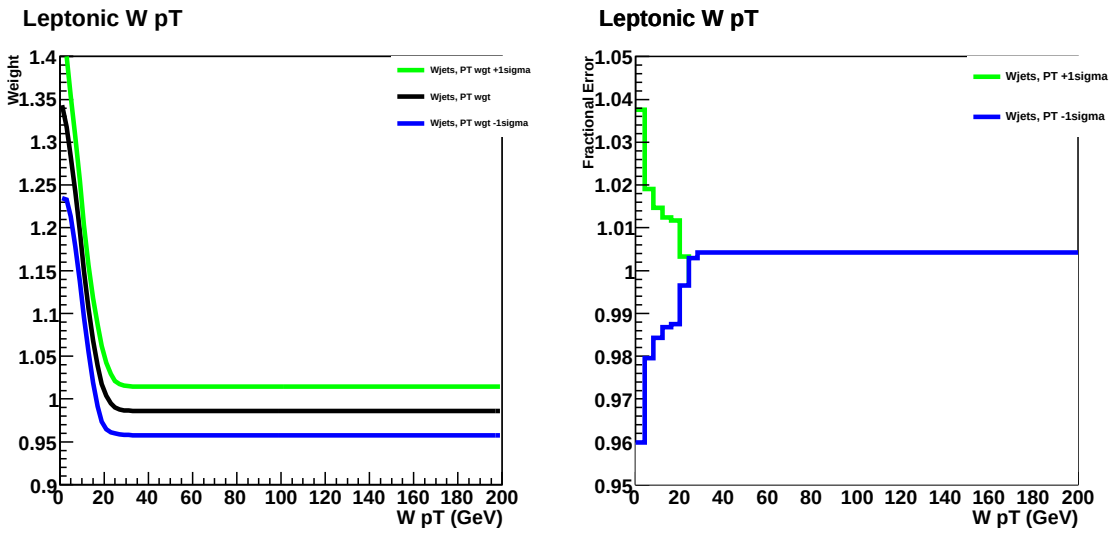

Figure 47: Uncertainties in p_T^W weighting in W+jets sample. Nominal, upper, and lower corrections, based on error matrix (left). Fractional uncertainty after removing normalization changes (right) for the combined electron and muon channels.

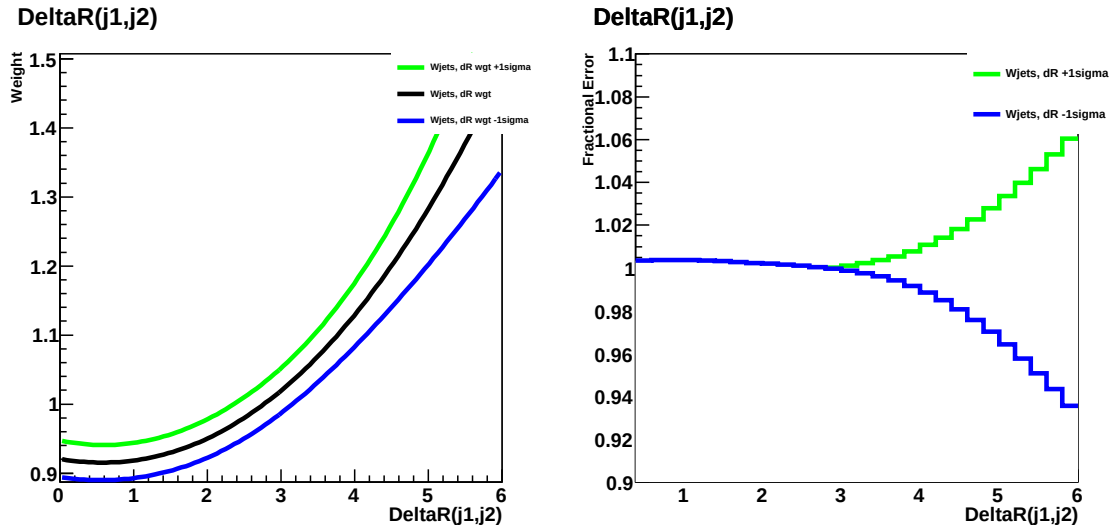

Figure 48: Uncertainties in ΔR weighting in W+jets sample. Nominal, upper, and lower corrections, based on error matrix (left). Fractional uncertainty after removing normalization changes (right) for the combined electron and muon channels.

6.7 Monte Carlo Normalization

The W/Z+jets samples generated by the DØ Common Sample Group are based on ALPGEN+PYTHIA. Because the ALPGEN+PYTHIA production cross sections are to

leading order (LO), a scale factor, k′, is applied to estimate the cross sections at next-to-next-to leading order (NNLO) accuracy. To calculate k′ for W+jets the NNLO inclusive W $\rightarrow \ell\bar{\nu}$ cross section is divided by the sum of the W+jets ALPGEN+PYTHIA cross sections. The k′ factor for Z+jets is calculated by the same method.

The $W + bb, W + cc, Z + bb$ and $Z + cc$ $(V + hf)$ samples use an additional scale factor, k_{HF}, which is a ratio of NLO/LO ratios for $V + hf$ and $V + lp$ samples (where hf stands for heavy flavor, and lp stands for light parton). To calculate k_{HF} for the $V + bb$ samples, the ratio of the $V + bb$+0lp (inclusive) NLO to LO cross sections from the event generator MCFM [111] is divided by the ratio of $V + 2lp$ (inclusive) NLO to LO MCFM cross sections. $V + cc$ k_{HF} factors are calculated using the same method. This analysis uses the k′ and k_{HF} factors calculated by the DØ V+jets Working Group as given in Table 15 [112].

The $t\bar{t}$ samples provided by DØ Common Sample Group group are also based on ALPGEN+PYTHIA. We normalize the $t\bar{t}$ to the cross section obtained from Ref. [113] which is equal to 7.04 pb, introducing a k′ factor of 1.38. Table 12 in Chapter 5 includes all k factors.

6.7.1 Normalization to Data

Applying inclusive k-factors does not fully correct large uncertainties in the LO calculation of W/Z+jets cross sections after application of event selections that select more exclusive final states. We therefore apply an additional scaling factor (s_{factor}), to both W+jets and Z+jets events to bring the total number of background events in agreement with data. The s_{factor} is determined by:

$$s_{factor} = \frac{N_{DATA} - N_{TOP} - N_{MJ} - N_{DIBOSON}}{N_{W+\text{JETS}} + N_{Z+\text{JETS}}}$$

	Scale Factors for V+Jets	
	k'	k_HF
W+lp	1.3	1
Wbb+lp	1.3	1.47
Wcc+lp	1.3	1.47
Z+lp	1.3	1
Zbb+lp	1.3	1.52
Zcc+lp	1.3	1.67
V+Jets s_factor		
pre-alpgen jet+wpt rewgt		1.12
post-alpgen jet+ wpt rewgt		1.12

Table 15: V+Jets scale factors. These factors account for NNLO corrections to inclusive production cross sections for the above analysis.

Where $N_{W+\text{JETS}}$ ($N_{Z+\text{JETS}}$) is the number of W+jets (Z+jets) events with all k$'$, k_{HF} and weighting factors applied. The derivation of the number of multijet events (N_{MJ}) is described in Sec. 7.1. The scale factors are listed in Table 15.

7 Combined SM Background Processes

A global event weight is applied to each event generated by Monte Carlo. This event weight includes the products of normalization factors for the luminosity and cross section, as well as the various weightings for efficiencies and kinematical corrections discussed in the previous section. Before the background processes can be summed and the final s_{factor} for V+jets calculated, the background from multijet events must be estimated from data.

7.1 Estimating the Multijet Background and V+Jets Contribution

In addition to the decay $W \to \mu\bar{\nu}$, muons can be produced via heavy flavor decays[23] or from $\pi^{\pm}$ and $K^{\pm}$ decays in the process of jet showering. Unlike other background processes, there are no accurate MC models for the muons produced in multijet (MJ) events, so this background must be derived from data.

Sec. 4.4 describes the calorimeter isolation requirements used to select muons originating from W bosons (TrackHalo < 2.5 and CalorimeterHalo < 2.5). To estimate the shape and normalization of the multijet background we reverse both isolation criteria in data passing all other preselection requirements to create an orthogonal anti-isolated sample ($N^{\text{data}}_{\text{ortho}}$). The distribution of multijet events should be similar to $N^{\text{data}}_{\text{ortho}}$ after correcting for $W \to \mu\bar{\nu}$ events that fail the isolation criteria. The multijet contribution is modeled by the difference between $N^{\text{data}}_{\text{ortho}}$ and an orthogonal Monte Carlo sample created from W/Z+jets, top, and diboson events with reversed-isolation requirements,($N^{\text{MC}}_{\text{ortho}}$).

[23]Approximately 0.5% of b and c quarks produced in $p\bar{p}$ interactions produce isolated muons. Please see Ref. [114] for details.

A bin-by-bin correction to $N_{\text{ortho}}^{\text{data}}$ is calculated in six distributions: $\not{E}_{\text{T}}$, p_T^{μ}, $\Delta\phi(\mu,\not{E}_{\text{T}})$, M_T^W, the p_T of the sub-leading jet (p_T^{j2}), and the invariant mass of the dijet system ($m^{(j1,j2)}$). These distributions are divided into 5 GeV wide or 0.1 radian wide bins according to the variable. The bin-by-bin correction is calculated in each of the above distributions using:

$$f_{MJ}^{(d,i)} \times N_{\text{ortho}}^{\text{data}(d,i)} = N_{\text{ortho}}^{\text{data}(d,i)} - N_{\text{ortho}}^{\text{MC}(d,i)} \tag{7.1}$$

where i is a bin index, d is one of the six distributions, and f_{MJ} is the corresponding multijet weight. A single orthogonal data event will have six associated weights from this process and each data event is corrected using the average of the six weights. We estimate uncertainty of the multijet background using the variance of the individual multijet weights.

Weighting the orthogonal events using the average of the $\not{E}_{\text{T}}$, p_T^{μ}, $\Delta\phi(\mu,\not{E}_{\text{T}})$, M_T^W, p_T^{jet2}, $m^{(j1,j2)}$ weights give shapes close to the original $N_{\text{ortho}}^{\text{data}} - N_{\text{ortho}}^{\text{MC}}$ distributions shown in Figs. 49 - 51. The black histogram is orthogonal data, blue is orthogonal MC, green is orthogonal (data - MC) and red is the weighted orthogonal data, the multijet model.

To compensate for the uncertainty in the W/Z+jets cross sections, we apply an additional scaling factor (s_{factor}), to both W+jets and Z+jets events to bring the total number of background events in agreement with data (see Sec. 6.7.1). To estimate the number of multijet background events we fit the p_T^{μ} and $\not{E}_{\text{T}}$ distributions in data to the template of MC plus multijet with the V+jets s_{factor} and multijet normalizations as free parameters. In order to remove a potential bias caused by the simultaneous derivation of the s_{factor} and the mulitjet normalization, the entire process is repeated after application of the s_{factor}. The normalizations are found to be stable after a

single iteration of the procedure.

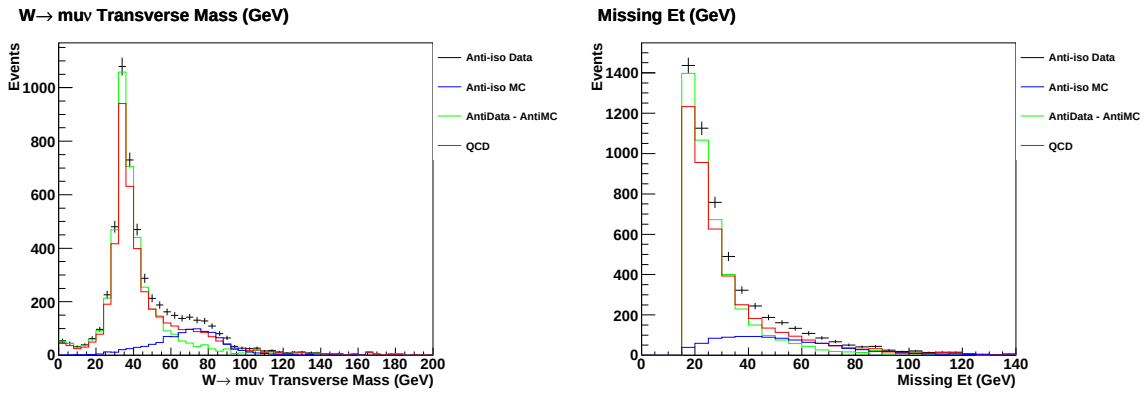

Figure 49: M_T^W (left) and $\not{E}_{\mathrm{T}}$ (right). The black histogram is orthogonal data, blue is orthogonal MC, green is orthogonal (data - MC) and red is the weighted orthogonal data, the multijet model.

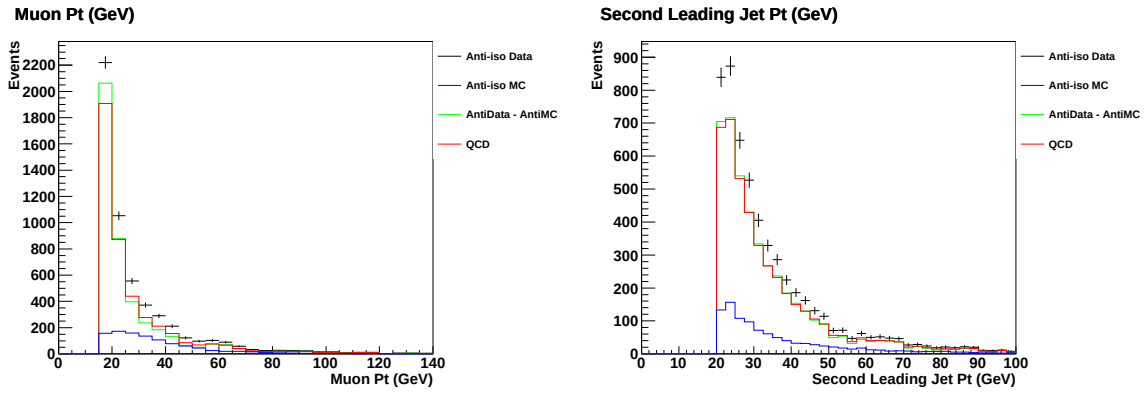

Figure 50: p_T^{μ} (left) and p_T^{jet2} (right). The black histogram is orthogonal data, blue is orthogonal MC, green is orthogonal (data - MC) and red is the weighted orthogonal data, the multijet model.

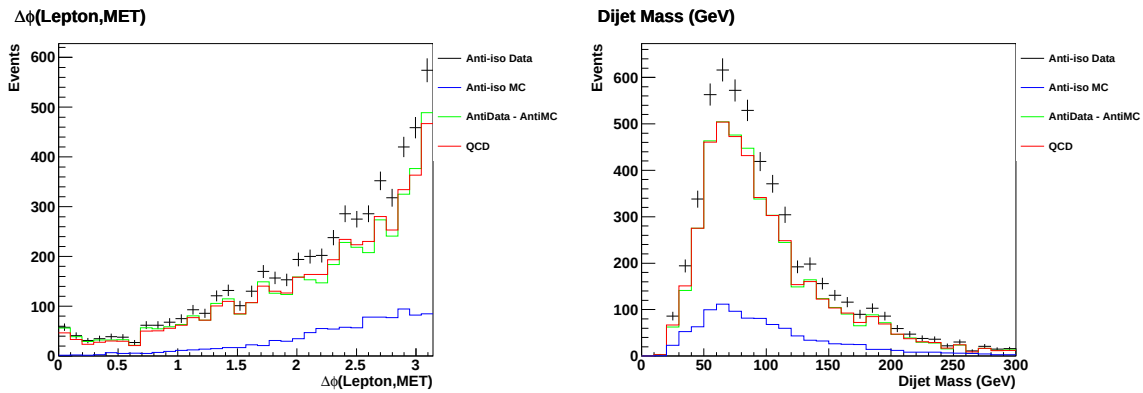

Figure 51: The $\Delta\phi(\mu,\not{E}_{\mathrm{T}})$ (left) and $m^{(j1,j2)}$ (right).The black histogram is orthogonal data, blue is orthogonal MC, green is orthogonal (data - MC) and red is the weighted orthogonal data, the multijet model.

7.2 Agreement between Data and Background

After deriving the multijet background, the η^{jet}, ΔR (j1,j2) and p_T^W weightings described in Sec. 6.5 and 6.6 are calculated and applied along with the final s_{factor} to the global event weight of the V+jets events. Histograms are filled with a range of physics quantities calculated from the momentum four-vectors, and weighted by the global event weight from each event. When the histograms from all background sources are combined, the shape of the combined background agrees with the data, indicating the backgrounds are a reasonable representation of the data and can be used to determine the input distributions for the random forest classifier. Various distributions are shown in Fig. 52 - 63. The signal shape shown in these distributions is for $M_H = 165$ GeV and the signal event count is multiplied by a factor of 300 for visibility.

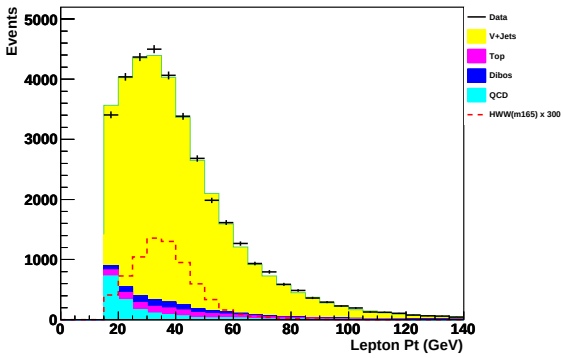

Figure 52: p_T^{μ}

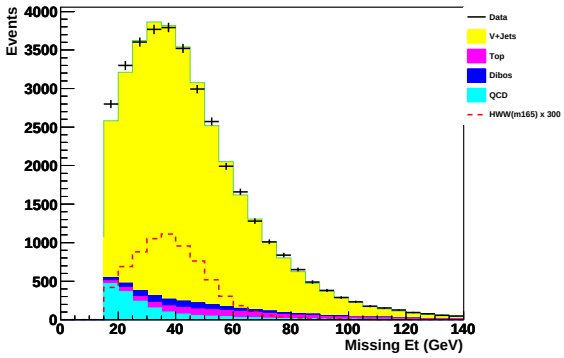

Figure 53: $\not{E}_{\mathrm{T}}$

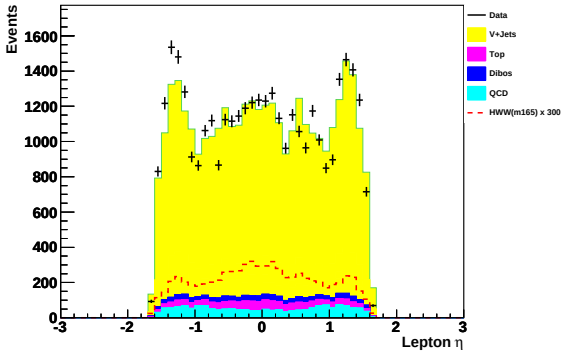

Figure 54: η_{μ}

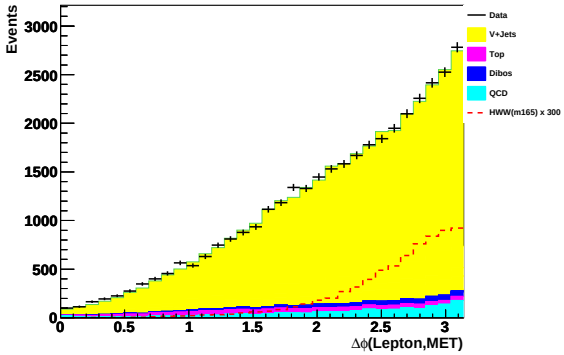

Figure 55: $\Delta\phi(\mu,\not{E}_{\mathrm{T}})$

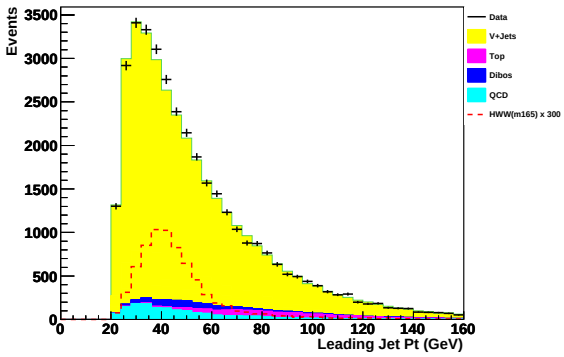

Figure 56: Leading jet η

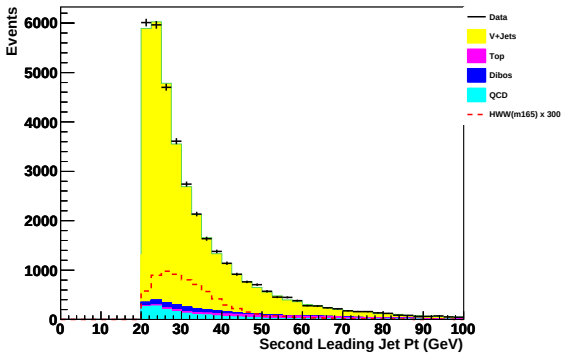

Figure 57: Second lead jet η

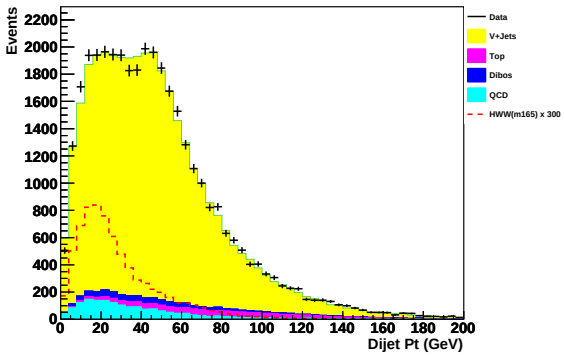

Figure 58: Dijet P_T

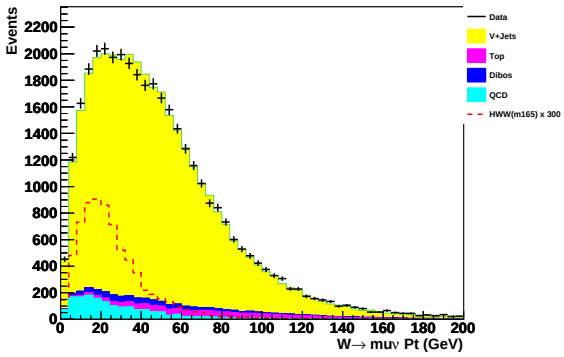

Figure 59: Leptonic W P_T

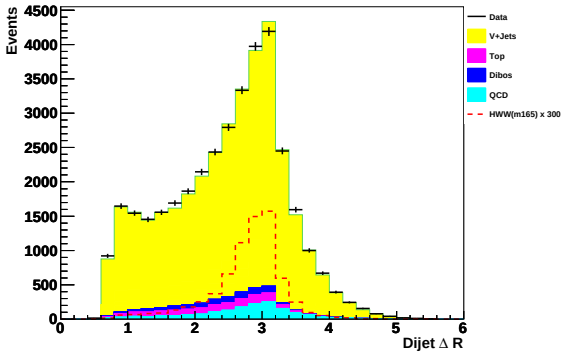

Figure 60: ΔR(j1, j2)

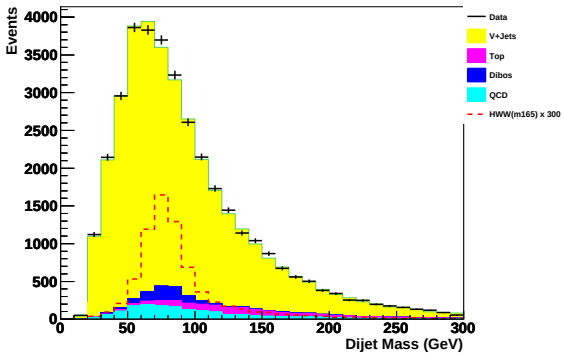

Figure 61: Dijet Mass

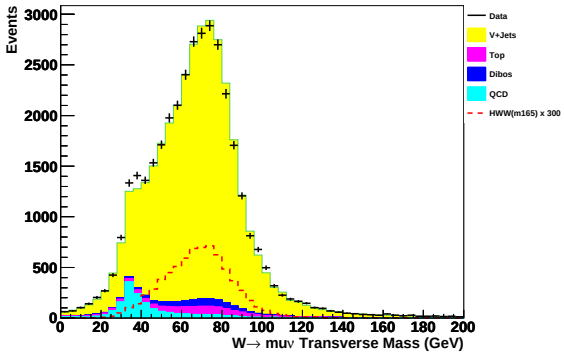

Figure 62: Leptonic W transverse mass (m_T)

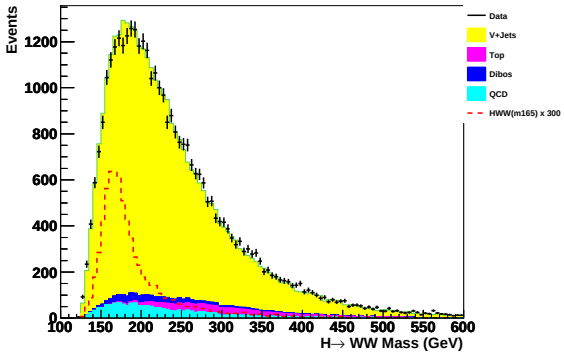

Figure 63: WW Mass

8 Multivariate Classification of Higgs Signal and SM Backgrounds

Classifiers using information from multiple variables are commonly applied to improve statistical sensitivities to the presence of small signals in large backgrounds in high energy physics analyses. A random forest (RF) classifier [115] is employed in this analysis. The random forest is composed of a collection of decision trees (DT) [115] trained to separate signal from background according to some figure of merit.

Initial work on the $H \rightarrow WW \rightarrow \mu\nu jj$ analysis employed a neural network multivariate classifier. Like the random forest classifier, a neural network is trained on signal and background samples from a fixed list of discriminating variables. Unlike the random forest composed of DT's defining a series of 1-D selections on variables, the neural network develops a mapping function dependent upon the correlations between all variables input, with the weights for each variable dependent upon the paths to the output. Neural networks can display erratic behavior when confronted with highly correlated variables, or too when many variables are chosen for training. A DT makes a series of 1-D selections on variables based on a figure of merit separating signal from background, thus two highly correlated variables are unlikely to be chosen for sequential selections and will not adversely impact the training.

The RF classifier was chosen for the final analysis because of the interpretability of its results, the speed with which it can be trained and tested, and for its flexibility in variable selection. An additional advantage of the random forest is its insensitivity to small changes in the data. Because the events in a random forest are spread over numerous decision trees, the RF is not sensitive to small changes in the training set and are more robust against noise in the data [116] [117]. The structure of a single decision tree classifier and the RF classifier used in this analysis are described below.

8.1 Decision Trees

Construction of a decision tree proceeds from an initial training sample of signal and background events normalized to the same integrated event count. These are combined to form the root node of the tree. From a set list of discriminant variables, the variable and selection on that variable that gives the best separation of signal and background is used to split the root node into two branch nodes: branch_1 labeled as *signal-like*, branch_2 labeled as *background-like*. The figure of merit used to decide the best split at each node is the Gini index impurity criteria[118] :

$$G = 2p(1-p) \tag{8.1}$$

where p is the fraction of correctly classified events in a node (i.e. the fraction of total events in the signal-like branch that are actually signal). At the root node, $p = 0.5$, and $G = 0.5$. For a perfectly classified node, $p = 1.0$, and $G = 0$. Splits are chosen to minimize the Gini index summed over the resulting branch nodes. Similar selections are repeated from each branch node until a minimum number of events remain in a node or if no selection is found that improves signal and background separation. These terminal nodes are referred to as *leaves*. Without a restriction on the minimum number of events in a terminal leaf, the tree can become over-training on the initial sample such that new events tested are poorly classified.

Each leaf has an associated Gini index for the impurity of its content. An event sent through the trained decision tree that ends in a signal-like leaf is given a classification output $\in [0, 1]$ based on the value of p, the purity for signal in that leaf. Similarly an event that terminates in a background-like leaf is given a classification of one minus the purity of background in that leaf [117].

8.2 Random Forest

Multiple decision trees trained on the full data set would always choose identical splits at each node, therefore we train a random forest (RF) composed of a collection of decision trees built from replicas of the training data set. These replicas are made by sampling with replacement from the original data set such that replicas are the same size as the original but may exclude some events and contain duplicates of others. This allows us to build multiple data sets with the same properties of the original for unique tree training. This technique is commonly referred to as **B**ootstrap **AGG**regat **ING** or "bagging" [119]. Discriminant variables are also sampled with replacement for each tree. A given test event will end at a signal-like leaf, or background-like leaf for each tree in the forest. The output of the RF is the average output of all trees, based on the purity values of their final nodes. The *bagged decision tree* classifier from the StatPatternReconition [117] software package was used in this analysis.

8.2.1 Input Distributions

More than 70 physical distributions were evaluated to select quantities that provide good signal/background separation power to construct the random forest. Each potential discriminant variable was evaluated against the combined background sources using the Kolmogorov-Smirnov (KS) distance parameter [120] as a measure of the difference in shape between normalized signal and background distributions. The set of most powerful discriminants was found to vary substantially as a function of M_H, however large overlap is observed in the preferred discriminants for each background source and M_H when using more than about ten input distributions.

To avoid the selection of poorly modeled distributions, only variables with data vs. background χ^2 probability of > 0.02 in the RF training sample (see Sec. 8.2.2)

are used as inputs in this analysis. The list of input variables is given in Table 16. Variables are used to train all mass points with the exception of the invariant mass of the WW system, which is used only for $m_H \geq 160$ GeV. Histograms of all RF input distributions can be found in Appendix A.

RF Inputs
3D Angle(Wlep, leading jet) in the H center-of-mass frame
Aplanarity: measure of p_T component out of the event plane defined by leading jets (j1,j2), μ, and $\not{E}_{\mathrm{T}}$
Centrality : $(\sum p_T\ )/(\sum \mathrm{E})$ for μ and all jets
3D angle between leading jets (j1,j2) in the H center-of-mass frame
$\Delta\phi(\mu, \not{E}_{\mathrm{T}})$
ΔR(j1,j2)
$m^{(\mathrm{j1,j2})}$
$p_T^{(\mathrm{j1,j2})}$
$m_T^{(\mathrm{j1,j2})}$
Scalar sum of p_T for all jets
Scalar sum of p_T for μ, j1, and j2
Scalar sum of p_T for μ, $\not{E}_{\mathrm{T}}$, and j1 and j2
$\mathrm{KT_{max}}$: $\Delta R(\mathrm{j1,j2}) * E_T^{\mathrm{j1}}/(E_T^{\mu} + \not{E}_{\mathrm{T}})$
$\mathrm{KT_{min}}$: $\Delta R(\mathrm{j1,j2}) * E_T^{\mathrm{j2}}/(E_T^{\mu} + \not{E}_{\mathrm{T}})$
E^{μ}
p_T^{μ}
Invariant Mass of μ, j1 and j2
$\not{E}_{\mathrm{T}}$
METbis : dot product of $\not{E}_{\mathrm{T}}$ and angular bisector of j1, j2
Minimum of $\Delta\phi(\mu$,j1) or $\Delta\phi(\mu$,j2)
Minimum of $\Delta\phi(\not{E}_{\mathrm{T}}$,j1) or $\Delta\phi(\not{E}_{\mathrm{T}}$,j2)
Minimum of ΔR($\not{E}_{\mathrm{T}}$,j1) or Δ R($\not{E}_{\mathrm{T}}$,j2)
p_T of j1
p_T of j2
$E^{\mathrm{j2}}/E^{\mathrm{j1}}$ in H center-of-mass frame
Sphericity: measure of the summed p_T^2 with respect to the event axis calculated from muon, j1, and j2
Sphericity calculated from μ, $\not{E}_{\mathrm{T}}$, j1 and j2
Scaled $\not{E}_{\mathrm{T}}$: $\sum_{n=0}^{numJets} (\sqrt{E^{\mathrm{jet}}}\ \times \sin\theta^{\mathrm{jet}} \times \cos\Delta\phi[\mathrm{jet}, MET]\ )^2$
m_T^W
p_T^W
WWbisDPhi : $\Delta\phi$ between leptonic W and dijet bisector
Invariant mass of the WW pair, (M_H). Used only for $m_H \geq 160$ GeV.
Transverse mass of the WW pair (m_T^H)

Table 16: Variables used as inputs to the random forest.

8.2.2 Training the Random Forest Classifier

Our signal and background events (including multijet background) are split into two samples, those with odd event numbers are used for selection of RF inputs and RF training, even numbered events are used for evaluation of the RF response and limit setting. The event number in MC corresponds to the order of event production in the sample. The odd numbered events are further split in half to define training and validation sub-samples. A separate RF is trained for each mass point in 5 GeV steps between $115 - 200$ GeV. The validation sample was used to determine the optimal RF structure by minimizing the quadratic loss figure of merit when varying the leaf size and number trees used to construct the RF, where the quadratic loss is:

$$\mathcal{QL} = \frac{\sum_{i=1}^{\text{Nval}} w_i (x_i - y_i)^2}{\sum_{i=1}^{\text{Nval}} w_i} \tag{8.2}$$

where Nval is the total number of validation events, w_i is the event weight, x_i is zero for background events, one for signal events, and represents the desired output of the RF, and y_i is the actual RF output for event i.

We varied the RF structures and examined the effects on the testing sample. This study only included the testing samples needed to calculate expected limits (described in detail in Chapter 10) on standard model Higgs boson production and excluded data used to calculate observed limits. Figure 64 expresses expected limits as a multiple of the predicted production rate of the standard model Higgs boson as function of M_H using outputs from RF's with varying parameters. The parameters examined were: the terminal leaf size, using the signal significance figure of merit in training (equal to the ratio of signal events to the square root of the number of

signal plus background events in a node), and removing variables of low discrimination power from the input distribution list. Variable discrimination power was determined by measuring the change in $\mathcal{QL}$ when a decision with respect to that variable was randomized and removal was based on the percentage change of $\mathcal{QL}$ (Fig. 64 shows results when removing variables with $\Delta\mathcal{QL} < 2\%$ and $< 5\%$). The limits calculated when maximizing the signal significance figure of merit in training are considerably worse than all other variations using the Gini index, thus the Gini index was selected as the figure of merit for the analysis.

Variables that are well modeled but poor discriminators for a particular M_H region will have no impact on a random forest, so the full list of input distributions from Sec. 8.2.1 are used as inputs to each RF. Details of the RF structure are listed in Table 17.

Parameters used for Random Forest Training
Number of trees: 50
Number of input variables: 33
Criterion for decision tree optimization: Gini index
Minimal number of entries per tree leaf: 500
Max number of sampled features: number of variables

Table 17: Details of Random Forest construction.

8.2.3 Random Forest Output

The RF outputs for $m_H = 165$ GeV are shown in Fig. 65. The full set of RF outputs for each M_H point can be found in Appendix B.

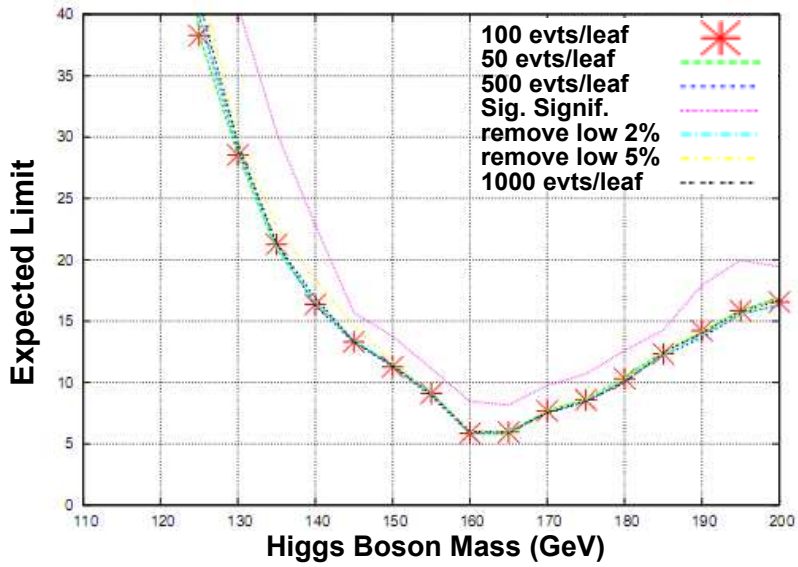

Figure 64: Examination of the expected limit when varying the parameters of the RF used for training. Limits are expressed as multiples of the standard model Higgs boson prediction as a function of M_H and are robust against variations in the terminal leaf size, and variable removal based on the percentage change of $\mathcal{QL}$. The expected limit worsens considerably when moving from the Gini Index to the signal significance figure of merit [88].

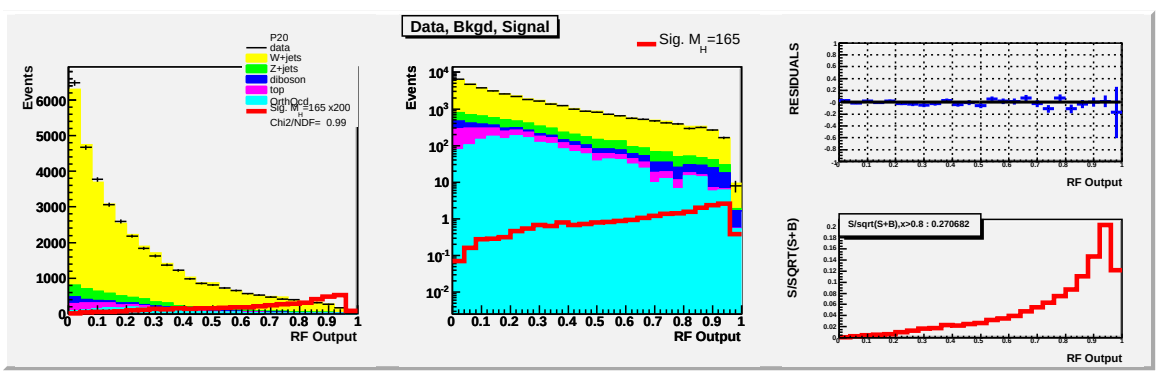

Figure 65: RF output for signal vs. individual background sources, $M_H = 165$ GeV in linear (left) and log scale (center). The signal is scaled (x200) for visibility in the left hand plot. Also shown are the residual differences between data and MC (top right) and the expected signal significance (signal/$\sqrt{(\text{signal} + \text{background})}$ for each bin of the RF output (bottom right).

9 Systematic Uncertainties

The measurements necessary to properly model the data set under analysis, described in Chapters 6−7, are a mixture of analysis-specific calculations (mulitjet derivation, η^{jet}, p_T^W, and $\Delta R(j1, j2)$ weighting) and corrections that are correlated with all analyses performed at DØ (e.g. luminosity, JES, muon identification). These measurements are not exact, each has a corresponding uncertainty approximated a Gaussian distribution, and variations are described in terms of one standard deviation $\pm 1\sigma$ fluctuations [121]. The effect of each systematic uncertainty is propagated through the trained random forest and applied in the limit setting process. Only designated testing events (even event numbers) are used in the evaluation of systematic uncertainties through the RF to avoid bias from testing on the same events used in training. Two types of systematic uncertainties are considered in this analysis:

- Overall ("flat") systematics, such as uncertainties on cross sections, that affect the relative normalizations of samples. Flat systematics have a uniform impact on each RF output bin for each mass point.

- Differential ("shape") systematics, such as the jet energy scale (JES) uncertainty, that affect the shape of the RF output distributions of both signal and background samples, contributing different normalization changes to each bin. Shape systematics can also vary from mass point to mass point. The magnitude of positive and negative systematics are treated as Gaussian distributions, but they need not be symmetric.

The systematics are propagated through the RF by independently varying each discriminant variable in the entire testing sample by $\pm 1\sigma$ and reevaluating of the RF to determine the resulting correlated fractional deviation from the unvaried (nominal)

distributions in each bin:

$$\text{FractionalUncertainty}_i = \frac{N_i^{\text{syst}} - N_i^{\text{nom}}}{N_i^{\text{nom}}} \tag{9.1}$$

where N_i^{syst} are the number of events in RF output bin i when varying the systematic by 1σ before testing, and N_i^{nom} are the number of events in RF output bin i in the nominal RF output distribution. The systematic uncertainties used in this analysis to derive limits on the rate of standard model Higgs boson production are described in more detail below and listed in Table 18. Figures 66-85 show examples of the fractional uncertainties from propagating $\pm 1\sigma$ systematics through the RF for signal and background samples.

Table 18: Systematic uncertainties for the $H \to WW \to \mu\nu jj$ analysis shown for $M_H = 165$ GeV. Uncertainties are listed as relative changes in normalization, in percent. Those affecting the shape of the RF discriminant are indicated with "Y".

Contribution	Shape	W+jets	Z+jets	Top	Diboson	$gg \to H$
Jet energy scale	Y	shape only	shape only	± 6.0	$\binom{+3.3}{-3.5}$	$\binom{+3.3}{-2.0}$
Jet identification	Y	shape only	shape only	± 3.3	± 1.3	± 3.5
Jet resolution	Y	shape only	shape only	$\binom{+0.5}{-0.3}$	$\binom{+1.0}{-0.5}$	$\binom{+2.0}{-1.8}$
Jet Vertex Confirm.	Y	shape only	shape only	± 3.8	± 3.8	± 4.8
Luminosity	-	-	± 6.1	± 6.1	± 6.1	± 6.1
Muon trigger	Y	± 0.5	± 0.5	± 0.5	± 0.25	± 0.25
Muon identification	-	± 4.0	± 4.0	± 4.0	± 4.0	± 4.0
ALPGEN tuning	Y	shape only	shape only	-	-	-
Cross Section	-	± 6.0	± 6.0	± 10.0	± 7.0	± 10.0
Heavy-flavor fraction	Y	± 20	± 20	-	-	-
PDF	Y	$\binom{+3.5}{-2.5}$	$\binom{+8.0}{-1.5}$	$\binom{+2.3}{-3.6}$	± 0.25	$\binom{+1.8}{-3.8}$
Multijet background	Y		± 26.2			

9.1 Flat Systematics

The following is a description of the flat systematics that are used in the analysis.

- Cross Sections: We use standard estimates for the uncertainties associated with the SM cross sections for light parton W/Z+jets (6%), diboson (7%) and top (10%) samples [122]. The uncertainty in the production rate of signal events (10%) is taken from Ref. [25]. Normalization changes due to choices of PDF are included in the quoted uncertainties.

- V+jets Heavy Flavor Rate: The uncertainty on the scale factor that is applied to set the $W/Z + bb$ and $W/Z + cc$ contributions relative to the $W/Z + lp$ contributions is 20%. [122]

- Multijet Production: We assign an uncertainty of 26.2% to the number of events produced by multijet production. This comes from the change in multijet normalization when a single fit of leptonic m_T^W is performed instead of a simultaneous fit of $\not\!\!E_{\mathrm{T}}$ and p_T^μ. The multijet normalization uncertainty is anti-correlated with the V+jets scale factor.

- Luminosity: We assign a 6.1% uncertainty to the luminosity measurement (Ref. [123]) used to normalize the MC. This includes a 4% uncertainty common to the Tevatron experiments and a 4.1% uncertainty specific to DØ. This is correlated across all MC samples.

- Muon ID and Trigger: We assign a combined 4% uncertainty due to muon ID and trigger efficiency uncertainties (Ref. [124]) correlated across all MC samples.

- Top JSSR Shifting: We assign a 1.8% uncertainty to top samples based on DØ Top group studies of the JSSR shifting model applied in top events. This is

related to differences in modeling jets from b quarks versus lights quarks and gluons [125].

9.2 Shape Systematics

The following is a description of the shape dependent systematics that are used in the analysis.

- Jet Energy Scale (JES): We assign a $\pm 1\sigma$ uncertainty to the Monte Carlo jet energies, to account for the uncertainty in the JSSR shifting correction factor. This is shape-only in V+jets samples because their normalization is scaled to data, and effects both shape and rate in other Monte Carlo samples. The RF outputs are reevaluated independently for a 1σ increase and a 1σ decrease in the JES correction for each Monte Carlo background sample using code provided by the DØ Jet ID group. This systematic is correlated across all MC samples. The $\pm 1\sigma$ JES fractional uncertainty is shown in Figs. 66−67.

  The relative data and MC calorimeter response to measuring energies of b quark initiated jets is in between that of gluon jets and the light quark jets JSSR uses for shifting corrections (Fig. 30). The $W + bb$ and $Z + bb$ samples have an additional uncertainty (D0_BJES) to account for changes in JES assumed by the shifting model [72]. This is estimated by reevaluating the RF output for $W + bb$ and $Z + bb$ samples with shifting turned off and taking the associated systematic to be one third the difference between the shifted and non-shifted samples:

  D0_BJES histo = NominalHisto ± (Un-ShiftedHisto - NominalHisto)/3

  D0_BJES is considered separately from the above JES systematic applied to all

V+jets samples and is shape-only because $W+bb$ and $Z+bb$ samples have normalizations scaled to data. The D0_BJES systematic has maximum associated fractional uncertainties $\mathcal{O}(0.4\%)$ and has negligible impact on limit calculation.

- Jet Energy Resolution (JER): We assign a $\pm 1\sigma$ uncertainty to the MC jet energies, to account for the difference in jet energy resolution between data and the simulation. The RF outputs are reevaluated independently for a 1σ increase and a 1σ decrease in the JER correction for each Monte Carlo background sample using code provided by the DØ Jet ID group. This is again shape-only in V+jets samples, effects both shape and rate in other MC samples, and is correlated across all MC samples. The $\pm 1\sigma$ JER fractional uncertainty is shown in Figs. 68−69.

- Jet ID and Reconstruction Efficiency: We assign a $\pm 1\sigma$ symmetric uncertainty to account for differences between data and simulation in the jet ID and reconstruction efficiencies. Because application of the correction is achieved through random removal of jets in MC, the RF output is reevaluated for a 1σ decrease in the Jet ID reconstruction independently for each Monte Carlo background sample using code provided by the DØ Jet ID group. This is again shape-only in V+jets samples, effects both shape and rate in other MC samples, and is correlated across all MC samples. This fluctuation is symmetrized to $\pm 1\sigma$ within the limit setting program, and the fractional uncertainty is shown in Figs. 70−71.

- Jet Vertex Confirmation: We assign a symmetrized uncertainty on the vertex confirmation scale factor to account for differences in vertex confirmation in data and MC. Because application of the scale factor is achieved through random removal of vertex confirmed jets in MC, this correction is based on a 1σ downward fluctuation symmetrized to $\pm 1\sigma$ within the limit setting program.

The RF output is reevaluated for a 1σ decrease in the vertex confirmation scale factor independently for each Monte Carlo background sample using code provided by the DØ Jet ID group. This is again shape-only in V+jets samples, effects both shape and rate in other MC samples, and is correlated across all MC samples. The vertex confirmation fractional uncertainty is shown in Figs. 72−73.

- ALPGEN Parameters and Corrections: We take into account uncertainties due to ALPGEN MLM parton-matching, underlying event and scale (α_s, renormalization, factorization) following the procedure outlined in Ref. [107]. The MLM correction using $m^{(j1,j2)}$ was described in Chapter 6. The systematic on the underlying event (ULE) model in ALPGEN+PYTHIA V+jets events was derived in a similar manner. For ULE, W+jets events were produced with the event generator HERWIG which is known to model the underlying event well [126], and compared with W+jets events produced with PYTHIA to get a parametrized $\pm 1\sigma$ fluctuation in terms of $m^{(j1,j2)}$ [127]. A systematic on the ALPGEN renormalization/factorization scale $q^2 = (M_W)^2 + \sum (p_T^{\text{jet}})^2$ and the scale of α_s at each vertex was derived by inspecting the $\Delta\chi^2$ between data and W+jets ALPGEN+PYTHIA events as the scales were changed. The $\pm 1\sigma$ scale variations were taken at the $\Delta\chi^2 = 1$ points from the minimum χ^2 and parametrized in terms of $m^{(j1,j2)}$. The RF output is reevaluated independently for each of the three ALPGEN uncertainties by applying $\pm 1\sigma$ ($m^{(j1,j2)}$) weighting functions provided by members of the DØ Higgs group, and reevaluating the RF for each V+jets Monte Carlo background sample. These systematics are shape-only and each is correlated across all V+jets samples. The $\pm 1\sigma$ MLM, ULE and scale fractional uncertainties are shown in Figs. 74−76.

- Trigger: The trigger normalization systematic is included in the 4% lepton ID and trigger uncertainty. For the shape, the preselection is re-run removing any explicit trigger requirement from the background MC. The RF output is reevaluated independently for each Monte Carlo background sample after removing the trigger requirement. To estimate the $+1\sigma$ fluctuation we take the associated systematic to be half the difference between the nominal and the no-trigger RF output:

  Trigger systematic histo = NominalHisto + (NoTriggersHisto - NominalHisto)/2.

  Because the trigger normalization is incorporated in the muon ID systematic, this systematic is considered to be shape-only for all MC samples. The trigger systematic is correlated across all MC samples. This fluctuation is symmetrized to $\pm 1\sigma$ within the limit setting program. The trigger fractional uncertainty is shown in Fig. 77.

- Multijet Shape: Six anti-isolated input distributions are used to determine our multijet shape (Sec. 7.1). The multijet shape uncertainty is estimated on an event by event basis by fluctuating the average of the six multijet event weights by $\pm$ 1 standard deviation of the six input multijet weights. Because the standard deviation of the multijet weights is quite small the resulting fluctuated shapes are largely unchanged. The very small fractional uncertainty associated with multijet shape for can be seen in Fig. 79. This is a shape-only systematic, and is in addition to the flat normalization uncertainty of 26.2%.

- Jet η, ΔR(j1,j2) and p_T^W weighting: We take the $\pm 1\sigma$ correlation matrix error bands calculated in the derivation of the jet and p_T^W ALPGEN weights (Sec. 6.6.2)

and create four individual shape-only systematics. The RF is reevaluated for V+jets samples after applying a 1σ weight variation, keeping all other weights fixed. The procedure is repeated eight times evaluate the $\pm 1\sigma$ systematic uncertainties for all four weights. These systematics are shape-only and each is correlated across all V+jets samples. The $\pm 1\sigma$ η^{jet}, ΔR(j1,j2), and p_T^W fractional uncertainties are shown in Figs. 80−83.

- PDF Shape: Shape systematic for the parton distribution functions (PDF). Both ALPGEN and PYTHIA use the leading order CTEQ6L1 parton distribution functions [92] to model initial states for partons in modeling the $p\bar{p}$ collisions (Chapter 5). The CTEQ collaboration evaluates deep inelastic scattering experiments and inclusive jet cross section measurements to determine probability densities for finding a parton within a hadron that carries a specific fraction of the hadron's momentum. Results are provided as PDF sets of leading order, and next-to-leading order. The CTEQ PDF sets correspond to the best fit of the experimental data using 20 separate fit parameters, each with an associated $\pm 1\sigma$ error. These uncertainties are calculated only for next-to-leading order PDF's (set CTEQ6.1M). Because ALPGEN and PYTHIA use the leading-order set CTEQ6L1, each MC sample is weighted to CTEQ6.1M using code provided by the DØ Top group [128], and then the RF is reevaluated 40 times, once for each associated $\pm 1\sigma$ error [129]. The $\pm 1\sigma$ pair that results in the largest fractional uncertainty is used as the PDF shape systematic. Because the PDF normalization uncertainty is contained in the flat cross section systematic, this systematic is considered to be shape-only for all MC samples. The $\pm 1\sigma$ PDF fractional uncertainty is shown in Figs. 84−85.

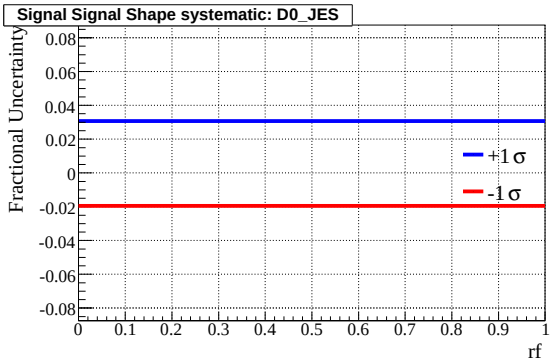

Figure 66: Signal mH=165, JES

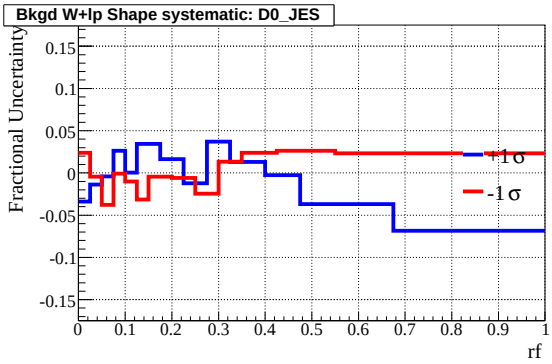

Figure 67: W+lp, JES

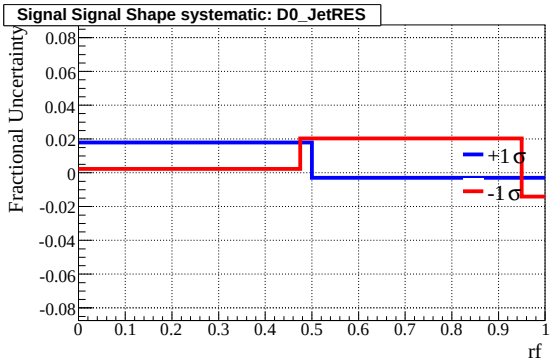

Figure 68: Signal mH=165, JetRES

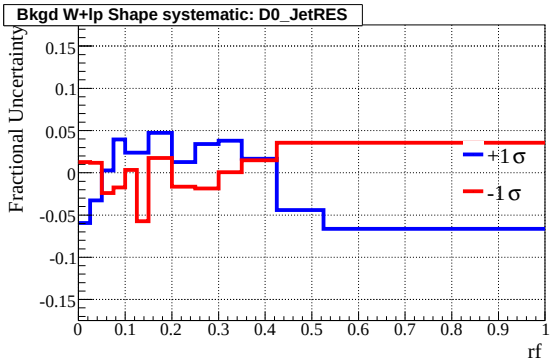

Figure 69: W+lp, JetRES

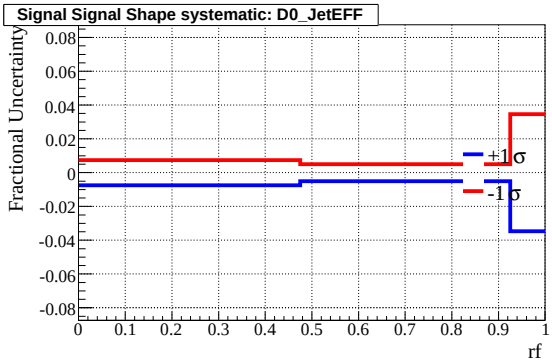

Figure 70: Signal mH=165, JetID

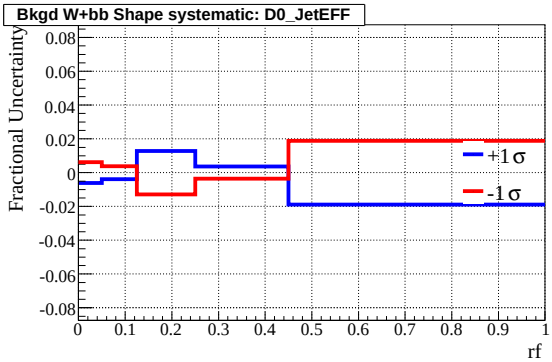

Figure 71: W+bb, JetID

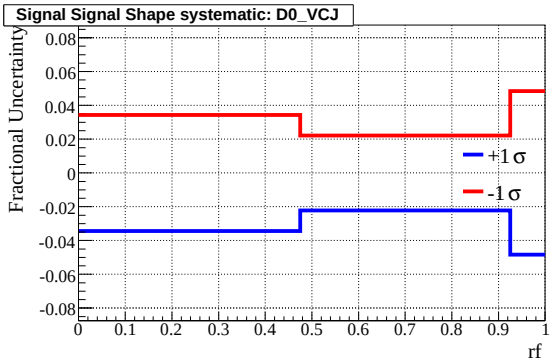

Figure 72: Signal mH=165, VCJets

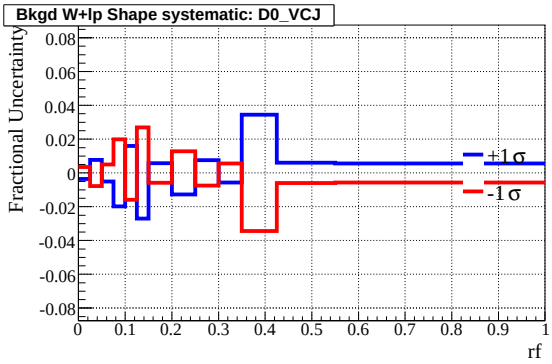

Figure 73: W+lp, VCJets

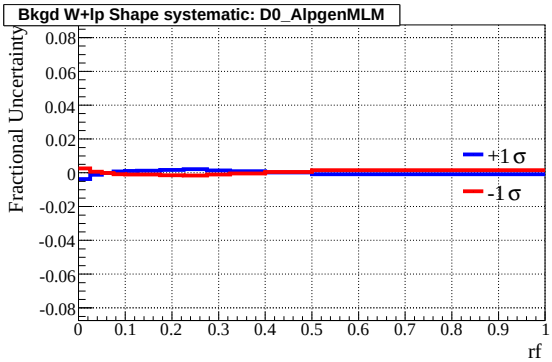

Figure 74: W+lp, AlpgenMLM

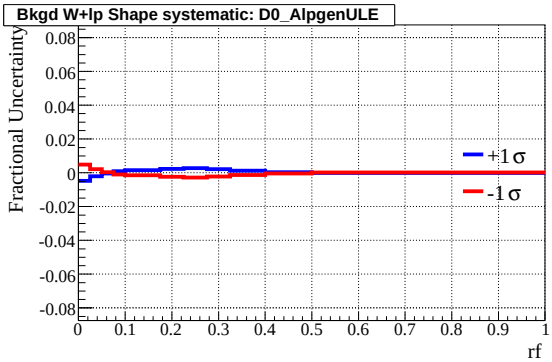

Figure 75: W+lp, AlpgenULE

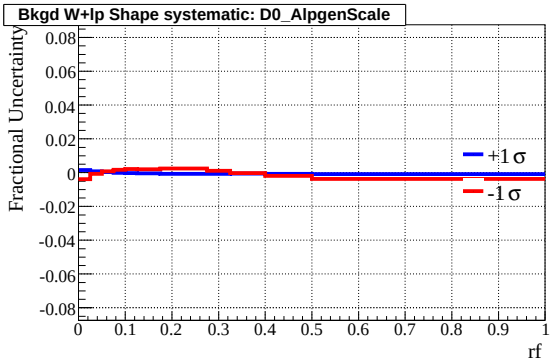

Figure 76: W+lp, AlpgenScale

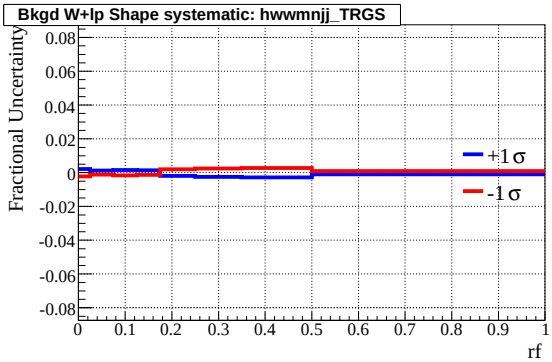

Figure 77: W+lp, Triggers

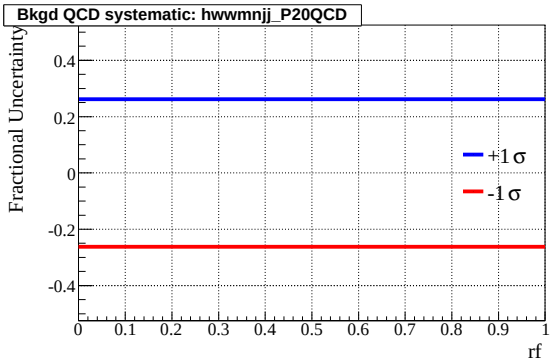

Figure 78: Multijet Normalization

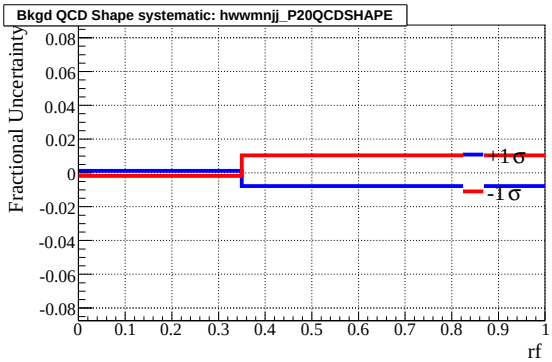

Figure 79: Multijet Shape

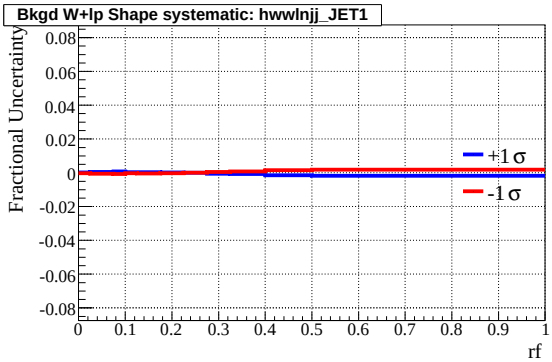

Figure 80: W+lp, j2eta Rewgt

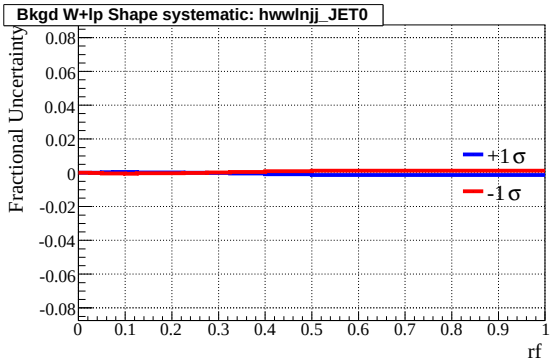

Figure 81: W+lp, j1eta Rewgt

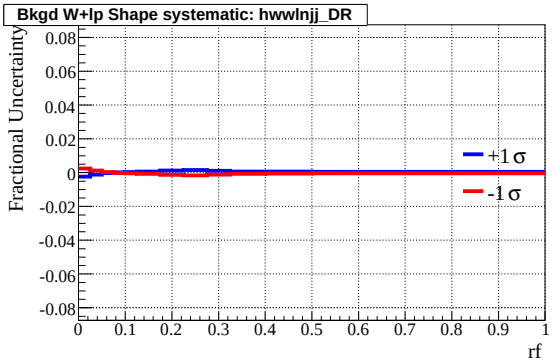

Figure 82: W+lp, ΔR(j1,j2) Rewgt

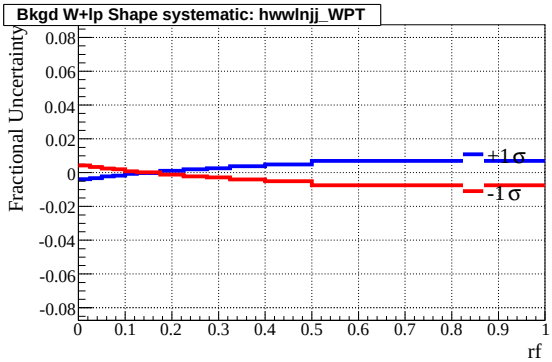

Figure 83: W+lp, p_T Wlep Rewgt

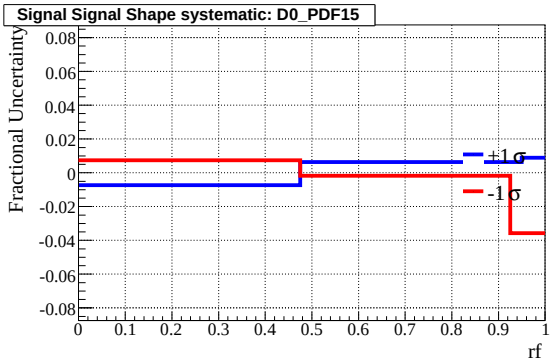

Figure 84: Signal mH=165, PDF

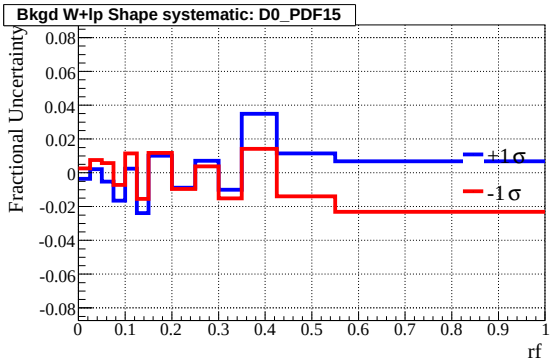

Figure 85: W+lp, PDF

10 Upper Limits on SM Higgs Boson Production for the $H \to WW$ Semileptonic Decay Channel

We perform a separate analysis for 18 hypotheses for the mass of the Higgs boson with each analysis employing a separate random forest classifier optimized for each M_H. Data, background and signal samples are tested against each RF. The output distributions of each RF are also examined with respect to variations of the systematic uncertainties. These output distributions, including systematic uncertainties effecting the their shapes and normalizations, serve as our discriminating variables and are used to determine an upper bound on the rate of production for the standard model Higgs boson. This analysis uses the CL_S method of limit evaluation implemented in the C++ based package COLLIE (**CO**nfidence **L**evel **LI**mit **E**valuator) [121][24] to calculate the limits on standard model Higgs production.

10.1 CL_S Method of Limit-Setting

To evaluate the sensitivity to signal in the data we begin by considering two possibilities:

- *b-only* hypothesis: The data consists of the sum of standard model background processes leaving $\mu\bar{\nu}jj$ final states in the detector.
- *s+b* hypothesis: The data consists of standard model backgrounds plus signal $H \to WW \to \mu\bar{\nu}jj$ events where the signal model is modified for each value of M_H under examination.

The parameter of interest that differentiates the two hypotheses being tested is referred to as the model parameter. The model parameter that changes for each

[24] maintained by the DØ Higgs group

test of the above hypotheses in this analysis is the mass of the Higgs boson used for generation of signal Monte Carlo, where M_H also determines the SM production and decay properties.

The CL_S method employs a test statistic that compares the likelihood the data is described by *s+b* to the likelihood the data is described by *b-only*. For each value of M_H, the RF output for signal and the RF output for the sum of the backgrounds are fixed numbers of events, the outcome of a specific experiment. Outcomes from a series of experiments are necessary to create probability distribution functions that will allow for meaningful comparisons of the likelihood for the observed data to be consistent with the *s+b* and *b-only* hypotheses. Simulated experiments (pseudo-experiments) are run to generate new *s+b* and *b-only* discriminant distributions (pseudo-data). To create the pseudo-data, the content of each bin in the RF discriminant is treated as one possible sampling from a Poisson distribution with a mean equal to the number of events observed either in the *s+b* or *b-only* hypothesis [121]. The Poisson probability for finding a number of events k using a Poisson mean m is given by:

$$P(k|m) = \frac{m^k e^{-m}}{k!} \tag{10.1}$$

In the nominal prediction for each background, each associated systematic $1 \rightarrow k$ is at its central value (η_k^0). Thus the total nominal prediction for the event content of bin i is:

$$p_i^0(\eta_1, ..., \eta_k) = \sum_{j=1}^{Background} p_{ij}(\eta_1^0, \eta_2^0, ..., \eta_k^0) \tag{10.2}$$

A change of any systematic $(\eta_1, ..., \eta_k)$ from its nominal value will shift the total bin content to a new value p_i:

$$p_i(\eta_1, ..., \eta_k) = \sum_{j=1}^{Background} p_{ij}(\eta_1^0, ..., \eta_k^0) \prod_{k=1}^{\text{Systematic}} \frac{p_{ij}(\eta_k)}{p_{ij}(\eta_k^0)} \tag{10.3}$$

where the number of events in each bin (p_i) is the sum of the contributions from each background source, and the number of events from each background is based on the values of the k systematics associated with that source. The number of events after fluctuations in the systematics is defined in terms of the deviation from the nominal number of events (p_{ij}^0). Equation (10.3) can be re-written as:

$$p_i(\eta_1, ..., \eta_k) = \sum_{j=1}^{Background} p_{ij}^0 \prod_{k=1}^{\text{Systematic}} (1 + R_k \sigma_{ijk}) \tag{10.4}$$

where σ_{ijk} is fractional change in the number of events from the nominal background j due to systematic k, R_k is the deviation from the nominal value of systematic k in terms of σ_k : $R_k = (\eta_k - \eta_k^0)/\sigma_k$, where R_k is normally distributed, and correlations across the bins (p_i) are explicitly preserved for each systematic. For each pseudo-experiment, the η_k are randomly drawn from a normal distribution with mean η_k^0 and standard deviation σ_k. Each bin i in the output of the pseudo-experiment has its content drawn randomly from a Poisson distribution (10.1) with a mean of p_i resulting in a final pseudo-datum, p_i'. A large number of pseudo-experiments are generated separately for the *s+b* and *b-only* hypothesis for each mass point under examination. In *s+b* generation, the summation in Eqn. (10.4) runs over the signal sample as well as all background sources. Statistical uncertainties on the p_i^0 due to limited statistics in the MC samples are also considered by varying the mean in Eqn. (10.1).

10.1.1 The Poisson Log-Likelihood Ratio

We treat the outcome of each *s+b* and *b-only* pseudo-experiment as set of Poisson counting experiments for each bin in the output distribution of the RF discriminant. For each experiment, we build a Poisson likelihood ratio (Q) :

$$\begin{aligned} Q(s,b,d) &= \prod_{i=1}^{\text{Nbins}} \frac{e^{-(s_i+b_i)}(s_i+b_i)^{d_i}/d_i!}{e^{-b_i}(b_i)^{d_i}/d_i!} \\ &= \prod_{i=1}^{\text{Nbins}} e^{-(s_i)} \left(\frac{s_i+b_i}{b_i}\right)^{d_i} \end{aligned} \tag{10.5}$$

where s_i is the number of signal events in bin i of the RF output distribution, b_i is number of background events and d_i is the number of observed data, or the number of events (p_i') from a single *s+b* or *b-only* pseudo-data trial in bin i. This can be re-written as a negative log-likelihood ratio (LLR):

$$\text{LLR} = -2\ln(Q) = 2\sum_{i=1}^{\text{Nbins}} (s_i - d_i \ln(1 + s_i/b_i)) \tag{10.6}$$

The LLR is evaluated for each set of pseudo-data for both the *b-only* and *s+b* hypotheses.

As an illustration, Fig. 86 shows example distributions when using a *s+b* hypothesis with large signal. The *s+b* LLR is shown as a red Gaussian, the *b-only* LLR is shown as a green Gaussian, with an LLR value for data in black. If there were no signal in the *s+b* hypothesis, the red and green curves would overlap with a median at zero. With the addition of signal, the median of the *s+b* LLR moves to the left, and the median of the *b-only* LLR moves to the right. If the background modeling perfectly described the data, the median of the *b-only* LLR would overlap with the LLR of the observed data. Those pseudo-experiments with LLR values to the right

of the observed data LLR are less signal-like (more background-like) than the data.

The Frequentist confidence level statistic is based on the fraction of *s+b* trials more background-like than data, indicated by the solid red curve (CL_{S+B}). Using the Frequentist confidence level statistic, the upper bound on standard model Higgs boson production at the 95% confidence level (C.L.) is set by increasing the cross section of the signal until $1 - CL_{S+B} = 0.95$. In basing its statistic on CL_{S+B}, the Frequentist C.L. does not include information on the modeling of the background alone, or the sensitivity to the signal with respect to the *b-only* LLR distribution. This can lead to false exclusions at 95% C.L. in cases where there is little signal sensitivity (LLR_{S+B} and LLR_B medians are close together) and there is a downward data fluctuation below background model predictions causing the observed LLR to move in the positive direction and $CL_{S+B} \leq 0.05$.

The semi-Frequentist confidence level statistic (CL_S) used in this analysis is more robust against false exclusions through the inclusion of the *b-only* model in limit setting. The ratio of the fraction of *s+b* trials more background-like than data (CL_{S+B}) to the fraction of *b-only* trials more background like than data (CL_B) is the semi-Frequentist confidence level statistic (CL_S):

$$CL_S = \frac{CL_{S+B}}{CL_B} \tag{10.7}$$

When we have no sensitivity to signal the LLR_{S+B} and LLR_B medians overlap and $CL_S = 1$ and false exclusions due to background fluctuations are possible. As we increase in sensitivity, the medians move apart and CL_S decreases. An upper bound on standard model Higgs boson production at the 95% confidence level (C.L.) is set by increasing the cross section of the signal until $1 - CL_S = 0.95$.

In addition to being more robust against false exclusions, the CL_S method is

more conservative in its confidence level setting than the Frequentist method. As an example, take the case of perfect background modeling: $CL_B = 0.5$. If $CL_{S+B} = 0.05$ the Frequentist method is satisfied to 95% C.L. but the *semi*-Frequentist CL_S statistic returns the more conservative 90% C.L.

The limits calculated with respect to the observed data LLR are referred to as the "observed" limits. An "expected" limit in the absence of signal is calculated with respect to the median of the *b-only* LLR distribution [130]. The distance between the medians of the *s+b* and *b-only* LLR distributions are an indication of the discriminating power of the input distributions to the CL_S method. The inclusion of systematics broadens the LLR distributions, increasing overlap between the two hypotheses and thus reducing the sensitivity of the measurement.

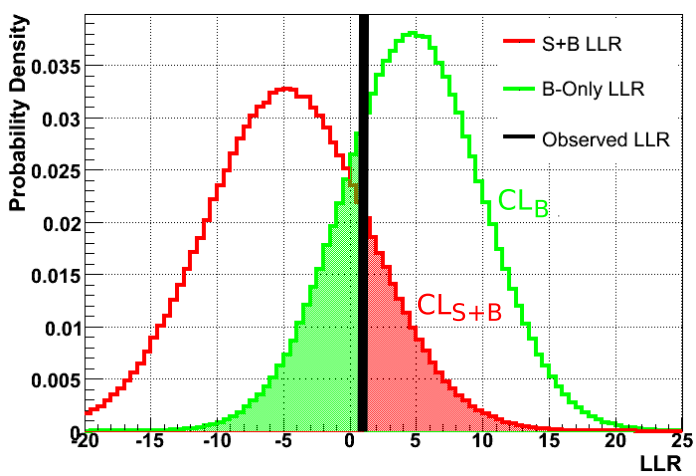

Figure 86: Example LLR distributions for an analysis with non-negligible signal. The red Gaussian represents the LLR distribution calculated with respect to the *s+b* hypothesis, the green Gaussian represents the LLR distribution calculated with respect to the *b-only* hypothesis and the observed LLR is a black line. The separation between the medians of the LLR distributions for *s+b* and *b-only* models increases with signal sensitivity. Any pseudo-experiment with LLR to the right of the observed data LLR is more background-like than data [121] [131].

10.1.2 Constraints on Models of Systematics

As discussed in Chapter 9 each systematic has an associated $\pm 1\sigma$ uncertainty, and the inclusion of these uncertainties degrades the final calculated limits. We use the information contained in the normalizations of the data and pseudo-experiments to provide an estimate of the true variance associated with a systematic which is frequently smaller than the initial estimates for their $\pm 1\sigma$ values. Using these new estimates, a set of *s+b* and *b-only* pseudo-experiments are generated. We again use a constraint of the total normalization of the (pseudo)data to find a best-fit systematics profile that maximizes the likelihood of describing the hypothesis being tested while maintaining any correlations between systematics[25]. Each LLR value used in limit setting will incorporate the systematics profile found for those (pseudo)data.

As an example of how normalization can be used to better constrain the systematic uncertainties, we will examine fitting pseudo-data with varying systematics to data. First pseudo-data is created using Eqn. 10.4 with randomly drawn R_k values to provide the mean (p_i) for the randomly sampled Poisson distributions. The value of each systematic is then varied to find a best-fit to data using the χ^2 function [132]:

$$\chi^2 = 2 \sum_{i=1}^{Nbins} \left[(p_i' - d_i) - d_i \ln \left(\frac{p_i'}{d_i} \right) \right] \tag{10.8}$$

Figure 87a shows the pull distribution for the flat luminosity uncertainty after performing $\mathcal{O}(10,000)$ fits to data, where the pull is defined as:

$$PULL_k = R_k^{\text{fit}} - R_k^{\text{prefit}} \tag{10.9}$$

Here R_k^{prefit} is the ($N\sigma_k$) deviation from nominal that was initially drawn, and R_k^{fit} is

[25]To accurately model the normalization of data, increases in event count due to a positive systematics fluctuation must be balanced by a downwards fluctuation elsewhere.

the ($N\sigma_k$) deviation from nominal for the luminosity after the fit. The R_k values are $\in [-4, 4]$, and 68% of the time $|R_k^{\text{prefit}}| \leq 1$. Fits using *s+b* pseudo-data are shown in red, and fits using *b-only* pseudo-data are shown in black. A width less than one indicates the systematic can be constrained (beyond the initial $\pm 1\sigma$) value by the data. A non-zero mean shows a preference for a nominal value for the systematic other than η_k^0 based on residual differences between the data and MC nominal RF outputs [121].

The pull of fits to pseudo-data using the background-only, or the signal plus background nominal RF outputs can give an indication of which systematics will have the largest contribution to the fits of pseudo-experiments used for limit setting (Fig. 87b). In this case, each bin i in the output of the pseudo-experiment has its content drawn randomly from a Poisson distribution (10.1) with a mean equal to the content of bin i in the background-only (or signal plus background) nominal RF output. Fig. 87b again shows the pull for luminosity. In this circumstance, $R_k^{\text{prefit}} = 0$, and the pull distribution represents the $N\sigma$ from nominal the fit pulled the luminosity systematic. The narrower the distribution, the less impact that systematic has on the fit [121]. Fits using background-only RF outputs are shown in black, and fits using signal plus background outputs are shown in red. Means from the Fig. 87a *s+b* (in green) and *b-only* (in blue) distributions are also shown.

To estimate the true variance associated with a systematic we examine the χ^2 fit of the data RF output using pseudo-data made from the background only, or signal plus background nominal RF output distributions when varying a single systematic in Eqn. 10.4 [132]. Figure 87c shows the χ^2 response to fits when varying the luminosity systematic as a function of the $N\sigma$ deviation from nominal post-fit. The $N\sigma$ changes corresponding to the $\Delta\chi^2 = 1$ from the minimum give improved estimates for the $\pm 1\sigma$ uncertainties to be used in the generation of pseudo-data for evaluation of the

limits.

Figure 88a shows how each systematic was fluctuated in units of $N\sigma$ in the best-fit to data using the *s+b* (in red) and *b-only* (in green) hypotheses for the analysis of $M_H = 165$ GeV. The fluctuations at $\approx 1\sigma$ are multijet normalization, jet energy scale, jet vertex confirmation, and PDF uncertainty which is slightly above 1σ. Figure 89 shows the reduction in size of per bin systematic variations in percent after fitting to the data. The per bin errors before fitting (in blue) are $\approx 10\%$, after the fit of *b-only* to data (in green), and after the fit of *s+b* to data (in red) the errors are $1 - 2\%$.

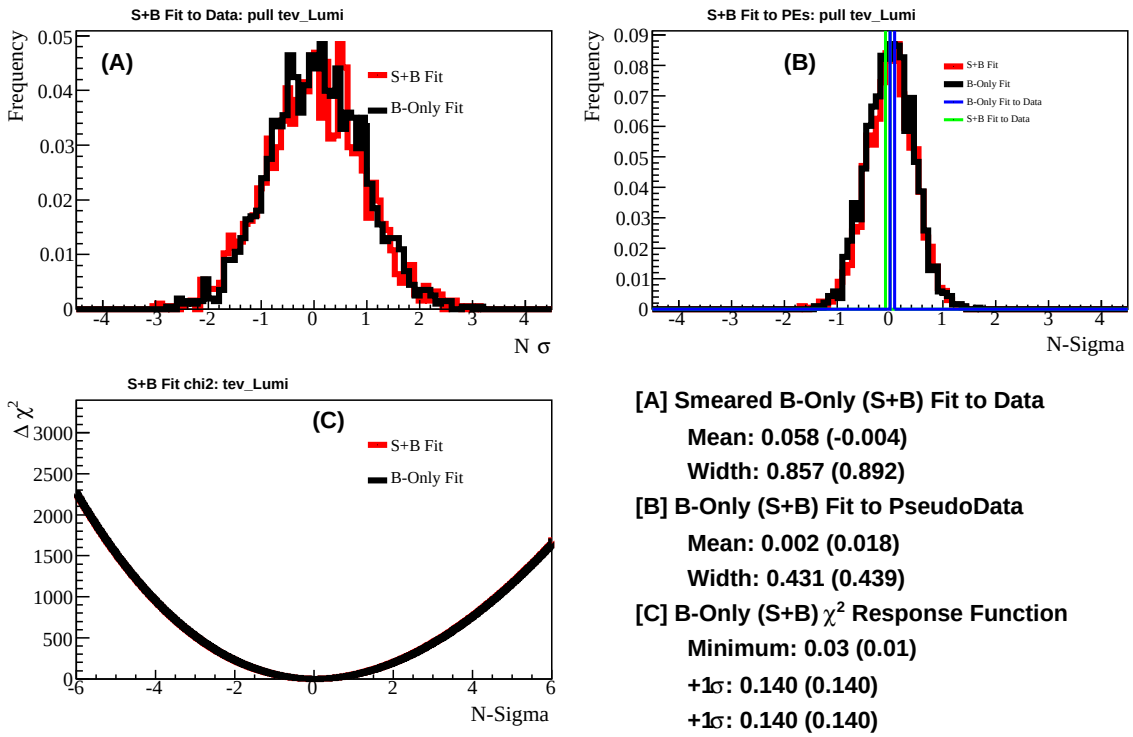

Figure 87: Fit tests for the luminosity uncertainty in the $H \rightarrow WW \rightarrow \mu\nu jj$ analysis of $M_H = 165$ GeV: A) Pull of luminosity distribution in fits to data; B) Pull of luminosity distribution in fits to pseudo-data; C) χ^2 response to fits of data. See text for details.

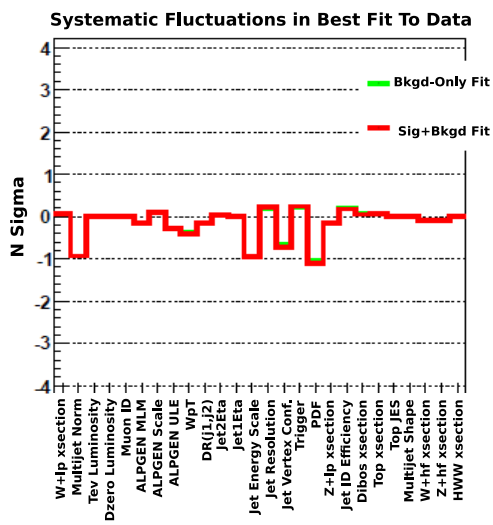

Figure 88: Best-fit values for systematics $(\hat{\eta}_1, \hat{\eta}_2, ..., \hat{\eta}_k)$ for data using the *s+b* (in red) and *b-only* hypotheses for the analysis of $M_H = 165$ GeV.

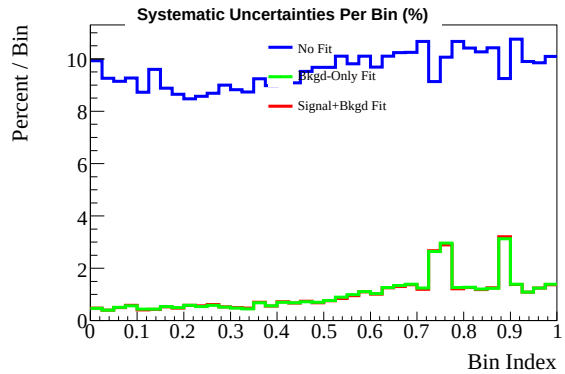

Figure 89: Size of per bin systematic variations in percent before fitting (in blue), after the fit of *b-only* to data (in green), and after the fit of *s+b* to data (in red) for the analysis of $M_H = 165$ GeV.

10.1.3 The Profile Log-Likelihood Ratio

The set of *s+b* and *b-only* pseudo-experiments used for limit setting are created using these new values for the $\pm 1\sigma$ of the systematics. To reduce the impact of the systematic uncertainties on the final LLR distributions, a profile likelihood is employed using a χ^2 for each pseudo-experiment to find the systematics profile that best describes the pseudo-data. This χ^2 incorporates normalization changes associated with each systematic, rather than the single systematic fluctuation used to determine the $\pm 1\sigma$ values used in pseudo-data generation.

The χ^2 function compares the predicted number of events in each bin using a specific systematics profile $(\eta_1, \eta_2, ..., \eta_k)$ to the measured number of events in each bin from the pseudo-experiment as in (10.8) but includes additional contributions to the χ^2 for the deviation of each systematic from its nominal value. A minimized χ^2 translates to a maximized likelihood for the hypothesis to describe the data. This fit

is performed for the output of the RF for data, as well as the output for each *s+b* and *b-only* pseudo-experiment to generate the LLR distributions used in limit setting.

The χ^2 function to be minimized is defined to be [121]:

$$\chi^2(H) = 2\sum_{i=1}^{Nbins}\left[\left(p_i^H(R_k^H) - d_i\right) - d_i \ln\left(\frac{p_i^H(R_k^H)}{d_i}\right)\right] + \sum_{k=1}^{Systematic}(R_k^H)^2 \qquad (10.10)$$

where d_i is the number pseudo-data events in bin i, p_i^H is the predicted number of events in bin i using (10.4) and $(\eta_1, \eta_2, ..., \eta_k)$, and R_k^H is the $N\sigma$ systematic k has varied from the nominal η_k^0, where R_k^H are chosen to minimize the χ^2. Correlated uncertainties will contribute a single R_k^H term to the χ^2.

Every pseudo-experiment will have two associated χ^2 minimizations, one with respect to the *s+b* hypothesis where p_i^H and R_k^H are generated using signal and background sources, in the other p_i^H and R_k^H are generated using only background. The two sets of optimal systematic settings $(\hat{\eta}_1, \hat{\eta}_2, ..., \hat{\eta}_k)$ that minimize the χ^2 functions are used to construction the profile log-likelihood ratio (LLR) test statistic [121]:

$$LLR = 2\sum_{i=1}^{Nbins}\left[(\hat{p}_i^{s+b} - \hat{p}_i^b) - d_i \ln\left(\frac{\hat{p}_i^{s+b}}{\hat{p}_i^b}\right)\right] + \sum_{k=1}^{Systematic}\left((\hat{R}_k^{s+b})^2 - (\hat{R}_k^b)^2\right) \qquad (10.11)$$

where the terms are analogous to Eqn. (10.10). When the d_i corresponds to a *s+b* pseudo-experiment, the LLR value contributes to LLR_{S+B}, a *b-only* pseudo-experiment has a corresponding LLR_B value. The LLR_{Obs} is constructed from minimizations where d_i is the number of data events in bin i of the RF output distribution for data.

10.2 Limits for the $H \rightarrow WW \rightarrow \mu\nu jj$ Channel

We assess the maximum statistical sensitivity for this analysis by evaluating the Poisson log-likelihood test statistic (10.6) ignoring the effects of systematics and calculating the corresponding limits on standard model Higgs boson production. Figure 90 shows the median from each *b-only* LLR distribution for the range $M_H = 115 - 200$ GeV as a dashed black line ($\mathrm{LLR_B}$) . The median from each *s+b* LLR distribution is shown as a dashed red line ($\mathrm{LLR_{S+B}}$), and the LLR of the observed data is shown as a solid black line ($\mathrm{LLR_{Obs}}$). Straight line extrapolations connect the 5 GeV mass steps. The green and yellow bands correspond to the $\pm 1\sigma$ and $\pm 2\sigma$ bands on $\mathrm{LLR_B}$. In the absence of signal, there is a 68% probability the $\mathrm{LLR_B}$ will fluctuate within the $\pm 1\sigma$ band, and a 95% probability for the $\mathrm{LLR_B}$ to fluctuate within the $\pm 2\sigma$ band.

This analysis is most sensitive in the region $155 \leq M_H \leq 175$, where the $\mathrm{LLR_{S+B}}$ and $\mathrm{LLR_B}$ have the largest separation. The $\mathrm{LLR_{Obs}}$ is closer to the $\mathrm{LLR_B}$ over the majority of the mass range, indicating the data is more similar to background than to the combination of signal and background. The majority of the $\mathrm{LLR_{Obs}}$ is within the 1σ band, showing the nominal backgrounds model the data well even before fitting within the systematics.

Figure 91 shows the ratio of 95% C.L. to the standard model expectation for production of the Higgs boson as a function of M_H. We observe no signal-like excess in data and in the absence of signal set an upper limit on standard model Higgs boson production at 5.1 times the standard model expectation at 95% C.L. for $M_H = 165$ GeV. The expected limit in the absence of signal at $M_H = 165$ GeV is 5.7 at 95% C.L.

Systematic uncertainties will broaden the LLR distributions and therefore degrade the sensitivity of the analysis. The LLR and associated limit plot when including

systematics using the profile log-likelihood ratio test statistic (10.11) are shown in Figs. 92 and 93. As expected with the inclusion of systematics the LLR distribution has broadened in Fig. 92 in comparison to Fig. 90. Though there are more regions in Fig. 92 where the $\mathrm{LLR_{Obs}}$ is more signal-like than background like, the fluctuations are within the 2σ band and consistent with the background-only hypothesis. Figures 94−99 show the full profile LLR test statistic distributions for each mass point with *s+b* in red, *b-only* in green, and the observed data LLR in black. Including systematics the expected limit at $M_H = 165$ GeV is 11.2 at 95% C.L., two times the expected limit without systematics. The observed limit at $M_H = 165$ GeV is also 11.2.

Table 19 lists the expected and observed limits in terms of standard model production rates for a Higgs boson in the range $M_H = 115 - 200$ GeV with and without systematics. Also shown is the ratio of expected limits with systematics to the expected limits without systematics to indicate the sensitivity loss due to systematics.

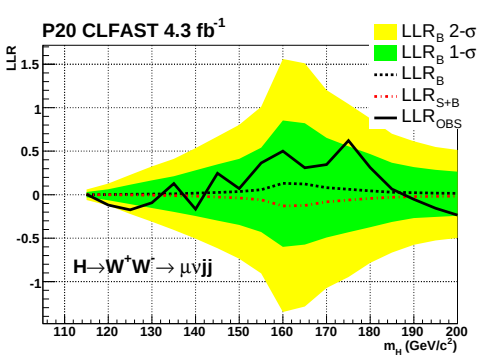

Figure 90: LLR comparisons when using the Poisson log-likelihood ratio test statistic ignoring systematics.

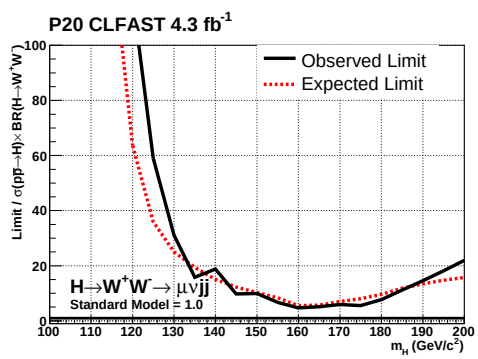

Figure 91: Ratio of the 95% C.L. limit to the SM expectation as a function of M_H for the $H \to WW \to \mu\nu jj$ channel. Limits are calculated using the Poisson log-likelihood ratio test statistic ignoring systematics.

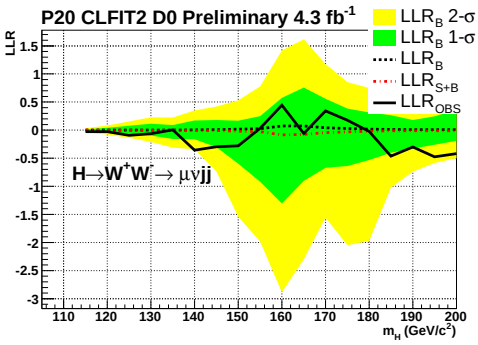

Figure 92: LLR comparisons when using the profile log-likelihood ratio test statistic including systematics.

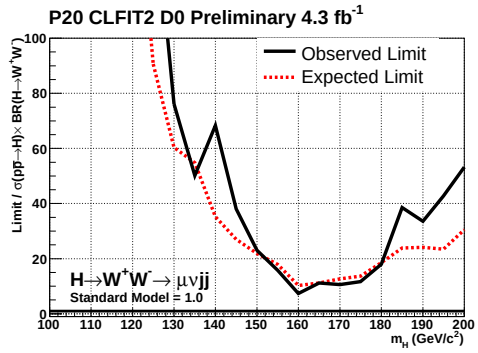

Figure 93: Ratio of the 95% C.L. limit to the SM expectation as a function of M_H for the $H \rightarrow WW \rightarrow \mu\nu jj$ channel. Limits are calculated using the profile log-likelihood ratio test statistic including systematics.

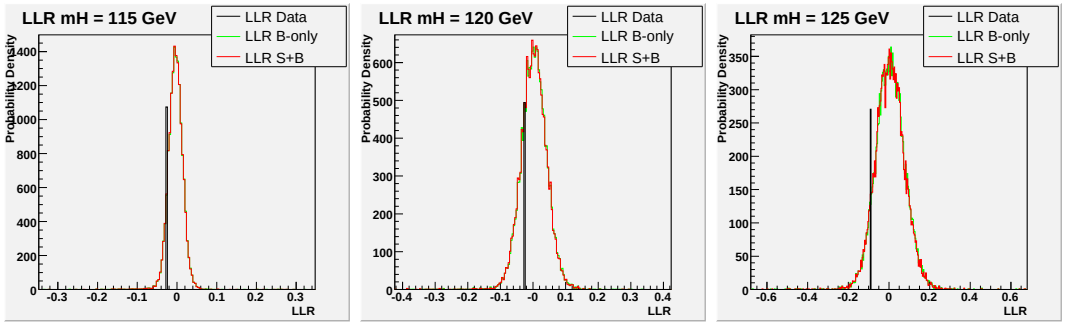

Figure 94: LLR distributions including systematics, $M_H = 115, 120, 125$ GeV

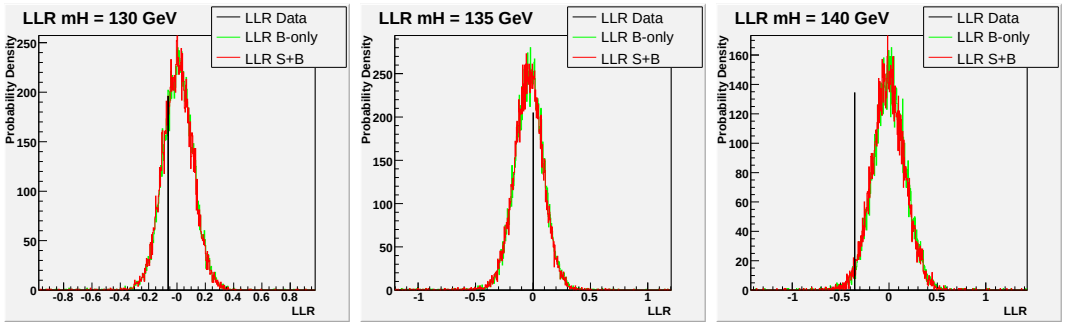

Figure 95: LLR distributions including systematics, $M_H = 130, 135, 140$ GeV

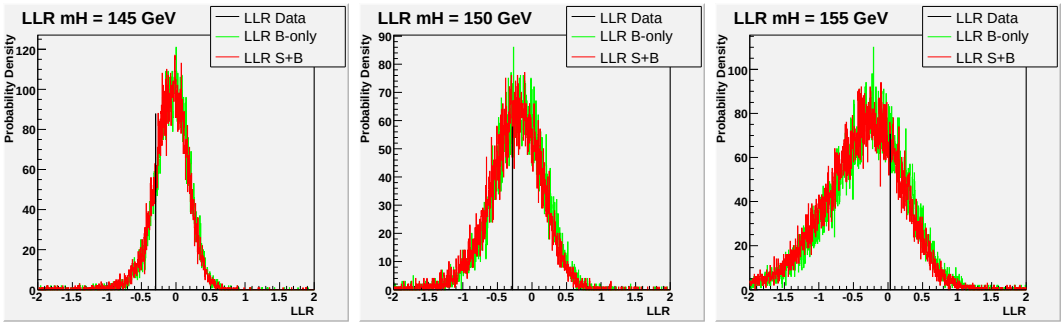

Figure 96: LLR distributions including systematics, $M_H = 145, 150, 155$ GeV

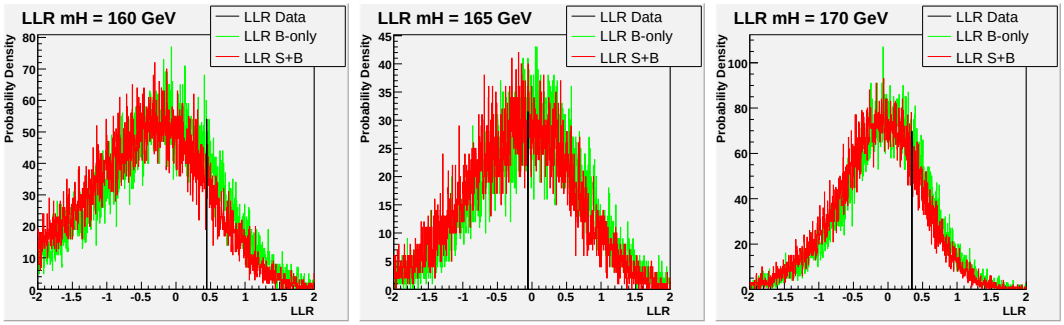

Figure 97: LLR distributions including systematics, $M_H = 160, 165, 170$ GeV

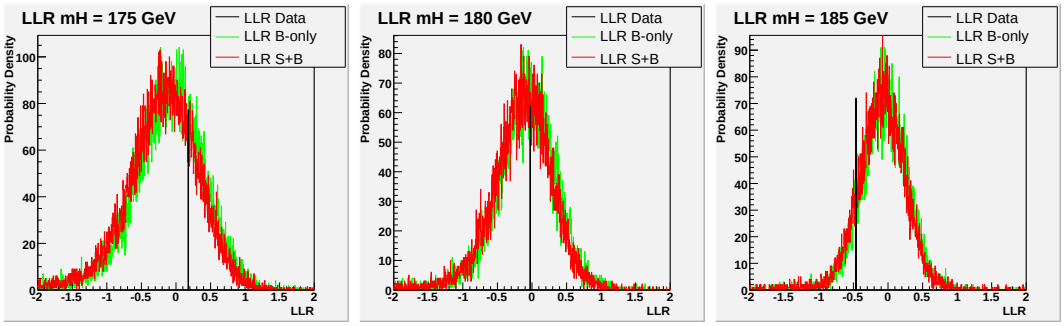

Figure 98: LLR distributions including systematics, $M_H = 175, 180, 185$ GeV

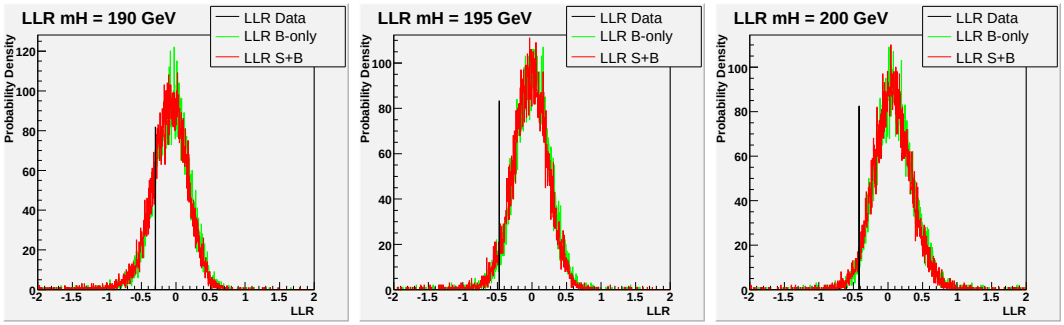

Figure 99: LLR distributions including systematics, $M_H = 190, 195, 200$ GeV

Limits for the HWWmunujj Channel						
ignoring systematics			including systematics			Ratio of
mH	Exp	Obs	mH	Exp	Obs	Exp limits
115	134	126	115	415	645	3.09
120	63.6	117	120	170	230	2.67
125	36.0	59.0	125	90.7	153.1	2.52
130	25.0	31.1	130	60.4	76.1	2.41
135	19.4	15.8	135	54.8	50.1	2.83
140	15.1	18.8	140	35.2	68.3	2.33
145	12.3	9.73	145	27.0	38.0	2.20
150	10.3	9.93	150	21.9	23.0	2.13
155	8.35	6.74	155	17.9	15.7	2.14
160	5.56	4.71	160	10.3	7.35	1.85
165	5.68	5.13	165	11.2	11.2	1.97
170	7.00	5.95	170	12.7	10.6	1.81
175	8.03	5.52	175	13.7	11.6	1.70
180	9.57	7.67	180	18.6	18.0	1.94
185	11.8	11.2	185	23.8	38.5	2.02
190	13.4	14.6	190	24.1	33.5	1.79
195	14.7	18.1	195	23.5	42.8	1.59
200	15.7	21.9	200	30.5	53.2	1.94

Table 19: Ratio of the 95% C.L. limit to the SM expectation as a function of M_H for $H \to WW \to \mu\nu jj$ using data collected from June 2006−June 2009. The ratio of expected limits with systematics to limits without systematics indicates the sensitivity loss due to systematic uncertainties.

10.3 Combined Limits for the Muon and Electron Semileptonic Decay Channels

The test statistics in (10.6) and (10.11) include the product of likelihoods of each bin in the $H \rightarrow WW \rightarrow \mu\nu jj$ final discriminant. Additional channels can be added to the final test statistic by multiplying likelihood ratios:

$$Q' = \prod_{j=1}^{\text{Nchannels}} \prod_{i=1}^{\text{Nbins}} Q_{ij} \tag{10.12}$$

which is equivalent to summing the log-likelihood ratios over the separate channels [121].

To achieve maximum sensitivity for the semileptonic final state, limits were calculated for the combined test statistics on both $H \rightarrow WW \rightarrow \mu\nu jj$ and $H \rightarrow WW \rightarrow e\nu jj$ channels. The combined results include correlations between channels in both rate and shape uncertainties in signal and background, leading to better constraints of systematics when using the profile log-likelihood test statistic. The increased data allow for more statistical precision when deciding the factor by which the signal must be increased to satisfy the test statistic to 95% C.L.

Four orthogonal sub-channels were combined: the $H \rightarrow WW \rightarrow \mu\nu jj$ analysis described in this dissertation using data collected between June 2006 and June 2009 (Run 2b), a version of the muon analysis using an earlier data set collected between August 2002 and February 2006 (Run 2a) and the corresponding Run 2a and Run 2b $H \rightarrow WW \rightarrow e\nu jj$ channels. The earlier and later data sets (Run 2a, Run2b) reflect changes to the detector and reconstruction software between the two data epochs. The differences from the event selection described in Chapter 4 are:

· Run 2a channels: The older data used a separate set of simulated signals and

backgrounds. Two jet preselections were relaxed for Run 2a.

- Older data were collected at lower instantaneous luminosities and had fewer minimum bias vertices, therefore jets with fewer than two tracks pointing back to the PV were used in analysis (no jet vertex confirmation).
- The gain in the inter cryostat region (ICR) has been steady decreasing over time leading to a miscalibration of the ICR energy scale [133]. Older MC more closely modeled the production of jets with low p_T in the inter cryostat region, therefore sub-leading jets with $p_T > 20$ were selected for analysis, independent of η^{jet}.

· Electron channels: The electron and muon channels are similar, but differences in fiducial effects and trigger modeling motivated corresponding differences in the preselections requirements.

- Electron reconstruction and identification is most efficient for the central calorimeter. The η range was restricted to $|\eta_{\text{elec}}| < 1.1$, as opposed to $|\eta_\mu| < 1.6$.
- The ELECTRON+JETS triggers in data were well modeled by the efficiency weights applied to MC. An electron event can pass any SINGLE ELECTRON or ELECTRON+JETS trigger for inclusion in analysis as opposed to the muon channel which uses the SINGLE MUON trigger suite exclusively. The advantage of including triggers with multiple objects is that the lepton p_T requirements can be relaxed at the trigger level. An event that fails a SINGLE LEPTON trigger may pass a LEPTON+JETS trigger leading to higher overall trigger efficiency.
- As in the muon channel, the electron channel vetos on events with a second

electron or any muon above a certain quality threshold.

The LLR and associated limit plot when including systematics using the profile log-likelihood ratio test statistic (10.11) for the combination of all $H \to WW \to \ell\nu jj$ channels are shown in Figs. 100−101. Table 20 lists the combined limits calculated with and without systematics. The smaller ratio of expected limits for the combined analyses in comparison to those in Table 19 is due to enhanced constraints on systematics from correlations in the uncertainties. The expected limit at $M_H = 165$ GeV is 5.5 at 95% C.L. and the observed limit is 3.8.

When dealing with small signals, large backgrounds, and large systematic uncertainties in the evaluation of limits, it is of central importance that an observation of signal in the data can be separated from a fluctuation of standard model backgrounds due to systematics. Figure 102 shows a plot of events per bin of RF output for data minus background (points), and signal (red line) multiplied by the expected limit for the $H \to WW \to \ell\nu jj$ analysis of $M_H = 165$ GeV. Outputs have been rebinned in COLLIE to reduce the sizes of statistical errors in signal and background output bins. The data have fluctuated below the background prediction in several bins, resulting in an observed limit lower than the expected limit. Also shown are the systematic uncertainty bands pre-fit (in turquoise) and post-fit (in blue). Here, the systematic uncertainties have been highly constrained in the fitting to the data, and the size of signal, when scaled to the expected limit, is outside the post-fit systematic uncertainty for high signal statistics RF output values.

Limits for the combined HWWlnujj Channels						
ignoring systematics			including systematics			Ratio of
mH	Exp	Obs	mH	Exp	Obs	Exp limits
115	99.9	54.4	115	223	244	2.23
120	43.3	46.4	120	94.0	138	2.17
125	27.4	24.8	125	58.9	90.0	2.15
130	18.2	11.9	130	35.5	39.7	1.96
135	13.5	6.41	135	26.4	24.9	1.96
140	10.2	6.77	140	19.9	36.7	1.94
145	8.16	3.62	145	15.9	13.9	1.95
150	6.72	3.52	150	11.7	12.3	1.73
155	5.31	1.88	155	8.57	5.87	1.61
160	3.65	2.03	160	5.23	4.12	1.43
165	3.55	1.06	165	5.47	3.79	1.54
170	4.25	1.29	170	6.25	4.00	1.47
175	4.77	0.61	175	7.47	5.52	1.57
180	5.49	2.95	180	8.84	14.9	1.61
185	6.72	4.03	185	10.3	16.8	1.53
190	7.57	6.63	190	11.5	22.4	1.52
195	8.11	6.42	195	11.3	19.2	1.39
200	8.64	7.48	200	12.1	16.1	1.40

Table 20: Ratio of the 95% C.L. limit to the SM expectation as a function of M_H for $H \to WW \to \ell\nu jj$ for combined Run 2a and Run 2b electron and muon data. The ratio of expected limits ignoring systematics to limits including systematics indicate the sensitivity loss due to systematic uncertainties. These are smaller for the combined analysis than for the individual $H \to WW \to \mu\nu jj$ channel.

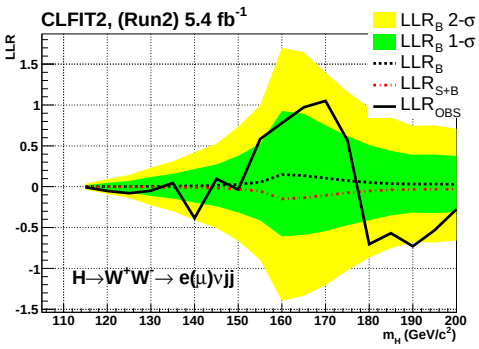

Figure 100: LLR comparisons when using the profile log-likelihood ratio test statistic including systematics in the combined $H \rightarrow WW \rightarrow \ell\nu jj$ channels.

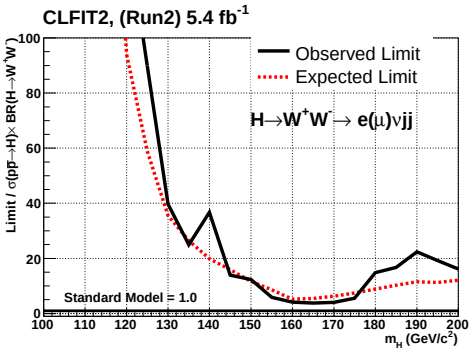

Figure 101: Ratio of the 95% C.L. limit to the SM expectation as a function of M_H for the combined $H \rightarrow WW \rightarrow \ell\nu jj$ channels. Limits are calculated using the profile log-likelihood ratio test statistic including systematics.

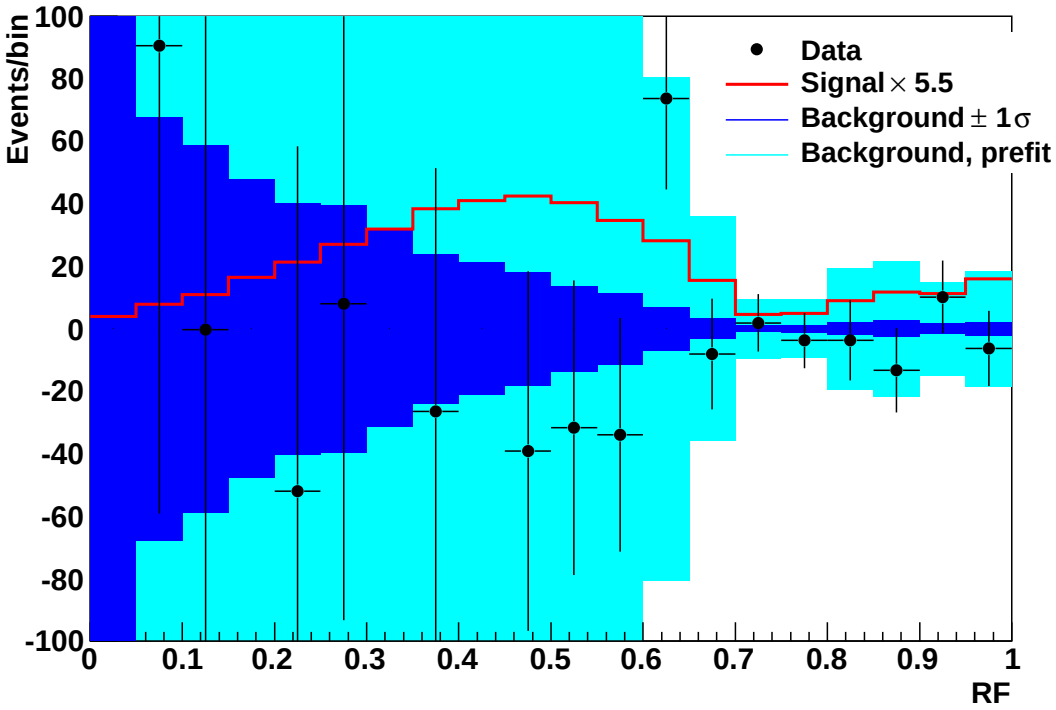

Figure 102: Number of events per bin in the RF output for data minus background (points) and signal (red line) scaled by the expected limit value for the $H \rightarrow WW \rightarrow \ell\nu jj$ $M_H = 165$ GeV analysis. Also shown are the per bin systematic uncertainties pre-fit (turquoise) and post-fit (blue). The scaled signal is outside of the post-fit systematic band in the high signal statistics RF output region. The output has been rebinned in COLLIE to reduce statistical errors in the signal and background samples.

11 Current Status and Future Outlook for SM Higgs Boson Searches at the Tevatron

In July 2010 the Tevatron experiments reported combined limits on the production of a standard model Higgs boson based on a variety of analysis channels with an average integrated luminosity of 5.9 fb^{-1} [8]. Figure 103 shows the July 2010 combined limits at 95% C.L. for $M_H = 100 - 200$ GeV. The Tevatron exclusion ranges where the observed limit (in black) dips below the SM Higgs boson production rate are marked by pale green vertical bands, the previous LEP exclusion is marked by a vertical purple band. Figure 103 also shows the combined expected limit as a dashed black line, along with the corresponding $\pm 1\sigma$ band in green, and $\pm 2\sigma$ band in yellow [8]. The addition of the semileptonic channels contributed to 6% higher total sensitivity at $M_H = 165$ GeV.

As of mid-July, the DØ detector has recorded more than 8 fb^{-1} to tape (Fig. 104) with CDF recording just under 8 fb^{-1} [134]. Because sensitivity scales with $\sqrt{\mathcal{L}}$, a large increase in sensitivity of the combined searches at the Tevatron could be gained without any contributing analysis improvement other than using the full dataset.

While we have achieved experimental sensitivities to set exclusions regions of $M_H = 100 - 109$ GeV and $M_H = 158 - 175$ GeV, the current (and future) goal of the Tevatron Higgs program is to find first evidence of standard model Higgs boson production. Figure 105 shows an estimate of the probability of observing 3σ evidence for combined standard model Higgs boson production at the Tevatron using up to 35 fb^{-1} of data based on the analyses used for the 2010 combined limits. The blue line is the estimated luminosity required for 3σ evidence accounting for the degradation of the tracking and silicon detectors due to radiation from the integrated luminosity exposure. The 3σ evidence estimation excluding detector aging is given by the bright

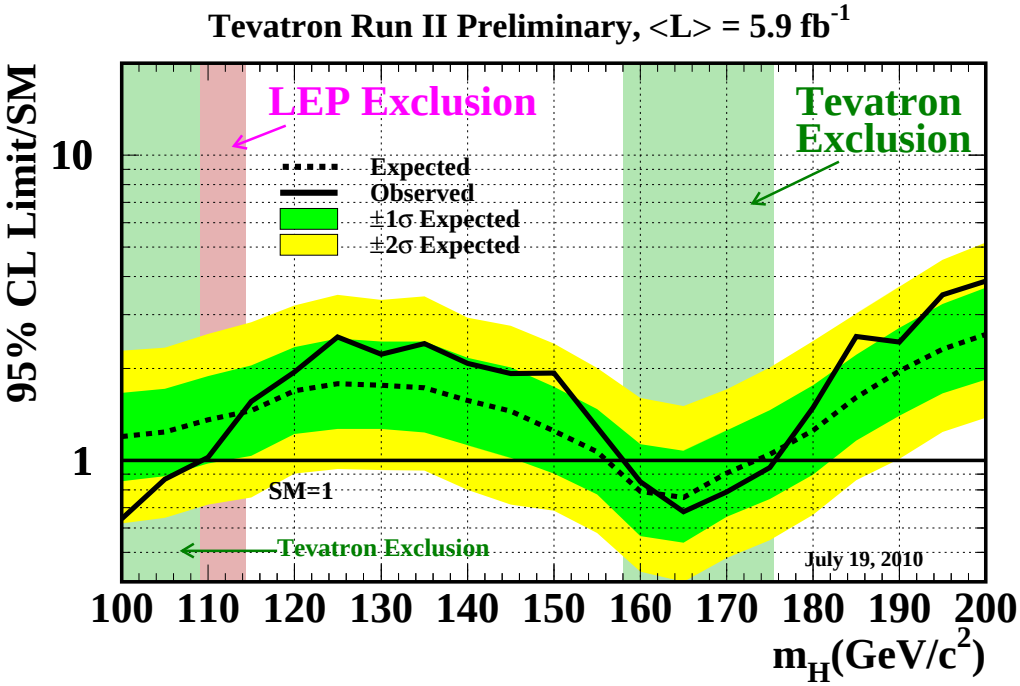

Figure 103: Observed and expected upper limits on standard model predictions of Higgs boson production from combined CDF and DØ direct searches. Limits are at 95% C.L. and are expressed as multiples of the standard model Higgs boson production prediction as a function of mass. The bands are the 1σ and 2σ fluctuations from the median of the background-only hypothesis. [8].

red line. Just as CL_S exclusions are defined in terms of the fractions of pseudo-experiments that are more background-like than the data, evidence and subsequent discovery are defined in terms of the fractions of _only experiments more signal-like than the data. For 3σ evidence, the fraction of *b-only* trials more signal-like than data is [135]:

$$1 - CL_B \leq 1.3 \times 10^{-3} \tag{11.1}$$

Estimates are also given for 95% C.L. exclusion with detector aging (green line), and without detector aging (dark red line). The two bands represent projected gains in sensitivity from analysis-specific improvements. These probabilities are based on expected sensitivities, and do not include current Tevatron exclusions.

An existing analysis can gain sensitivity through increasing the amount of data passing preselection, improving background modeling, and advancing methods in signal and background separation. In addition to using the full data set available, analyses can optimize preselection by expanding the list of well modeled triggers required to fire, loosening lepton ID and reducing p_T requirements on physics objects. To improve sensitivity in high-mass and low-mass channels with jets in the final state, an analysis can be split into sub-channels of exclusive bins of jet multiplicity to reduce associated systematics from multijet modeling. The addition of NLO corrections to better model exclusive jet final states in V+jets events may also offer substantial improvements in understanding background contributions.

Improvements to the resolution of dijet mass reconstructed from heavy flavor jets has been a major area of research for the low mass channels based on matrix elements of the $H \to bb$ decay. Matrix element level kinematics of the Higgs boson decay may be more fully exploited across analysis channels as analyses mature. When work on the $H \to WW \to \mu\nu jj$ analysis first began in 2007 it was common for neural networks to be used as multivariate classifiers for high-mass Higgs boson searches. Techniques such as the random forest method of signal/background discrimination described in this dissertation, and matrix element inputs to multivariate classifiers have become more prevalent in recent years in direct searches.

As the Tevatron experiments move forward, an important consideration will be the reduction of correlated uncertainties across analyses. Recall there was a factor of two decrease in sensitivity for the expected limit for the $H \to WW \to \mu\nu jj$ analysis

at $M_H = 165$ GeV with the inclusion of systematics. As the luminosity profile of Run 2b changes, the DØ physics object ID and algorithm groups will continue to update efficiency measurements and trigger parametrizations to allow for smooth addition of data. The DØ Monte Carlo generation farms can also regenerate newer Monte Carlo samples with updated zero bias overlay, using updated ALPGEN and PYTHIA settings such as the higher MLM p_T matching threshold (Sec. 6.4) that been found in recent studies to better model the data .

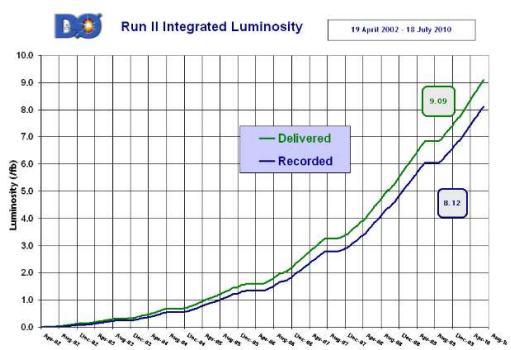

Figure 104: Integrated luminosity delivered (in green) recorded (in blue) for the DØ experiment for all of Run 2b through July 2010 [136].

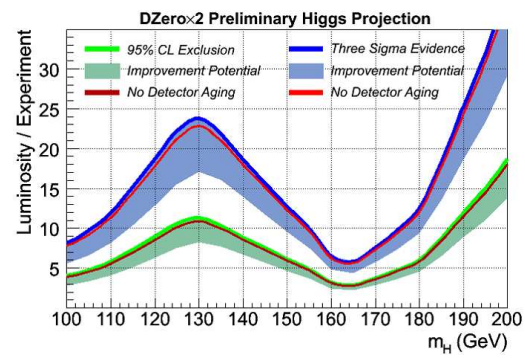

Figure 105: Preliminary Higgs boson sensitivity projections as a function of integrated luminosity for the Tevatron based on the analyses used in the July 2010 Tevatron exclusion limits [137].

The Large Hadron Collider (LHC) as of July 2010 has collected 400 nb^{-1} of integrated luminosity at $\sqrt{s} = 7$ TeV [138]. The current LHC run plan is to collect 1 fb^{-1} before a shutdown in December 2011 to make accelerator upgrades necessary to increase to the center of mass energy $\sqrt{s} = 14$ TeV.

At the 35th International Conference on High Energy Physics held in July 2010, both LHC multipurpose detector experiments (CMS [139], ATLAS [140]) presented Monte Carlo based predictions for standard model Higgs boson exclusions after 1 fb^{-1} of data at $\sqrt{s} = 7$ TeV. The CMS experiment predicts exclusion sensitivity in the $M_H = 145 - 190$ GeV range (Fig. 106) at 95% C.L. with 1 fb^{-1} of data, while ATLAS

predicts exclusion sensitivity at 95% C.L from 135 − 188 GeV (Fig. 107).

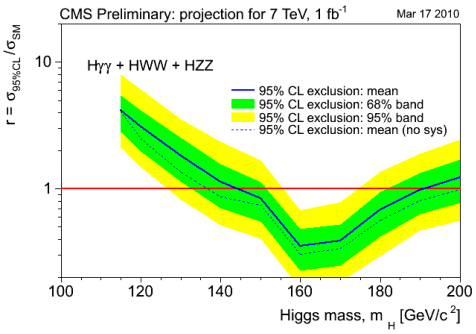

Figure 106: Predictions for standard model Higgs boson sensitivities at the CMS experiment with 1 fb^{-1}of data at $\sqrt{s}$= 7 TeV [141].

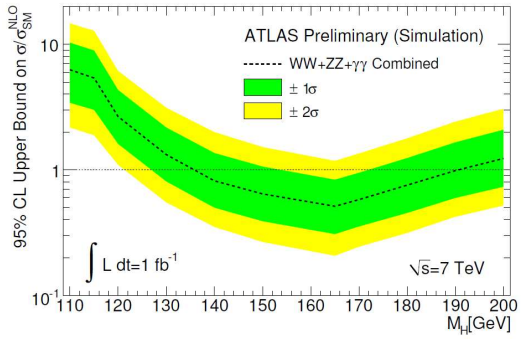

Figure 107: Predictions for standard model Higgs boson sensitivities at the ATLAS experiment with 1 fb^{-1}of data at $\sqrt{s}$= 7 TeV [142].

At current luminosities, the CDF and DØ experiments will have recorded more than 10 fb^{-1} when the Tevatron is scheduled to shut-down at the end of September 2011, just as the LHC finishes recording its first fb^{-1}. The LHC's 1 fb^{-1} exclusions are expected in the mass range of maximum sensitivity for the Tevatron combined searches and thus may serve as confirmation of the results from CDF and DØ.

The indirect constraints currently prefer a low mass SM Higgs boson (Fig. 5). The Tevatron has reached SM sensitivity and excluded to 95% C.L. the low mass region $M_H = 100 - 109$ GeV due to the sensitivity of the associated production channel analyses (WH, ZH). At the LHC the associated production channels are suppressed due to the pp initial states. The main contributions to the LHC low mass Higgs program will be from the $H \to \gamma\gamma$ channel, which has a small branching ratio (Fig. 7) and will require multiple fb^{-1} of data to reach SM sensitivity.

Sensitivity to production of a standard model Higgs boson at the Tevatron remains relevant in the era of the LHC through the addition of new search channels such as $H \to WW \to \mu\nu jj$, and the constant refinement of existing analyses. If the Higgs

boson exists the LHC will make the 5σ discovery, but if its mass is less than 200 GeV the Tevatron will show the world exactly where to look, and may rule out a SM Higgs boson altogether.

12 Conclusions

This dissertation documents the first search for a standard model Higgs boson in the decay channel $H \rightarrow WW \rightarrow \mu\nu jj$ using 4.3 fb^{-1} of data collected by the DØ experiment from June 2006 - June 2009 at $\sqrt{s} = 1.96$ TeV. Simulated $H \rightarrow WW \rightarrow \mu\nu jj$ signal events are produced in 5 GeV steps for $M_H = 115 - 200$ GeV and normalized to their NNLO cross sections. Events selected for analysis contain a single well isolated muon, $\not{E}_{\mathrm{T}}$, and two or more jets.

The main background process for this channel is W+jets where $W \rightarrow \mu\bar{\nu}$. All background processes from production of vector bosons and top quarks are simulated with Monte Carlo generators and normalized to their standard model cross sections. The multijet background is modeled from data passing all preselection requirements except muon isolation. Corrections due to reconstruction differences in data and Monte Carlo are applied to all simulated samples. Because of uncertainties in V+jets cross sections, V+jets background normalizations are increased by a scaling factor such that data and background passing preselection have the same integrated event count. Additional corrections are applied to V+jets backgrounds due to physics modeling inaccuracies in the ALPGEN+PYTHIA simulated events.

Using 33 variables selected for discriminating power between signal with $M_H = 145, 165, 185$ GeV and combined background, a random forest of decision trees is trained to separate signal-like events from background-like events for $M_H = 115 - 200$ GeV. The output of testing the data, combined backgrounds, and signal for each random forest is the final discriminant used for evaluation of limits.

No significant excess of signal is observed in data, and a semi-Frequentist CL_S method of limit calculation using a Poisson log-likelihood test statistic with profiled systematics is used to set upper limits on standard model Higgs boson production to

95% C.L. For $M_H = 165$ GeV the observed upper limit at 95% C.L. is:

$$(\sigma(gg \to H) \times BR(H \to WW \to \mu\bar{\nu}jj))/\sigma_{SM} < 11.2 \quad (11.2 \text{ exp}) \quad 4.3 \text{ fb}^{-1}$$

$$(\sigma(gg \to H) \times BR(H \to WW \to \ell\bar{\nu}jj))/\sigma_{SM} < 5.5 \quad (3.8 \text{ exp}) \quad 5.4 \text{ fb}^{-1}$$

When semileptonic channels are combined with the other DØ and CDF direct Higgs searches the standard model Higgs boson is excluded in the range $158 < M_H < 175$ GeV at 95% C.L.

Recent theoretical calculations [143] of the fully differential width for the $H \to WW \to \ell\nu jj$ decay in terms of measurable kinematic variables has highlighted the importance of the semileptonic final state as a future probe of the standard model Higgs both at the Tevatron and at the LHC. The work presented in this dissertation has established the analysis strategy for $H \to WW \to \mu\nu jj$ at the DØ experiment and will be used as the foundation for future semileptonic searches.

In the forty years since the Higgs mechanism was introduced, the standard model has performed remarkably well in describing the production and decays of the elementary particles. From the prediction of the of the W and Z bosons in the 1960's to the discovery of the top quark in the 1990's, every fermion and boson predicted by the standard model has been observed in experiment, except for one.

We are now on the threshold of discovering the final piece of the standard model, the Higgs boson. The observation and subsequent study of a SM Higgs boson would allow us to probe the mechanism of electroweak symmetry breaking and the origin of mass at the electroweak scale. If the SM Higgs does not exist, then something must take its place. If the Higgs is excluded in the predicted mass range, or if something Higgs-like is discovered but does not have the properties and couplings that match the standard model predictions, that will be definitive evidence for fundamentally new

physics at the electroweak scale. The experimental results of the next three years will give us an unprecedented insight into the mechanism of mass, or show that the answer lies beyond the standard model.

A Random Forest Input Distributions

Comparison plots for data vs. background for $H \rightarrow WW \rightarrow \mu\nu jj$ RF input distributions. Preselection events used for testing the RF are excluded from these plots. The overlayed signal ($M_H = 165$ GeV) has its event count scaled by a factor of 300 for shape comparison. The χ^2 probability at the top of each plot is the usual p-value obtained by integrating the residual χ^2 distribution above that observed in the data.

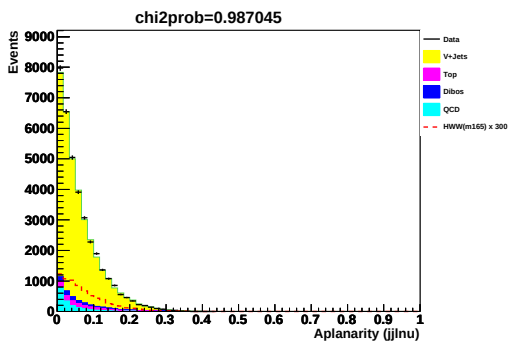

Figure 108: RF input: Aplanarity: measure of p_T component out of the event plane defined by leading jets (j1,j2), μ, and $\not{E}_{\mathrm{T}}$.

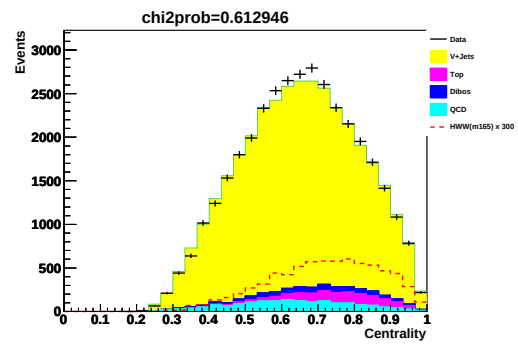

Figure 109: RF input: Centrality : $(\sum p_T)/(\sum \mathrm{E})$ for μ and all jets.

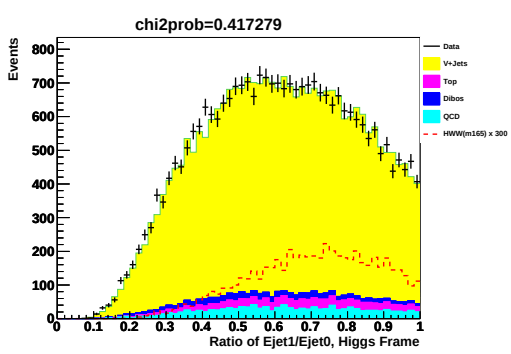

Figure 110: RF input: $E^{\mathrm{j2}}/E^{\mathrm{j1}}$ in H center-of-mass frame.

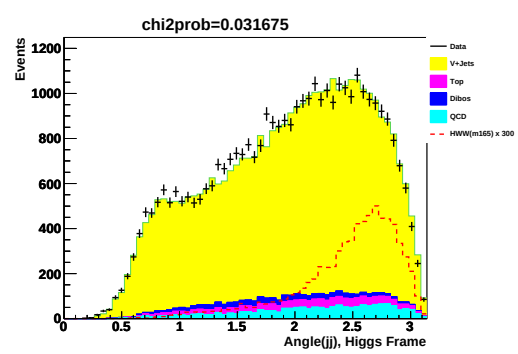

Figure 111: RF input: 3D angle between leading jets (j1,j2) in the H center-of-mass frame.

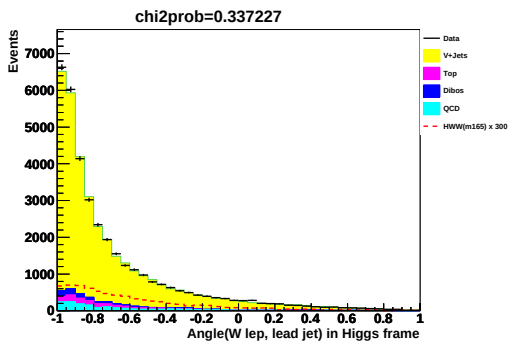

Figure 112: RF input: 3D Angle(Wlep, leading jet) in the H center-of-mass frame.

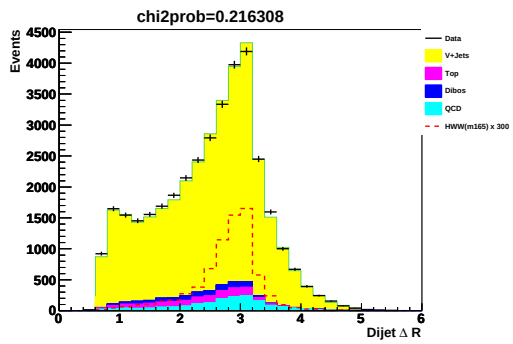

Figure 113: RF input: ΔR(j1,j2).

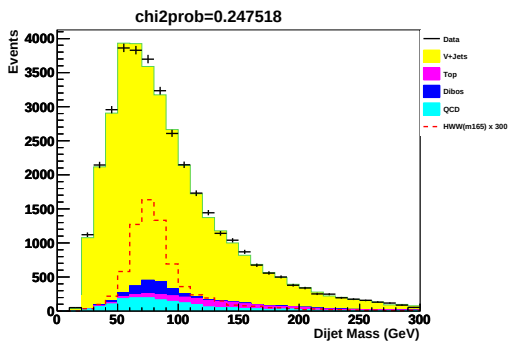

Figure 114: RF input: .

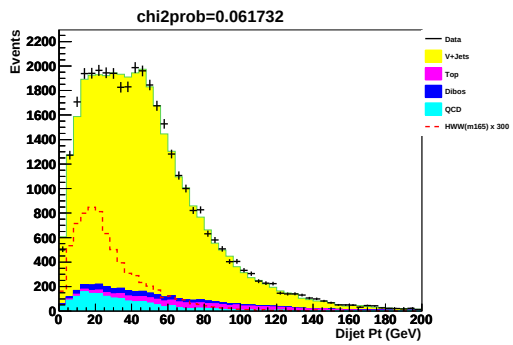

Figure 115: RF input: .

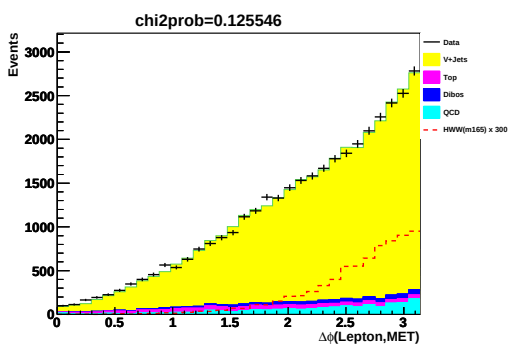

Figure 116: RF input: $\Delta\phi(\mu, \not{E}_{\mathrm{T}})$.

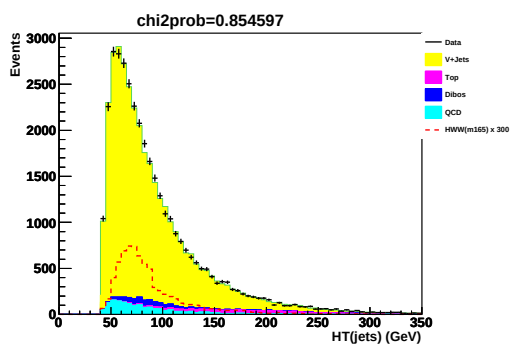

Figure 117: RF input: Scalar sum of p_T for all jets.

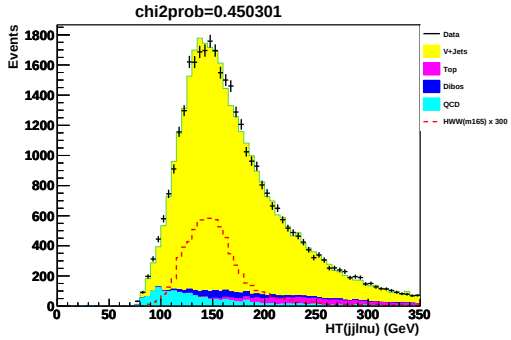

Figure 118: RF input: Scalar sum of p_T for μ, $\not{E}_{\mathrm{T}}$, and j1 and j2.

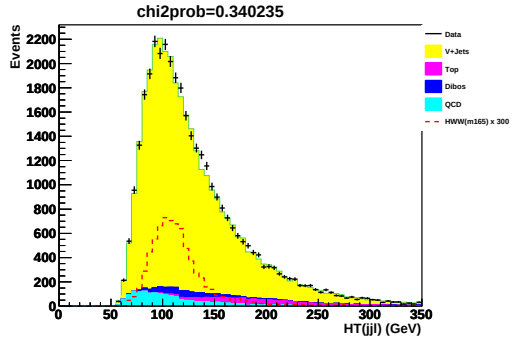

Figure 119: RF input: Scalar sum of p_T for μ, j1, and j2.

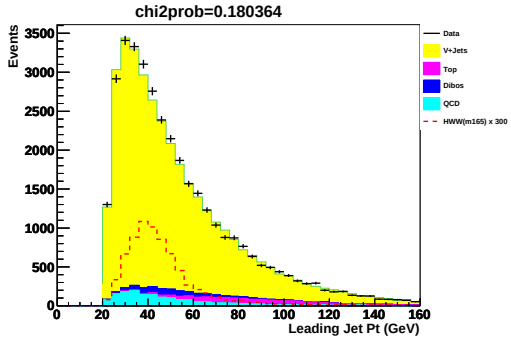

Figure 120: RF input: p_T of j1.

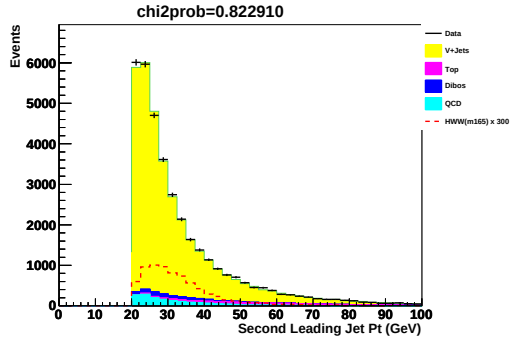

Figure 121: RF input: p_T of j2.

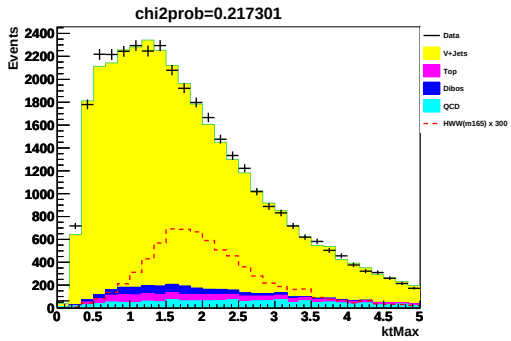

Figure 122: RF input: $\mathrm{KT_{max}}$: $\Delta R(\mathrm{j1,j2}) * E_T^{\mathrm{j1}}/(E_T^{\mu} + \not{E}_{\mathrm{T}})$.

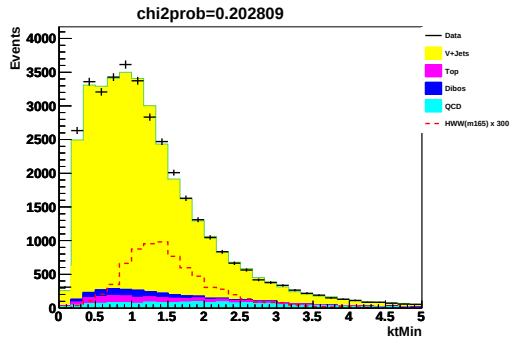

Figure 123: RF input: $\mathrm{KT_{min}}$: $\Delta R(\mathrm{j1,j2}) * E_T^{\mathrm{j2}}/(E_T^{\mu} + \not{E}_{\mathrm{T}})$.

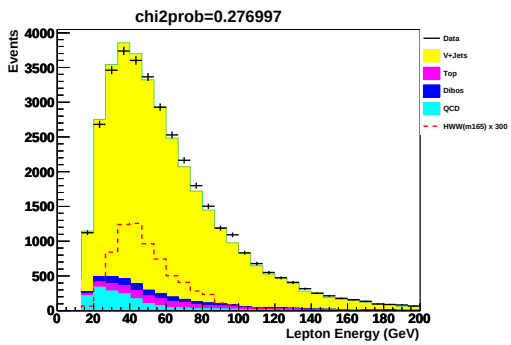

Figure 124: RF input: E^{μ}.

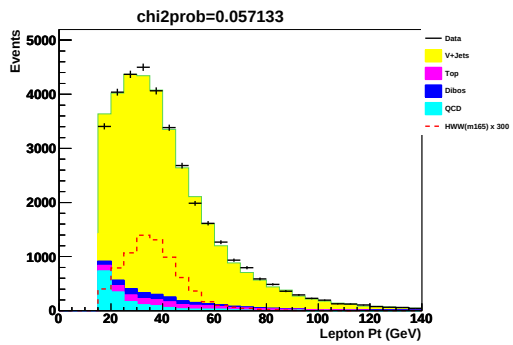

Figure 125: RF input: p_T^{μ}.

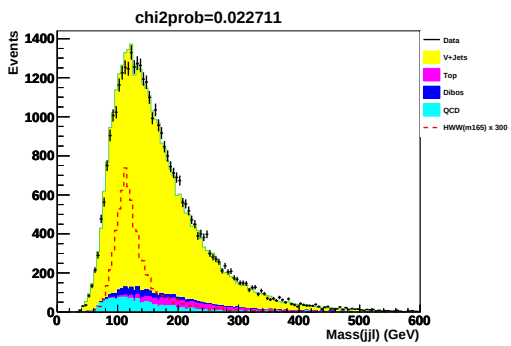

Figure 126: RF input: Invariant Mass of μ, j1 and j2.

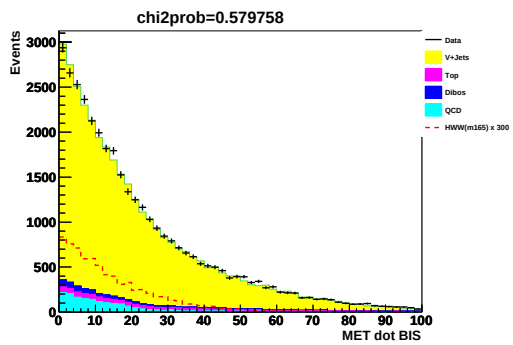

Figure 127: RF input: METbis : dot product of $\not{E}_{\mathrm{T}}$ and angular bisector of j1, j2.

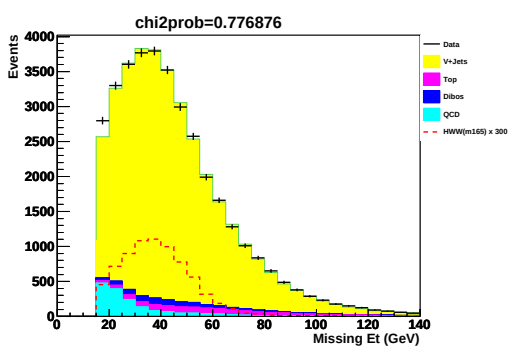

Figure 128: RF input: $\not{E}_{\mathrm{T}}$.

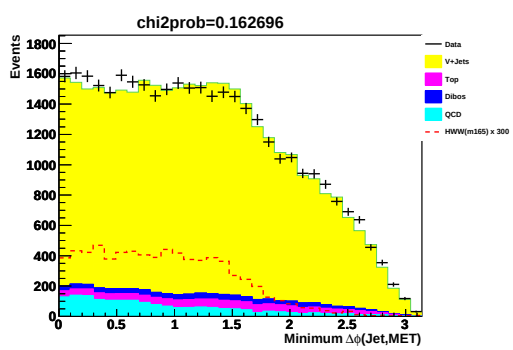

Figure 129: RF input: Minimum of $\Delta\phi(\not{E}_{\mathrm{T}},\mathrm{j1})$ or $\Delta\phi(\not{E}_{\mathrm{T}},\mathrm{j2})$.

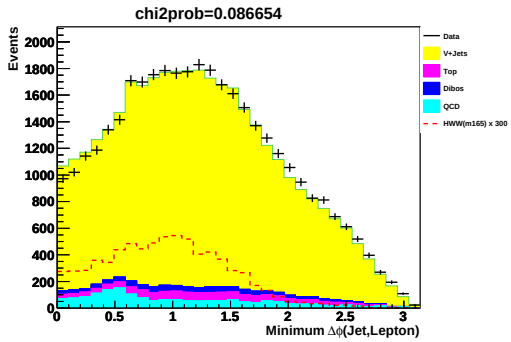

Figure 130: RF input: Minimum of $\Delta\phi(\mu$,j1) or $\Delta\phi(\mu$,j2).

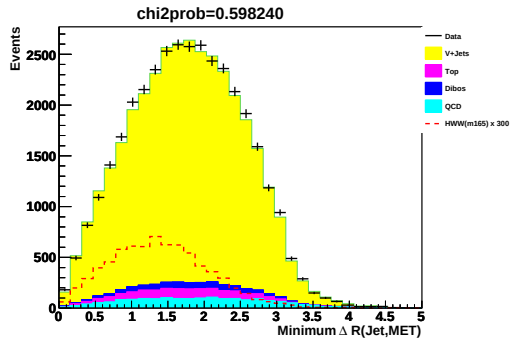

Figure 131: RF input: Minimum of ΔR($\not{E}_{\rm T}$,j1) or Δ R($\not{E}_{\rm T}$,j2).

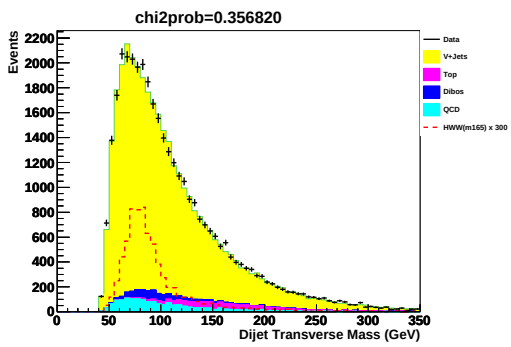

Figure 132: RF input: $m_T^{(\rm j1,j2)}$.

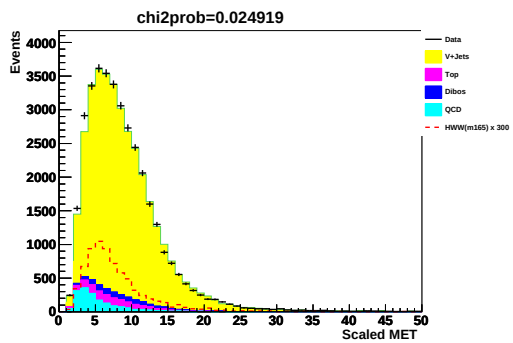

Figure 133: RF input: Scaled $\not{E}_{\rm T}$: $\sum_{n=0}^{numJets} (\sqrt{E^{\rm jet}} \times \sin\theta^{\rm jet} \times \cos\Delta\phi[{\rm jet}, MET]\ )^2$.

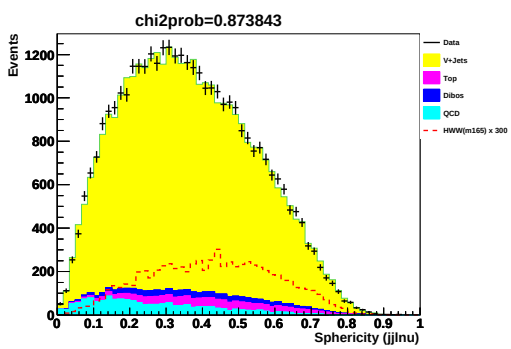

Figure 134: RF input: Sphericity: measure of the summed p_T^2 with respect to the event axis calculated from μ, $\not{E}_{\rm T}$, j1 and j2.

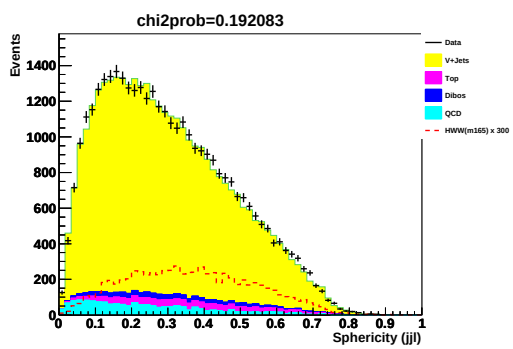

Figure 135: RF input: Sphericity: measure of the summed p_T^2 with respect to the event axis calculated from muon, j1, and j2.

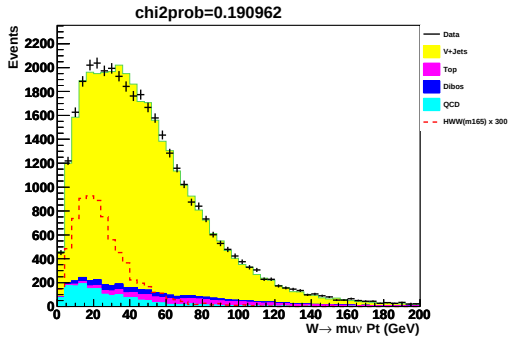

Figure 136: RF input: p_T^W.

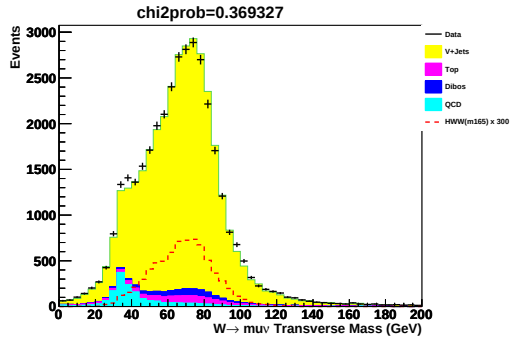

Figure 137: RF input: m_T^W.

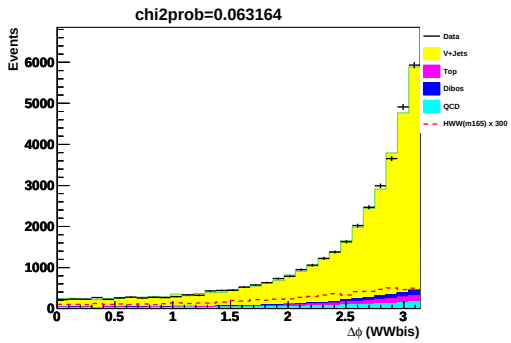

Figure 138: RF input: .

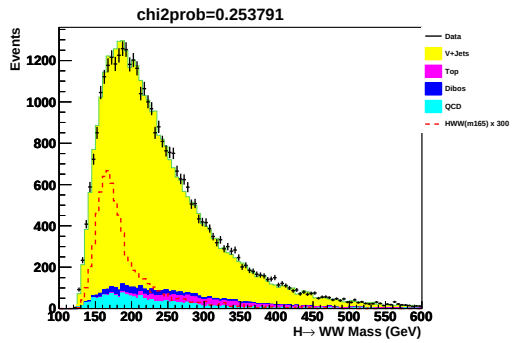

Figure 139: RF input: Invariant mass of the WW pair, (M_H).

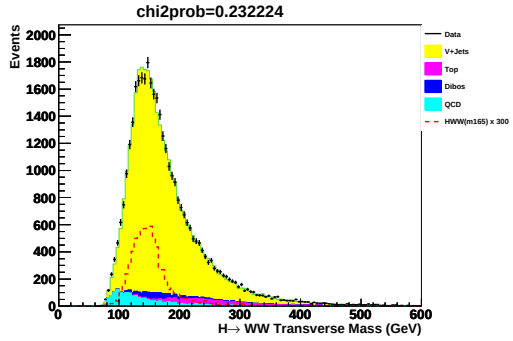

Figure 140: RF input: Transverse mass of the WW pair (m_T^H).

B RF Output Distributions

RF output for signal vs. individual background sources, $M_H = 115 - 200$ GeV in linear (left) and log scale (center). The signal is scaled (x200) for visibility in the left hand plot. Also shown are the residual differences between data and MC (top right) and the signal significance (signal/$\sqrt{(\text{signal} + \text{background})}$ (bottom right) for each RF output bin.

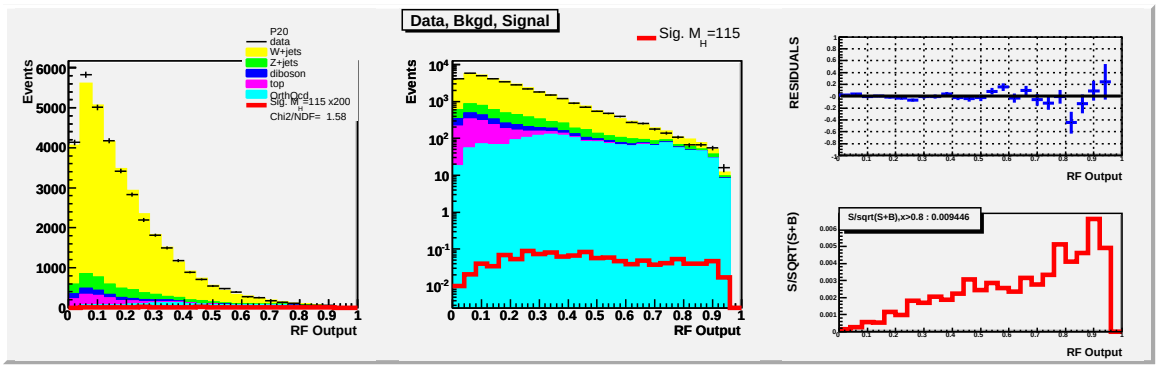

Figure 141: RF output distribution: $M_H = 115$ GeV

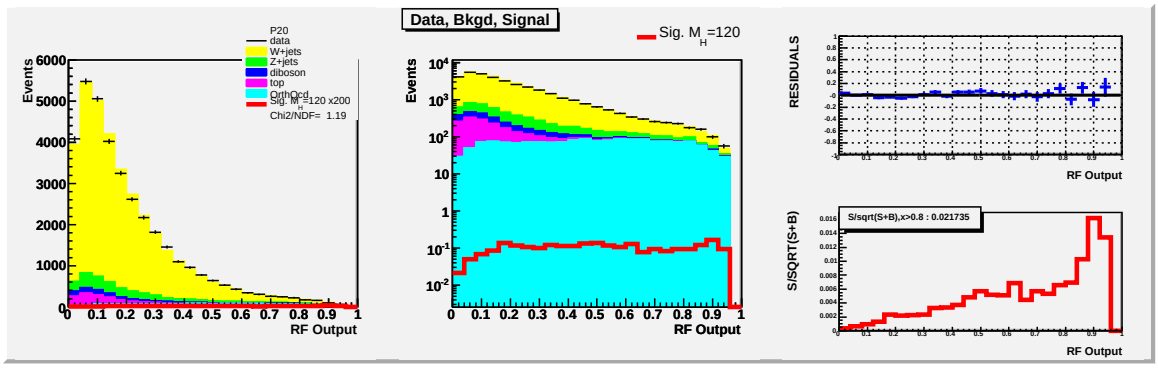

Figure 142: RF output distribution: $M_H = 120$ GeV

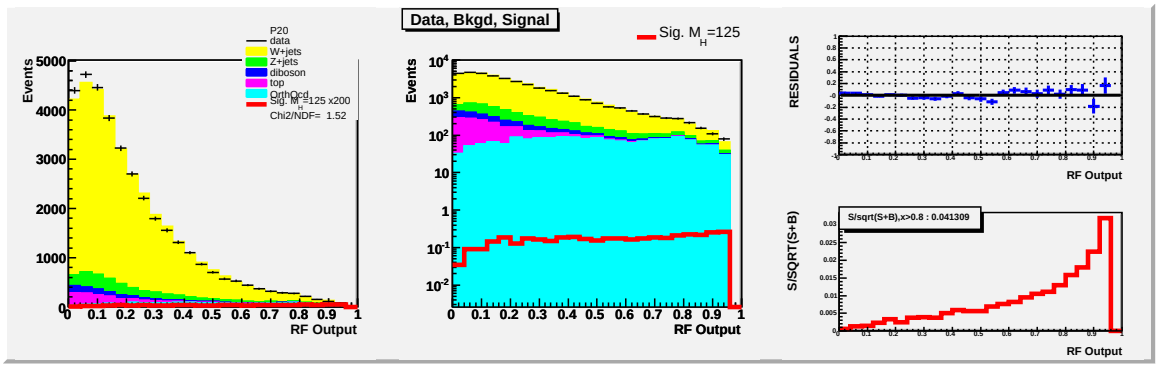

Figure 143: RF output distribution: $M_H = 125$ GeV

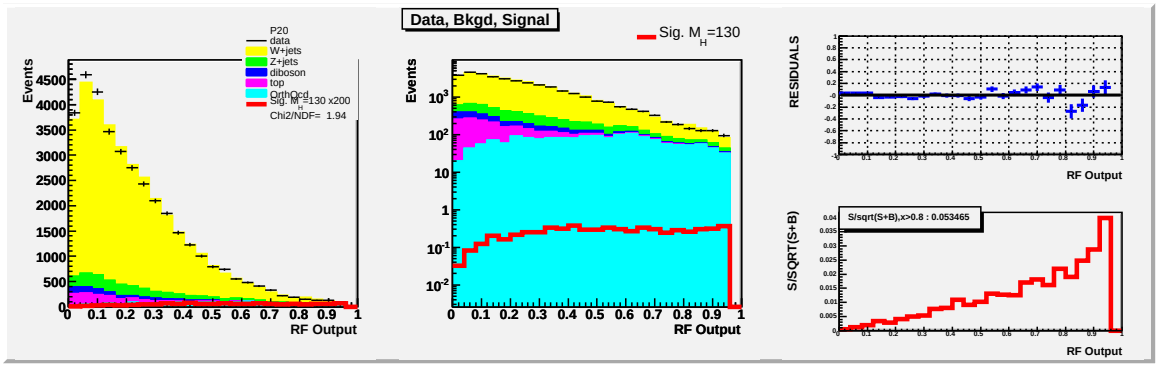

Figure 144: RF output distribution: $M_H = 130$ GeV

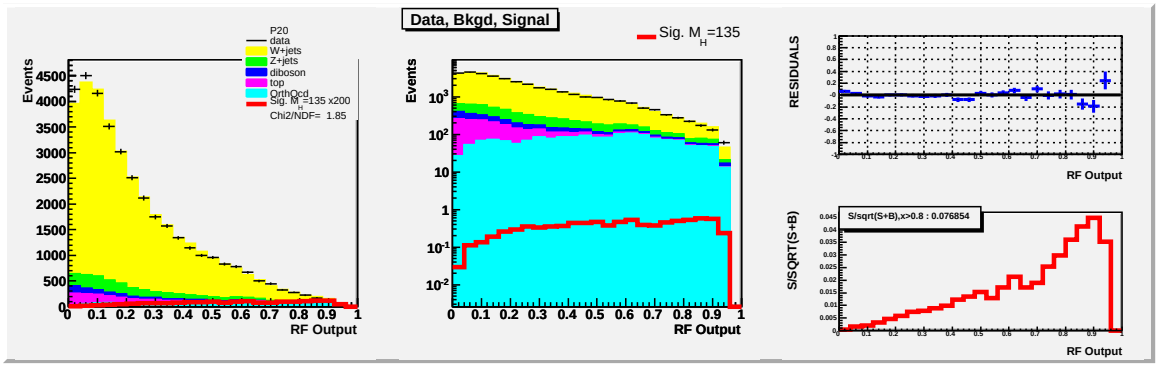

Figure 145: RF output distribution: $M_H = 135$ GeV

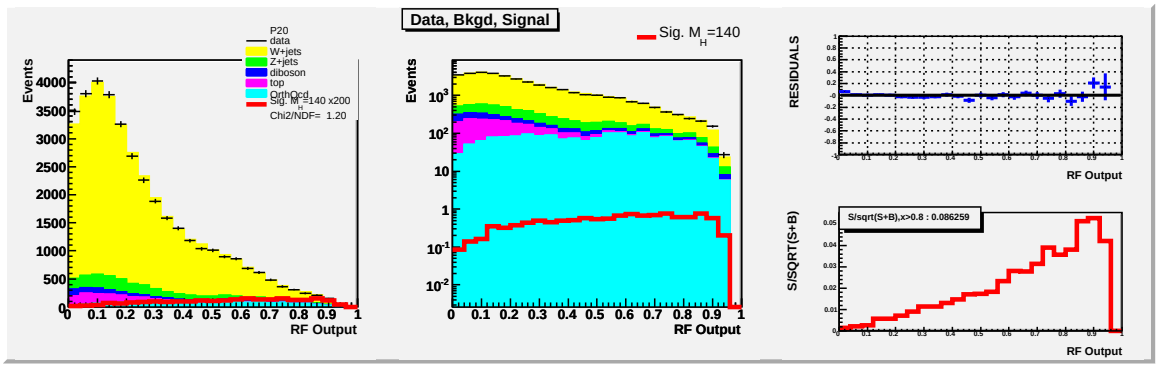

Figure 146: RF output distribution: $M_H = 140$ GeV

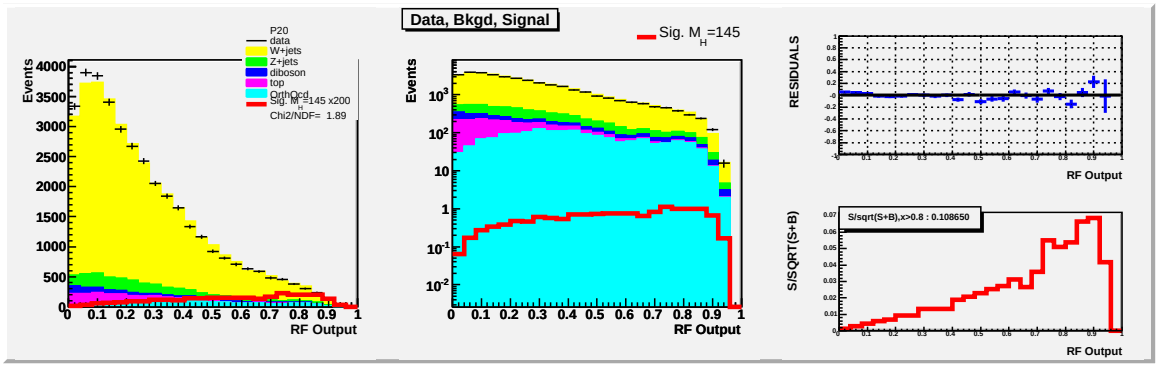

Figure 147: RF output distribution: $M_H = 145$ GeV

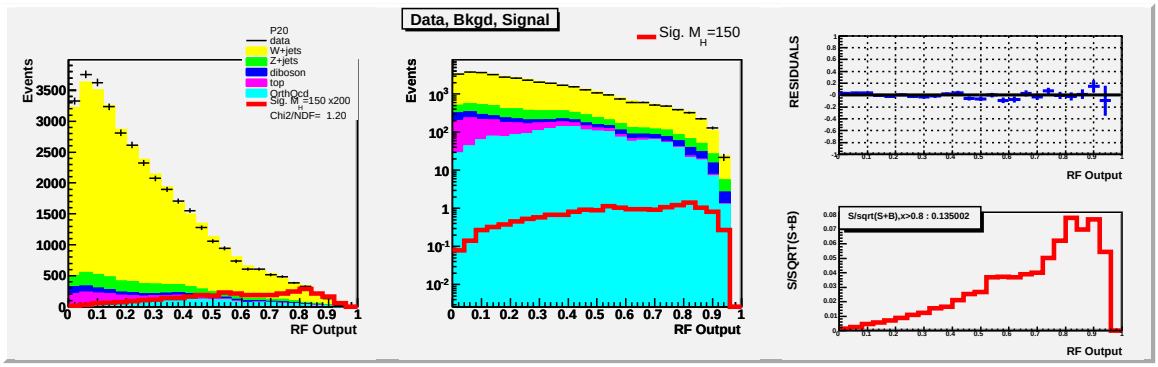

Figure 148: RF output distribution: $M_H = 150$ GeV

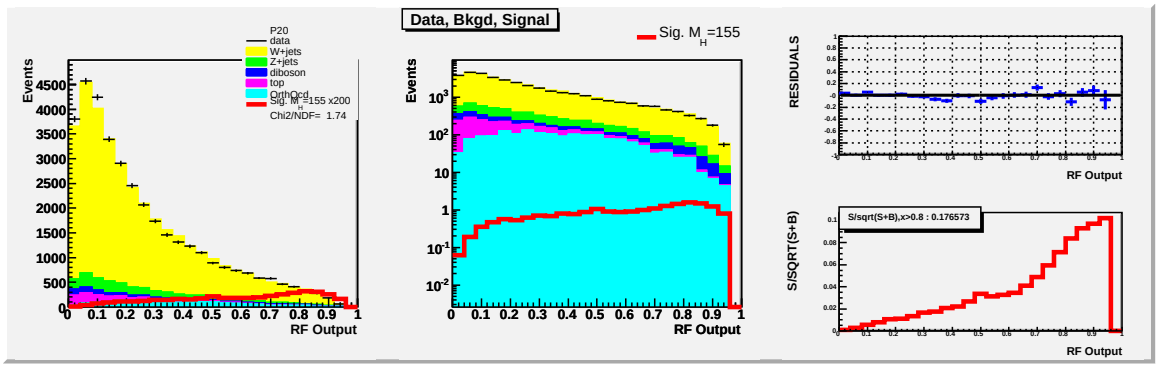

Figure 149: RF output distribution: $M_H = 155$ GeV

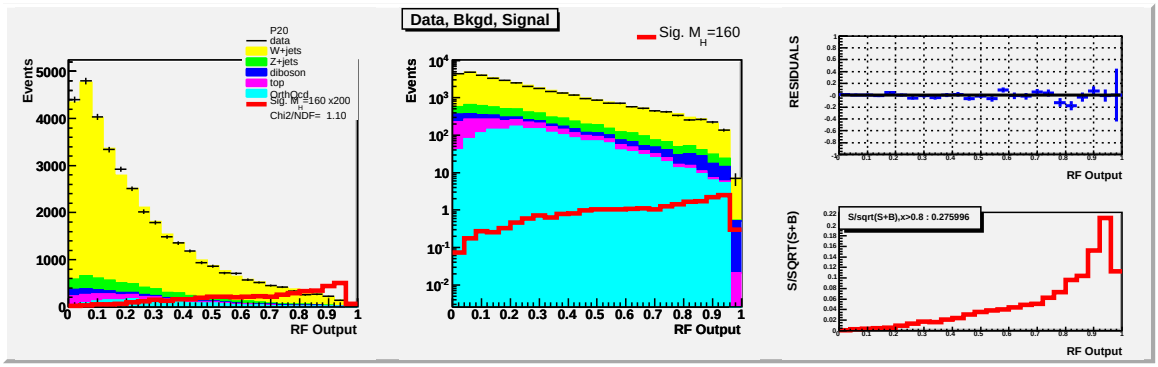

Figure 150: RF output distribution: $M_H = 160$ GeV

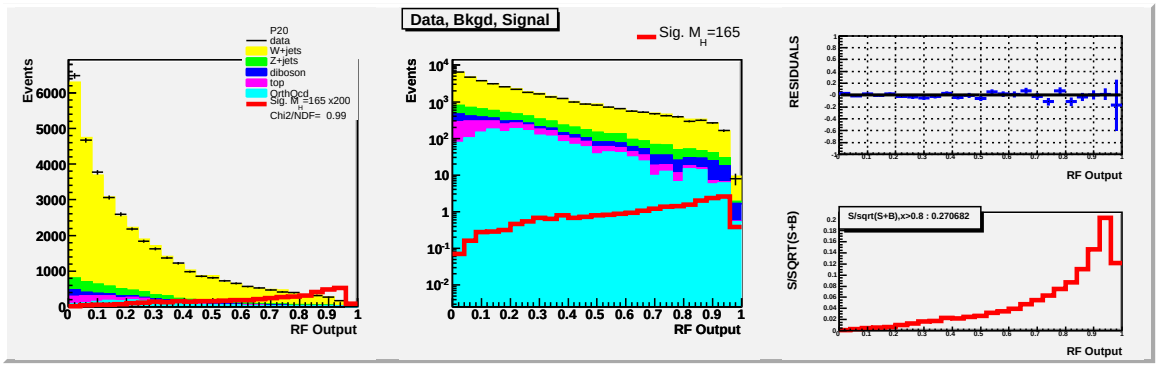

Figure 151: RF output distribution: $M_H = 165$ GeV

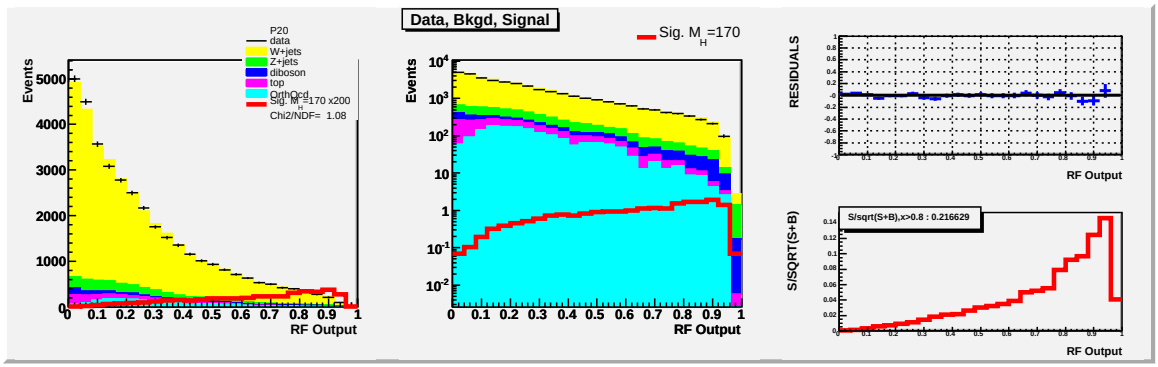

Figure 152: RF output distribution: $M_H = 170$ GeV

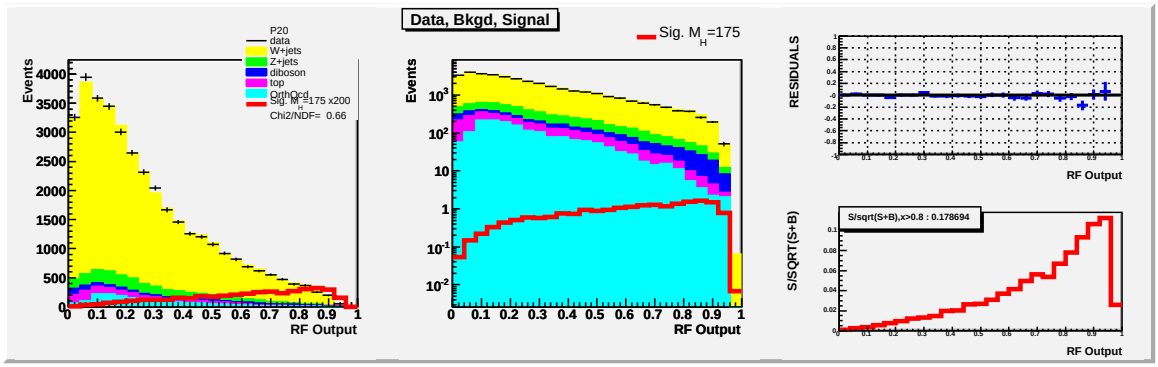

Figure 153: RF output distribution: $M_H = 175$ GeV

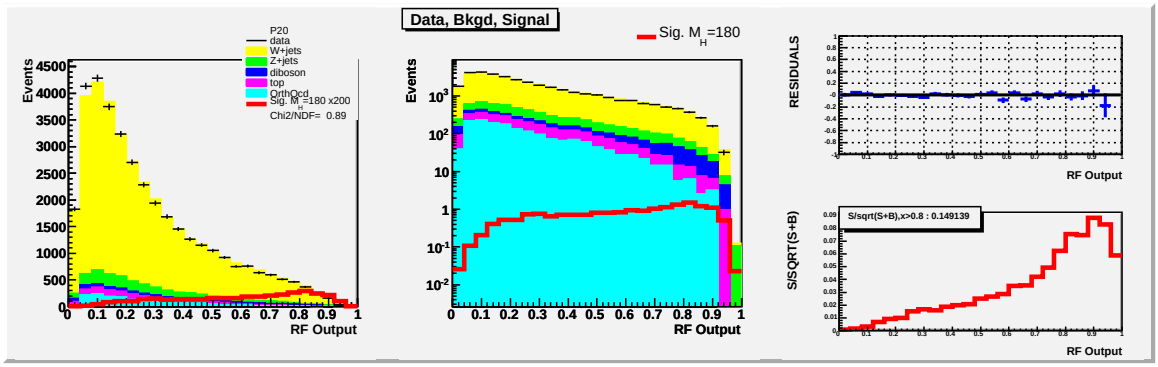

Figure 154: RF output distribution: $M_H = 180$ GeV

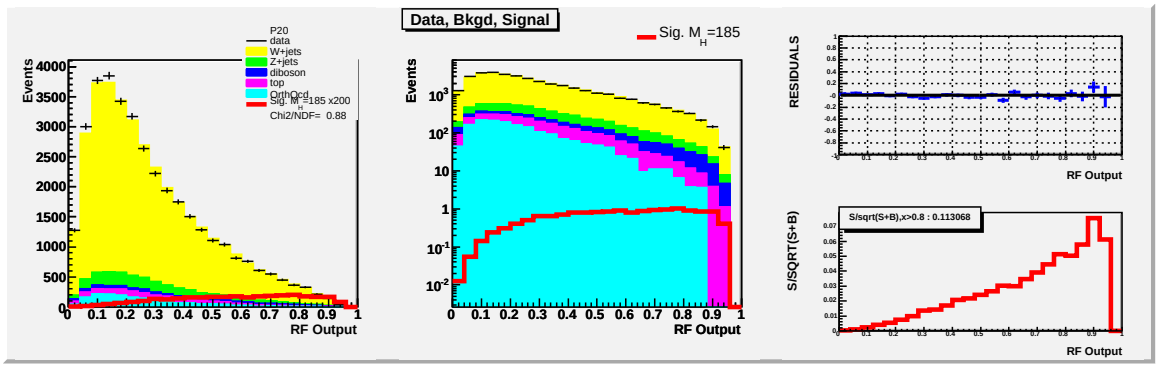

Figure 155: RF output distribution: $M_H = 185$ GeV

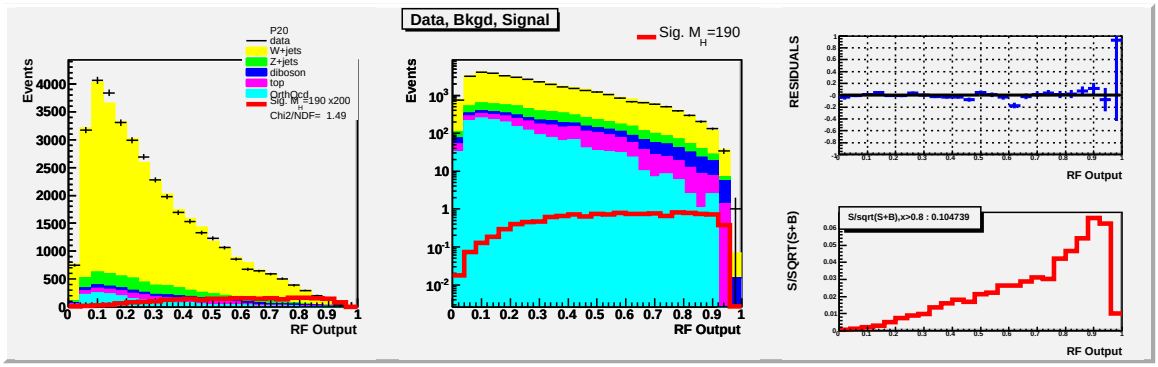

Figure 156: RF output distribution: $M_H = 190$ GeV

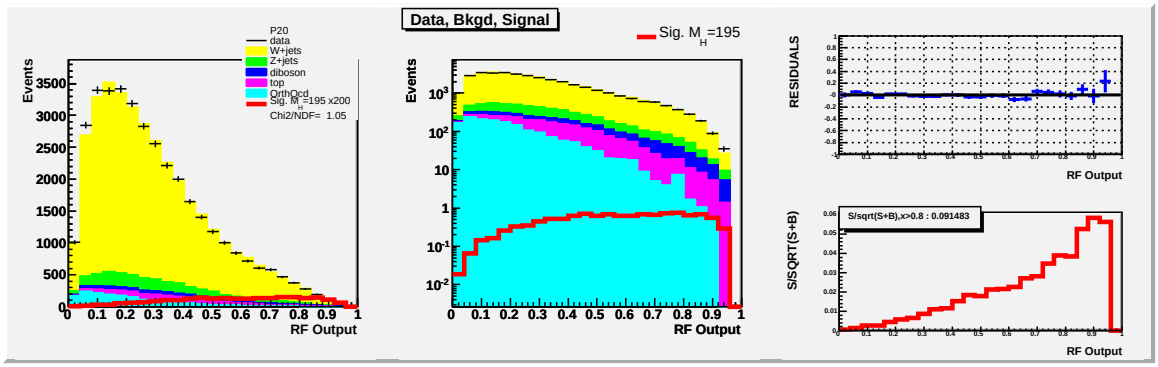

Figure 157: RF output distribution: $M_H = 195$ GeV

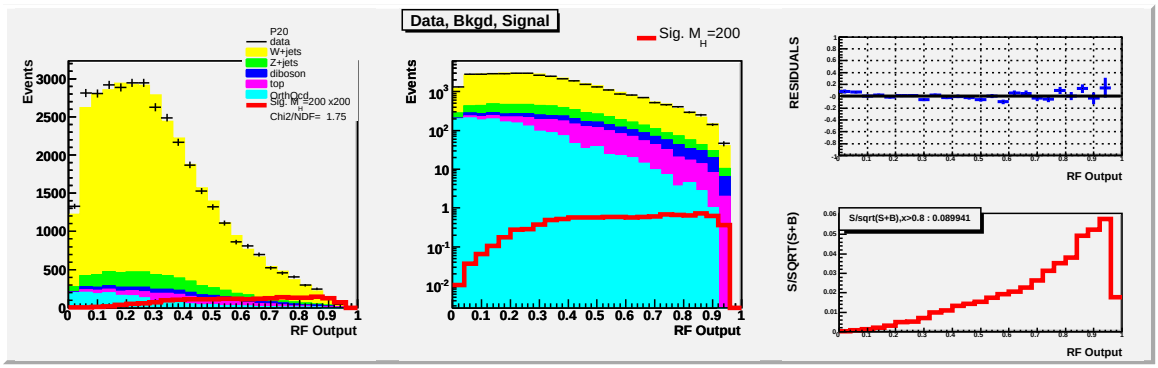

Figure 158: RF output distribution: $M_H = 200$ GeV

C Vector Boson Fusion in Comparison to Gluon-Fusion Signal

This analysis considers only gluon-fusion production (ggH) as a source of signal. Future iterations of the analysis will incorporate vector boson fusion (VBF) as an additional signal source. Table 21 shows the increases in signal event yield using our ggH-optimized preselection if we incorporate VBF in the range $M_H = 115 - 200$ GeV.

We select our RF input distributions using a KS-distance test between our combined backgrounds and ggH masses 145, 165 and 185 GeV. Figures 159-189 show the shapes of RF input distribution for VBF (in blue) and ggH (in red) signals versus data (in black) for $M_H = 145, 165, 185$ GeV. The samples have been normalized for shape comparison. The shape of VBF signal for many of the RF input distributions is dissimilar from ggH, and is closer in shape to the data, which are known to be dominated by V+jets backgrounds. Testing VBF signal on a RF trained with the ggH signal model results in VBF being classified as more background-like (Appx. D).

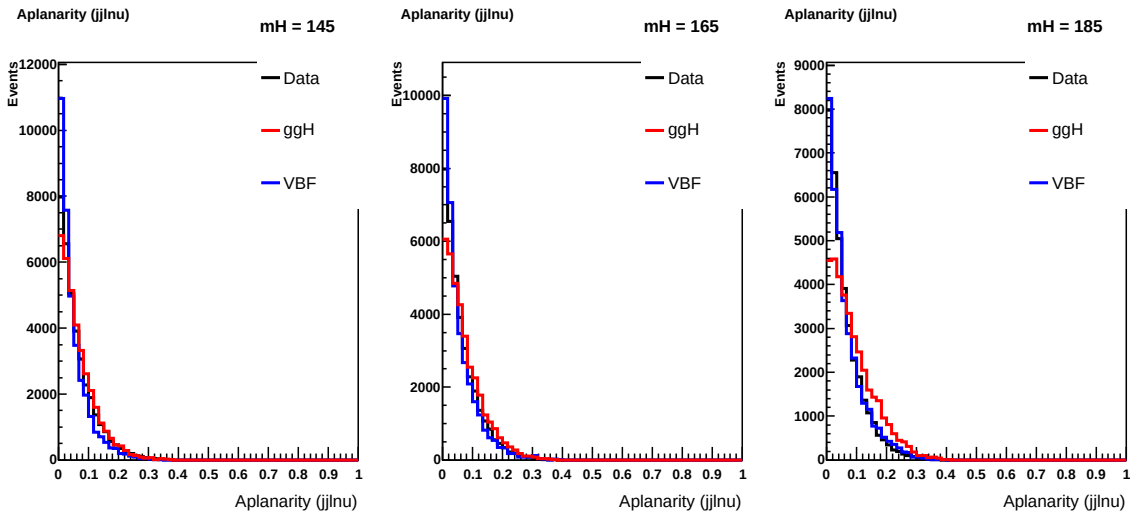

Figure 159: From left to right, mH = 145, 165, 185 GeV. Data is in black, ggH signal is in red and VBF signal is in blue. Shown is Aplanarity: measure of p_T component out of the event plane defined by leading jets (j1,j2), μ, and $\not{E}_{\mathrm{T}}$.

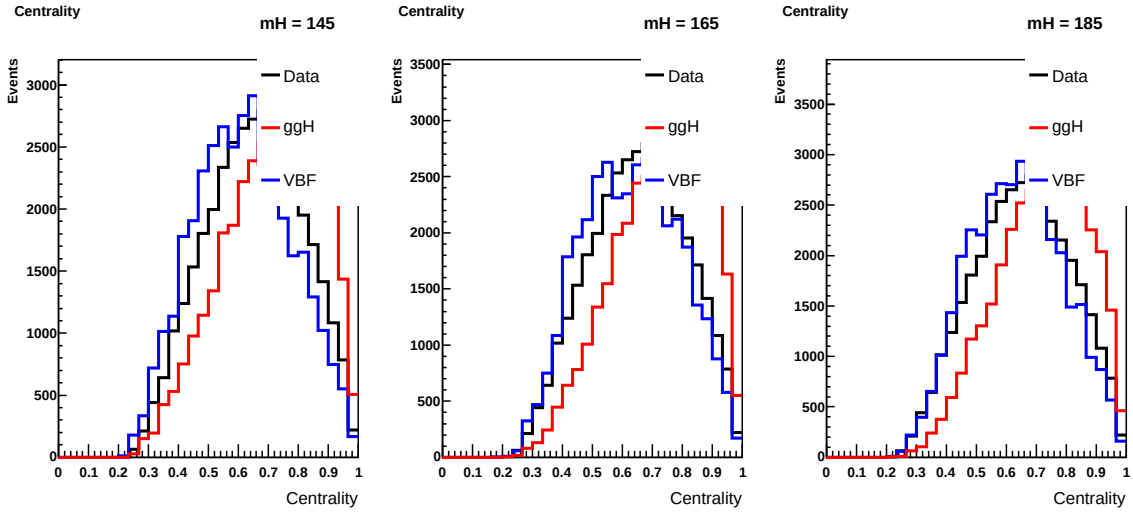

Figure 160: From left to right, mH = 145, 165, 185 GeV. Data is in black, ggH signal is in red and VBF signal is in blue. Shown is Centrality : $(\sum p_T\ )/(\sum \mathrm{E})$ for μ and all jets.

Number of Signal Events Passing Preselection			
mH	ggH	VBF	% increase when adding VBF to ggH
115	1.21	0.28	25.83
120	2.41	0.49	21.83
125	4.07	0.77	21.06
130	6.35	1.11	19.04
135	8.81	1.48	18.44
140	11.78	1.88	17.19
145	14.98	2.29	16.29
150	17.78	2.60	15.58
155	20.30	2.89	15.11
160	23.85	3.23	14.16
165	23.82	3.23	14.12
170	21.53	3.16	15.38
175	20.32	3.05	15.63
180	18.23	2.78	16.01
185	15.28	2.45	16.74
190	13.18	2.17	17.05
195	11.79	2.01	17.75
200	10.78	1.84	17.66

Table 21: Events passing preselection in the $H \rightarrow WW \rightarrow \mu\nu jj$ channel using ggH and VBF signal samples.

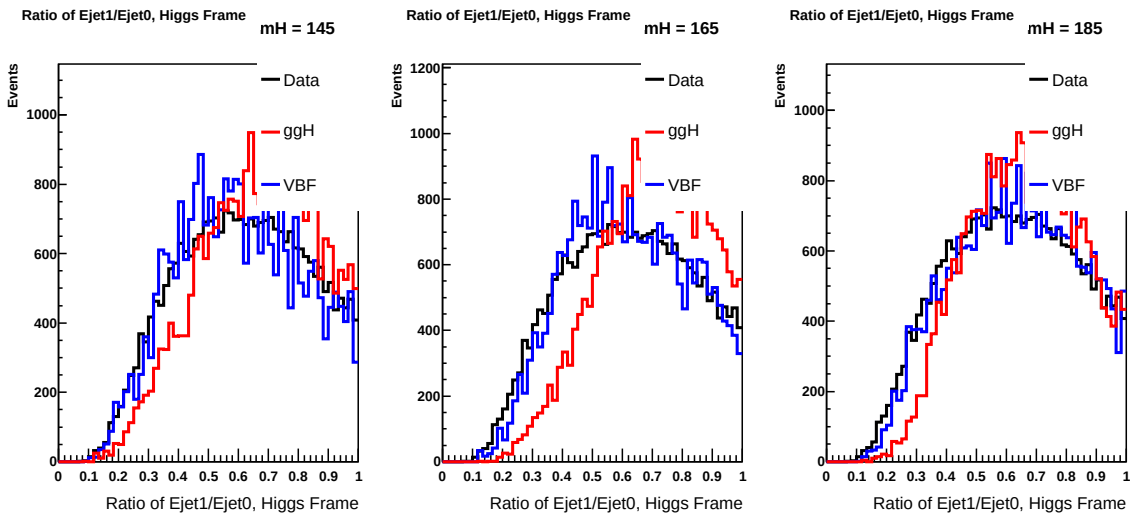

Figure 161: From left to right, mH = 145, 165, 185 GeV. Data is in black, ggH signal is in red and VBF signal is in blue. Shown is $E^{\mathrm{j2}}/E^{\mathrm{j1}}$ in H center-of-mass frame.

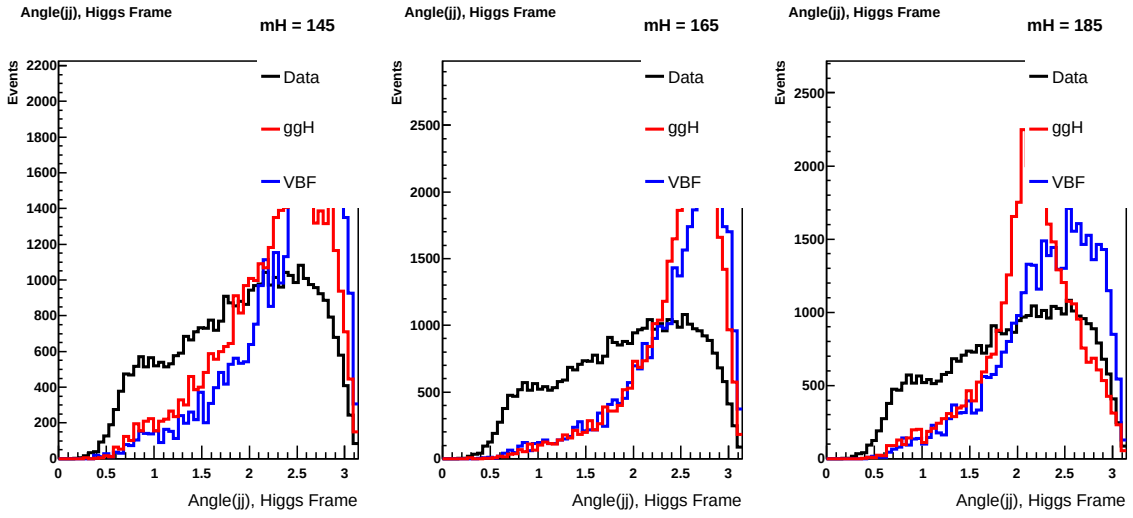

Figure 162: From left to right, mH = 145, 165, 185 GeV. Data is in black, ggH signal is in red and VBF signal is in blue. Shown is 3D angle between leading jets (j1,j2) in the H center-of-mass frame.

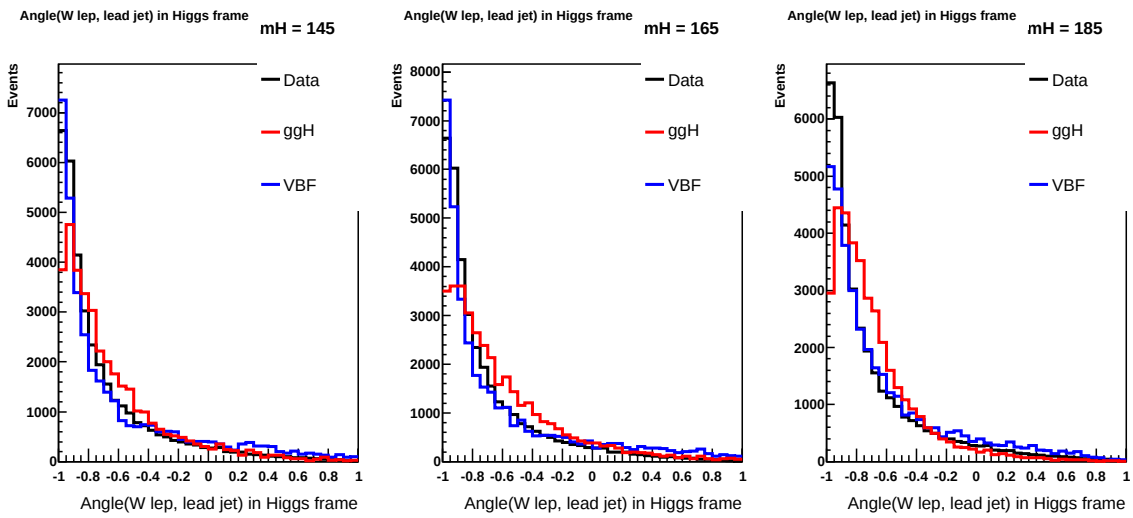

Figure 163: From left to right, mH = 145, 165, 185 GeV. Data is in black, ggH signal is in red and VBF signal is in blue. Shown is 3D Angle(Wlep, leading jet) in the H center-of-mass frame.

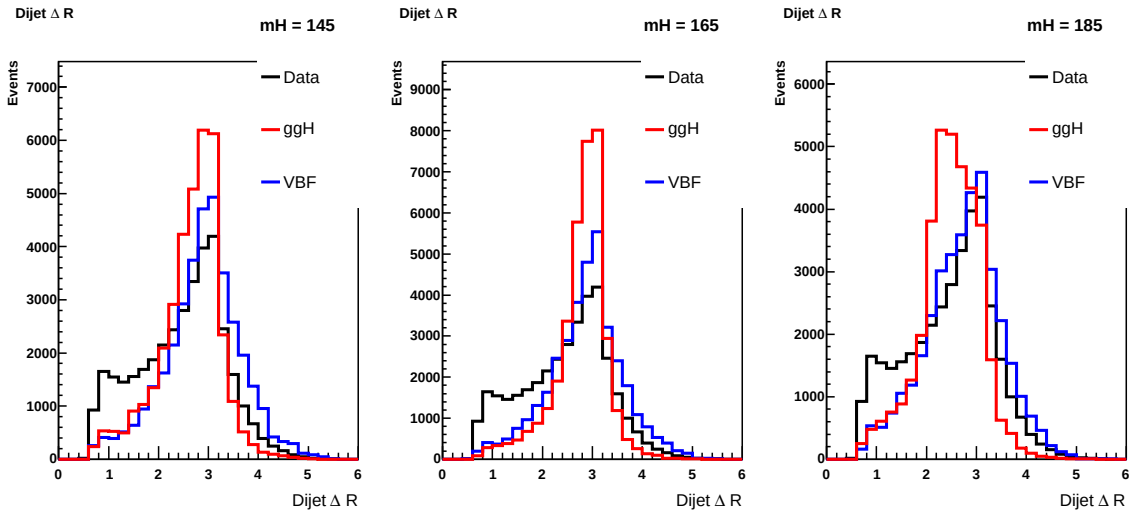

Figure 164: From left to right, mH = 145, 165, 185 GeV. Data is in black, ggH signal is in red and VBF signal is in blue. Shown is ΔR(j1,j2).

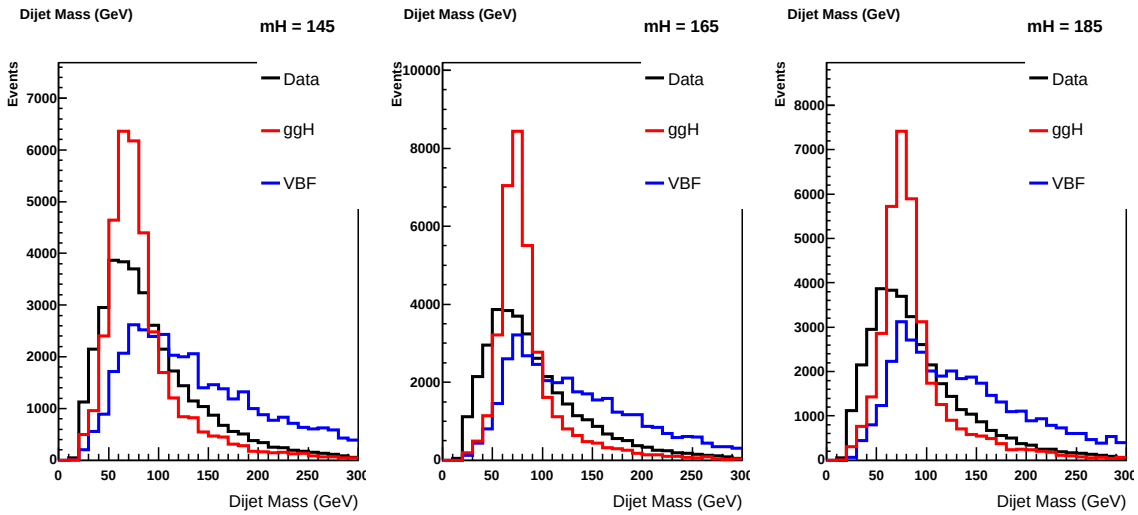

Figure 165: From left to right, mH = 145, 165, 185 GeV. Data is in black, ggH signal is in red and VBF signal is in blue. Shown is $m^{(\mathrm{j1,j2})}$.

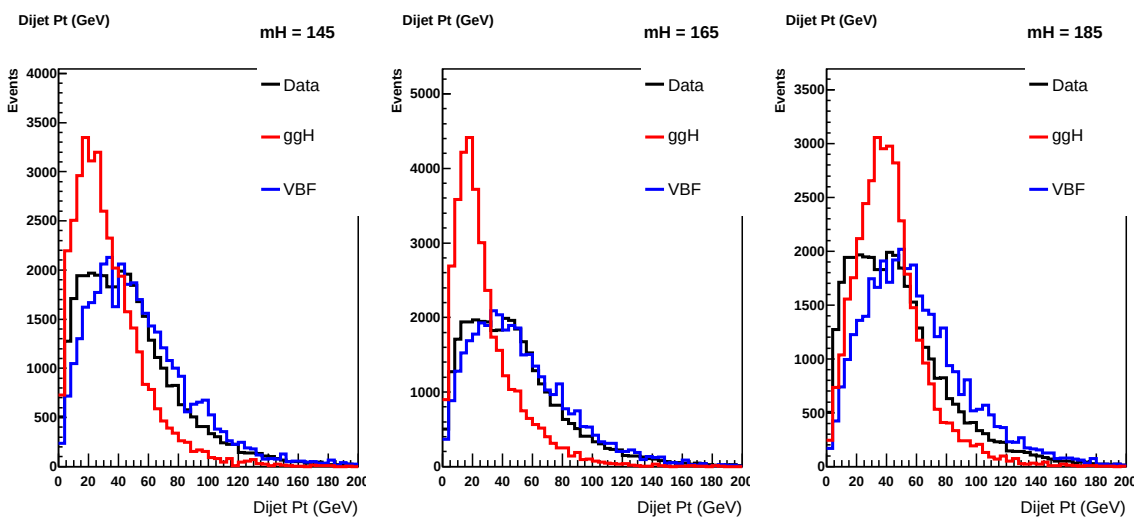

Figure 166: From left to right, mH = 145, 165, 185 GeV. Data is in black, ggH signal is in red and VBF signal is in blue. Shown is $p_T^{(\mathrm{j1,j2})}$.

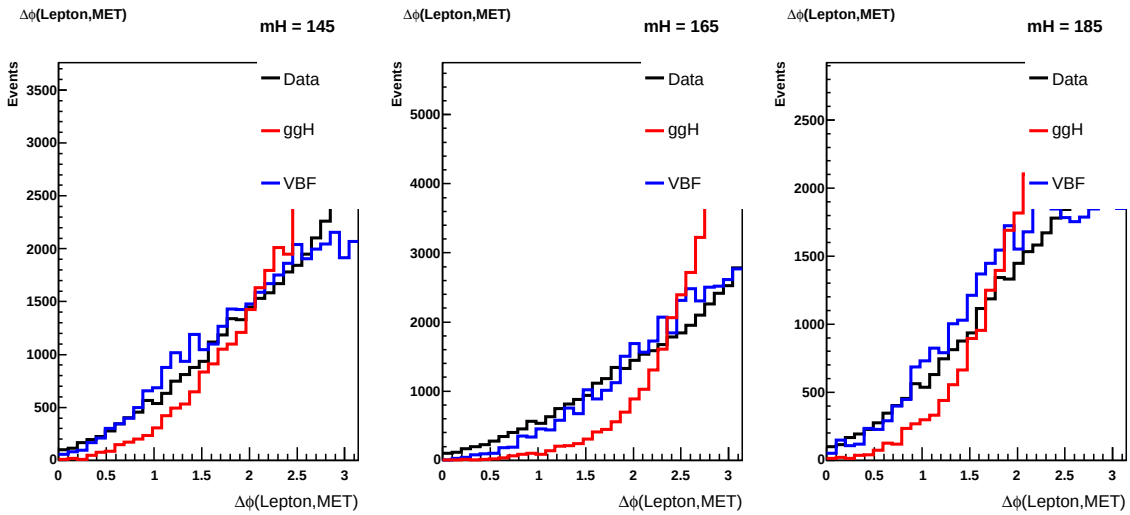

Figure 167: From left to right, mH = 145, 165, 185 GeV. Data is in black, ggH signal is in red and VBF signal is in blue. Shown is $\Delta\phi(\mu, \not{E}_{\mathrm{T}})$.

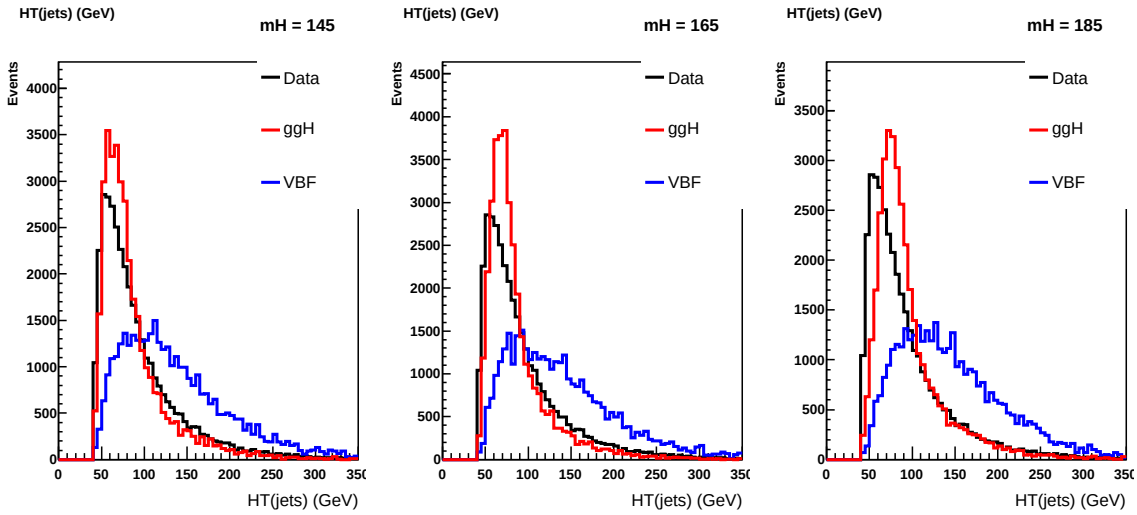

Figure 168: From left to right, mH = 145, 165, 185 GeV. Data is in black, ggH signal is in red and VBF signal is in blue. Shown is Scalar sum of p_T for all jets.

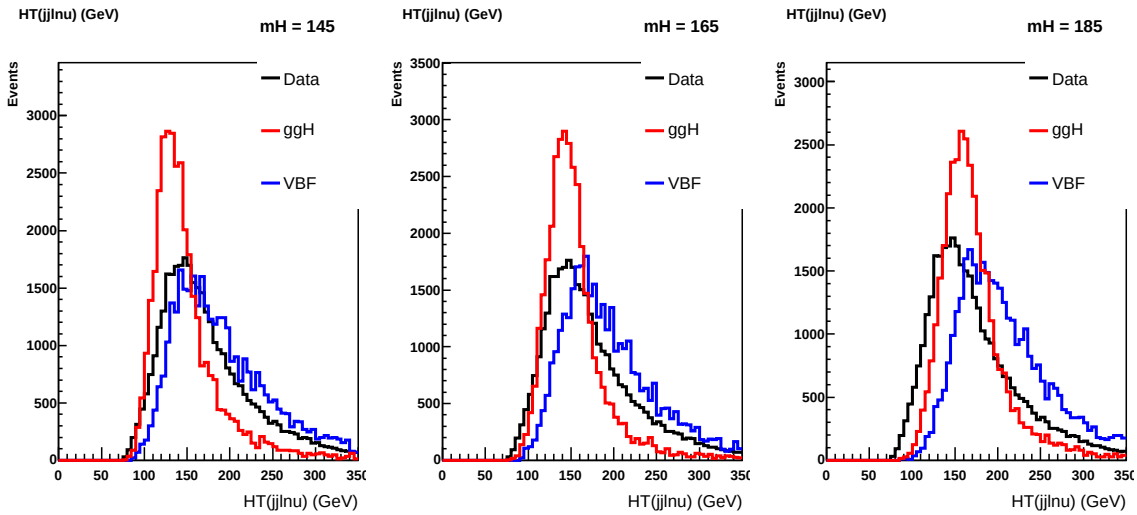

Figure 169: From left to right, mH = 145, 165, 185 GeV. Data is in black, ggH signal is in red and VBF signal is in blue. Shown is Scalar sum of p_T for μ, $\not{E}_{\mathrm{T}}$, j1, and j2.

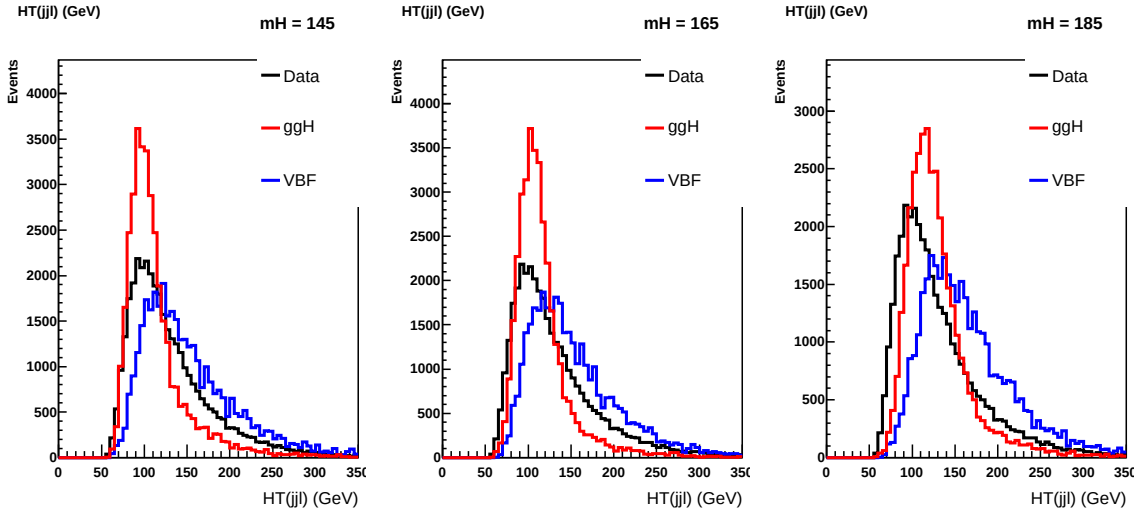

Figure 170: From left to right, mH = 145, 165, 185 GeV. Data is in black, ggH signal is in red and VBF signal is in blue. Shown is Scalar sum of p_T for μ, j1, and j2.

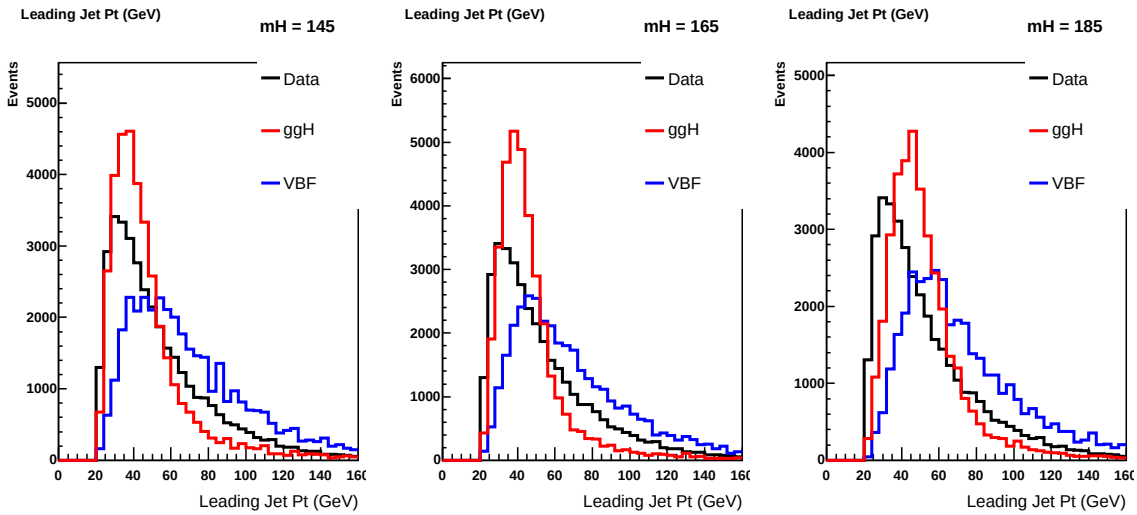

Figure 171: From left to right, mH = 145, 165, 185 GeV. Data is in black, ggH signal is in red and VBF signal is in blue. Shown is p_T of j1 .

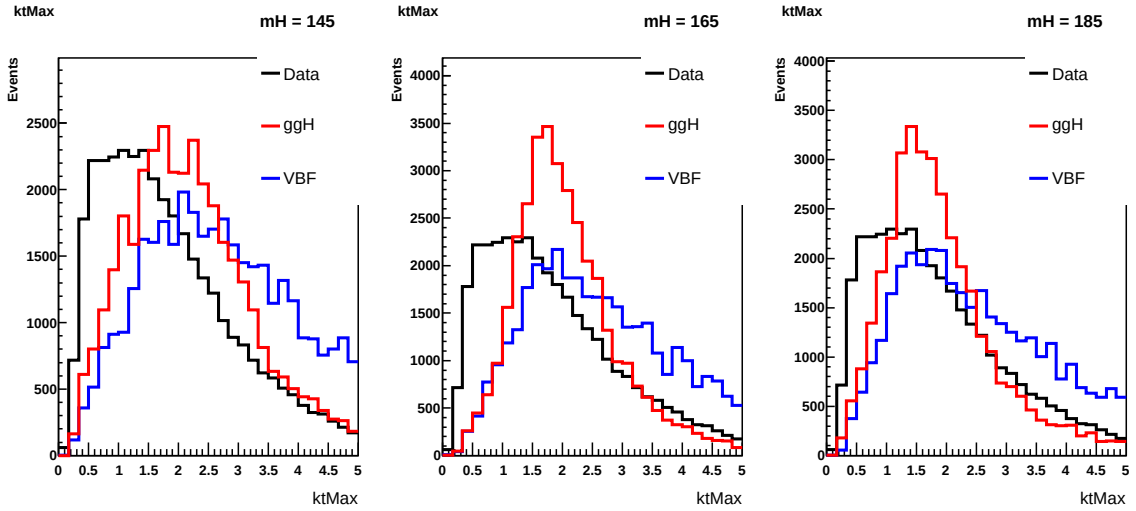

Figure 172: From left to right, mH = 145, 165, 185 GeV. Data is in black, ggH signal is in red and VBF signal is in blue. Shown is $\mathrm{KT_{max}} : \Delta R(\mathrm{j1,j2}) * E_T^{\mathrm{j1}}/(E_T^{\mu} + \not{E}_{\mathrm{T}})$.

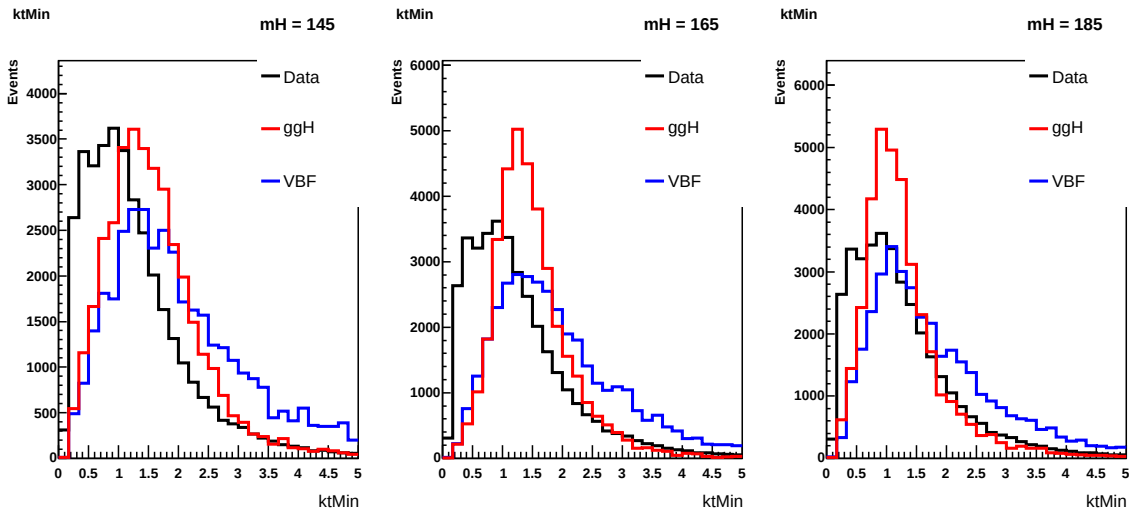

Figure 173: From left to right, mH = 145, 165, 185 GeV. Data is in black, ggH signal is in red and VBF signal is in blue. Shown is $\mathrm{KT_{min}}$: $\Delta R(\mathrm{j1,j2}) * E_T^{\mathrm{j2}}/(E_T^{\mu} + \not{E}_{\mathrm{T}})$.

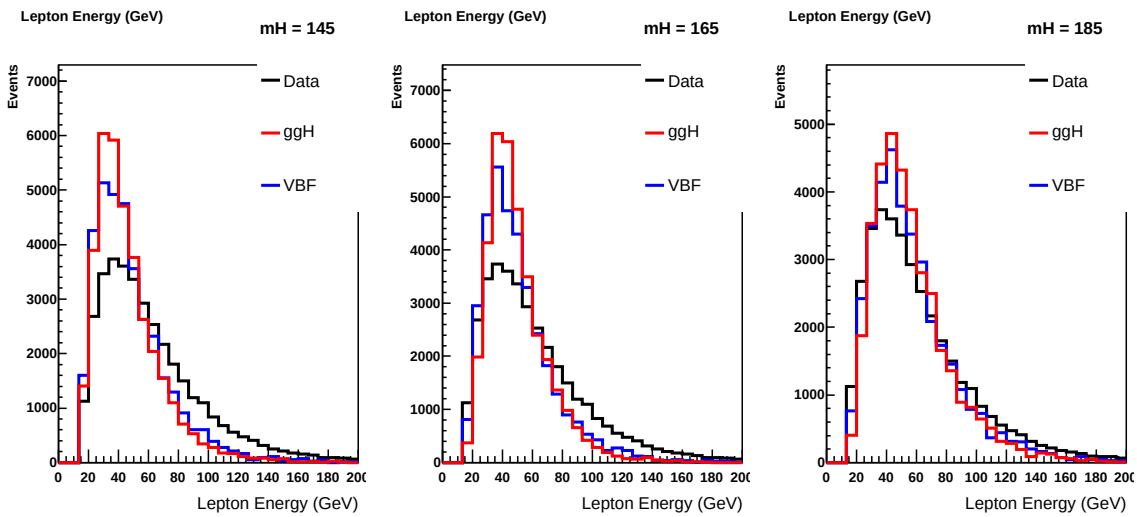

Figure 174: From left to right, mH = 145, 165, 185 GeV. Data is in black, ggH signal is in red and VBF signal is in blue. Shown is E^{μ} .

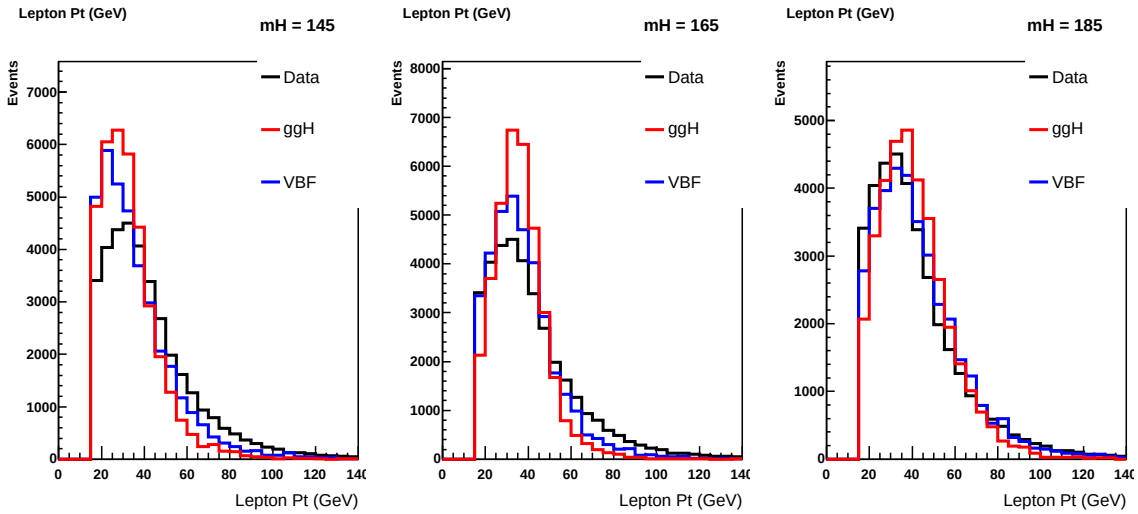

Figure 175: From left to right, mH = 145, 165, 185 GeV. Data is in black, ggH signal is in red and VBF signal is in blue. Shown is p_T^{μ}.

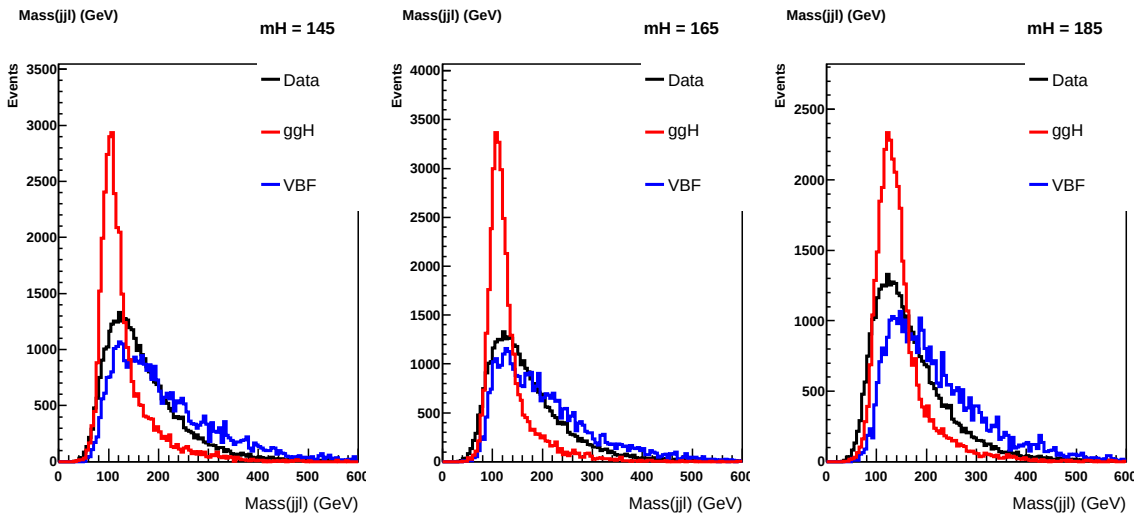

Figure 176: From left to right, mH = 145, 165, 185 GeV. Data is in black, ggH signal is in red and VBF signal is in blue. Shown is Invariant Mass of μ, j1 and j2.

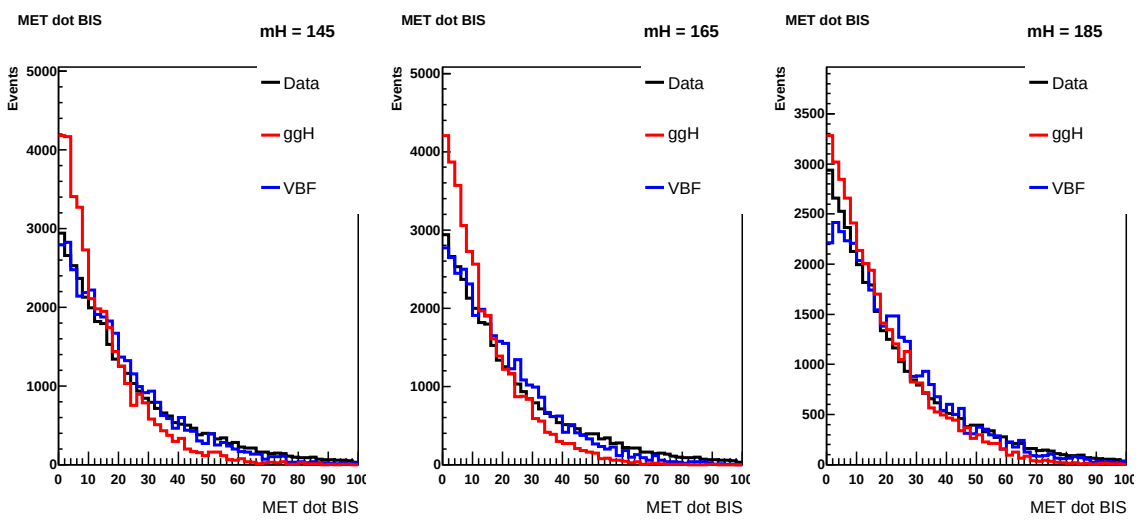

Figure 177: From left to right, mH = 145, 165, 185 GeV. Data is in black, ggH signal is in red and VBF signal is in blue. Shown is METbis : dot product of $\not{E}_{\mathrm{T}}$ and angular bisector of j1, j2.

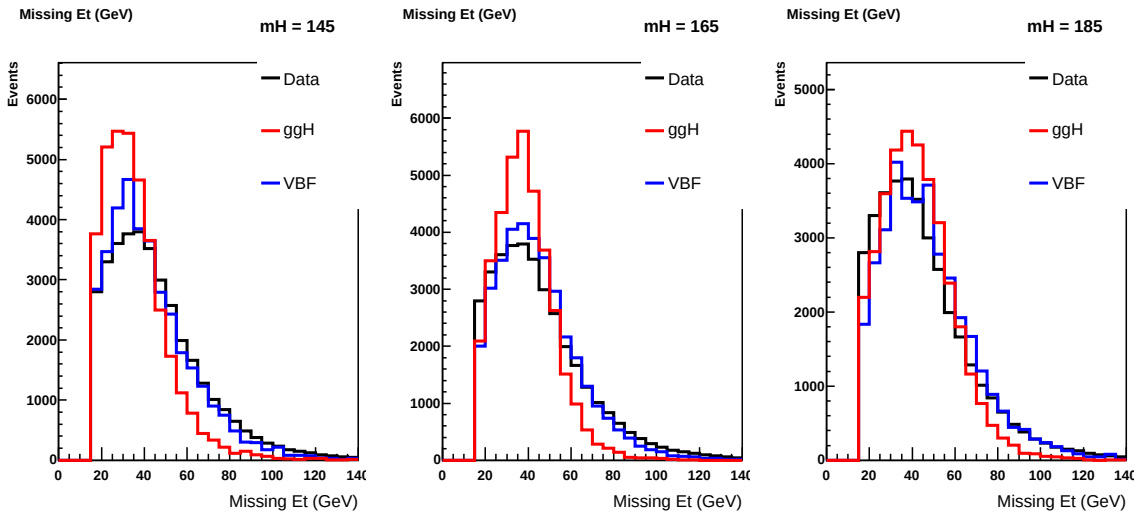

Figure 178: From left to right, mH = 145, 165, 185 GeV. Data is in black, ggH signal is in red and VBF signal is in blue. Shown is $\not{E}_{\mathrm{T}}$.

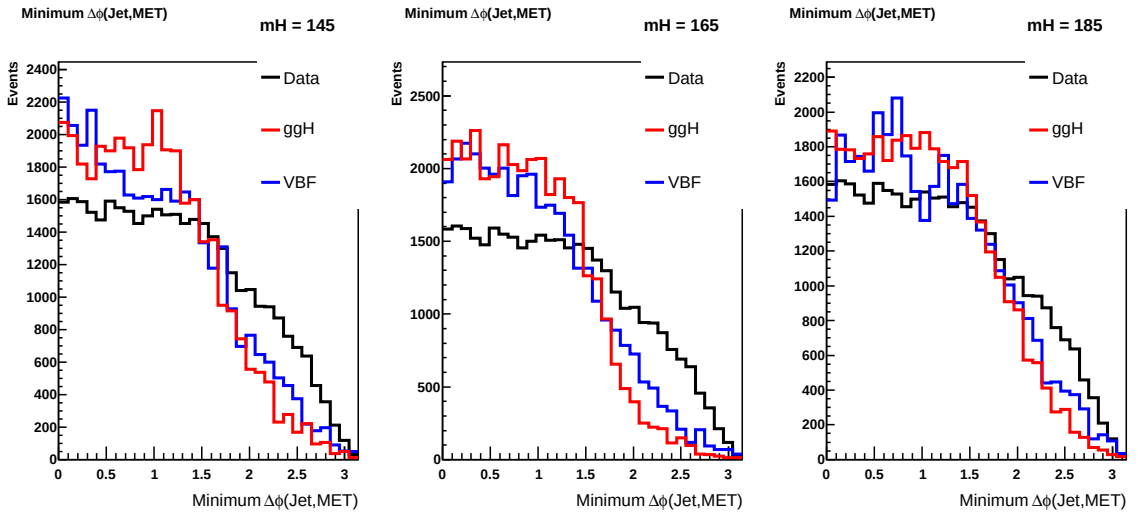

Figure 179: From left to right, mH = 145, 165, 185 GeV. Data is in black, ggH signal is in red and VBF signal is in blue. Shown is Minimum of $\Delta\phi(\not{E}_{\mathrm{T}},\mathrm{j1})$ or $\Delta\phi(\not{E}_{\mathrm{T}},\mathrm{j2})$.

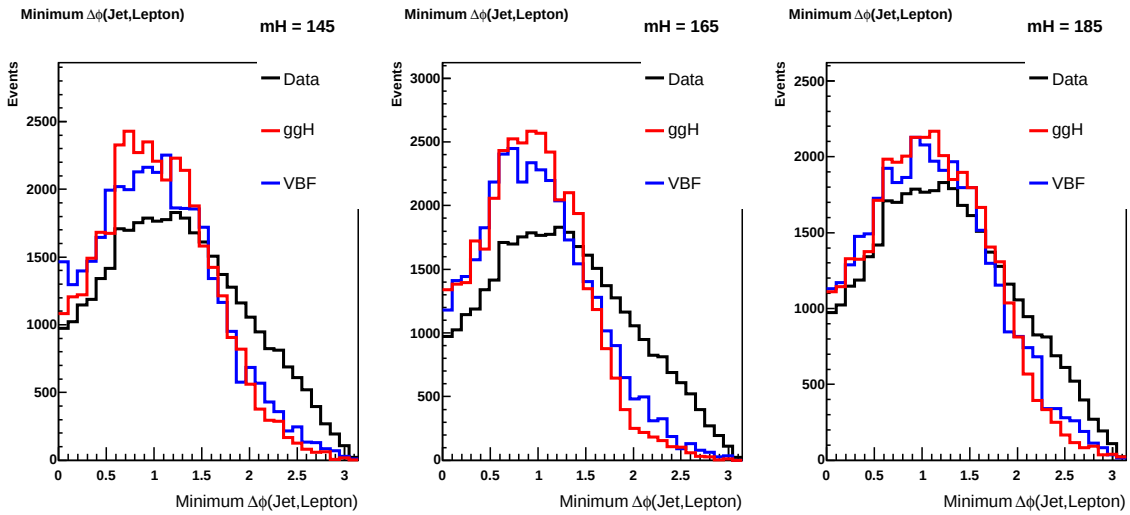

Figure 180: From left to right, mH = 145, 165, 185 GeV. Data is in black, ggH signal is in red and VBF signal is in blue. Shown is Minimum of $\Delta\phi(\mu$,j1) or $\Delta\phi(\mu$,j2).

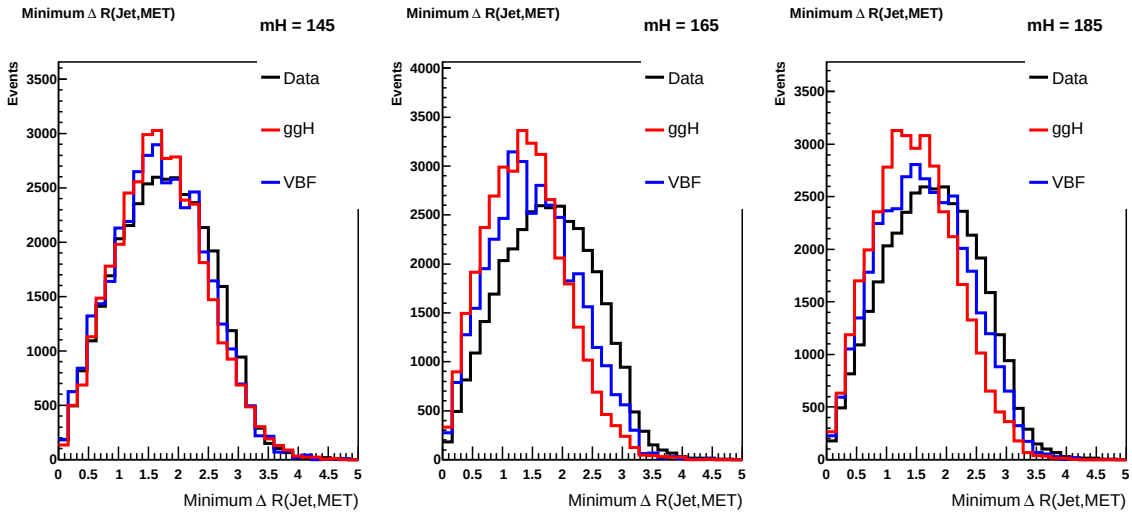

Figure 181: From left to right, mH = 145, 165, 185 GeV. Data is in black, ggH signal is in red and VBF signal is in blue. Shown is Minimum of ΔR($\not{E}_{\mathrm{T}}$,j1) or Δ R($\not{E}_{\mathrm{T}}$,j2).

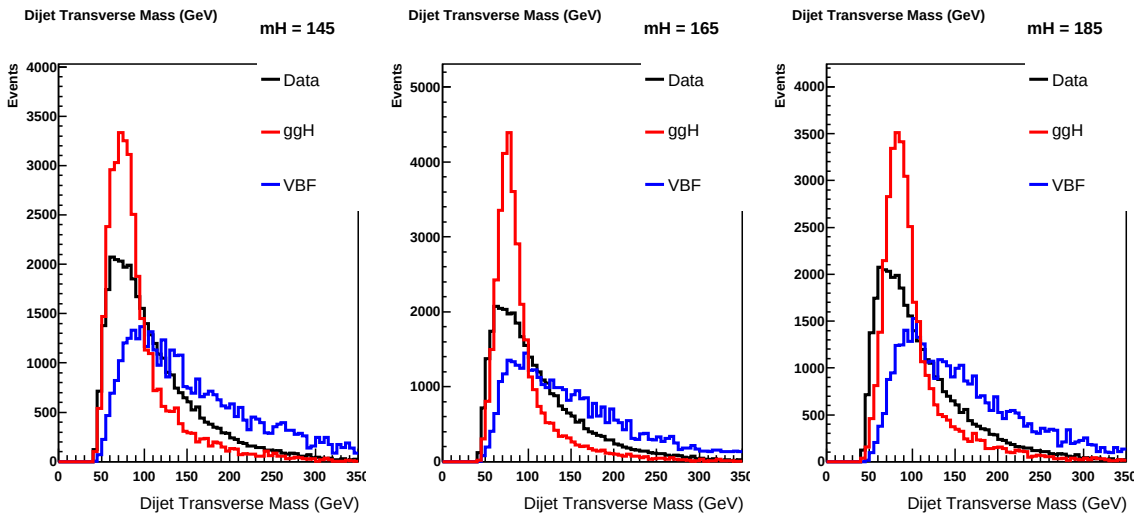

Figure 182: From left to right, mH = 145, 165, 185 GeV. Data is in black, ggH signal is in red and VBF signal is in blue. Shown is $m_T^{(\mathrm{j1,j2})}$.

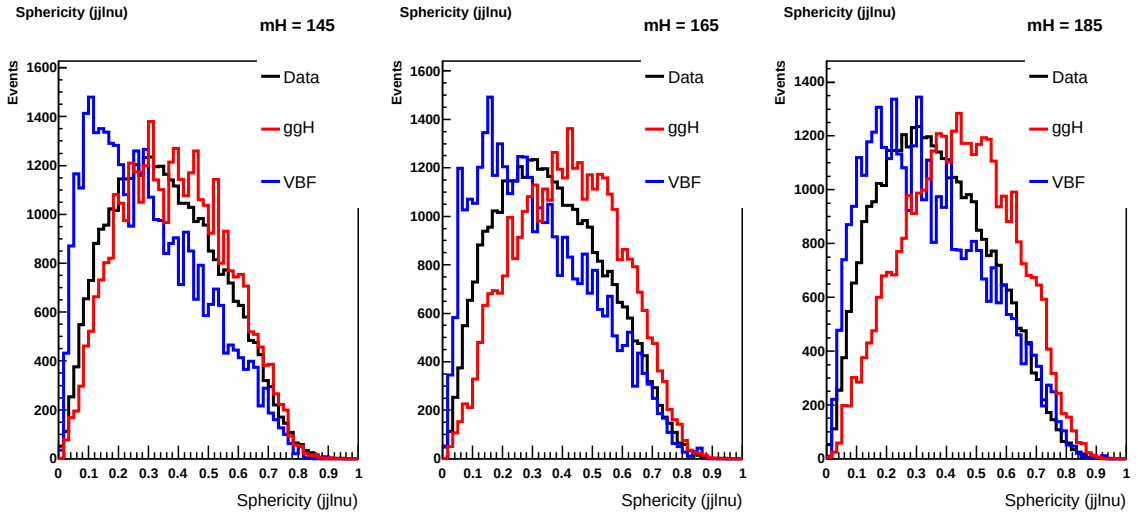

Figure 183: From left to right, mH = 145, 165, 185 GeV. Data is in black, ggH signal is in red and VBF signal is in blue. Shown is Sphericity: measure of the summed p_T^2 with respect to the event axis calculated from μ, $\not{E}_{\mathrm{T}}$, j1 and j2.

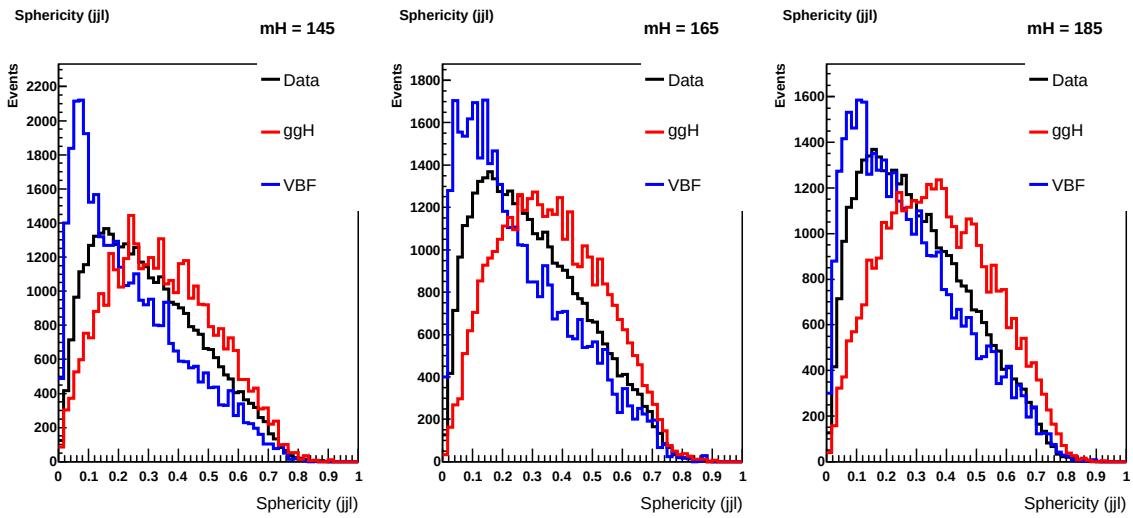

Figure 184: From left to right, mH = 145, 165, 185 GeV. Data is in black, ggH signal is in red and VBF signal is in blue. Shown is Sphericity: measure of the summed p_T^2 with respect to the event axis calculated from muon, j1, and j2.

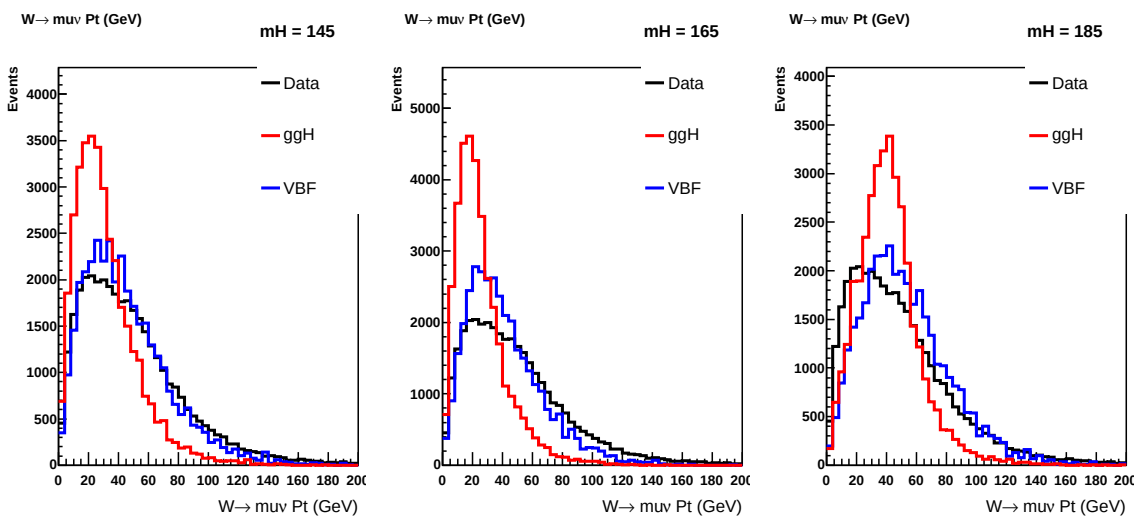

Figure 185: From left to right, mH = 145, 165, 185 GeV. Data is in black, ggH signal is in red and VBF signal is in blue. Shown is p_T^W.

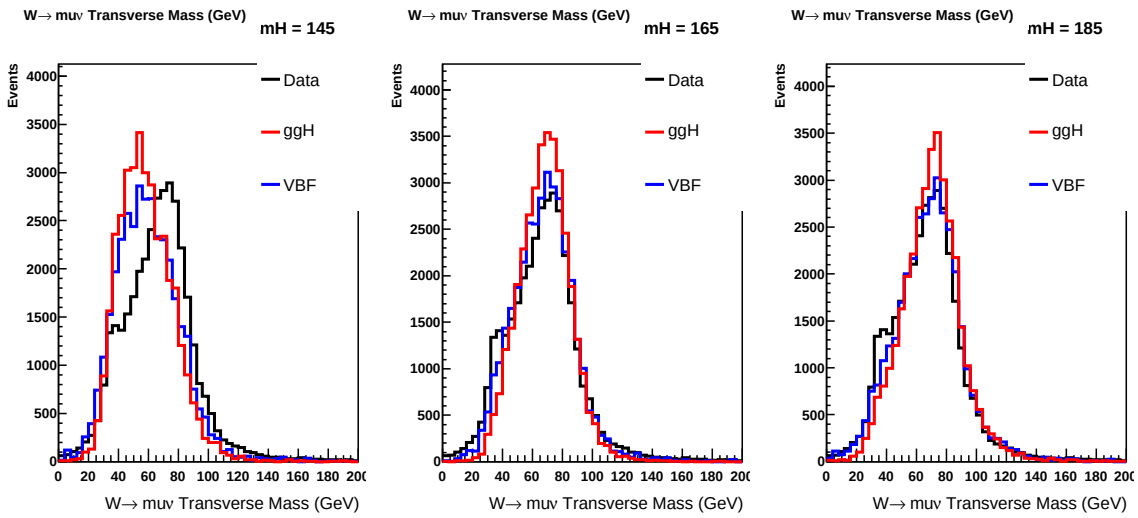

Figure 186: From left to right, mH = 145, 165, 185 GeV. Data is in black, ggH signal is in red and VBF signal is in blue. Shown is m_T^W.

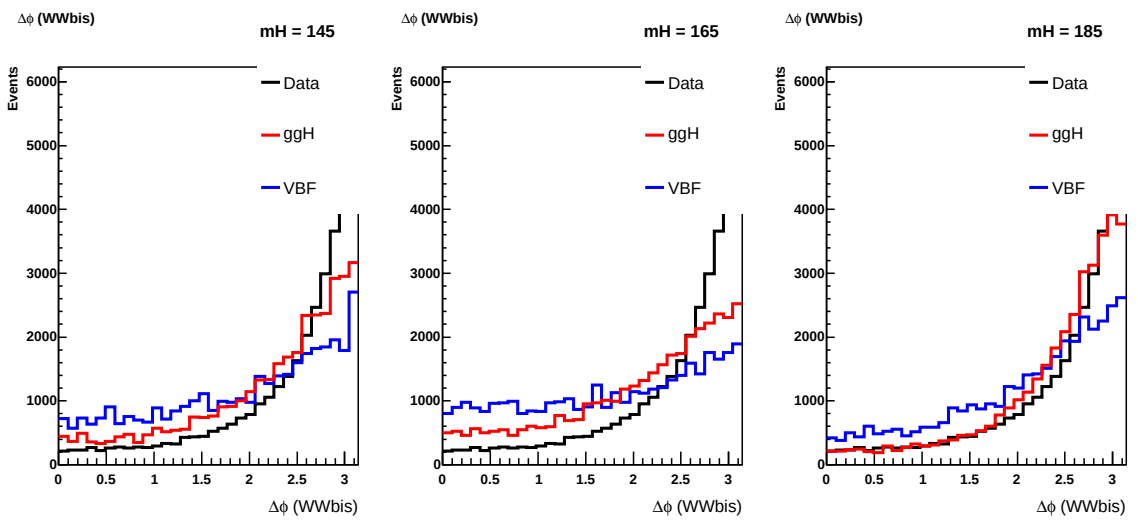

Figure 187: From left to right, mH = 145, 165, 185 GeV. Data is in black, ggH signal is in red and VBF signal is in blue. Shown is WWbisDPhi : $\Delta\phi$ between leptonic W and dijet bisector.

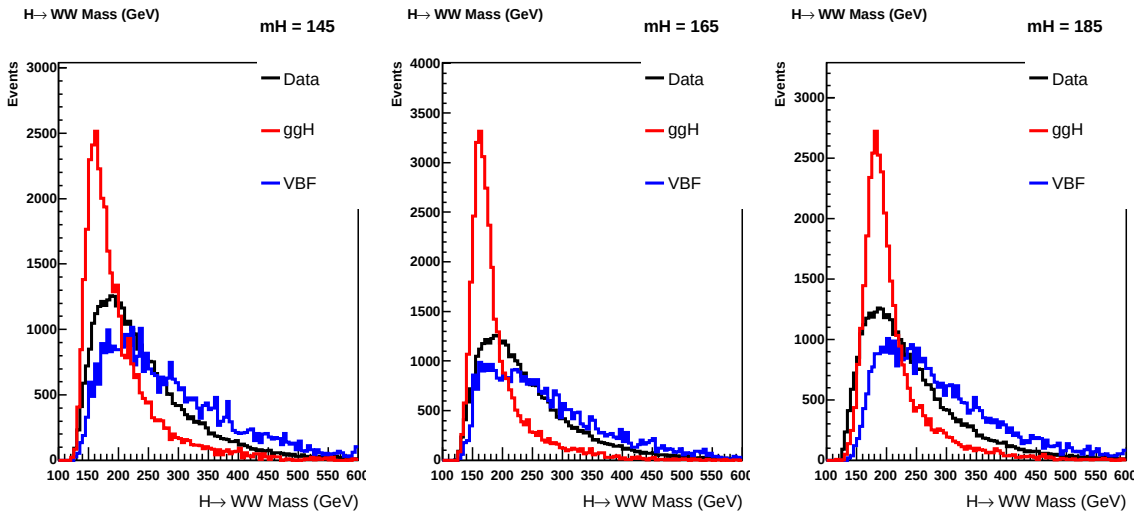

Figure 188: From left to right, mH = 145, 165, 185 GeV. Data is in black, ggH signal is in red and VBF signal is in blue. Shown is Invariant mass of the WW pair, (M_H).

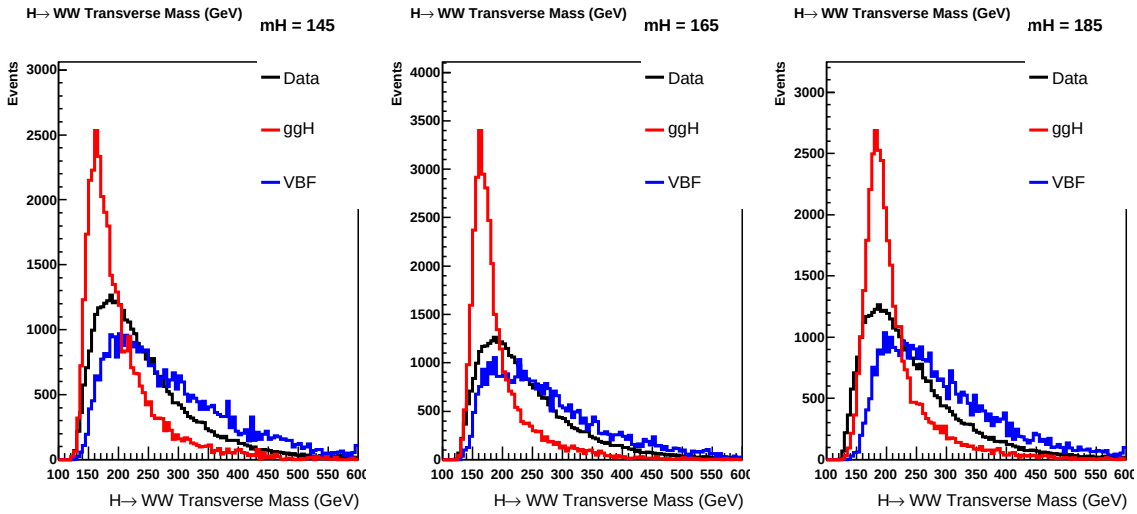

Figure 189: From left to right, mH = 145, 165, 185 GeV. Data is in black, ggH signal is in red and VBF signal is in blue. Shown is Transverse mass of the WW pair (m_T^H).

D Signal Sources in Addition to Gluon-Fusion $H \rightarrow WW \rightarrow \mu\nu jj$

Other signals will have small contributions to the total signal yield in addition to vector boson fusion (Appx. C) such as: gluon-fusion $H \rightarrow WW \rightarrow \tau\nu jj$ (taunujj), and gluon-fusion $H \rightarrow ZZ \rightarrow \ell\bar{\ell}jj$ (ggHZZ). Associated production $WH \rightarrow \ell\bar{\nu}bb$ (WHlvbb) can considerably increase signal yields for $M_H \lesssim 145$ GeV. Table 22 shows the increase in total signal events passing our preselection if we incorporate the above signals in addition to ggH signal samples in the range $M_H = 115 - 200$ GeV.

Using RF inputs from Sec. 8 (Appx. A) our RF is trained over the combined background and ggH signal samples. Figures 191−**??** show the results of testing the ggH-trained RF on the various signals for $M_H = 115 - 200$ GeV. The signals have been properly normalized and stacked for relative contribution and classification comparison. The WH process (in purple) dominates at low mass and simulated samples are not available for $M_H > 150$ GeV where the contributions from this channel are negligible. The ggH process (in red) dominates for $M_H \geq 145$, with the second largest contribution coming from VBF (in blue).

Figure 208 shows the difference in expected limits for the $H \rightarrow WW \rightarrow \mu\nu jj$channel when using ggH only (red) and all five signal sources combined (black). There is a significant contribution at low mass from WH, while there is little contribution in our region of maximal ggH sensitivity, $155 \leq M_H \leq 175$, and small contributions at high mass coming from VBF. The incorporation of these additional signals is a planned improvement for the update of the semileptonic analyses.

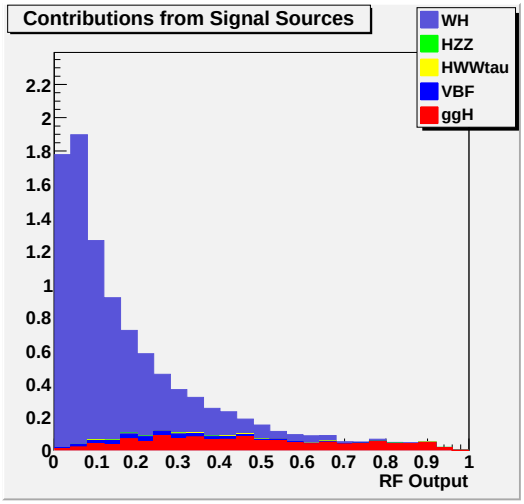

Figure 190: RF output for various signals: $M_H = 115$ GeV

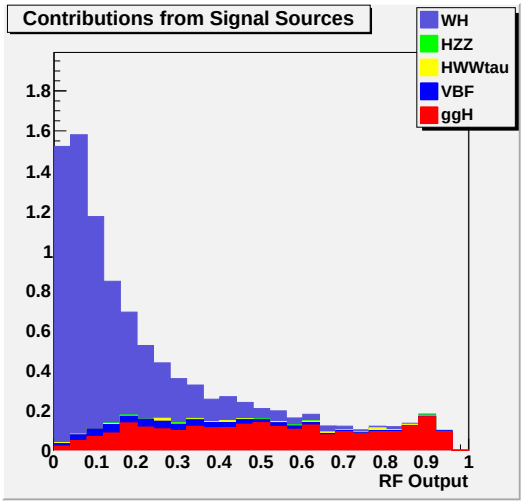

Figure 191: RF output for various signals: $M_H = 120$ GeV

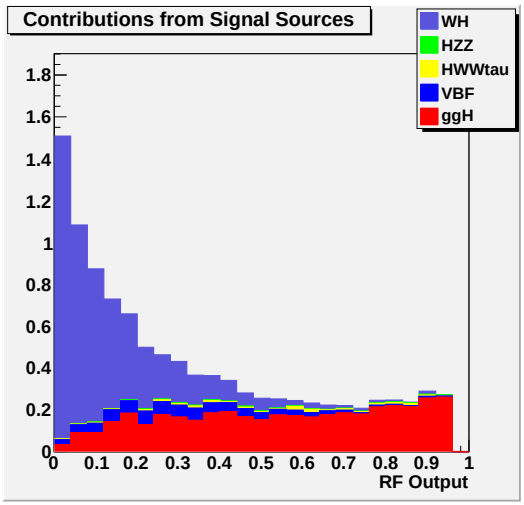

Figure 192: RF output for various signals: $M_H = 125$ GeV

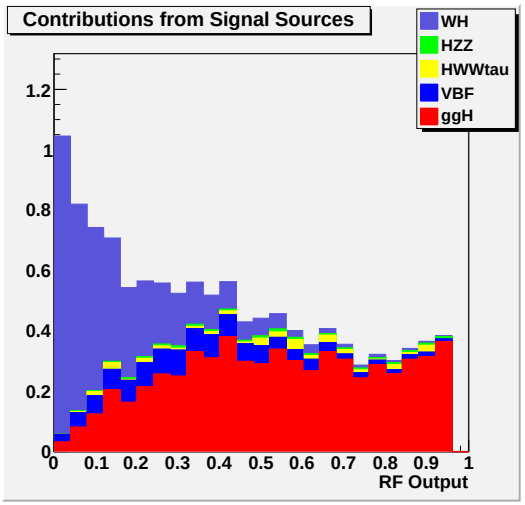

Figure 193: RF output for various signals: $M_H = 130$ GeV

Number of Signal Events Passing Preselection						
mH	ggH	VBF	ggHZZ	taunujj	WH lvbb	% increase when adding all to ggH
115	1.21	0.28	0.03	0.05	8.28	714.05
120	2.41	0.49	0.05	0.10	6.88	312.03
125	4.07	0.77	0.09	0.16	5.43	158.48
130	6.35	1.11	0.14	0.29	4.2	90.39
135	8.81	1.48	0.21	0.34	3.04	57.55
140	11.78	1.88	0.27	0.54	2.15	41.09
145	14.98	2.29	0.32	0.73	1.43	31.84
150	17.78	2.60	0.35	0.91	0.86	26.55
155	20.30	2.89	0.31	1.07	–	21.03
160	23.85	3.23	0.18	1.38	–	20.08
165	23.82	3.23	0.09	1.26	–	19.23
170	21.53	3.16	0.09	–	–	15.10
175	20.32	3.05	0.13	1.25	–	21.80
180	18.23	2.78	0.23	1.24	–	23.31
185	15.28	2.45	0.55	0.90	–	25.52
190	13.18	2.17	0.72	0.86	–	28.45
195	11.79	2.01	0.76	0.75	–	29.86
200	10.78	1.84	0.78	0.78	–	31.54

Table 22: Events passing preselection in the $H \rightarrow WW \rightarrow \mu\nu jj$ channel using various signal samples.

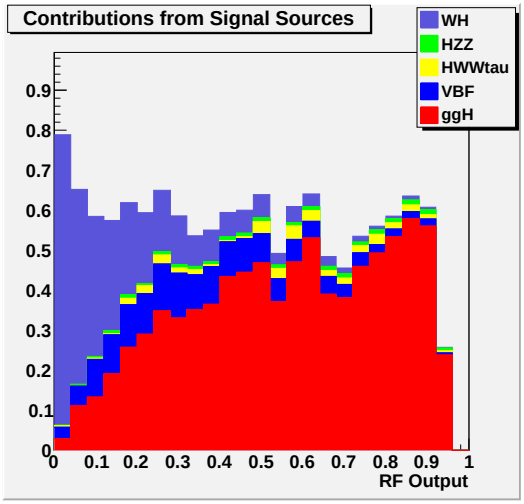

Figure 194: RF output for various signals: $M_H = 135$ GeV

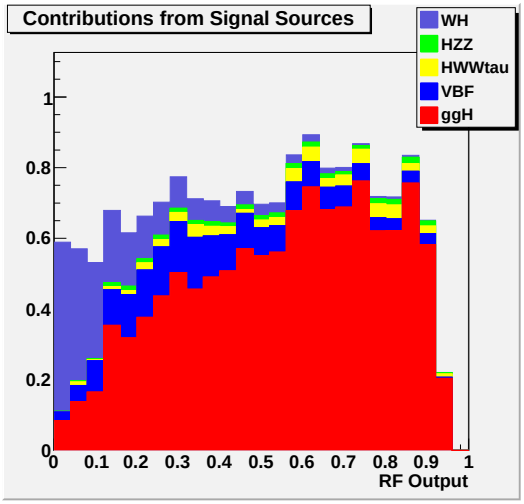

Figure 195: RF output for various signals: $M_H = 140$ GeV

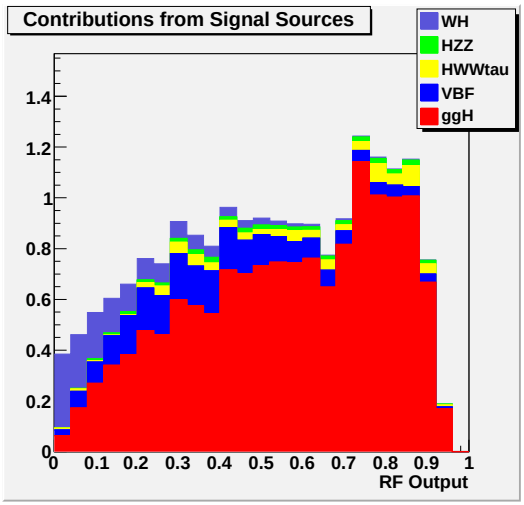

Figure 196: RF output for various signals: $M_H = 145$ GeV

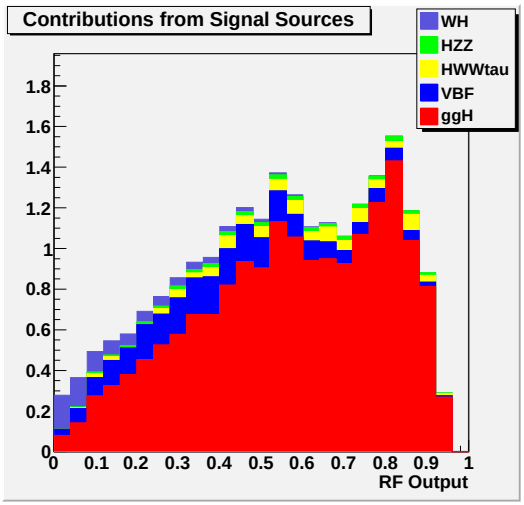

Figure 197: RF output for various signals: $M_H = 150$ GeV

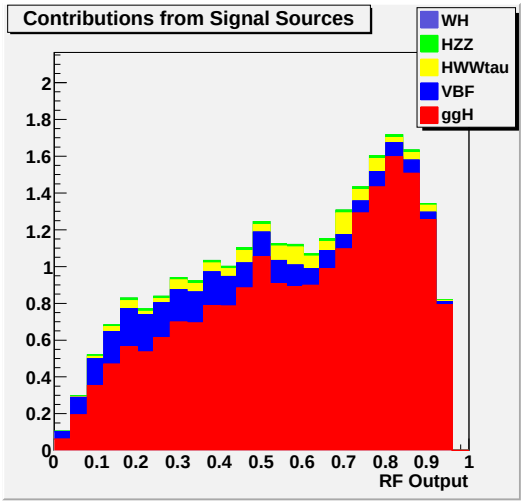

Figure 198: RF output for various signals: $M_H = 155$ GeV

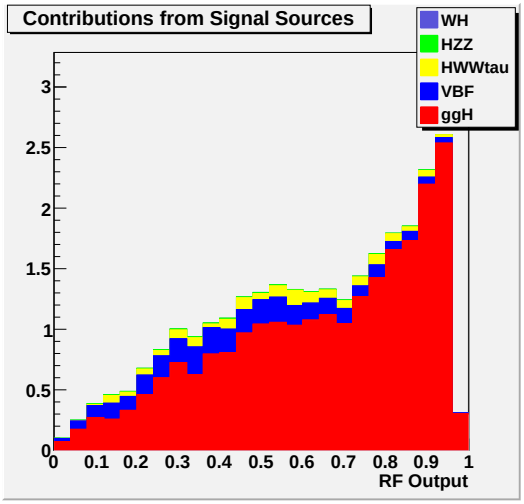

Figure 199: RF output for various signals: $M_H = 160$ GeV

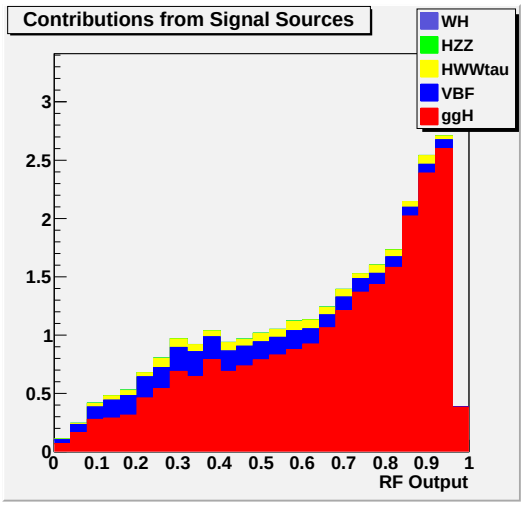

Figure 200: RF output for various signals: $M_H = 165$ GeV

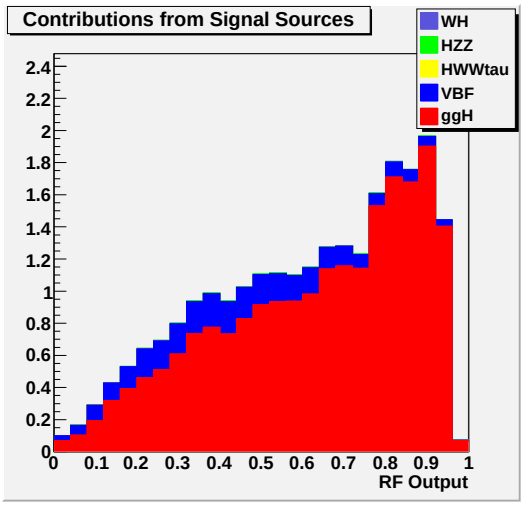

Figure 201: RF output for various signals: $M_H = 170$ GeV

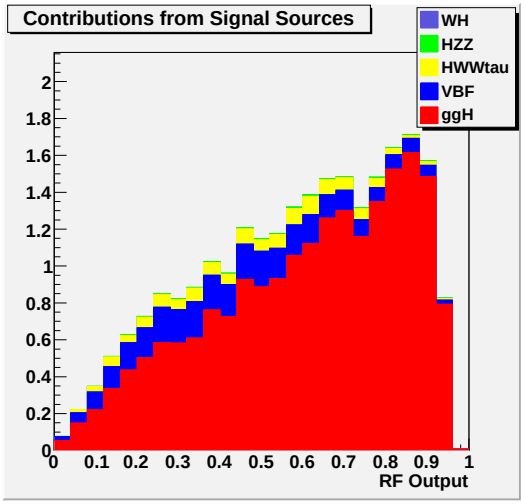

Figure 202: RF output for various signals: $M_H = 175$ GeV

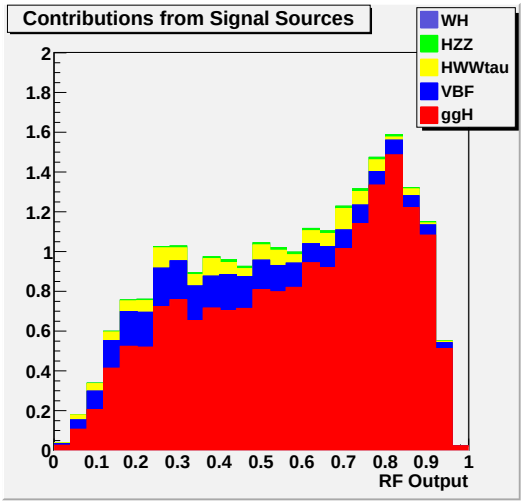

Figure 203: RF output for various signals: $M_H = 180$ GeV

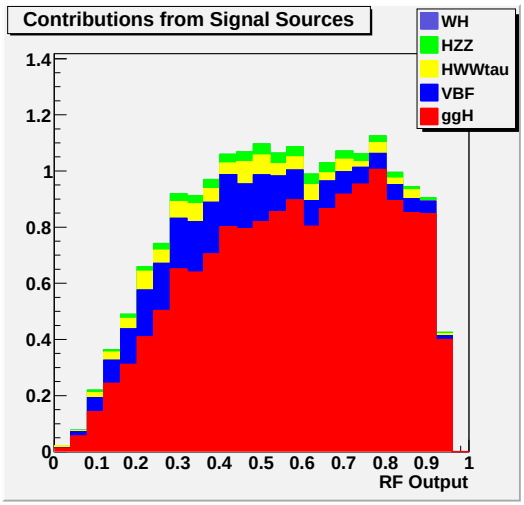

Figure 204: RF output for various signals: $M_H = 185$ GeV

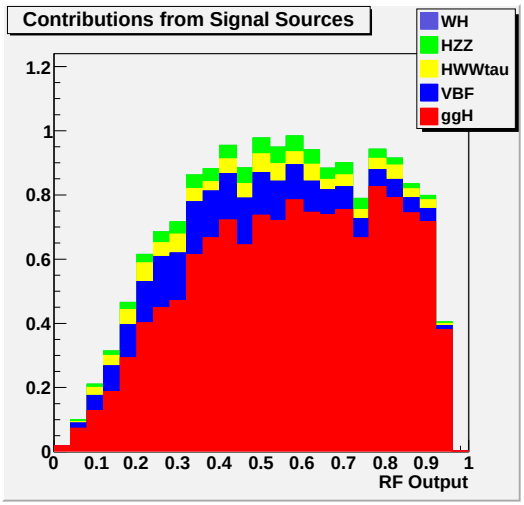

Figure 205: RF output for various signals: $M_H = 190$ GeV

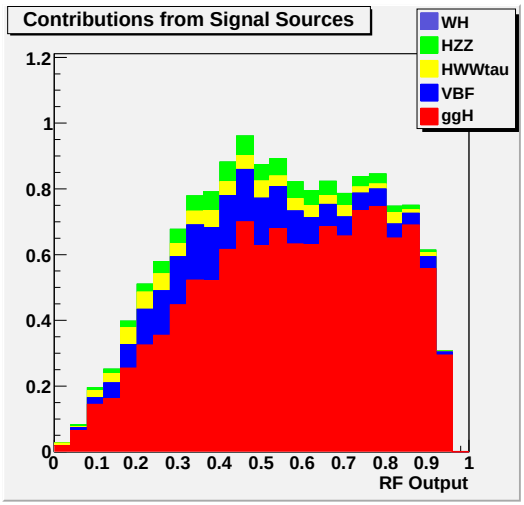

Figure 206: RF output for various signals: $M_H = 195$ GeV

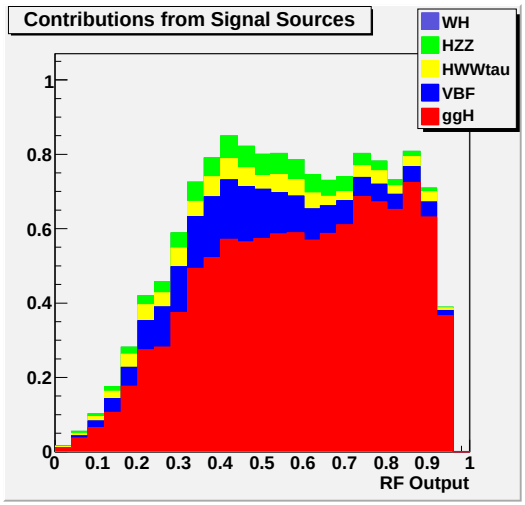

Figure 207: RF output for various signals: $M_H = 200$ GeV

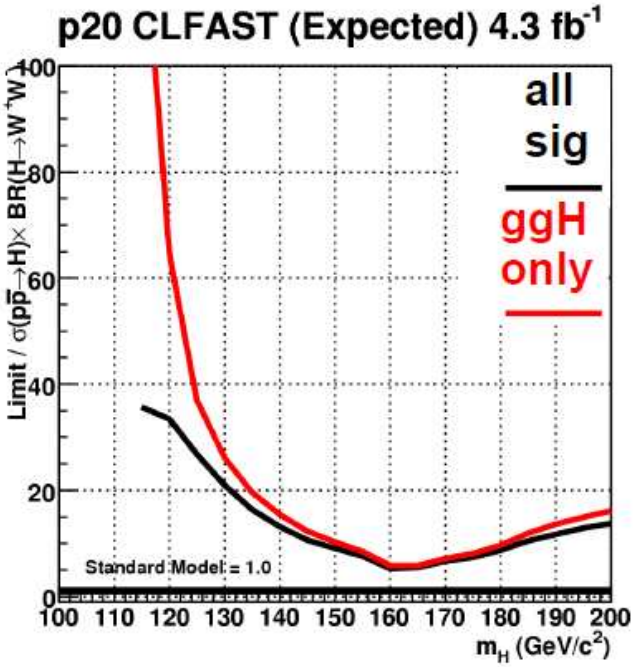

Figure 208: The expected limits using the Poisson log-likelihood ratio test statistic ignoring systematics when using all signals (black) and using (red) only. The main contribution at low mass comes from the WH associated production process.

References

[1] S. Weinberg, Phys. Rev. Lett. **19**, 1264–1266 (1967)

[2] P.W. Higgs, Phys. Rev. Lett. **12**, 132 (1964)

[3] F. Englert, R. Brout, Phys. Rev. Lett. **13**, 321 (1964).

[4] G.S. Guralnik, C.R. Hagen, T.W.B. Kibble, Phys. Rev. Lett. **13**, 585-587 (1964)

[5] ALEPH, DELPHI, L3 and OPAL Collaborations, "Search for the Standard Model Higgs Boson at LEP," arXiv:hep-ex/0306033v1 (2003)

[6] The DØ Experiment, http://www-d0.fnal.gov/index.html

[7] The Collider Detector at Fermilab (CDF), http://www-cdf.fnal.gov/

[8] TEVNPH Working Group for the CDF and D0 Collaborations, "Combined CDF and D0 Upper Limits on Standard Model Higgs-Boson Production with up to 6.7 fb^{-1} of Data," FERMILAB-CONF-10-257-E (2010)

[9] C. Amsler et al., Phys. Lett. B **667**, 1 (2008 and 2009 partial update for the 2010 edition)

[10] D. McMahon, "Quantum Field Theory Demystified," McGraw Hill (2008)

[11] A. Djouadi,"The Anatomy of Electro-Weak Symmetry Breaking. I: The Higgs boson in the Standard Model," arXiv:hep-ph/0503172v2 (2005)

[12] S. F. Novaes, "Standard Model: An Introduction," arXiv:hep-ph/0001283v1 (2000)

[13] P. Langacker, "Introduction to the Standard Model and Electroweak Physics," arXiv:0901.0241v1 [hep-ph] (2009)

[14] S. Dawson, "Introduction to Electroweak Symmetry Breaking," arXiv:hep-ph/9901280v1 (1999)

[15] J. Goldstone, A. Salam, S. Weinberg, Phys. Rev. Lett. **127**, 965–970 (1962)

[16] D. Griffiths, "Introduction to Electrodynamics," Prentice Hall (1999)

[17] MuLan Collaboration, D. B. Chitwood et al., Phys. Rev. Lett. **99**, 032001 (2007)

[18] S. Dawson, "Higgs Boson Branching ratios," http://quark.phy.bnl.gov/d̃awson/chap3.ps (2003)

[19] J.M. Campbell, R.K. Ellis, Phys. Rev. D **60**, 1130066 (1999)

[20] J. Casas, J. Espinosa, M. Quiros, "Improved Higgs Mass Stability Bound in the Standard Model and Implications for Supersymmetry," arXiv:hep-ph/9409458 (1994)

[21] K. Riesselmann, "Limitations of a Standard Model Higgs Boson," arXiv:hep-ph/9711456v1 (1997)

[22] M. Quiros, "Constraints on the Higgs boson properties from the effective potential," arXiv:hep-ph/9703412v2 (1997)

[23] LEP Electroweak Working Group et al.,"Precision Electroweak Measurements and Constraints on the Standard Model," CERN-PH-EP/2009-023 (2009)

[24] LEP Electroweak Working Group, http://lepewwg.web.cern.ch/LEPEWWG/plots/summer2010/

[25] http://maltoni.home.cern.ch/maltoni/TeV4LHC/SM.html

[26] M. Carena, H.E. Haber, Prog. in Part. Nucl. Phys. **50**, 152 (2003)

[27] TEVNPH Working Group for the CDF and D0 Collaborations, "Combined CDF and DØ Upper Limits on Standard Model Higgs-Boson Production with 2.1-5.4 fb^{-1} of Data," FERMILAB-CONF-09-557-E (2009)

[28] C.D. Curtis et al., IEEE Transactions on Nuclear Science, Vol. NS-26, No. 3, 3760-3762 (1979)

[29] Tevatron Run II Handbook, http://www-bd.fnal.gov/lug/runII_handbook/

[30] Fermilab Beams Division Accellerator Details Page, http://www-bd.fnal.gov/public/chain.html

[31] Fermilab Web Picturebook, http://www.fnal.gov/pub/about/whatis/picturebook/descriptions/00_635.html

[32] DØ Collaboration, V. Abazov et al., "The Upgraded DØ Detector," Fermilab-Pub-05/341-E (2006)

[33] A.R. Baden, "Jets and Kinematics in Hadronic Collisions," International Journal of Modern Physics A, Volume 13, Issue 11, (1998)

[34] M. Kirby, "SMT DAQ Shifter Tutorial" (2007)

[35] R. Angstadt et al., "The Layer 0 Inner Silicon Detector of the D0 Experiment," arXiv:0911.2522v1 [physics.ins-det] (2009)

[36] DØ Collaboration, S. Abachi et al., Nucl. Instrum. Methods A **338**, 185 (1994)

[37] U. Bassler, "Calorimetry," Hadron Collider Physics Summer School (2008)

[38] Particle Data Group, http://pdg.lbl.gov/2009/AtomicNuclearProperties/

[39] C. Grupen, "Physics of Particle Detection," Proceedings of the 10th ICFA School on Instrumentation in Elementary Particle Physics (2003)

[40] B.R. Martin, "Nuclear and Particle Physics: An Introduction," John Wiley & Sons, Ltd. (2006)

[41] DØ Collaboration, V. Abazov et al., "The Muon Run II DØ Detector," Fermilab-Pub-05/034-E (2005)

[42] M. Church et al., "Tevatron Run-II Beam Collimation System," Proceedings of the 1999 Particle Accelerator Conference (1999)

[43] T. Edwards et al., "Determination of the effective inelastic $p\bar{p}$ cross-section for the D0 Run II luminosity measurement," FERMILAB-TM-2278-E (2004)

[44] B. Casey et al., "The DØ Run 2b Luminosity Constant," DØ Note 5945 (2009)

[45] D. Edmunds, "Trigger Framework Tutorial," http://www.pa.msu.edu/hep/d0/l1/framework/tfw_tutorial_april_2009.pdf (2009)

[46] M. Mulhearn, "Level 2 Trigger System," http://www-d0.hef.kun.nl///fullAgenda.php?ida=a10523 (2010)

[47] J. Kraus, "L2 Shifter Tutorial," http://www-d0.hef.kun.nl///fullAgenda.php?ida=a09108 (2009)

[48] R. Jesik, "The V16 Global Trigger List," http://www-d0.fnal.gov/computing/algorithms/tsg/d0_private/Rick_v16-note.pdf

[49] J. Temple, R. McCroskey, K. Johns, "Upgrade of the Level 1 Muon Trigger Logic for the v13 Trigger List," DØ Note 4566 (2006)

[50] A. Maciel, S. Uzunyan, C. Leonidopoulos, J. Kowalkowski, "The L2-Muon Trigger, Methods and Algorithms," DØ Note 4756 (2005)

[51] A. Maciel, "Muon Timing at Level-2," DØ Note 4445 (2004)

[52] D. Bauer, "Level 3 Muon Tools: p17 certification," DØ Note 4887 (2005)

[53] B. Lee, "Data Flow in the D0 DAQ," DØ DAQ Shifer Tutorials (2009)

[54] DØ Reco,
http://www-d0.fnal.gov/computing/algorithms/howto/howtoreco.html

[55] Common Analysis Format (CAFe),
http://www-d0.fnal.gov/Run2Physics/cs/caf/

[56] DØ Common Sample Group,
http://www-d0.fnal.gov/Run2Physics/cs/index.html

[57] R. Van Kooten et.al, "Tracking Algorithm Recommendation Committee (TARC) Report II" (2003)
http://d0server1.fnal.gov/www/Computing/Web/Meeting/
Reviews/TARC/TARC2Recom.pdf

[58] G. Borrisov, "Technical Details of AA Tracking", Presentation at All DØ Meeting, Feb. 28, 2003

[59] A. Khanov, "HTF: histogramming method for finding tracks," DØ Note 3778 (2000)

[60] A. Schwartzman, C. Tully, "Primary Vertex Reconstruction by Means of Adaptive Vertex Fitting," DØ Note 4918 (2005)

[61] A. Garcia-Bellido et al., "Primary Vertex certification in p14," DØ Note 4320 (2004)

[62] A. Schwartzman, Y. Peters, H. Greenlee, "Adaptive Primary Vertex Certification in p17," DØ Note 5192 (2006)

[63] E. Busato, B. Andrieu "Jet Algorithms in the DØ RunII Software," DØ Note 4457 (2004)

[64] G. Blazey et al., "Run II Jet Physics: Proceedings of the Run II QCD and Weak Boson Physics Workshop," arXiv:hep-ex/0005012v2 (2000)

[65] A. Harel, "Jet ID Optimization," DØ Note 4919 (2005)

[66] A. Harel, R. Wagner, "Improved L1 Confirmation," DØ Note 4932 (2005)

[67] B. Casey, G. Facini, M. Rangel, "Jet ID/VC Efficiencies and Scale Factors using Dijet events," DØ Note 6058 (2010)

[68] DØ Jet ID Page, http://www-d0.fnal.gov/phys_id/jets/jetid.html

[69] The DØ Collaboration, "Measurement of the inclusive jet cross section in $p\bar{p}$ collisions at $\sqrt{s}$= 1.96 TeV," PRD draft (2010)

[70] DØ Jet Energy Scale http://www-d0.fnal.gov/phys_id/jes/public/plots_v7.1/

[71] N. Makovec, J.F. Grivaz, "Shifting, Smearing and Removing Simulated Jets," DØ Note 4914 (2005)

[72] J.F. Grivaz, "JSSR/JES uncertainties: recommendations for ICHEP," presentation at Joint Algorithms/Physics Conveners Meeting (2010) http://www-d0.hef.kun.nl//fullAgenda.php?ida=a101032&fid=57

[73] O. Peters, "Muon Segment Algorithm," http://www-d0.fnal.gov/nikhef/muon_reco/segmentreco/

[74] B. Tuchming, "Update of Muon Central Matching for p16," Presentation at MuonID/Algorithms Meeting, Oct. 21, 2003

[75] D. Whiteson, "Muon Tracking in the Calorimeter," DØ Note 3996 (2002)

[76] P. Calfayan et al., "Muon Identification Certification for p17 data," DØ Note 5157 (2006)

[77] DØ Muon Algorithms and Identification group "Muon Identification Certification for the Summer 2009 Extended Dataset," DØ Note 6025 (2010)

[78] M. Cooke et al., "Muon Momentum Oversmearing Update for p20 Data," DØ Note 6031 (2010)
TMBMuon::ActAsSmeared code for muon smearing,
http://www-d0.fnal.gov/Run2Physics/cs/caf/classes/html/TMBMuon_8cpp-source.html

[79] DØ EM Alogrithms and Idenfication group, *emreco* source code,
emreco/rcp/EMReco.rcp, emreco/rcp/EMReco-scone.rcp,
emreco/rcp/CalScone0401.rcp

[80] O. Atramentov, D. Bandurin, Y. Liu, H. Yin, "Study of electron track matchining parameters with Run IIb data," DØ Note 5635 (2008)

[81] DØ EM Alogrithms and Idenfication group, *em_util* source code,
em_util/src/EMTrackMatchChi2.cpp,
em_util/rcp/EMTrackMatchChi2_v2_(data/mc).rcp

[82] M. Narain, "Electron Identification in the DØ Detector," FERMILAB-Conf_93/054-E (1992)

[83] DØ EM idenfication variables,
http://www-d0.fnal.gov/phys_id/emid/d0_private/variables.html

[84] M. Aoki, "Electron Likelihood in p20," DØ Note 5675 (2009)
DØ EM ID group, "Electron Likelihood in p14," DØ Note 4449 (2004)

[85] http://www-d0.fnal.gov/Run2Physics/cs/caf/classes/
html/classTMBCaloCell.html

[86] S. Trincaz-Duvoid, P. Verdier, "Missing ET Reconstruction in p17," DØ Note 4474 (2004)

[87] S. Calvet, P. Verdier, E. Kajfasz, "Towards Missing ET Certification and Unclusered Energy Studies," DØ Note 4927 (2005)

[88] S. Zelitch et al., "Search for standard-model Higgs production in the lepton + jets final state for $H \to WW \to \ell\nu jj$ decay in 5.4 fb^{-1} of Run II Data," DØ Note 5851 (2010)

[89] Sekaric,
http://www-d0.hef.kun.nl//askArchive.php?base=agenda
&categ=a06635&id=a06635s1t1/transparencies
Couderc,
http://www-d0.hef.kun.nl//askArchive.php?base=agenda
&categ=a06647&id=a06647s1t1/transparencies
Duflot,
http://www-d0.hef.kun.nl//askArchive.php?base=agenda
&categ=a061360&id=a061360s1t2/transparencies

[90] T. Sjöstrand et al., "PYTHIA 6.3 Physics and Manual," LU TP 03-38, hep-ph/0308153 (2003)

[91] M.L. Mangano et al.,"ALPGEN, a generator for hard multiparton processes in hadronic collisions," hep-ph/0206293v2 (2003)

[92] J. Pumplin et al., "New Generation of Parton Distributions with Uncertainties from Global QCD Analysis," arXiv:hep-ph/0201195v3 (2002)

[93] F. Caravaglios, M.L. Mangano, M. Moretti, R. Pittau, "A New Approach to Multi-jet Calculations in Hadron Collisions," arXiv:hep-ph/9807570v1 (1998)

[94] M. Mangano, "Merging multijet matrix elements and shower evolution in hadronic collisions,"
Presentation at 2004 Lund University
http://mlm.web.cern.ch/mlm/talks/lund-alpgen.pdf

[95] DØ ALPGEN parameters,
http://www-d0.fnal.gov/computing/MonteCarlo/generators/common_alpgen.html

[96] Y. Fisyak, J. Womersley, "DØgstar: DØ GEANT Simulation o f the Total Apparatus Response," DØ Note 3191 (1997)

[97] GEANT Manual,
http://wwwasdoc.web.cern.ch/wwwasdoc/geantold/H2GEANTBASE001.html

[98] DØ Sim Page,
http://www-d0.fnal.gov/computing/MonteCarlo/simulation/d0sim.html

[99] ggH: Grazzini and de Florian, Phys. Lett. B **674**, 291-294 (2009) (arXiv:0901.2427[hep-ph]). WH and ZH: Baglio and Djouadi, "Predictions for Higgs production at the Tevatron and the associated uncertainties," arXiv:1003.4266 [hep-ph] (2010)

[100] M.L. Mangano et al., "Matching Parton Showers and Matrix Elements," hep-ph/0602031 (2006)

[101] D. Gillberg, "Heavy Flavour Removal and Determination of Weighting Factors for ALPGEN W+jets Monte Carlo," DØ Note 5129 (2006)

[102] A.Pukhov et al,"CompHEP", hep-ph/9908288 (1999)

[103] M. Angelou et al., "Top Trigger Efficiency Measurements and the top_trigger package," DØNote 4512 (2004)

[104] P. Calfayan, "Combination of Single Muon Triggers in p17 data by using an inclusive OR," DØ Note 5329 (2008)

[105] M. Syphers, "Hadron Collider Accellerator Basics," Hadron Collider Physics Summer School (2008)

[106] H. Schellman, "The longitudinal shape of the luminous region at D0," DØNote 5142 (2006)

[107] W. Fisher, J. Haley, D. Price, "Studies of Alpgen parameters, corrections and associated uncertainties," DØ Note 5966 (2009)

[108] The DØ Collaboration, "Measurement of the shape of the boson transverse momentum distribution in $p\bar{p} \to Z/\gamma* \to ee + X$ events produced at $\sqrt{s} = 1.96$ TeV," arXiv:0712.0803v2 [hep-ex] (2008)

[109] M. Shamim, T. Bolton, "Generator Level Reweighting of pT of Z Boson," DØ Note 5565 (2008)

[110] G. Hesketh, "W pT Re-weighting for Alpgen and Pythia," DØ Note 5786 (2008)

[111] S. Muanza, "A Compilation of MCFM v5.1 Cross Sections," DØ Note 5300 (2006)

[112] J.-F. Grivaz, "News," Presentation at DØ V+Jets Working Group Meeting, June 24, 2008

http://www-d0.hef.kun.nl/fullAgenda.php?ida=a081147

[113] S. Moch and P. Uwer, Phys. Rev. D **78** 034003 (2008) [arXiv:0804.1476].

[114] Z. Sullivan, E. Berger, "Isolated leptons from heavy flavor decays: Theory and data," arXiv:1003.4997v3 [hep-ph] (2010)

[115] L. Breiman, "Random Forests," Machine Learning **45**, 5-32 (2001).

[116] W. Fisher, J. Haley, J. Sekaric, "First Measurement of Diboson Production in Lepton Plus Jet Decays," DØ Note 5544 (2008)

[117] I. Narsky, "StatPatternRecognition: A C++ Package for Statistical Analysis of High Energy Physics Data," arXiv:physics/0507143v1 (2005)

[118] L. Breiman, J. Friedman, R. Olshen, C. Stone, "Classification and Regression Trees," Wadsworth International Group, (1984)
S. B. Gelfand, C. S. Ravishankar, E. J. Delp, "An iterative growing and pruning algorithm for classification tree design," IEEE Transaction on Pattern Analysis and Machine Intelligence, 13(2):163–174, (1991)

[119] I. Narsky, "Optimization of Signal Significance by Bagging Decision Trees," arXiv:physics/0507157v1 (2005)

[120] NIST/SEMATECH e-Handbook of Statistical Methods,
"Kolmogorov-Smirnov Goodness-of-Fit Test,"
http://www.itl.nist.gov/div898/handbook/eda/section3/eda35g.htm

[121] W. Fisher, "Collie: A Confidence Level Limit Evaluator," DØ Note 5595 (2010)

[122] DØ Higgs Group Meeting,
http://www-d0.hef.kun.nl//askArchive.php?base=agenda&categ=
a091096&id=a091096s1t0/transparencies

[123] T. Andeen et al., "The DØ experiment's integrated luminosity for Tevatron Run IIa," FERMILAB-TM-2365-E (2006)

[124] DØ Collaboration, "Combined Upper Limits on Standard Model Higgs Boson Production from the DØ Experiment in 2.1-5.4 $fb^{-}1$ of Data," DØ Note 6008-CONF (2009)

[125] C. Schwanenberger, Correspondence with DØ Top Team, June 17, 2010

[126] M. Seymour, "Underlying Event Models," Presentation at the 2004 TEV4LHC conference,
http://conferences.fnal.gov/tev4lhc/talks/040916_TeV4LHC_QCD/
05_Michael_Seymour_1_M.Seymour_UEtalk.pdf

[127] W. Fisher, "Systematics Uncertainty Update," Talk at 2009 DØ Low Mass Higgs working group meeting,
http://www-d0.hef.kun.nl//fullAgenda.php?ida=a

[128] K. Harder, "PDF Reweighting Package for CAF," Presentation at 2006 DØ Common Samples Group meeting,
http://www-d0.hef.kun.nl//fullAgenda.php?ida=a061130

[129] V. Buscher, J.F. Grivaz, T. Nunnemann, M. Wobisch, "Conclusions of Mini-Workshop on PDF uncertainties and related topics," DØ Note 4618 (2004)

[130] W. Fisher, "Calculating Limits for Combined Analyses," DØ Note 4975 (2006)

[131] W. Fisher, "Collie: A Confidence Level Limit Evaluator," Tutorial given at Fermilab, June 15, 2009

[132] W. Fisher, "Systematics and Limit Calculations," DØ Note 5309, (2006).

[133] J. Stark, "Time dependence of the absolute ICD energy scale from low energy jets in ZB events," Presentation at DØ Horn Force meeting, Aug. 27, 2010

[134] CDF Official Luminosity Web Page
http://www-cdfonline.fnal.gov/ops/opshelp/stores/kumac/store_tot.gif

[135] T. Junk, "Sensitivity, Exclusion and Discovery with Small Signals, Large Backgrounds, and Large Systematic Uncertainties," CDF/DOC/STATISTICS/PUBLIC/8128 (2007)

[136] DØ RunII Operations Page,
http://d0server1.fnal.gov/Projects/Operations/D0RunII_DataTaking.htm, July 17, 2010

[137] D. Denisov, G. Punzi, R. Roser, S. Soldner-Rembold, "Answers to PAC Questions on Higgs Searches at CDF and DØ," Presentation at Fermilab Physics Advisory Committee meeting, Aug. 27, 2010

[138] R. Assmann, Status of LHC Operations Report, July 27, 2010
http://indico.cern.ch/getFile.py/access?contribId=0
&resId=1&materialId=slides&confId=101927

[139] The CMS experiment, http://cms.web.cern.ch/cms/index.html

[140] The ATLAS experiment, http://atlas.ch/

[141] M. Gataullin, "Prospects for Higgs Boson Searches with CMS," Presentation at ICHEP 2010

[142] T. Masubuch, "ATLAS Higgs Sensitivity for 1 fb^{-1}at the LHC running at 7 TeV," Presentation at ICHEP 2010

[143] Bogdan A. Dobrescu, Joseph D. Lykken, "Semileptonic decays of the standard Higgs boson," arXiv:0912.3543v1 [hep-ph] (2009)